

Measurement of Muon Neutrino Interactions in Carbon and Water with the T2K Near Detector ND280

THÈSE

*présentée à la Faculté des Sciences de l'Université de Genève
pour obtenir le grade de docteur ès Sciences, mention Physique*

par

Lucie Maret
de
Vollèges (Valais, Suisse)

Thèse n° 5411



**UNIVERSITÉ
DE GENÈVE**

FACULTÉ DES SCIENCES

DOCTORAT ÈS SCIENCES, MENTION PHYSIQUE

Thèse de Madame Lucie MARET

intitulée :

**«Measurement of Muon Neutrino Interactions in Carbon and
Water with the T2K Near Detector ND280»**

La Faculté des sciences, sur le préavis de Monsieur A. BLONDEL, professeur ordinaire et directeur de thèse (Département de physique nucléaire et corpusculaire), Monsieur F. SANCHEZ NIETO, professeur ordinaire et codirecteur de thèse (Département de physique nucléaire et corpusculaire), Madame M. KOWALSKA, professeure assistante (Département de physique nucléaire et corpusculaire), Madame S. BOLOGNESI, professeure (Département de physique des particules, Commissariat à l'énergie atomique et aux énergies alternatives (CEA), Saclay, Gif-sur-Yvette, France), autorise l'impression de la présente thèse, sans exprimer d'opinion sur les propositions qui y sont énoncées.

Genève, le 6 novembre 2019

Thèse - 5411 -

Le Doyen

N.B. - La thèse doit porter la déclaration précédente et remplir les conditions énumérées dans les "Informations relatives aux thèses de doctorat à l'Université de Genève".

Crois et tu comprendras ; la foi
précède, l'intelligence suit.

Saint Augustin

The story of neutrino physics started less than hundred years ago and many exciting discoveries have been made over the past century since W. Pauli postulated the existence of this mysterious particle, detected for the first time in the 1950s. However, many crucial questions still remain unanswered. The phenomenon of neutrino oscillations was demonstrated by the SNO and Super-Kamiokande experiments. This discovery showed that neutrinos have mass, which requires an extension of the Standard Model, in a non-unique way. Since then, more precise measurements of the parameters governing neutrino oscillations have been performed, but some of the questions are remaining. Nowadays modern long-baseline neutrino oscillation experiments are probing the CP-violation phase δ_{CP} , searching for Charge-Parity violation in the lepton sector. A large contribution to the uncertainty on oscillation measurements comes from nucleus-neutrino interactions. It is therefore essential to increase our neutrino cross-section knowledge and to study nuclear effects that occur when neutrino interact with nuclei in order to make precision measurements in neutrino physics.

This thesis relates a neutrino cross section measurement on carbon and on oxygen nuclei done with the near detector ND280 of the long-baseline neutrino experiment T2K. This experiment, based in Japan, consists of a muon (anti-)neutrino beam produced at J-PARC and sent towards the Super-Kamiokande far detector. The latter is designed to probe muon neutrino disappearance and electron neutrino appearance in the muon neutrino beam. Comparisons of neutrino and anti-neutrino mode measurements provide information about CP-violation. The ND280 detector, located near the neutrino beam source, allows to constrain the unoscillated neutrino flux and to determine neutrino cross sections.

Charged-current muon neutrino interactions with no pion in the final state are studied thanks to very large statistics coming from ND280 measurements. A selection of events with interactions in the Fine-Grained Detectors (FGDs) water and scintillator layers is conducted and used to perform a binned likelihood fit in outgoing muon kinematic variables. Measuring neutrino interactions on oxygen is important for T2K oscillation measurements as the far detector is made of water. Event samples with interactions in both materials are used in a joint-analysis. The cross section on carbon is extracted from the fully-active plastic fibers in the two FGDs and the one on oxygen is evaluated thanks to interactions in the interleaved water layers that are reconstructed in the scintillator layers of the second FGD. The idea of the fit is to vary a set of parameters until the prediction best describes the data. Template parameters reweight the number of events in each bin, while systematic parameters add prior knowledge about neutrino flux, cross-section model and detector response. Cautious studies have been carried on in order to evaluate systematic uncertainties and to propagate them onto the final measurement. Statistical uncertainties dominate, therefore improved results are expected in the future.

L'histoire de la physique des neutrinos commença il y a moins d'un siècle, lorsque W. Pauli postula l'existence d'une particule "qu'on ne peut pas détecter"¹. Cette particule *invisible* fut tout de même détectée, et ce pour la première fois dans les années cinquante. Par la suite, plusieurs phénomènes passionnants furent découverts en physique des neutrinos. Cependant, plusieurs questions primordiales pour notre compréhension de l'Univers en lien avec ces mystérieuses particules restent ouvertes. Les expériences SNO et Super-Kamiokande démontrèrent par leurs observations que les neutrinos *oscillent*, impliquant que ceux-ci ont une masse. Hors, cette assertion est contraire aux prédictions du Modèle Standard. Depuis, les paramètres d'oscillation des neutrinos ont été mesurés avec une plus grande précision, mais certaines questions restent sans réponse. De nos jours, les expériences observant l'oscillation des neutrinos sur des longues distances à l'aide de faisceaux cherchent à montrer que la symétrie Charge-Parité (CP) est brisée par les leptons. Or, les incertitudes sur ces mesures sont dominées par notre méconnaissance des interactions de neutrinos avec les noyaux atomiques. Élargir notre compréhension des réactions nucléaires induites par des interactions de neutrinos est donc déterminant pour atteindre des mesures de précision en physique des neutrinos.

Ce document décrit en détails une mesure de section efficace de neutrinos avec des noyaux atomiques de carbone et d'oxygène effectuée à l'aide du détecteur proche ND280 de l'expérience T2K. Cette expérience de physique des particules, basée au Japon, consiste en un faisceau de neutrinos ou d'anti-neutrinos muoniques qui est produit à J-PARC et envoyé en direction du détecteur lointain Super-Kamiokande. Ce dernier permet d'étudier la disparition de neutrinos muoniques ainsi que l'apparition de neutrinos électroniques dans le faisceau constitué initialement de neutrino muoniques. En comparant les résultats obtenus avec un faisceau de neutrino et d'anti-neutrinos, il est possible d'extraire des informations sur la violation CP. Le détecteur proche ND280 est situé à proximité de la source de neutrinos et permet d'obtenir des mesures du flux de neutrinos avant qu'ils n'oscillent et de déterminer différentes sections efficaces.

Dans le cadre de cette thèse, la section efficace de neutrinos muoniques interagissant par courants chargés et ne produisant pas de pion est étudiée à l'aide de données accumulées par le détecteur ND280 entre 2010 et 2017. Des événements caractérisés par une interaction de neutrino dans les couches de scintillateurs et d'eau des détecteurs à grains fins (FGD1 et FGD2) sont sélectionnés, puis traités grâce à une méthode de maximum de vraisemblance (*maximum likelihood fit*) optimisée pour réduire autant que possible la dépendance aux modèles. Cette méthode consiste à analyser de manière conjointe des interactions produites dans le carbone constituant les fibres scintillantes des deux FGDs ainsi que des interactions dans les molécules

¹W. Pauli, 1930.

d'oxygène des couches d'eau intercalées entre les couches de scintillateurs du second FGD. Ces dernières sont reconstruites grâce aux fibres scintillantes suivant la couche d'eau. La méthode du maximum de vraisemblance consiste à faire varier un ensemble de paramètres jusqu'à trouver une prédiction, dépendant de ces paramètres, qui décrit le plus fidèlement possible les données mesurées. Les événements sont répartis dans des *bins* associés à des intervalles de valeurs de quantité de mouvement et de cosinus de l'angle d'émission du muon produit dans la réaction. Un paramètre est attribué à chacun de ces *bins*, permettant de pondérer son contenu, et de plus des paramètres systématiques sont variés afin d'ajouter des connaissances préalables sur le flux de neutrinos, le modèle de sections efficaces ainsi que la réponse du détecteur. Une étude attentive des erreurs systématiques s'appliquant à nos mesures a été menée afin d'évaluer les marges d'incertitude sur les mesures finales. Il s'avère que la composante dominante de l'incertitude totale provient de l'erreur statistique, ce qui présage une marge d'amélioration certaine pour de futures mesures qui comprendront un nombre plus élevé d'événements.

Acknowledgements

This thesis work is obviously about physics, but it is also about people I have met throughout this big adventure. People who helped me not only debugging my code or understanding physics puzzles, but also people with whom I had *nihonshu* at Shinchon's or at the Pono-pono at the end of very tough meeting days in Tokai, or people who sometimes had to endure my bad moods in stressful moments. So I would like to thank everyone who contributed to the content of this work but also participated in keeping my mood and motivation at their best during the time of my PhD thesis.

To begin I would like to thank Pr. Alain Blondel, who offers me the opportunity to start this thesis and introduced me to the T2K collaboration. Thank you for helping me doing my first steps through the big jungle of a PhD thesis. I also thank Pr. Federico Sanchez as well, who guided me during this last year and would always give me precious advises in the moments I was lost and throughout the finalisation of the thesis. Thank you for being not only a good scientist, but also an understanding and open-minded person. I also thank the Swiss National Fund for Research and the Département de l'Instruction Public for financing the research I have been conducting for the past four years.

I thank Etam Noah for his helpful proofreading of this document and Laura Molina Boeno for reviewing my work within the T2K collaboration. I want to thank Sara Bolognesi and Magdalena Kowalska for having accepted to be part of the jury for this thesis work and to review it. And I feel very grateful to Sara who, as I was starting my work in T2K and had no idea what to work on for my thesis, proposed me to join the cross-section group by working with her, Margherita Buizza Avanzini and Sandrine Emery. I thank the two of them as well for their help, and specially Margherita who helped me a lot to start this project and kept supporting me and answering questions all the way towards the end of this work. A big thanks to Ciro Riccio, for your help, for your very nice and clean scripts you kindly shared with me, as well as for the drinks we shared. And a huge thanks to Andrew Cudd, for turning the cross-section fitter into such a userfriendly and fast framework. I will never thank you enough for how useful your help has been while working on the code.

This analysis would never have evolved that way without the discussions I have had within the T2K cross-section and selection development groups during meetings or on Slack. So I would like to thank everyone involved in these discussions for their comments and feedbacks, in particular Sasha Izmaylov who helped me a lot in the selection developments.

I have to dedicate a special paragraph to Stephen Dolan, who was able to make me feel confident and hopeful again every time I was feeling completely lost and had no idea what to do. You have been so patient answering my (sometimes stupid) questions and your advises have been an invaluable support. Thanks also for all the menu translations in *izakayas* and for our

discussions on the chairlift in Hokkaido. I hope you will keep sharing your enthusiasm about physics and skiing with everyone!

I would also like to thank my other T2K-ski fellows, David, Stéphane, Lukas, Luke, Sophie, Pierre, Clarence, with whom I had the chance to enjoy the Japanese powder in Myoko and Hokkaido after having a hard time during T2K collaboration meetings. Thank you for the good time spent on the piste, eating *ramen* and drinking *nihonshu* after skiing.

A special thanks to the J-PARC user's office secretaries. You have been so lovely and welcoming during each of my stays in Tokai, and it was a pleasure to take part of your cultural DIY activities. Thank you Mako, for your friendship and for having recommended to me the best fabrics stores in Tokyo, which I would never forget to visit after T2K collaboration meetings.

Teaching is also a part of a thesis and I had the great chance to be part of the Physiscope, hosting classes at the Université de Genève and presenting physics experiments to the general audience. I enjoyed transmitting my fascination for physical phenomena and showing to kids and teenagers that physics can be a lot of fun. I enjoyed their curiosity and questions and, most of it, I enjoyed to see their happy faces when they were leaving the Physiscope room. So I thank Olivier, Céline, the technicians and the rest of the Physiscope team for their amazing work.

Un autre aspect, moins intéressant, d'un doctorat est la partie administrative. Heureusement, la disponibilité et l'efficacité de Liliane ont été une aide inconsiderable. Merci aussi à Nathalie, sans qui notre bureau n'aurait pas rendu jalouses toutes les personnes s'y arrêtant. Je me rappellerai toujours de la journée passée à faire des déménagements, remplir des bennes de vieux classeurs et sortir des vieilles étagères en métal à l'esthétique douteuse pour les remplacer ensuite par de la jolie verdure. Merci d'avoir égayé ces moments lorsque j'ai occupé ce grand bureau toute seule pendant plusieurs mois!

Merci, avant ça, à Leïla, qui a été ma première voisine de bureau et qui m'a énormément aidée lors de mes débuts de doctorat. J'aurai gardé en tête certains de tes conseils jusqu'au bout. Merci aussi à Saba qui, en plus d'être physicienne, a des talents de jardinière et a démultiplié les pots de plantes vertes de manière impressionnante. Grâce à toi, notre bureau est devenue une jolie jungle. Merci Robert, pour tes nombreux vélos, skis, souliers de marche et crampons qui défilent dans notre bureau, et pour ta bonne humeur. Merci à mes collègues-pause-de-midi-à-la-RTS, Matthieu, Yves, Cyril, Séb, Frank, Andrii et Francesco, pour ces bons moments de détente et de rires. Et pendant que j'y suis, merci à l'équipe de la cafétéria de la RTS pour votre sympathie et pour ces délicieux repas quotidiens qui m'ont nourrie tout au long de mon doctorat!

Merci du fond du coeur à ma collègue de travail, voisine de bureau et amie précieuse Stéphanie, avec qui j'ai ri et pleuré, mais surtout ri. Nos pauses pâtisserie ont complètement changé la couleur de mes journées de travail.

Merci mes chères Deb, Sandy, Gigi et Cathy, pour les paillettes que vous mettez dans ma vie. Pour ces moments forts en émotions partagés avec vous sur scène lors de week-ends qui m'ont permis de déconnecter de mon travail quand j'en ai eu besoin.

Merci mes amies Caro et Oriane, qui font partie des femmes les plus courageuses que je connaisse. C'était une fierté de participer avec vous à la grève féministe suisse le 14 juin 2019, je n'oublierai jamais cette journée mémorable. Merci aussi à Flore et Maman, pour votre compagnie et votre engagement avec moi lors de la manifestation.

Merci Sylvain, pour les moments de douceur et de rires que tu as apportés à la fin de mon doctorat. Ma fin de thèse n'aurait jamais été aussi apaisée sans toi.

Et enfin, Maman, Papa, je vous remercie d'avoir éveillé ma curiosité pour le monde qui nous entoure et mon ouverture d'esprit. Papa, merci de m'avoir initié aux joies de l'informatique dès mon plus jeune âge et Maman, merci de m'avoir encouragée à affronter un monde majoritairement masculin pour m'y faire ma place. Merci pour votre soutien inconditionnel du début à la fin de mes études.

Contents

Abstract	iii
Résumé	v
Acknowledgements	vii
Introduction	1
1 Neutrino Physics	3
1.1 A brief history of the neutrino	3
1.1.1 The particle that cannot be detected	3
1.1.2 The different types of neutrinos	4
1.1.3 The problem of solar neutrinos	6
1.2 Neutrinos oscillation	6
1.2.1 Neutrinos oscillation theory	6
1.2.2 Why do neutrinos <i>oscillate</i> ?	10
1.2.3 Neutrino oscillation experiments	14
1.3 Neutrino interactions for accelerator based experiments	15
1.3.1 Charged-Current Quasi-Elastic Interactions	16
1.3.2 Charged-Current Resonant Interactions	17
1.3.3 Deep Inelastic Scattering	18
1.3.4 Nuclear effects in neutrino-nucleus scattering	18
1.3.5 Neutrino-nucleus interaction generators	21
1.4 Neutrino energy reconstruction	23
2 The T2K Experiment	25
2.1 The T2K beam	26
2.1.1 Off-axis technique	27
2.1.2 The neutrino flux	28
2.2 The Far Detector Super-Kamiokande	29
2.3 The ND280 off-axis near detector	31
2.3.1 The Multi-Pixel Photon Counter (MPPC)	32
2.3.2 The Pi-Zero Detector (P0D)	32
2.3.3 The Fine-Grained Detectors (FGD)	33
2.3.4 The Time Projection Chambers (TPC)	35

2.3.5	The UA1 Magnet	37
2.3.6	The Side Muon Range Detector (SMRD)	38
2.3.7	The Electromagnetic Calorimeter (ECal)	38
2.4	The INGRID on-axis near detector	38
2.5	The ND280 software	39
3	Motivations, strategy and inputs for the cross-section extraction	41
3.1	Motivations	41
3.1.1	Benefits of a FGD1 + FGD2 joint analysis	41
3.1.2	Improvements with respect to previous T2K analyses	42
3.2	Analysis strategy	42
3.2.1	Cross section and signal definition	43
3.2.2	Cross-section extraction	44
3.3	Event selection and other inputs for cross-section extraction	47
3.3.1	Monte Carlo and data samples	47
3.3.2	Analysis binning	49
3.3.3	Event selection	51
4	Evaluation of the uncertainties on cross-section measurement	71
4.1	Detector systematic uncertainties	71
4.1.1	Uncertainty evaluation	72
4.1.2	The covariance matrix	73
4.1.3	Resulting pre-fit detector uncertainty inputs	74
4.2	Flux systematic uncertainties	75
4.3	Model systematic uncertainties	77
4.4	Proton FSI systematic uncertainty	79
4.5	Uncertainties on the final measurement	81
4.6	Estimation of the contribution from each source to the total uncertainty	82
5	Final cross-section results	85
5.1	Fitter specific features	85
5.1.1	Fit parameters	85
5.1.2	χ^2 definitions and goodness of fits	86
5.2	Fit validation	86
5.3	Post-fit parameters and event distributions	87
5.4	Cross-section measurement	94
5.4.1	Integrated neutrino flux	94
5.4.2	Number of target nucleons	94
5.4.3	Cross-section results in kinematic bins	96
5.4.4	Integrated cross-section results	108
5.4.5	Integrated cross-section results in restricted phase space	109
	Conclusion and future prospects	111
A	Vertex backward migration in FGD2	113
B	Fit validation	141
	Bibliography	195

Why is matter dominating over antimatter in our Universe? This question is still puzzling physicists nowadays, as there should be as much antimatter as matter existing in the Universe if they have symmetrical properties. One of the necessary conditions for having only very little antimatter is the violation of Charge-Parity (CP) symmetry [1]. CP violation is allowed within the Standard Model of particle physics and it has been observed in quark mixing [2]. However, this asymmetry is not sufficient to explain the matter-antimatter asymmetry in the Universe. Exploring CP violation in the leptonic sector could provide new hints to answer this fundamental question. It has now been observed through neutrino oscillation [3] that neutrinos, which were expected to be massless, do have mass. The fact that they have mass opens the question: do neutrinos violate CP similarly to quarks? Modern long-baseline neutrino oscillation experiments are close to providing an answer to this question with measurements of the CP-violating phase (δ_{CP}) in the leptonic mixing matrix, known as the PMNS matrix.

The T2K Experiment is exploring neutrino oscillation phenomena by measuring muon neutrino disappearance and electron neutrino appearance in muon neutrino and anti-neutrino beams produced by an accelerator. Recent results have been published and show evidences for CP violation: CP-conservation, corresponding to $\delta_{\text{CP}} = 0, \pi$, is *not* included in the 2σ confidence interval for the CP violating phase [4].

A predominant source of uncertainty in oscillation measurements comes from the lack of knowledge of neutrino-nucleus interactions. It is therefore crucial to probe accurately neutrino cross sections in order to improve the precision of CP-violating phase measurements. Within this thesis work muon neutrino interactions with water and hydrocarbon nuclei are studied. A flux integrated cross section is measured with the T2K near detector ND280.

The first chapter gives an introduction to the history of the neutrino and to the physics theory of neutrino oscillation and neutrino-nucleus interactions. After that the T2K Experiment and its detectors are presented in the second chapter. In the third and forth chapters all the steps of this analysis are exposed and details are provided on the analysis strategy, event selection and evaluation of cross-section uncertainties. Finally the extracted cross-section is presented in the last chapter.

1.1 A brief history of the neutrino

Before describing neutrino physics in details it is worth looking back in the past and review the history of this mysterious particle. We will go chronologically through the important discoveries made in neutrino physics in order to introduce major physical phenomena and challenges in this field. The history of neutrino prediction and its first detection will be presented first. Then we will expose the various problems physicists had to face while studying neutrinos, for instance answering the question of how many different neutrino types exist and solving the problem of solar neutrino anomaly.

1.1.1 The particle that cannot be detected

It all started with observations of the β -decay. This process consists in a nucleus of atomic number Z decaying into a nucleus of atomic number $Z - 1$ accompanied by an electron. An example of β -decay is $C_6^{14} \rightarrow N_7^{14} + e^-$. The outgoing atom has a smaller mass than the parent atom, therefore the electron was expected to carry the energy difference in order to fulfill the energy conservation principle. However observations showed that not only the electron energy is not enough to recover the total energy but the energy distribution of the electron is continuous! The expected electron energy is represented in red in Fig. 1.1. In 1930 W. Pauli wrote a famous letter proposing the existence of a neutral particle of spin $\frac{1}{2}$ and zero mass that would be emitted in the β -decay alongside the electron. The missing energy would be carried by that invisible light particle, solving the energy conservation problem, but creating a new sort of problem : W. Pauli postulated a particle that cannot be detected. A few years later, E. Fermi wrote a theory for the β -decay where he took into account the recently postulated neutral light particle [5]. The probability of interaction was estimated to be $\sigma < 10^{-44} \text{ cm}^2$ by H. Bethe and R. Peierls [6].

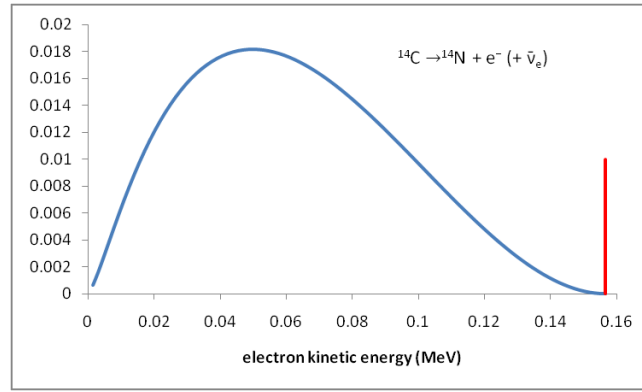


Figure 1.1: Energy spectrum of the outgoing electron in a β -decay. Source : t2k-experiment.org

After the Second World War many developments were made in nuclear fission. As neutrinos are produced in nuclear fission physicist F. Reines, who was involved in nuclear weapons tests, thought of using the bomb for direct detection of neutrinos. Teaming up with the experimentalist C. Cowan he faced the huge technical challenge of designing a detector that is able to resist close to the nuclear bomb, take data in a short time and be large enough to detect neutrinos. They designed a large detector for that time back in the fifties : one cubic meter! Measurements close to bomb tests not being the most convenient ones, they then started to measure particles close to the Brookhaven nuclear reactor. In 1953 hints of signal were detected but there was still a lot of background, that turned out to be coming from cosmic rays. Hence they decided to locate the detector underground so that the Earth is shielding the detection from cosmic rays. The improved detector was located 11 meters from the reactor at Savannah River plant and 12 meters underground. Eventually a non ambiguous signal was measured, neutrino has been observed for the first time [7]. Frederick Reines was awarded by the Nobel Prize in 1995 for the first detection of the neutrino.

1.1.2 The different types of neutrinos

In the 1950s only two types of charged leptons were known, the electron and the muon, easily differentiated by their masses. The tau lepton was discovered much later in 1975. Moreover the charged leptons were known to have an associated antiparticle with opposite charge. Two questions therefore arose : Is the neutrino different from its antiparticle? Are the neutrinos produced with an electron or a muon different?

Answering the first question was done by investigating the conversion of some heavy isotopes involving a neutrino in the process. According to the lepton number conservation law, stating that the number of leptons minus the number of antileptons is conserved, the β -decay produces an antineutrino whereas the isotope is reacting with a neutrino. Thus the isotope reaction should only be observed if the neutrino and antineutrinos would be the same particles. Ray Davis was able to investigate this process in the period 1955-1960, showing that neutrino and antineutrino are distinct particles.

The second question can be resolved by looking at the neutrino produced in a pion decay, which is associated to a muon, and find out if it can then be converted into an electron. This process would show that the neutrinos associated with muons and electrons are of the same kind. The energy reached by nuclear decay being much too small to produce pions or muons directly, a proton beam from an accelerator was required. In the experiment conducted in 1962 protons were sent onto a target, producing pions that then decay into muons and neutrinos.

Every other particle than neutrinos was then absorbed by a steel shield, resulting in a beam of muon-associated neutrinos. If muon- and electron-associated neutrinos would be identical, muon and electron tracks would be observed. However, only few electron tracks were observed, compatible with backgrounds. It was now clear that two types of neutrinos exist, associated to the two charged leptons [8].

In 1988, L. Lederman, M. Schwartz and J. Steinberger received the Nobel Prize for "the neutrino beam method and the demonstration of the doublet structure of the leptons through the discovery of the muon neutrino".

After T. Lee and C. Yang suggested that parity could be violated by weak interactions [9], C. Wu and R. Garwin designed two different experiments that confirmed that hypothesis a year later [10, 11]. Then a model was developed to explain parity violation observed in weak interactions [12, 13, 14]. This two-component ν theory predicts a zero mass and helicity that is either positive (right-handed ν_R) or negative (left-handed ν_L). Results from M. Goldhaber's experiment confirmed that theory and only left-handed neutrinos ν_L were found [15].

By 1962 it became clear that the neutrino has a distinguishable antiparticle and that the now-called *electron-neutrino* (ν_e) and *muon-neutrino* (ν_μ) are different particles. Moreover the lepton number is conserved by electrons and muons separately and parity and charge conjugation are not conserved by weak interactions.

Finally a third lepton was discovered, called τ . In the mid-1970s evidences were shown at the SLAC accelerator [16]. Consequently and according to the Standard Model [17, 18] there should be an associated neutrino to this new lepton, which was discovered and established in the 1980's [19]. Interactions of τ neutrino were first observed in 2000 by the DONUT experiment [20]. At about the same time indeed, a LEP experiment measuring the Z-decays showed there are three light neutrino species that couple to the Z-boson [21, 22]. In Fig. 1.2 a schematic table represents the particles of the Standard Model.

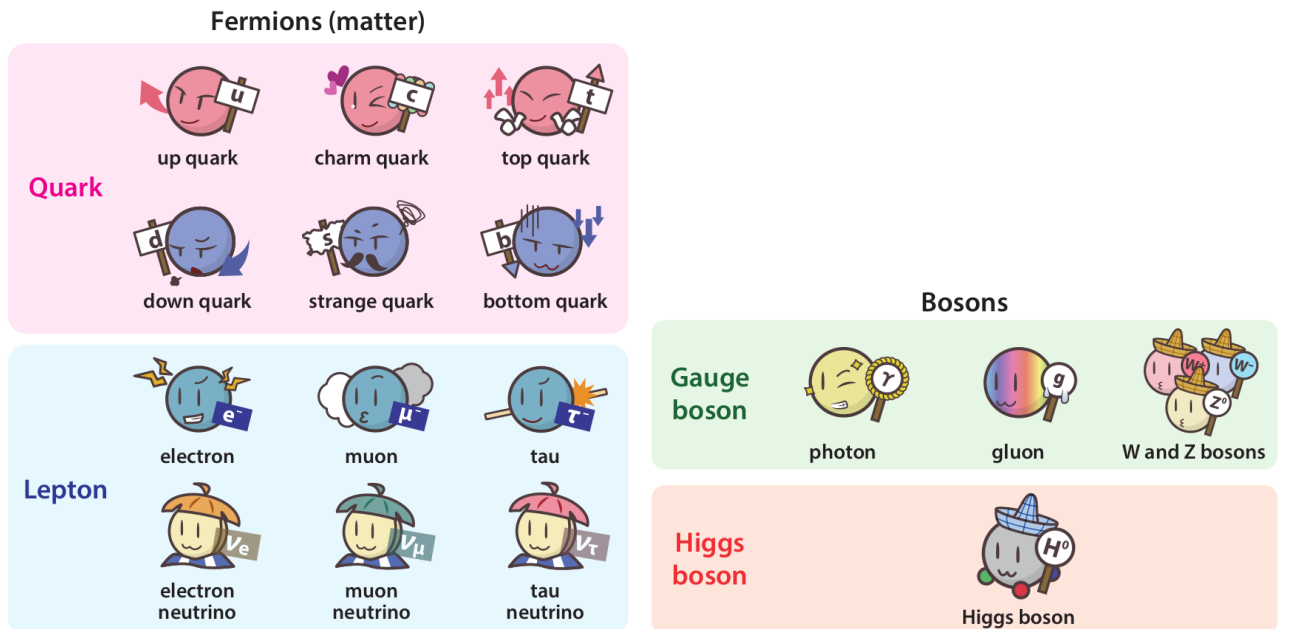


Figure 1.2: The particles of the Standard Model : 6 quarks, 6 leptons, the gauge bosons which carry forces between those particles and the Higgs boson which give them a mass. Designer: Yuki Akimoto (Higgstan / higgstan.com)

1.1.3 The problem of solar neutrinos

After the neutrino discovery physicists realised that this particle could be an ideal tool to probe environments that undergo nuclear reactions. In the late 1960s R. Davis and J. Bahcall set up an experiment called Homestake to measure electron-neutrino emissions from the sun in order to study nuclear reactions taking place beyond the surface of the sun. However the measured neutrino flux was about three times smaller than the model predictions [23]. Early attempts to explain this discrepancy suggested that something was wrong either in the measurements or in the solar model predictions.

In the early 1990s observations of helioseismology agreed with Bahcall's predictions. Other experiments taking measurements on neutrinos, SAGE [24], GALLEX [25] and Super-Kamiokande [26], corroborated the Homestake observations : Some neutrinos were missing! Fortunately a possible solution to the missing neutrinos had been proposed by B. Pontecorvo. He suggested that neutrinos could change their flavour states as they propagate [27]. Therefore the reduction of the electron-neutrino flux measured on Earth would be explained by the fact that a fraction of the electron-neutrinos emitted by the sun *oscillate* onto other flavour state as they travel from the sun. The SNO experiment was able to measure both the electron-neutrino flux and the total neutrino flux from the sun. In 2002 they confirmed the oscillation hypothesis by observing an electron-neutrino flux that is about a third of the model prediction and a total neutrino flux that is compatible with the prediction [28]. This was a strong evidence for the neutrino oscillation theory developed by Pontecorvo.

In addition, in 1998, the Super-Kamiokande experiment provided evidence for neutrino oscillation as well by observing neutrinos coming from cosmic ray induced showers in the Earth atmosphere [3, 29, 30, 31]. The flux of electron and muon atmospheric neutrinos were measured and, in principle, the atmospheric neutrino flux is predictable. However the muon neutrino flux was showing some discrepancy with the predictions. The disagreement was explained by the disappearance of muon-neutrinos that oscillate into τ -neutrinos.

The SNO and Super-Kamiokande experiments showed strong evidence for the neutrino oscillations. Neutrinos undergo oscillations only under the condition that they carry a non-zero mass. However, both Fermi's original model and the modern Standard Model of the electroweak interactions predict a massless neutrino. Therefore these discoveries demonstrated that the neutrino *must* have mass. It was the first laboratory evidence of physics beyond the Standard Model. In 2015 they were awarded the Nobel Prize in Physics.

Neutrino oscillations now have been studied with increased accuracy with various kind of experiments measuring neutrinos from both nuclear reactors and accelerator beams. Modern experiments keep improving the measurement precision on neutrino oscillation. In the following section the physics of this phenomenon will be explained in more details.

1.2 Neutrinos oscillation

In the previous section the history of a major discovery in neutrino physics is explained : The phenomenon of neutrino *oscillation*, originally proposed by B. Pontecorvo [32] and also further developed by Z. Maki, M. Nakagawa and S. Sakata [33]. We now describe the formalised theory of neutrino oscillation (Sec.1.2.1) and discuss more deeply the question *why* neutrinos do oscillate (Sec.1.2.2). Finally we give an overview of modern experiments measuring oscillation (Sec.1.2.3).

1.2.1 Neutrinos oscillation theory

Neutrinos are created in the flavour states of the weak interaction, $|\nu_\alpha\rangle$, $\alpha = e, \mu, \tau$ as they are produced associated to a charged lepton and they propagate in the mass eigenstates $|\nu_i\rangle$,

$i = 1, 2, 3$ if one assumes that flavour and mass bases do not coincide. The superposition of the mass states can be expressed as

$$|\nu_\alpha\rangle = \sum_i U_{\alpha i}^* |\nu_i\rangle \quad (1.1)$$

where the leptonic mixing matrix U is known as the PMNS matrix (Pontecorvo-Maki-Nakagawa-Sakata). Considering only the three known flavours it can be written as follow :

$$\begin{aligned} U &= \begin{bmatrix} U_{e1} & U_{e2} & U_{e3} \\ U_{\mu1} & U_{\mu2} & U_{\mu3} \\ U_{\tau1} & U_{\tau2} & U_{\tau3} \end{bmatrix} \\ &= \begin{bmatrix} 1 & 0 & 0 \\ 0 & c_{23} & s_{23} \\ 0 & -s_{23} & c_{23} \end{bmatrix} \begin{bmatrix} c_{13} & 0 & s_{13}e^{-i\delta_{\text{CP}}} \\ 0 & 1 & 0 \\ -s_{13}e^{-i\delta_{\text{CP}}} & 0 & c_{13} \end{bmatrix} \\ &\quad \times \begin{bmatrix} c_{12} & s_{12} & 0 \\ -s_{12} & c_{12} & 0 \\ 0 & 0 & 1 \end{bmatrix} \begin{bmatrix} e^{i\alpha_1/2} & 0 & 0 \\ 0 & e^{i\alpha_2/2} & 0 \\ 0 & 0 & 1 \end{bmatrix} \end{aligned} \quad (1.2)$$

where the notation $c_{ij} = \cos \theta_{ij}$ and $s_{ij} = \sin \theta_{ij}$ is used. The mixing matrix shows the following properties :

- It is parametrised by
 - the so-called *mixing-angles* θ_{12} , θ_{23} and θ_{13} ,
 - a Dirac CP-violating phase δ_{CP} ,
 - Majorana CP-violating phases α_1 and α_2 .
- The non-zero off-diagonal terms result in neutrinos created in superpositions of mass states.
- A condition to write a matrix as a product of unitary matrices is that U should be unitary. Note that unitarity is a theoretical assumption inherent in the majority of analyses. It is the basis for the validity of the 3 neutrino paradigm. However this assumption leads to limitations of the model [34, 35]. For instance in the seesaw model the PMNS matrix is not unitary.
- The last term of the matrix has physical consequences only if neutrino are Majorana particles. Even in the case of Majorana neutrinos it does not affect neutrino oscillation since the Majorana phases cancel in UU^* .
- For antineutrinos, U becomes U^* instead.
- CP conservation requires U to be real, i.e. $\delta_{\text{CP}} = 0, \pi$.

Oscillation probability in vacuum

We can now derive the oscillation probability, that is the probability for a neutrino created in a flavour state α to be measured in a flavour state β . The initial state is a combination of the mass eigenstates $|\nu_i(0)\rangle$ at time $t = 0$. Note that quantum coherence will be discussed later on in Section 1.2.2. At a time $t > 0$ each mass state is written as

$$|\nu_i(t)\rangle = e^{-i(E_i t - \vec{p}_i \cdot \vec{x})} |\nu_i(0)\rangle \quad (1.3)$$

where E_i and \vec{p}_i are the energy and momentum of the propagating neutrino and \vec{x} is its position relative to the initial position at $t = 0$. In the ultra-relativistic limit, which is justified as the neutrino masses m_i are so small, we have $|\vec{p}_i| \gg m_i$ and the energy of the travelling neutrino can be approximated by

$$E_i = \sqrt{p_i^2 + m_i^2} \simeq p_i + \frac{m_i^2}{2p_i} \approx E + \frac{m_i^2}{2E} \quad (1.4)$$

where E is the neutrino total energy. With the distance travelled $L \sim t$, each mass state can now be written as

$$|\nu_i(L)\rangle = e^{-im_i^2 \frac{L}{2E}} |\nu_i(0)\rangle \quad (1.5)$$

This describes how each neutrino mass state propagates. It is important to notice that the different *mass* states propagate with different phases that depend on the mass. This is why the *flavour* state (initially $|\nu_\alpha\rangle$) evolves with time and can change to other flavour states. In other words, when a neutrino is measured after travelling for a distance L , it interacts with another particle and its state is projected onto the state with flavour corresponding to the outgoing lepton ($|\nu_\beta\rangle$). Using (1.1) and (1.5), the probability for oscillating can be computed,

$$\begin{aligned} P(\nu_\alpha \rightarrow \nu_\beta) &= |\langle \nu_\beta(L) | \nu_\alpha(0) \rangle|^2 = \left| \sum_i \langle \nu_i(L) | U_{\beta i} \cdot \sum_j U_{\alpha j}^* |\nu_j(0)\rangle \right|^2 \\ &= \left| \sum_i U_{\alpha i}^* U_{\beta i} e^{-im_i^2 \frac{L}{2E}} \right|^2 \end{aligned} \quad (1.6)$$

Playing with some mathematical tricks the probability can be rewritten as

$$\begin{aligned} P(\nu_\alpha \rightarrow \nu_\beta) &= \delta_{\alpha\beta} - 4 \sum_{i>j} \text{Re} \left(U_{\alpha i}^* U_{\beta i} U_{\alpha j} U_{\beta j}^* \right) \sin^2 \left(\frac{\Delta m_{ij}^2 L}{4E} \right) \\ &\quad + 2 \sum_{i>j} \text{Im} \left(U_{\alpha i}^* U_{\beta i} U_{\alpha j} U_{\beta j}^* \right) \sin \left(\frac{\Delta m_{ij}^2 L}{4E} \right) \end{aligned} \quad (1.7)$$

where we define the squared mass difference $\Delta m_{ij}^2 \equiv m_i^2 - m_j^2$. One should notice that neutrino oscillation conserves the total lepton number, although it does not conserve the flavour lepton number as expected, due to mixing.

The probability of oscillation depends on :

- the mixing angles θ_{12} , θ_{23} and θ_{13} ;
- the CP-violating phase δ_{CP} ;
- the square of the mass splitting Δm_{ij}^2 .

These are the parameters that modern neutrino oscillation experiments aim to measure. In particular the measurement of the CP-violating phase is a good characterisation of CP-violation in the neutrino-sector. If it can be demonstrated that neutrinos violate the CP-symmetry it could be a very interesting path to explore in order to understand the matter-antimatter imbalance in the Universe.

Oscillation probability in matter

In the above paragraph we have described oscillation for neutrinos propagating in vacuum. However, in most of experiments neutrinos travel through the Earth and undergo forward scattering from particles they encounter in the medium.

Three effects are observed when neutrino travel through matter. First and similarly to light refraction when photons propagate through a medium, a direct effect of the neutrino coherent elastic forward scattering is the appearance of a phase difference, which in the case of neutrino is called "effective mass". As a consequence the oscillation probability change and effective parameters can be derived in order to compute the new probability. Second, the expression with effective parameters shows that approaching a certain electron number density and squared-mass difference combination leads to a resonance effect. A third effect, called *adiabaticity*, happens if the matter density is constant. In this case the evolutions of the effective massive neutrinos are decoupled. The propagation then obeys the same physics than in vacuum, with different parameters.

The full matter effect description is beyond the scope of this work and details can be found for example in [36, 37].

As neutrino interact through neutral-current scattering from electron, neutron or proton or through charged-current scattering of an electron (illustrated in Feynman diagrams in Fig. 1.3), matter do affect the oscillation physics. Most important consequences will be briefly described here.

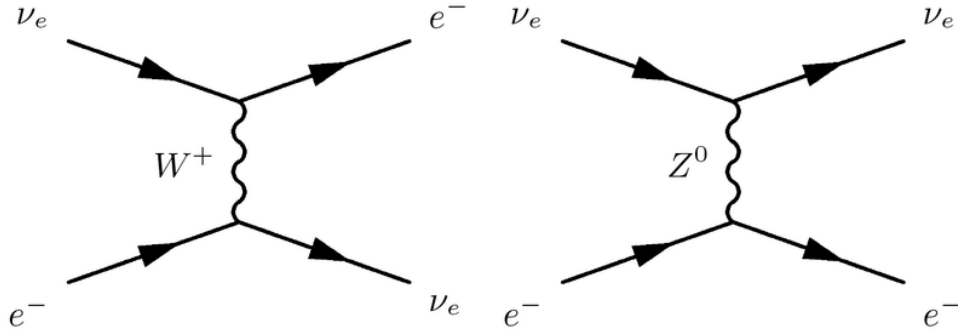


Figure 1.3: Feynman diagrams of charged-current (left) and neutral-current (right) neutrino scattering with electrons. Note that the right diagram also works with neutrons or protons instead e^- .

In the vacuum oscillations are only sensitive to the square of the neutrino mass splitting, whereas they are sensitive to the sign when matter effects are taken into account. Indeed solar neutrino observations allowed to determine that ν_2 is heavier than ν_1 . Whether ν_3 is the heaviest neutrino (*normal* neutrino mass hierarchy, "NH") or the lightest neutrino (*inverted* neutrino mass hierarchy, "IH") is one of the major unknowns in neutrino physics.

Another characteristic of the matter effects is the difference in neutrino and antineutrino. Indeed the charged-current channel is not available to antineutrino since matter is not made of positrons. In long-baseline experiments matter effects enhance the oscillation probability for neutrinos (antineutrinos) if $\Delta m_{ij}^2 > 0$ ($\Delta m_{ij}^2 < 0$) with respect to propagation in vacuum. Neutrino oscillations in matter offer an interesting probe for CP violation by looking at the difference

$$P(\nu_\alpha \rightarrow \nu_\beta) \neq P(\bar{\nu}_\alpha \rightarrow \bar{\nu}_\beta) \quad (1.8)$$

Therefore it is extremely important to account for matter effects when searching for CP violation

in the neutrino sector.

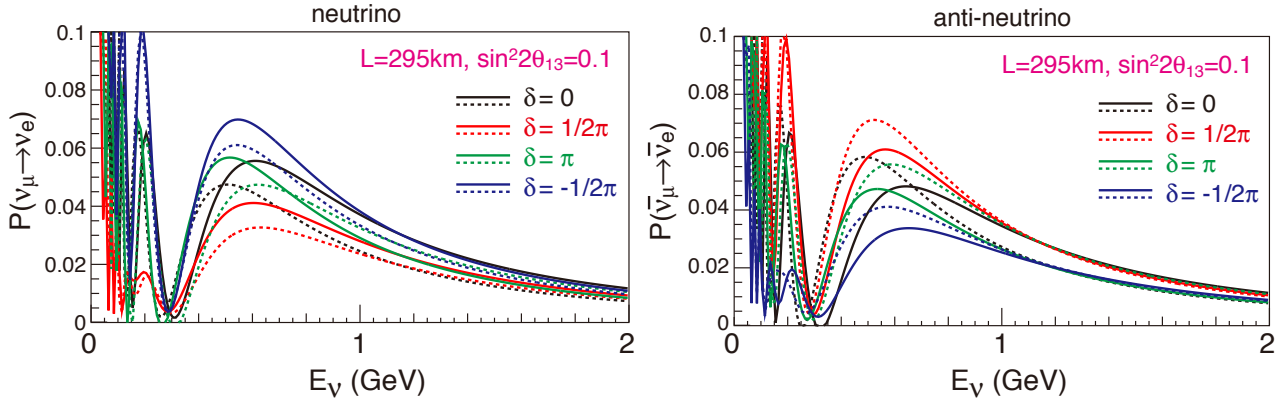


Figure 1.4: $\nu_\mu \rightarrow \nu_e$ (left) and $\bar{\nu}_\mu \rightarrow \bar{\nu}_e$ (right) oscillation probability as a function of neutrino true energy for a 295 km baseline. Different colors correspond to different values of the CP-violation phase δ_{CP} . Solid (dashed) lines are for normal (inverted) mass hierarchy. Source : t2k.org

1.2.2 Why do neutrinos *oscillate* ?

As seen in the introduction the neutrino flavour states $|\nu_e\rangle$, $|\nu_\mu\rangle$ and $|\nu_\tau\rangle$ are not the mass eigenstates $|\nu_i\rangle$. The neutrino state $|\nu_\alpha\rangle$ created in a W-decay alongside a charged lepton α is a quantum superposition of the mass eigenstates, as written in Eq.(1.1). In the neutrino mass eigenstate basis, the neutrino propagates as mass eigenstates $|\nu_i\rangle$ with amplitude for a proper time τ_i^ν equal to $\exp(-im_i^\nu \tau_i^\nu)$. Therefore we expect to measure a mass of

$$\langle m_{\nu_\alpha} \rangle = \sum_i |U_{\alpha i}|^2 m_i \quad (1.9)$$

which is a distribution with three peaks at m_1 , m_2 and m_3 with probabilities equal to $|U_{\alpha 1}|^2$, $|U_{\alpha 2}|^2$ and $|U_{\alpha 3}|^2$ respectively, as schematically represented in Fig. 1.5. However, what happens if one would try to measure the neutrino mass for instance in a pion decay? As a *gedankenexperiment* let us estimate the gap between the peaks of the three neutrino mass eigenstates compared to the width that would be obtained in an *ideal* measurement with an imaginary perfect detector precision.

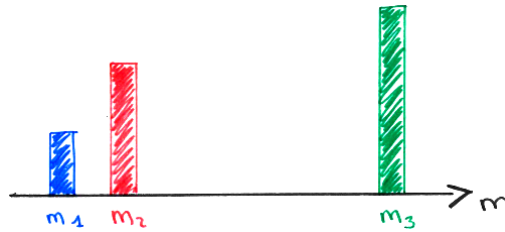


Figure 1.5: Schematic representation of the neutrino mass distribution that we expect to measure.

Neutrino mass measurement in a pion decay

We consider the pion decay into a muon and an electron neutrino in the pion rest frame. After the pion decay, the neutrino interacts with a target via W-boson exchange and produces an

electron plus something, i.e.

$$\begin{aligned}
 \pi &\rightarrow \mu + \nu_\mu \\
 \nu_\mu &\text{ oscillates to } \nu_e \\
 \nu_e + \text{target} &\rightarrow e + X
 \end{aligned}
 \tag{1.10}$$

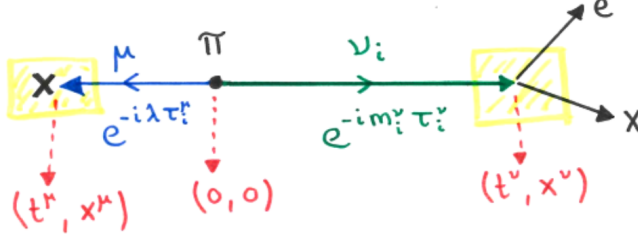


Figure 1.6: Schematic representation of the pion decay. The coordinates written in red are the spacetime points in the pion rest frame.

The amplitudes for the muon and the neutrino ν_i to propagate yield :

$$\begin{aligned}
 \mu &\sim e^{-i\lambda\tau_i^\mu} \\
 \nu_i &\sim e^{-im_i^\nu\tau_i^\nu}
 \end{aligned}
 \tag{1.11}$$

where $\lambda = m^\mu - i\frac{\Gamma_\mu}{2}$ with muon decay width Γ_μ . The neutrino decay width is zero. The neutrino proper time τ_i^ν depends on neutrino energy, hence it depends on the mass eigenstate i . Since the muon and the neutrino are entangled, the muon proper time τ_i^μ also depends on i . We now look at how the kinematics variables depend on the mass eigenstates i .

Momentum dependance on the mass eigenstates

To estimate the kinematic variable dependance on the mass eigenstate i we compute the difference in p^μ for different neutrino mass states ν_i and ν_j . Using the pion rest-frame energy of the muon,

$$E^\mu = \frac{(m^\pi c^2)^2 + (m^\mu c^2)^2 - (m^\nu c^2)^2}{2m^\pi}
 \tag{1.12}$$

and

$$(cp^\mu)^2 = (E^\mu)^2 - (m^\mu c^2)^2
 \tag{1.13}$$

one finds

$$\frac{d(cp^\mu)}{d[(m^\nu)^2]} = \frac{E^\mu}{cp^\mu} \cdot \frac{dE^\mu}{d[(m^\nu)^2]}
 \tag{1.14}$$

Thus the difference in the momenta is

$$\Delta p_{ij}^\mu \equiv p_j^\mu - p_i^\mu = \frac{E^\mu}{p^\mu} \cdot \left(-\frac{\Delta m_{ij}^2}{2m^\pi} \right)
 \tag{1.15}$$

Using the values¹ $\Delta m_{ij}^2 \simeq 2.4 \cdot 10^{-3} \text{eV}^2/c^4$ and $m^\pi \simeq 1.4 \cdot 10^2 \text{MeV}/c^2$ the order of magnitude of Δp_{ij}^μ can be rated as

$$\Delta p_{ij}^\mu \approx -\frac{\Delta m_{ij}^2}{2m^\pi} c \approx \frac{2.4 \cdot 10^{-3}}{2 \cdot 1.4 \cdot 10^8} \text{eV}/c \approx 10^{-11} \text{eV}/c
 \tag{1.16}$$

¹All values used in this section are from PDG 2015.

Quantum mechanics optimal precision that can be achieved

Now let us investigate the precision that could possibly be achieved even in the best experiment conditions, considering the quantum nature of the particles. According to Heisenberg's uncertainty principle,

$$\tau \cdot \Delta m^\pi c^2 \geq \frac{\hbar}{2} \quad (1.17)$$

we obtain, using the pion decay mean life time $\tau \simeq 2.6 \cdot 10^{-8}$ s,

$$\Delta m^\pi \geq \frac{\hbar}{2\tau c^2} \approx \frac{6.6 \cdot 10^{-16} \text{ eV s}}{2 \cdot 2.6 \cdot 10^{-8} \text{ s}} \cdot \frac{1}{c^2} \approx 10^{-8} \text{ eV}/c^2 \quad (1.18)$$

Propagating the error on m^π into

$$p^\mu = \frac{\sqrt{[(m^\pi)^2 + (m^\mu)^2 - (m^\nu)^2]^2 - 4(m^\pi)^2(m^\nu)^2}}{2(m^\pi)^2} \quad (1.19)$$

we find

$$\Delta p_{\text{meas}}^\mu = \Delta m^\pi \underbrace{\left(\frac{(m^\pi)^2 + (m^\mu)^2 - (m^\nu)^2}{A} - \frac{A}{2(m^\pi)^2} - \frac{4(m^\nu)^2}{A} \right)}_{\sim 1} \quad (1.20)$$

where we have defined $A = \sqrt{[(m^\pi)^2 + (m^\mu)^2 - (m^\nu)^2]^2 - 4(m^\pi)^2(m^\nu)^2}$. Thus we obtain

$$\Delta p_{\text{meas}}^\mu \sim \Delta m^\pi \approx 10^{-8} \text{ eV}/c \quad (1.21)$$

Conclusion

In the case of a neutrino produced in a pion decay the muon momenta associated with the different neutrino mass eigenstates are separated by a distance of

$$\Delta p_{ij}^\mu \approx 10^{-11} \text{ eV}/c \quad (1.22)$$

and the uncertainty associated to the width of the pion due to its quantum nature is

$$\Delta p_{\text{meas}}^\mu \approx 10^{-8} \text{ eV}/c \quad (1.23)$$

We remind that if one would measure the neutrino mass a distribution with three peaks at m_1 , m_2 and m_3 is expected in ideal conditions, as illustrated in Fig. 1.5. We estimated the gap between the peaks to be the order of 10^{-11} eV/c. However, the uncertainty due to the decay width of the parent particle is around 10^{-8} eV/c, which is much larger than the separation of the momenta for different neutrino mass eigenstates. This can be illustrated by adding the pion spectrum to previous figure, as can be seen in Fig. 1.7. We can conclude that because of the quantum nature of particles it is impossible to determine the neutrino mass eigenstates by measuring the neutrino mass from kinematics. This is different from quarks where the mass differences are much larger than the decay width of the quarks.

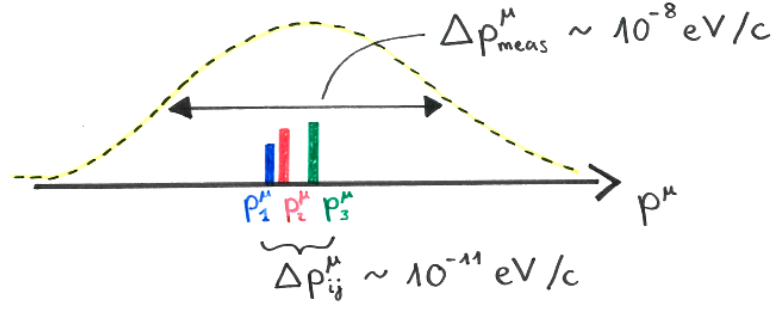


Figure 1.7: Schematic representation of the neutrino mass distribution that we expect to measure.

An analog to the double-slit experiment

This quantum effect can be compared to the outcome of the double-slit experiment, that was first performed with light by Thomas Young in the beginning of the 19th Century. In Young's experiment photons are sent to a wall that has two slits. On the other side the photons are detected on a screen. The observed result is a wave pattern on the screen. An illustration of the setup is shown in Fig. 1.8. The exact same effect has also been shown with electrons instead of light.

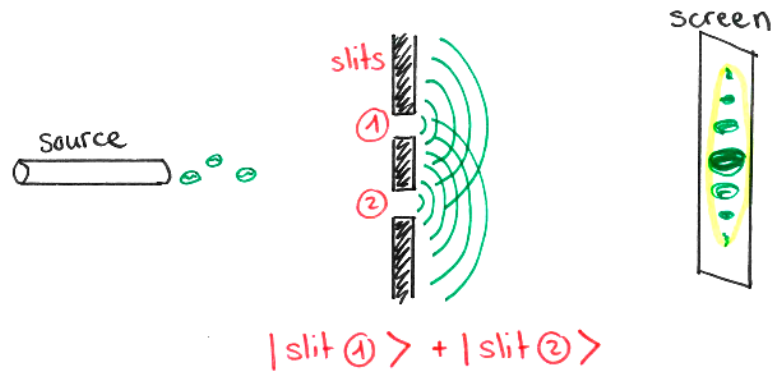


Figure 1.8: Schematic representation of the double-slit experimental setup and the interference pattern created on the screen.

It is impossible to determine which slit the particle went through to end up in some position on the screen, as it is impossible to determine in which mass eigenstate the neutrino propagates before being detected in some flavour eigenstate. Only the probability to detect a photon in that position on the screen or a neutrino in that flavour can be known.

As we did in the case of the neutrino it is possible to illustrate Heisenberg's uncertainty principle also in that experiment,

$$\Delta x \Delta p \geq \frac{\hbar}{2} \quad (1.24)$$

If photons or electrons are sent through a slit of width Δx , after passing through the hole photons have a momentum uncertainty equal to Δp and therefore the image appearing on the screen is larger than the slit.

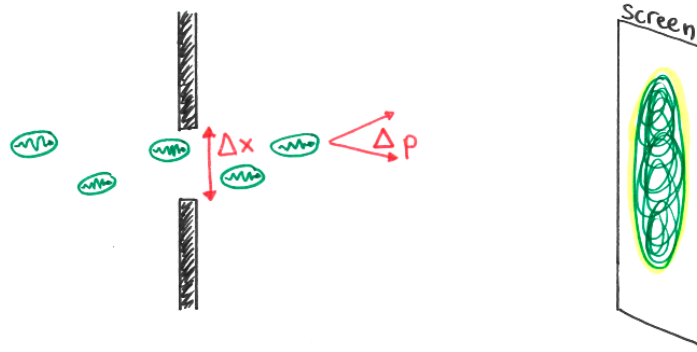


Figure 1.9: Application of Heisenberg's uncertainty principle in the double-slit experiment.

Both the oscillation of neutrinos and the diffraction pattern of photons or electrons are good demonstrations of the fundamental principle of quantum mechanics. In both case it shows the wave-particle duality and the limitation in measurements due to the quantum nature of particles. More details on neutrino oscillation can be found in [38]

1.2.3 Neutrino oscillation experiments

As already mentioned in Sec.1.1, several ways of neutrino productions are used in order to study their physical properties. One can take benefit of neutrinos already being produced either naturally in the Sun, in the atmosphere or in the Universe, or artificially in nuclear reactors. Moreover technologies allow to produce neutrino beams with accelerators since the 1960's.

Solar neutrino experiments

A historical overview of the solar neutrino anomaly was already given in Sec.1.1.3. As seen the sun is a large neutrino factory : ν_e 's are constantly released in nuclear reactions. Over the years the constraints on the solar neutrino flux and the detector technologies improved a lot. In the 1990s Gallium tank detectors were developed by GALLEX [39], SAGE [40] and GNO [41] experiments. Then new types of detectors were designed using heavy water for the SNO experiment [42] and pure liquid scintillator for the Borexino experiment [43].

Atmospheric neutrino experiments

Cosmic rays interacting with the Earth atmosphere generate hadronic showers, mainly pions. Therefore ν_e 's and ν_μ 's are produced, allowing measurements of ν_e , $\bar{\nu}_e$, ν_μ and $\bar{\nu}_\mu$ at different energies and zenith angles, that relate to different travel distances. Such measurements are sensitive to θ_{23} and $|\Delta m_{32}^2|$. The IceCube experiment, which is taking advantage of the South Pole ice as detector volume, recently published oscillation results for neutrinos in energy range of 6 – 56 GeV [44]. Atmospheric neutrinos are also measured by the Super-Kamiokande experiment [30, 31]; precision measurements and determination of the neutrino mass hierarchy are expected to be observed by the future long-baseline neutrino oscillation experiments Hyper-Kamiokande [45] and DUNE [46].

Reactor neutrino experiments

Setups similar to the Savannah River experiments (Sec.1.1.1) are still exploited by experiments such as RENO [47], Double Chooz [48, 49] and Daya Bay [50, 51]. A neutrino detector is

placed near a nuclear reactor, where a pure flux of $\bar{\nu}_e$ is produced by β -decays utilising their characteristic light signal due to e^+e^- annihilation and neutron capture. The ν_e disappearance channel can be studied and this type of experiment is usually sensitive to θ_{13} and $|\Delta m_{32}^2|$.

Accelerator neutrino experiments

As seen in Sec.1.2.1 the oscillation probability varies with the distance L and neutrino energy E_ν . Accelerator-based long baseline experiments exploit this by measuring neutrinos, produced with a certain energy spectrum, at a distance that maximises the oscillation probability. K2K [52], the predecessor of T2K, is one of them. In addition to the far detector that measures oscillated neutrino flux, a near detector is placed just after the neutrino beam production point in order to constrain the neutrino flux. Protons are accelerated and smashed onto a nuclear target producing mesons, mainly pions and then kaons, which then decay into neutrinos and leptons. ν_μ or $\bar{\nu}_\mu$ are produced, depending on the polarisation (positive or negative) that is used to focus the charged-particle beam before they decay into neutrinos. One of the most convenient feature of such experiments is the ability to take off-axis measurements, which allow narrow-peaked energy spectrum. Modern long-baseline experiments such as T2K [53] and NO ν A [54] use off-axis detectors.

This type of experiment allow studies of the ν_μ and $\bar{\nu}_\mu$ disappearance channels ($\nu_\mu \rightarrow \nu_e$ and $\bar{\nu}_\mu \rightarrow \bar{\nu}_e$), which give sensitivity to θ_{23} and $|\Delta m_{32}^2|$. Moreover CP symmetry can be tested by comparing $\nu_\mu \rightarrow \nu_e$ and $\bar{\nu}_\mu \rightarrow \bar{\nu}_e$. ν_e and $\bar{\nu}_e$ appearance channels can also be measured and they give not only sensitivity to θ_{13} but also to the still unknown δ_{CP} phase.

1.3 Neutrino interactions for accelerator based experiments

When neutrinos scatter off nuclei they undergo different types of interactions with the contained nucleons. At neutrino energies in the range of the GeV, the main interaction channel is Charged-Current (CC) Quasi-Elastic (QE) with a W -boson exchanged between the neutrino and the nucleon, producing a charged lepton and inverting the nucleon isospin, e.g. $\nu_\ell + n \rightarrow \ell + p$. As can be observed in Fig. 1.10 around 1.0 GeV the neutrino energy allows pion production through resonant scattering. At a few GeVs the energy becomes high enough to resolve the quark content in the target nucleon. The latter is broken up and hadronic jets are produced. The different neutrino-nucleus interaction modes will be described in Sections 1.3.1, 1.3.2 and 1.3.3.

Describing neutrino-nucleus interactions can be very tedious not only because of the overlay in energies of the different interaction channels but also because the nucleus is a complex object and many nuclear effects enter the game. One has to account for the initial state of the nucleus. Firstly nucleons are not at rest but move in the nuclear medium, secondly they are not free particles and the proximity between nucleons gives rise to multinucleon interactions, such as the so-called "2p2h", that are complex to model. Moreover the outgoing particles are travelling in a highly dense nuclear medium, thus they are likely to interact before leaving the nucleus. In Sec.1.3.4 a description of nuclear effects due to nucleon initial and final states will be given. Then an overview of neutrino-nucleus interaction generators will be shown in Section 1.3.5.

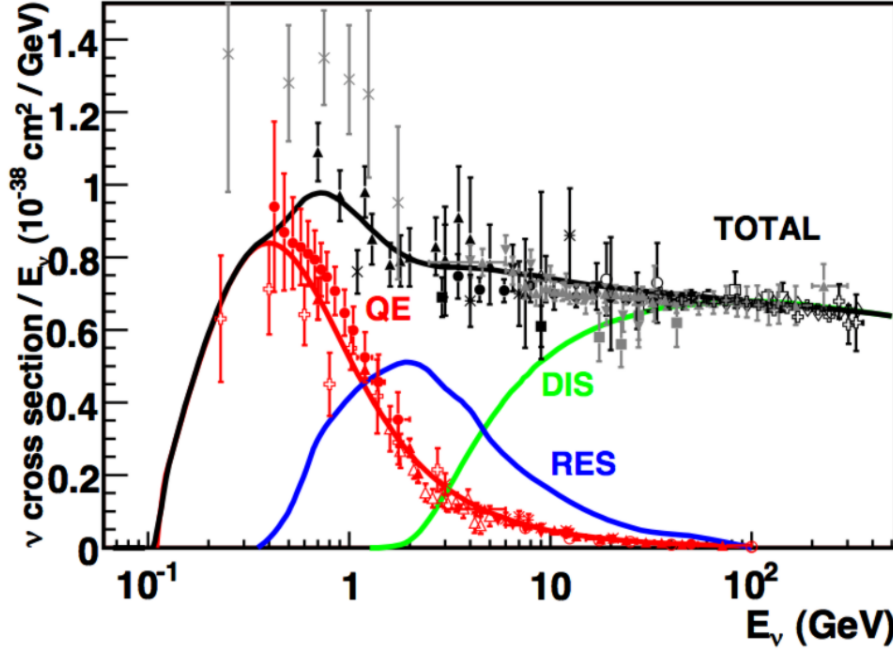


Figure 1.10: Muon neutrino cross-section broken down by interaction modes and as a function of the neutrino energy. Available data up to 2012 compared to NUANCE prediction. Figure from [55]

1.3.1 Charged-Current Quasi-Elastic Interactions

As can be seen in Fig. 1.10 up to ~ 1.5 GeV the main contribution to the neutrino cross section comes from CCQE interactions. It is extremely difficult to compute the cross section analytically since the nucleon is a complex object. However it is possible to parametrise it in terms of parameters that can be measured by electron scattering and β -decay experiments. The differential cross section in the four-momentum transfer squared Q^2 is given by the Llewellyn-Smith model [56],

$$\frac{d\sigma}{dQ^2} = \frac{M^2 G_F^2 \cos^2 \theta_c}{8\pi E_\nu^2} \left(A(Q^2) \pm B(Q^2) \frac{s-u}{M^2} + C(Q^2) \frac{(s-u)^2}{M^4} \right) \quad (1.25)$$

where \pm stands for neutrino/antineutrino, M is the nucleon mass, G_F the Fermi coupling constant, θ_c the Cabbibo angle and E_ν the neutrino energy. s and u are the Mandelstam kinematic variables and for an outgoing lepton of mass m_ℓ they can be rewritten as $s-u = 4ME_\nu - Q^2 - m_\ell^2$. $A(Q^2)$, $B(Q^2)$ and $C(Q^2)$ are given by

$$\begin{aligned} A(Q^2) &= \frac{4m_n E_\nu - Q^2}{m_n^2} \\ &\quad \times \left[\left(1 + \frac{Q^2}{4m_n^2}\right) F_A^2 - \left(1 - \frac{Q^2}{4m_n^2}\right) F_1^2 + \frac{Q^2}{4m_n^2} \left(1 - \frac{Q^2}{4m_n^2}\right) F_2^2 + \frac{Q^2}{m_n^2} \tau F_1 F_2 \right] \\ B(Q^2) &= \frac{Q^2}{m_n^2} F_A (F_1 + F_2) \\ C(Q^2) &= \frac{1}{4} (F_A^2 + F_1^2 + \tau F_2^2) \end{aligned} \quad (1.26)$$

where $\tau = (\mu_p - 1)\mu_n$ with the magnetic moments $\mu_{p,n}$ of the proton and neutron respectively. They are functions of the nucleon form factors F_1 , F_2 and F_A , which characterise the internal

charge distribution of the nucleons. In the case of a scattering with a stationary target nucleon the form factors are described by a dipole, i.e. $F(Q^2) \propto (1 - \frac{Q^2}{M_x^2})^{-2}$ with an empirical parameter M_x . The parameters of the vector form factors $F_{1,2}$ are accurately determined by observation of the electro-magnetic interactions in electron scattering experiments. It has been shown that it is well described by a dipole for $Q^2 < 2 \text{ GeV}$. At higher energies extensions to $F_{1,2}$ have to be used to palliate the deviations from the dipole approximation. The axial form factor F_A is assumed to behave as a dipole with two parameters,

$$F_A(Q^2) = \frac{g_A}{1 + \frac{Q^2}{(M_A^{\text{QE}})^2}} \quad (1.27)$$

where g_A is the axial vector coupling constant that can be determined by measuring polarised neutron β -decay observations. M_A^{QE} is the nucleon axial mass, it is the only parameter in the model that is not constrained. Measurements of neutrino interactions with light nuclei (hydrogen) in bubble chamber experiments have provided a value of $M_A^{\text{QE}} = 1.014 \pm 0.014 \text{ GeV}$ [57]. However later measurements of interactions on heavier target nuclei by MiniBooNE showed disagreements with bubble chamber results. This is known as the "MiniBooNE M_A^{QE} puzzle".

The easiest way to estimate CCQE cross section is to use the plane wave impulse approximation [58]. Assuming no FSI (see Section 1.3.4) and a known distribution of the target nucleon momenta and binding energies, one can calculate the cross section as an incoherent sum of contributions from individual nucleons.

1.3.2 Charged-Current Resonant Interactions

In a neutrino-nucleus scattering, if the center-of-mass energy is above the mass of a delta baryon it can excite a resonance state, resulting in a pion production from the delta baryon decay. An example of such process is illustrated on the Feynman diagram in Fig. 1.11. There are three possible charged-current resonant pion production interactions,

$$\begin{aligned} \nu_\ell + p &\rightarrow \ell^- + p + \pi^+ \\ \nu_\ell + n &\rightarrow \ell^- + p + \pi^0 \\ \nu_\ell + n &\rightarrow \ell^- + n + \pi^+ \end{aligned} \quad (1.28)$$

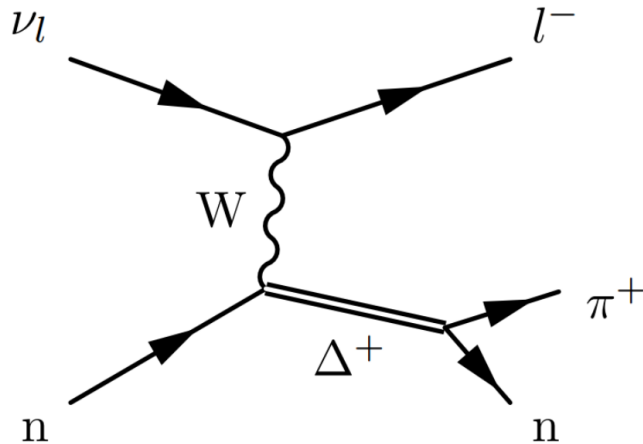


Figure 1.11: Feynman diagram of an example of charged-current neutrino resonant pion production interaction through W-boson exchange.

Single pion resonance interactions are the main contribution to the cross-section at neutrino energies between 1.5 GeV and 5 GeV. At higher energies other inelastic resonant processes can occur, such as single photon, kaon or multi-pion productions, however they are not discussed in this study since they are not relevant in the T2K neutrino beam energy.

Such interactions are usually described by the Rein-Sehgal model [59] in neutrino simulations, with Partially Conserved Axial vector Current (PCAC) lepton mass correction for charged-current interactions [60]. In a similar way than the Llewellyn model for CCQE interactions (see Section 1.3.1) the Rein-Sehgal model is parametrised in terms of nuclear form factors to account for extended nuclear targets. Those form factors are different ones however and they depend on two parameters that cannot be determined by electron scattering measurements, namely M_A^{RES} and C_A^5 .

1.3.3 Deep Inelastic Scattering

At higher energies neutrinos become even able to resolve the quark content within the nucleons and break it, producing jets of hadrons. This interaction mode, called Deep Inelastic Scattering (DIS) is dominant at neutrino energies above 10 GeV. Fig. 1.12 shows a Feynman diagram illustrating this process.

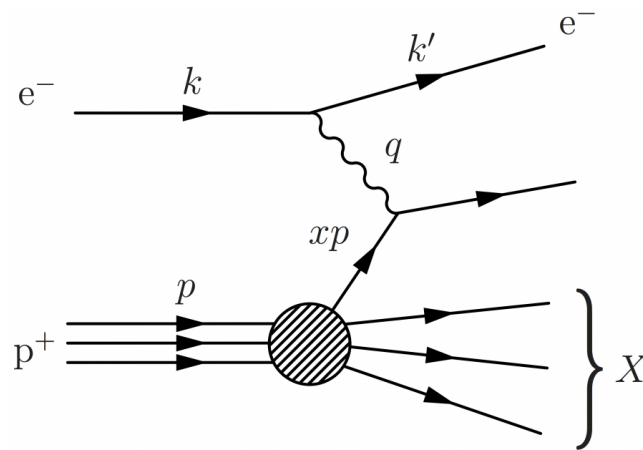


Figure 1.12: Feynman diagram of deep inelastic scattering.

Neglecting the μ mass one can estimate the DIS cross section as a function of two variables x and y ,

$$\frac{d\sigma}{dxdy} = \frac{G_F^2(x, Q^2)m_t}{\pi} E_\nu \left[\frac{y^2}{2} 2xF_1(x, Q^2) + \left(1 - y - \frac{m_t xy}{2E_\nu}\right) F_2(x, Q^2) + y \left(1 - \frac{y^2}{2}\right) F_3(x, Q^2) \right] \quad (1.29)$$

where $F_{1/2/3}(x, Q^2)$ are the nucleon structure functions for DIS.

This interaction mode have been probed in order to validate the Standard Model and nuclear structures, therefore there is a lot of neutrino data available at high energies. However it is not clear if information can be extrapolated accurately to energy ranges relevant for accelerator-based neutrino experiments.

1.3.4 Nuclear effects in neutrino-nucleus scattering

In Section 1.3.1 CCQE interactions are described between neutrinos and free nucleons. This description is sufficient to model interactions on very light nucleus. However present neutrino

experiments use targets made of complex nuclei (carbon, oxygen, argon, etc) not only because the probability of interaction is proportional to the target nucleon density, but also because nowadays technologies still need more developments in order to be able to use high-pressure hydrogen target material. Studying neutrino-nucleon interactions in such nuclei requires an accurate knowledge of the nucleon behaviour within the nuclear medium. One needs to account for the nucleus initial state, for instance the initial momenta of the nucleons and their possible correlations, as well as the outgoing particle interactions within the nuclear medium. In this section we discuss briefly each of these effects and how they are typically modelled.

Nucleon Initial State

When dealing with complex nucleus targets the nucleons can no longer be considered as free particles. When a neutrino scatters off a nucleus the nucleons have an initial non-negligible momentum, which is referred to as *Fermi motion*. Moreover the nucleons are bound in the nucleus with a nuclear binding energy E_B . The initial state of the nuclear medium is modelled with spectral functions and different models are used attempting to describe the most accurately the initial state nucleon momenta.

The most common and quite simple model is the 'global' Relativistic Fermi Gas (RFG) model. Nucleons are assumed to be non-interacting Fermions, each feeling the same constant binding potential. As in a Fermi gas, all momentum states are filled up to Fermi momentum p_F , which depends on the number of nucleons contained in the nucleus. This limit can be visualised in Fig. 1.13 where the momentum distribution is shown for a carbon nucleus ($p_F \approx 230$ MeV/c).

An improved version of the RFG model is the 'local' Fermi gas (LFG) model, which uses a potential depending on the *local* nuclear density. It is well known from electron scattering data that the density varies with the nuclear radial position. Therefore a density function $\rho(r)$ is calculated under the local density approximation and a continuum of RFG's with Fermi momentum varying with the radial position, $p_F(r) \propto \rho(r)^{1/3}$ is built.

O. Benhar and collaborators [61] have developed a more accurate model that accounts for nucleon-nucleon interactions within the nuclear medium. The latter can alter the distribution of initial state nucleon momenta. This model considers the modifications to the orbits due to nuclear interaction potential, called *short range correlations*. This allows for initial nucleon momentum higher than the Fermi momentum, which can be seen in Fig. 1.13.

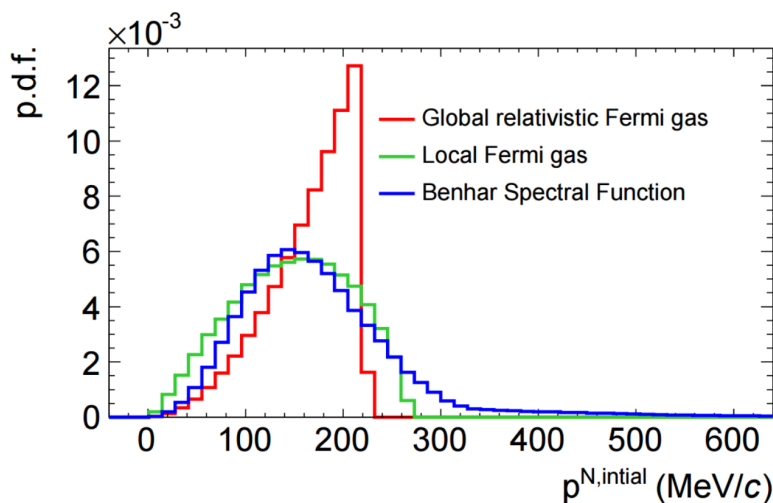


Figure 1.13: Simulations made with NuWro to compare different models of initial momentum distribution of nucleon within a carbon nucleus. Figure from [62]

Nucleon Correlations

The description of nucleons as isolated particles in neutrino-nucleus scattering is a simplistic approach. Possibly a neutrino may interact with a bound state of two or more nucleons. Such process has already been shown to have a non-negligible contribution in electron scattering [63, 64]. In neutrino experiments, although no evidence were found for such process it has become clear that nucleon correlations have an impact on oscillation and cross-section measurements at neutrino energy range around 1 GeV. Neutrino interactions with correlated nucleons are difficult to distinguish from quasielastic reactions, it is therefore important to investigate them.

Two models have been proposed by Nieves [65] and Martini [66], who refer to CCQE interactions as *1-particle 1-hole* (1p1h) and to interactions with two nucleons as *2-particles 2-holes* (2p2h) since this reaction leaves two nucleons in the final state, thus creating two "holes" in the initial nucleus. 2p2h interactions typically arise from short range correlation of a nucleon pair or from Meson Exchange Current (MEC).

Moreover to account for the impact of the nuclear medium on an electroweak propagator models also need to include a correction factor that is called Random Phase Approximation (RPA), depending on Q^2 . Indeed at low Q^2 the propagator is not able to probe individual nucleons so the 2p2h cross-section is suppressed, while at medium Q^2 it is enhanced. At large Q^2 this effect disappears. The RPA correction factor for CCQE interactions $\sigma_{\text{CCQE}}/\sigma_{\text{RPA}}$ on carbon is shown in Fig. 1.14.

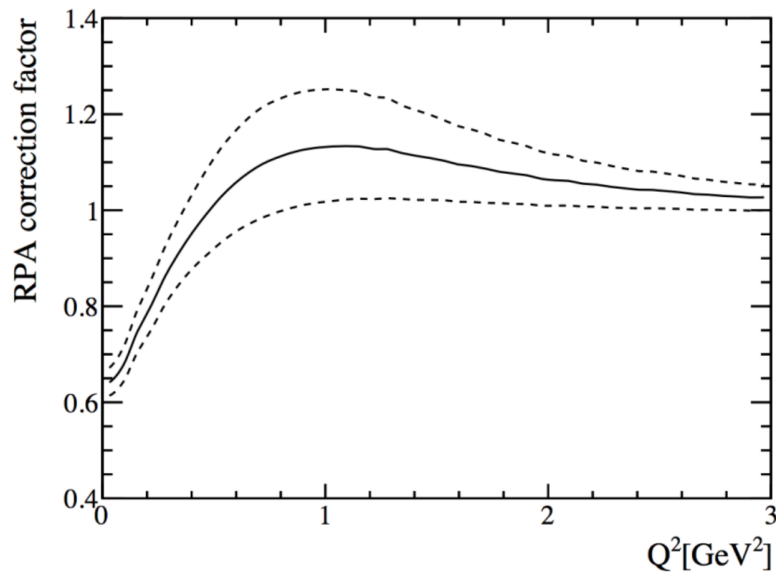


Figure 1.14: Random Phase Approximation (RPA) correction factor prediction for CCQE neutrino interactions on carbon. Dotted lines show approximate uncertainty bands. Figure from [65]

Currently most of neutrino simulations do not account properly for nucleon correlations but use effective or simplified models. Moreover the kinematics of particles produced in 2p2h interactions is characterised with very approximate models in most of the neutrino generators. Nowadays such interactions are widely studied and new measurements become able to bring more and more information about them, such as these recent T2K results [67].

Final State Interactions

When observing neutrino reactions, measurements are made after the particles escape the nucleus. However, before particles leave the nucleus they propagate through a highly dense

nuclear medium and they are likely to interact with other particles. Particle produced in the neutrino interaction may scatter off nucleons, loose energy or even kick nucleons out of the nucleus. If the energy is high enough they may excite a Δ resonance, producing an extra pion. These outgoing particles may undergo charge exchanges. Therefore particles leaving the nucleus (and being measured) may therefore differ a lot from the ones exiting the interaction vertex. Such re-interactions are called Final State Interactions (FSI) and must be understood in order to make a proper measurement.

FSI are very difficult to model and constrain with external data. Most of the neutrino interaction generators use an intranuclear cascade model. Within such model each hadron produced in the neutrino-nucleon interaction is propagated step by step independently through the nuclear medium. Step widths depend on the hadron mean free path, that is determined from external hadron scattering data. At each step the interaction probability for the different reactions is computed accounting for the local nuclear density and an interaction is simulated accordingly. The possible reactions are elastic scattering, hadron production or absorption and charge exchange. Their interaction probabilities are tuned from external data. Fig. 1.15 shows a visualisation of a cascade model for FSI. Another possible model for FSI is the semi-classical model. More details on the FSI implementation in neutrino-nucleus interaction simulations are given in [68, 69, 70].

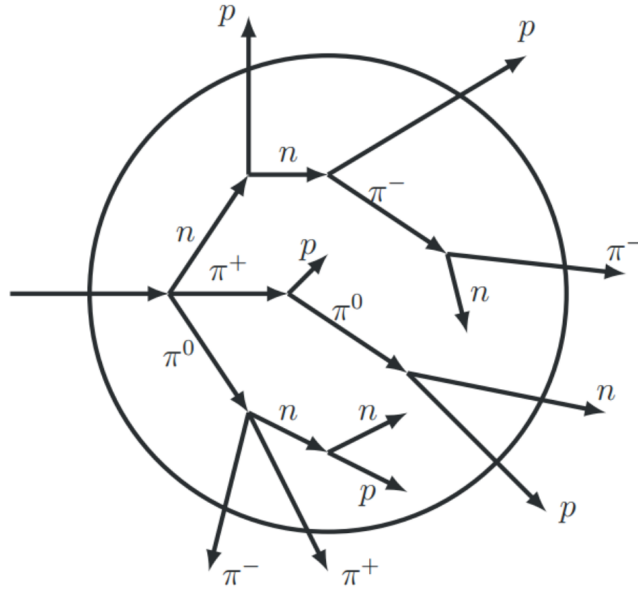


Figure 1.15: Schematic representation of Final State Interactions (FSI) in a cascade model. Figure from [71]

1.3.5 Neutrino-nucleus interaction generators

In neutrino experiments Monte Carlo simulations play a fundamental role in making predictions of the neutrino event rates at different energies. Various event generators are used to simulate neutrino-nucleus interactions ; the generators commonly used in the T2K experiment are NEUT [72, 73], GENIE [74], NuWro [75, 71], GiBUU [76] and NUANCE [77]. They mainly differ in the model and the parameters used. Table 1.1 shows an overview of the generators employed in this analysis, showing the models used for the different reactions and nuclear effects.

Table 1.1: Features of the neutrino generators used in studies presented in this document.

Generator	NEUT 5.3.2 [72, 73]	GENIE 2.8.0 [74]	NuWro 11q [75]
CCQE	Llewellyn-Smith QE [56]	Relativistic Fermi Gas + Bodek-Ritchie tail [78]	Llewellyn-Smith QE
Axial mass	$M_A^{\text{QE}} = 1.21 \text{ GeV}$ [79]	$M_A^{\text{QE}} = 0.99 \text{ GeV}$	$M_A^{\text{QE}} = 1.0 \text{ GeV}$
Res. Pion	Rein-Sehgal [59]	Rein-Sehgal	Single Δ model by Adler-Rarita-Schwinger
Axial mass	$M_A^{\text{RES}} = 1.21 \text{ GeV}$	$M_A^{\text{RES}} = 1.12 \text{ GeV}$	$M_A^{\text{RES}} = 0.94 \text{ GeV}$
2p2h	Nieves model [65, 80]	None (empirical MEC model added in v.2.12.4)	Nieves model (different implementation than NEUT)
DIS	Parton distribution function GRV98 [81] + corrections by Bodek and Yang [82]		Bodek and Yang approach
FSI	Semi-classical intranuclear cascade model	Parametrised model of FSI (GENIE's "hA" model)	Semi-classical cascade model

1.4 Neutrino energy reconstruction

In order to determine the oscillation parameters, the oscillation probability (1.7) has to be studied for various neutrino energies E_ν for a given baseline L . Usually the neutrino rate is compared with two detectors, one is near the neutrino source and the second one is far. The neutrino event rates are

$$\begin{aligned} N_{\text{near}}(E_\nu) &= \sigma_{\text{near}}(E_\nu) \Phi(E_\nu) \varepsilon_{\text{near}}(E_\nu) \\ N_{\text{far}}(E_\nu) &= \sigma_{\text{far}}(E_\nu) \Phi(E_\nu) \varepsilon_{\text{far}}(E_\nu) \cdot P_{\text{osc}}(E_\nu) \end{aligned} \quad (1.30)$$

where σ_{near} (σ_{far}) is the neutrino cross section of the near (far) detector, Φ is the neutrino flux at the source and $\varepsilon_{\text{near}}$ (ε_{far}) is the near (far) detector acceptance. In the ideal case of near and far detectors that are the same ($\varepsilon_{\text{near}} = \varepsilon_{\text{far}}$ and $\sigma_{\text{near}} = \sigma_{\text{far}}$) and a monochromatic beam ($\Phi(E_\nu) = \delta(E_\nu - E_0)$), the oscillation probability can be extracted using (1.30)

$$P_{\text{osc}}(E_\nu) = \frac{N_{\text{far}}(E_\nu)}{N_{\text{near}}(E_\nu)} \quad (1.31)$$

However, in a realistic experiment the neutrino flux is usually provided as a spectrum of energies. Thus the energy of the neutrino has to be reconstructed from the final states of the reactions. The far and near neutrino rates are the convolutions of (1.30) over the whole range of energies,

$$\begin{aligned} P_{\text{osc}}(p_\mu^{\text{reco}}, \theta_\mu^{\text{reco}}) &= \frac{N_{\text{far}}(p_\mu^{\text{reco}}, \theta_\mu^{\text{reco}})}{N_{\text{near}}(p_\mu^{\text{reco}}, \theta_\mu^{\text{reco}})} \\ &= \frac{\int \sigma_{\text{far}}(E_\nu) \Phi(E_\nu) \varepsilon_{\text{far}}(E_\nu) \cdot P_{\text{osc}}(E_\nu) \cdot P(p_\mu^{\text{reco}}, \theta_\mu^{\text{reco}} | E_\nu) dE_\nu}{\int \sigma_{\text{near}}(E_\nu) \Phi(E_\nu) \varepsilon_{\text{near}}(E_\nu) \cdot P(p_\mu^{\text{reco}}, \theta_\mu^{\text{reco}} | E_\nu) dE_\nu} \end{aligned} \quad (1.32)$$

The integrand is multiplied by the probability $P(p_\mu^{\text{reco}}, \theta_\mu^{\text{reco}} | E_\nu)$ for a neutrino with energy E_ν to be detected with reconstructed lepton variables $p_\mu^{\text{reco}}, \theta_\mu^{\text{reco}}$. In the discrete case this is called the *smearing* matrix. Since it is accounting for the detector performances, Monte Carlo simulations and event generators are required to compute the smearing matrix and it is therefore model dependent. However the model dependency is largely eliminated by doing a measurement in the muon kinematic observables $p_\mu, \cos \theta_\mu$. Moreover, the cross sections σ_{near} and σ_{far} need predictions from theory so they also rely on models. This is why an accurate knowledge of neutrino interaction models is crucial in oscillation analyses.

There are two different ways to reconstruct the energy. The first one is a good approximation at energies up to ~ 2 GeV. The neutrino energy is estimated with the kinematics of the outgoing lepton and the four-body kinematic formula. For $\nu_\ell + n \rightarrow \ell + p$ assuming the nucleon is a stationary target and the scattering is elastic, we have following approximation:

$$E_\nu^{\text{reco}} = \frac{m_p^2 - (m_n - E_b)^2 + m_\ell^2 + 2(m_n - E_b)E_\ell}{2(m_n - E_b - E_\ell + p_\ell \cos \theta_\ell)} \quad (1.33)$$

where E_b is the nuclear binding energy of the neutron, m_n and m_p the neutron and proton masses respectively and $p_\ell, \theta_\ell, m_\ell$ and E_ℓ are the momentum, angle, mass and energy of the outgoing lepton. As it does not account for Fermi motion of the nucleon the estimated energy is smeared. Moreover there is a bias coming from 2p2h contribution or resonant pion absorption that can be misidentified as quasielastic reactions. Those two inelastic contributions are illustrated in Fig. 1.16 and more details about nuclear effects in neutrino-nucleus scattering will be given in Section 1.3.4.

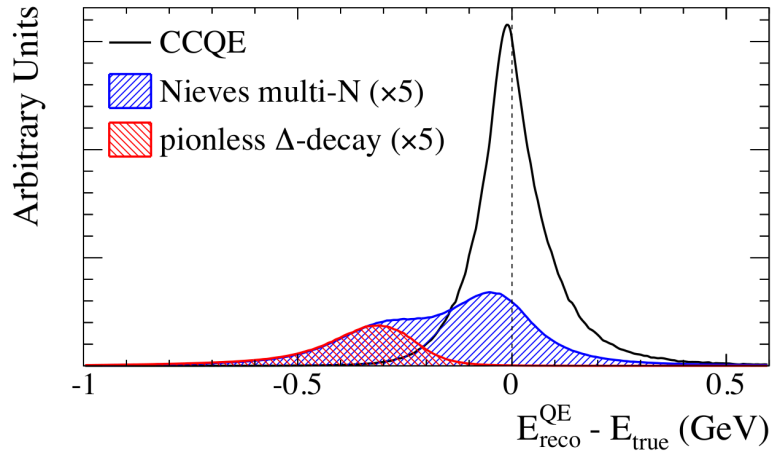


Figure 1.16: Difference between the energy reconstructed with the four-body kinematic formula and the true energy for quasielastic events. Simulation is performed with NEUT and the T2K flux. The 2p2h and pion absorption contributions are scaled by a factor of 5.

The second method to reconstruct the neutrino energy is useful for energies > 2 GeV, where inelastic reactions dominate and the four-body kinematics cannot be assumed. This method uses calorimetric information, the energy contributions from each final state particle are summed up to estimate E_{ν}^{reco} . It is less affected by wrong identifications, however it must rely on models for invisible particles, e.g. neutral hadrons.

Several studies have been performed on the energy smearing impact on oscillation measurements [83, 84, 85]. With the current detector technologies studies show that the kinematic approach is more robust than the calorimetric method, keeping in mind the disadvantage of a non-accurate knowledge on neutrino-nucleus scattering.

The T2K Experiment

The T2K Experiment [53] is a long-baseline neutrino experiment probing the physics of neutrino oscillations. Muon neutrinos are produced at the J-PARC facilities and can be observed with a near detector complex located 280 meters downstream from the beam source and a far detector at 295 kilometers. T2K aims at measuring the neutrino mixing parameters through electron neutrino appearance from muon neutrino beam (θ_{13}) and through muon neutrino disappearance (Δm_{23}^2). It also has the ability to probe $\sin^2 2\theta_{23}$ and CP violation (δ_{CP}) [86, 87] thanks to the ability to polarise the beam to either produce neutrinos or antineutrinos. Moreover T2K allows to study neutrino interactions at energies that cover the transition from resonant interactions to deep inelastic scattering.

The Super-Kamiokande water Cherenkov far detector is exploited to measure the oscillated flux. The near detector is crucial to characterise signals and backgrounds observed at the far detector: it includes an on-axis detector, INGRID, that measures the neutrino beam direction and profile; moreover an off-axis detector, ND280, measures the muon neutrino flux and its energy spectrum just after the production. It also quantifies the electron neutrino contamination and makes cross-section measurements.

The construction of the T2K beamline, that is represented in Fig. 2.1, was completed in 2009 and data taking for physics analysis started in January 2010.

In this chapter we describe the T2K beam, explaining how the neutrino flux is produced. We then give a description of the far detector Super-Kamiokande and of the near detector complex with its different sub-detectors. We end this chapter by giving a brief overview of the software that is used to analyse data taken at the near detector.

2. The T2K Experiment

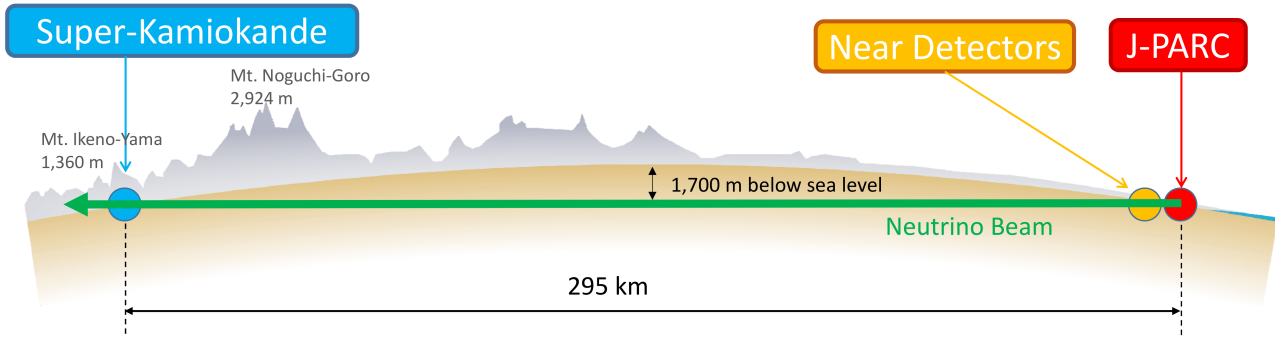


Figure 2.1: Schematic representation of the T2K beamline. Source: t2k.org

2.1 The T2K beam

The T2K neutrino beam is generated at J-PARC in Tokai (Ibaraki, Japan). A proton beam is produced by the primary beamline, which consists in a linear accelerator (LINAC) and a rapid-cycling synchrotron (RCS). Protons are then injected into the main ring (MR) synchrotron and accelerated up to 30 GeV, before they can be extracted for the secondary beamline, which is represented in Fig. 2.2. Protons are steered towards a graphite target, interacting with it to produce secondary pions which are focused by three magnetic horns excited by a 250 kA (−250 kA) current pulse. Particles travel through a 96 m decay volume where they decay into (anti)muons and muon (anti)neutrinos. Other particles are stopped by the beam dump. After the beam dump a muon monitor (MUMON) is used to monitor the neutrino beam intensity and direction [88].

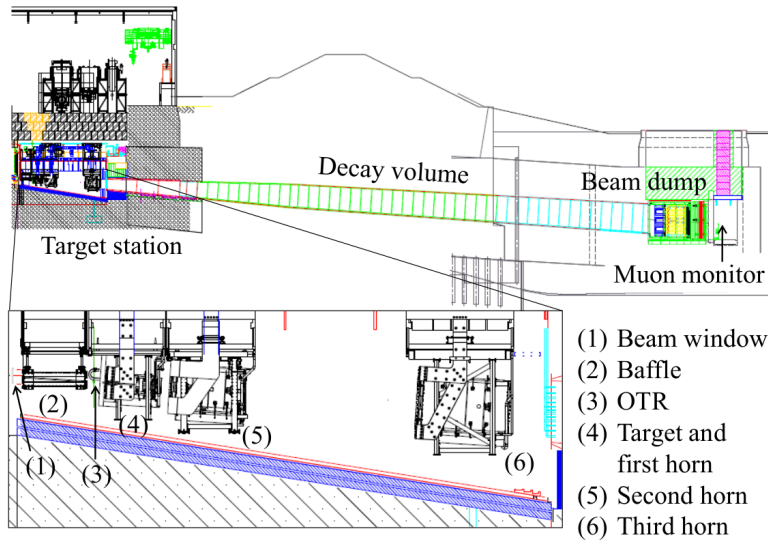
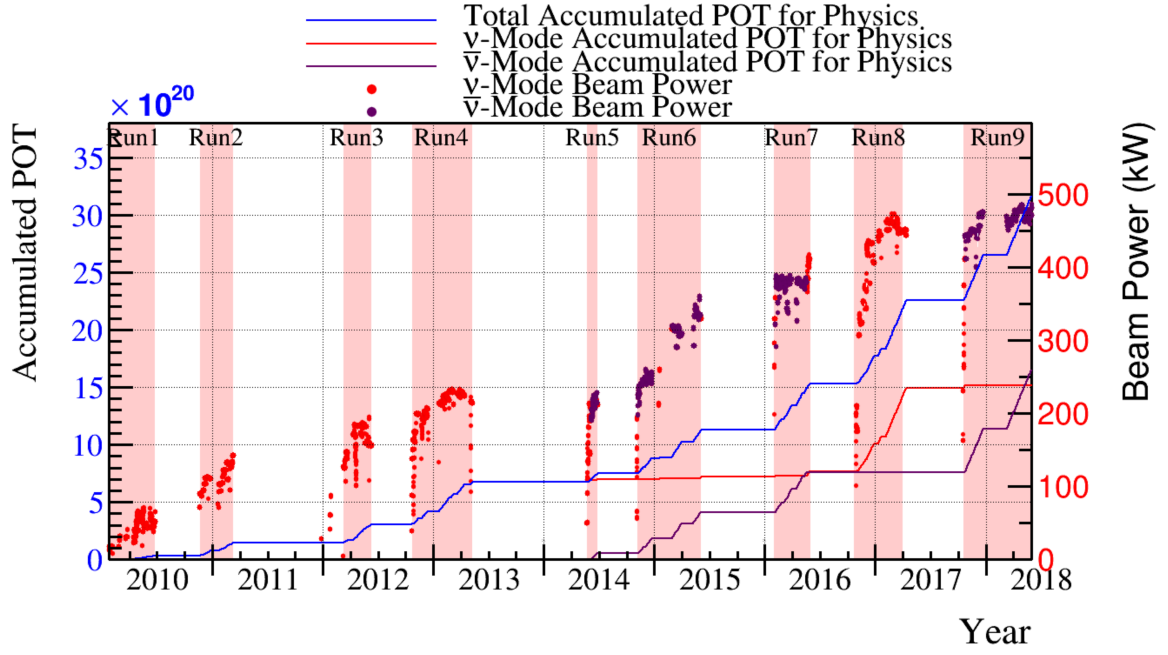


Figure 2.2: Side view of the secondary beamline. The length of the decay volume is around 96 meters. Source: [89]

Since 2010 a fluence of 3.16×10^{21} protons on target (POT) has been reached, of which about 52% were in antineutrino mode (Reverse Horn Current). Thanks to many developments a beam power of about 500 kW was achieved in 2018. The evolution of accumulated POT and beam power is shown in Fig. 2.3.



23 Jan. 2010 – 31 May 2018

POT total: 3.16×10^{21}

ν -mode 1.51×10^{21} (47.83%)

$\bar{\nu}$ -mode 1.65×10^{21} (52.17%)

Figure 2.3: Total accumulated Protons On Target (lines) and beam power (dots) for the T2K data taking from 2010 to 2018 in neutrino (red) and antineutrino (purple) modes. Source: t2k.org

2.1.1 Off-axis technique

In order to produce a narrow-band neutrino beam, an off-axis method is employed. The beam is directed with an angle of 2.5° with respect to the line between the neutrino source and the far detector. This technique allows the production of a neutrino beam with energy peaked at 0.6 GeV. As can be seen in Fig. 2.4 this energy maximises the effect of muon neutrino oscillation at the Super-Kamiokande location.

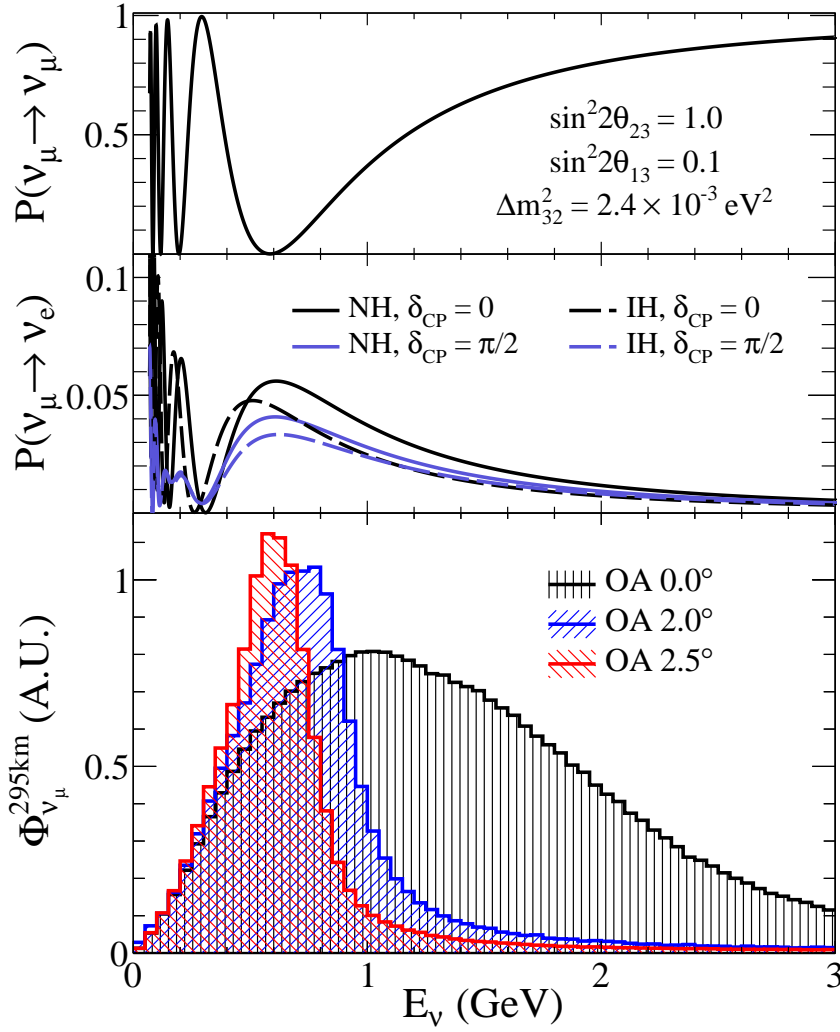


Figure 2.4: Comparison of the oscillation probability for $\nu_\mu \rightarrow \nu_\mu$ (top) and for $\nu_\mu \rightarrow \nu_e$ (middle) to the T2K flux (bottom) on axis and at different off-axis angles. Source: t2k.org

2.1.2 The neutrino flux

The T2K neutrino flux is predicted with Monte Carlo simulations based on experimental data [89]; an update on the flux prediction uncertainty can be found in [90]. A dedicated experiment at CERN, NA61/SHINE [91, 92] is designed to measure hadron production by ~ 30 GeV protons on a graphite target. In the prediction, primary interactions of protons with carbon are based on NA61/SHINE data. Other interactions inside the target are simulated by FLUKA [93] and outside the target by GEANT3 [94].

Predicted neutrino and antineutrino fluxes at the T2K near detector are shown in Fig. 2.5 for Forward Horn Current (FHC, neutrino mode) and Reverse Horn Current (RHC, antineutrino mode).

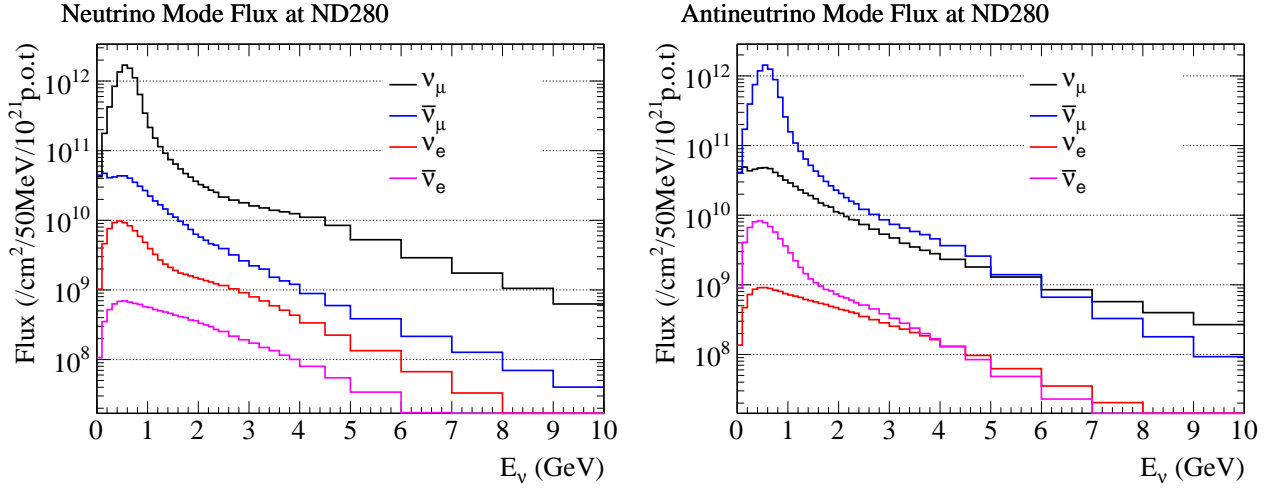


Figure 2.5: T2K neutrino and antineutrino fluxes at the near detectors for Forward Horn Current (ν mode, left) and Reverse Horn Current ($\bar{\nu}$ mode, right). Source: t2k.org

2.2 The Far Detector Super-Kamiokande

Super-Kamiokande is a water Cherenkov detector located 295 km away from the T2K neutrino beam source. Running since 1996 it is designed for charged particle observation and various results have been published on proton lifetime limits [95, 96] and oscillation measurements in atmospheric and solar neutrinos [3, 29, 30, 31]. Since 2010 the Super-Kamiokande detector has also been collecting data to look for $\nu_\mu \rightarrow \nu_e$ ($\bar{\nu}_\mu \rightarrow \bar{\nu}_e$) appearance and ν_μ ($\bar{\nu}_\mu$) disappearance from the T2K muon (anti)neutrino beam [86, 87]. As it has been running for a long time the Super-Kamiokande detector operates in a very stable way with a well-known behaviour.

The detector is made of a cylindrical tank located 1 km underground in a former mine within Mt. Ikenoyama, near Kamioka. A schematic representation of the detector and surrounding facilities is shown in Fig. 2.6. The inner detector is filled with 50 ktons of pure water and the walls are covered with about 11,000 Hamamatsu Photo-Multiplier Tubes (PMTs) able to detect light coming from the inside of the tank. The outer detector also has PMTs but only about 2,000 PMTs. This is sufficient to provide an accurate veto of backgrounds such as cosmic ray muons and other particles coming from interactions outside the detector.

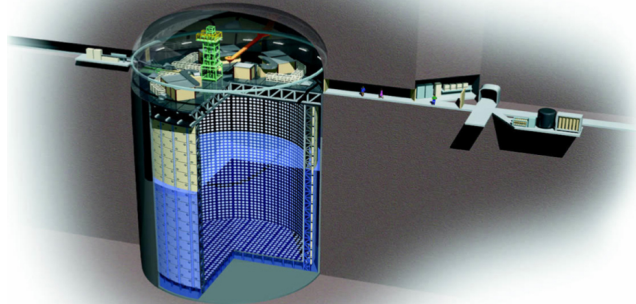


Figure 2.6: Overview of the Super-Kamiokande detector complex.

2. The T2K Experiment

Neutrino interactions produce charged particles. Above a certain energy threshold those particles emit a cone of Cherenkov photons while travelling faster than the speed of light through the water, resulting in a ring-shaped hit pattern seen by the PMTs. The observed light ring provides information about event vertex position and momenta of the outgoing particles. Muons and electrons are accurately distinguished. Electrons, due to their smaller mass, scatter off other particles while traversing the water and therefore produce electromagnetic showers. The ring pattern seen by the PMTs is therefore "fuzzy", as can be seen on an example in Fig. 2.7. On the other hand muons produce a sharp ring as they travel through the detector without changing their momentum, because of their relatively large mass. An example of a light ring created by a muon is shown in Fig. 2.8. The difference with the electron light ring can be seen by eye and is also easily determined by a particle identification algorithm.

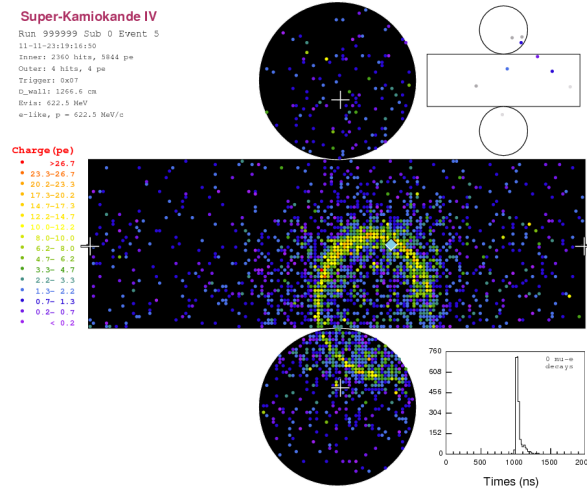


Figure 2.7: An event display coming from a true CC electron neutrino interaction at Super-Kamiokande.

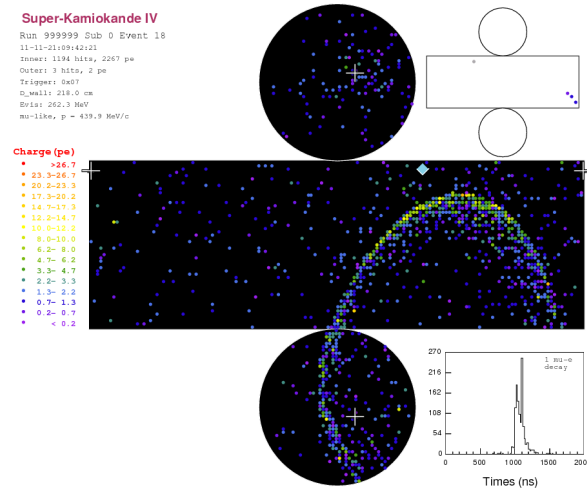


Figure 2.8: An event display coming from a true CC muon neutrino interaction at Super-Kamiokande.

2.3 The ND280 off-axis near detector

In order to study neutrino oscillations, the energy spectrum, flavour content and interaction rates of the unoscillated beam need to be measured. This is done thanks to a set of detectors placed 280 meters downstream of the production target. The near detector complex, represented in Fig. 2.9, consists of a magnetised off-axis tracking detector ND280 and an on-axis detector INGRID. In this section we will describe the different ND280 sub-detectors, that can be seen in Fig. 2.10, and INGRID will be described in Section 2.4.

The z axis is defined by convention to be along the nominal neutrino beam axis, the x and y axes are the perpendicular horizontal and vertical axes respectively.

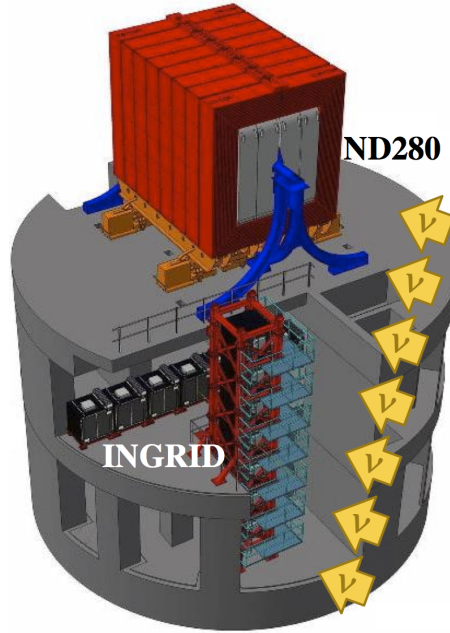


Figure 2.9: The T2K near detector complexe. Source: t2k.org

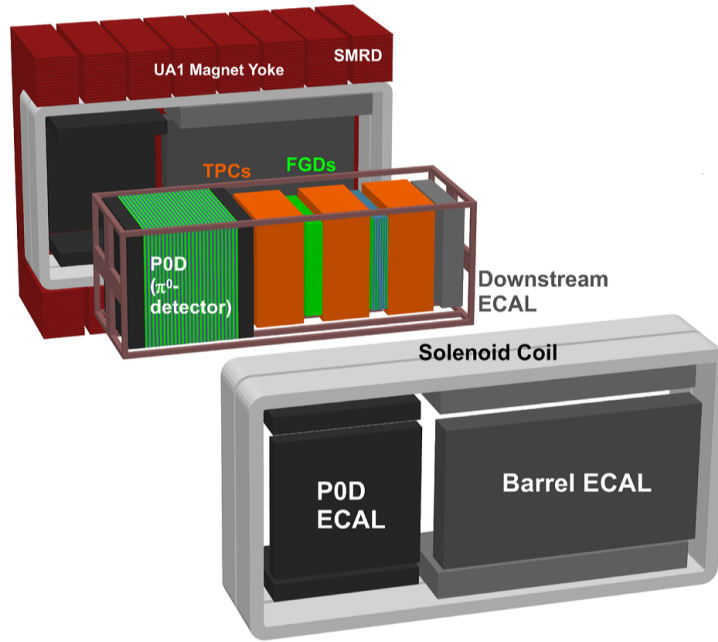


Figure 2.10: Schematic representation of the opened ND280 detector. Source: [53]

2.3.1 The Multi-Pixel Photon Counter (MPPC)

In ND280 many photosensors are needed to detect the light from scintillator detectors and wavelength-shifting fiber readout. Multi-anode PMT's are common for this task but unfortunately they are not suitable for ND280 as they cannot operate in a magnetic field environment. Therefore multi-pixel avalanche photodiodes (MPPC) were chosen as they satisfy the ND280 requirements. More details can be found in [97].

2.3.2 The Pi-Zero Detector (P0D)

The π^0 detector (P0D) [98] is designed to measure neutral current interactions in water, for instance $\nu_\mu + N \rightarrow \nu_\mu + N + \pi^0 + X$. It is made of scintillator modules with interleaved water target bags that can be operated filled with water or emptied. The P0D permits to reconstruct charged particle tracks (μ and π) and electromagnetic showers (e^- and γ from π^0). Measurements in both configurations, with and without water, are then analysed using a subtraction technique, allowing to extract a cross section on water. Different cross-section results from P0D measurements have been published already, such as single π^0 production rate in neutral current interactions [99], ν_μ CC- 0π interactions [100] and ν_μ and $\bar{\nu}_\mu$ charged current inclusive cross sections [101].

Fig. 2.11 shows a representation of the 40 scintillator modules (P0Dules), each of them being made of one plane with bars in the x direction and another plane in the y direction. The scintillator bars are optically read out by Hamamatsu MPPCs (see Sec.2.3.1). The center contains the water layers sandwiched in between the carbon layers. The front and rear sections, called upstream and downstream ECAL respectively, have only scintillator layers and are used as veto regions to reject events from interactions from outside the P0D. An example of event is shown in Fig. 2.12.

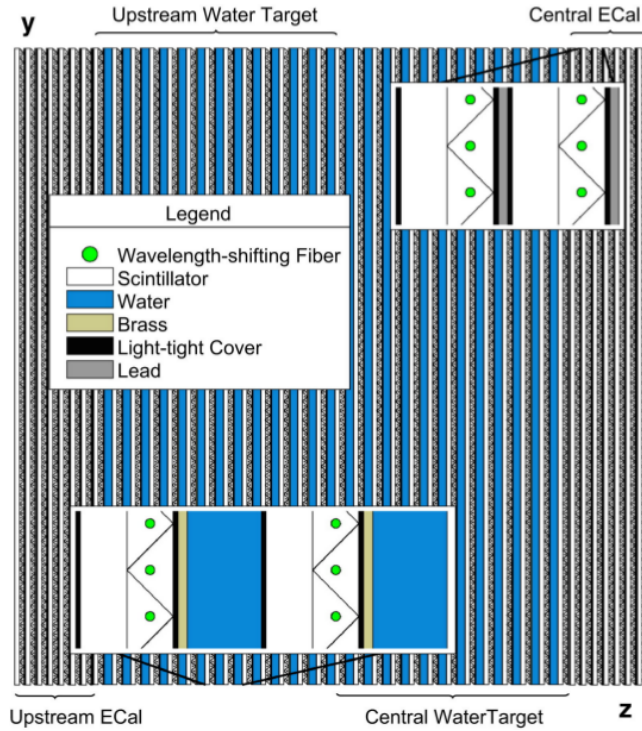


Figure 2.11: Schematic representation of the P0D layers. Source: [53]

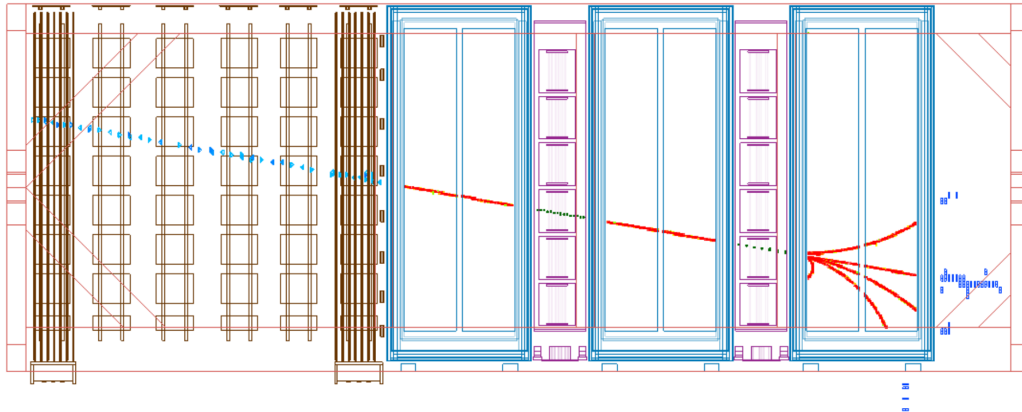


Figure 2.12: Event display showing an event with a muon track entering via the front face of the P0D detector, continuing to the TPC and FGD tracker region and producing secondary particles on the way. The secondary particles are then stopped in the ECal detectors. Source: [53]

2.3.3 The Fine-Grained Detectors (FGD)

The two Fine-Grained Detectors (FGD1 + FGD2) [102] are fully active scintillator trackers sandwiched in between the TPCs (see Section 2.3.4). They contain the target mass for neutrino interactions and their fine segmentation allows a precise reconstruction of the interaction vertex and outgoing particle tracks. The second FGD has interleaved water layers, thus cross sections on water and on carbon can be extracted through a comparison of interaction rates in the two FGDs.

Each FGD detector is made of 1.1 tons of target material. Both of them contain so-called XY modules, each of the modules being made of two layers of 192 polystyrene scintillator bars

2. The T2K Experiment

(C_8H_8) that are perpendicular to the neutrino beam direction. The scintillator bars are oriented either in the x or y direction alternately, which allows particle track reconstruction. They are mirrored at one end and attached to MPPCs (see Section 2.3.1) at the other end. Photosensors are mounted along sides of the XY modules in order to collect the scintillation light emitted by passing-through particles. The intensity of the light, measured by recorded photoelectrons, gives an estimation of the energy deposit and time of arrival of travelling particles.

The FGDs provide accurate measurements of track angles, but they do not measure particle curvature accurately enough to extract the momentum. However, if the particle track is fully contained in the FGD, for instance for high-angle tracks, the momentum can be estimated based on the distance travelled by the charged particle ("momentum by range") by summing the energy deposits from the vertex to the end of the track. The FGDs also enable to identify the particles by use of the total energy loss and the length of the track. The particle identification method (FGD PID) is similar to the one described later on for the TPC PID in Section 2.3.4.

The first FGD, FGD1, is the most upstream one. It is composed of 15 XY scintillator modules. The second FGD, FGD2, has 7 XY modules and 2.5 cm thick layers of target water placed in between the scintillator modules. Sideviews of the fiducial volumes are shown in Fig. 2.13 and 2.14 for the two FGDs respectively. The elemental composition of the FGD scintillator modules is detailed in [103] and the water modules are described precisely in [104].

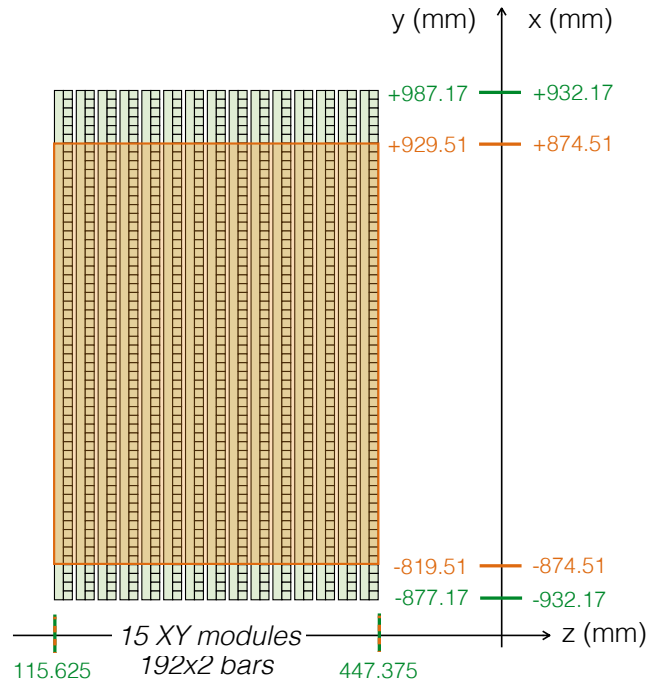


Figure 2.13: Sideview of the FGD1 fiducial volume. Source: [105]

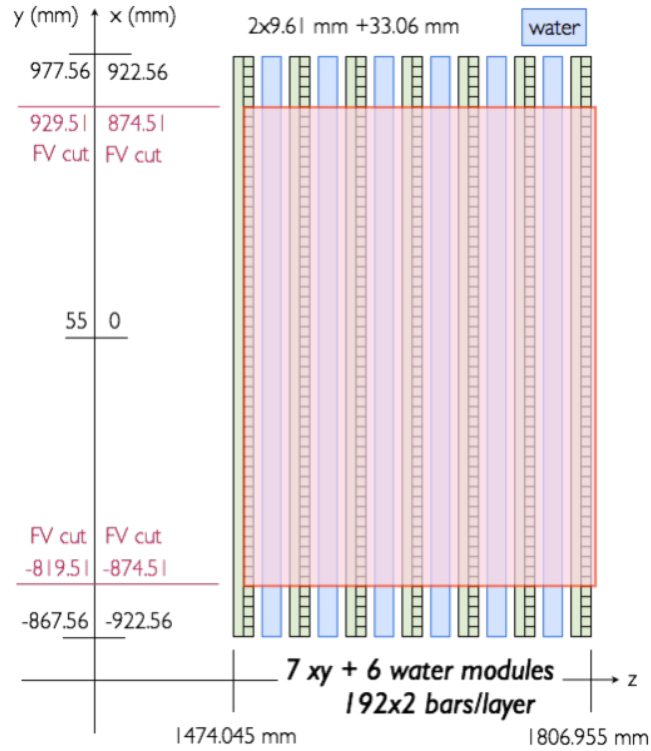


Figure 2.14: Sideview of the FGD2 fiducial volume. Source: [106]

2.3.4 The Time Projection Chambers (TPC)

The three Time Projection Chambers (TPC1 + TPC2 + TPC3) have a major tracking role in the near detector. As can be seen in Fig. 2.10 they are placed in such a way that they surround the FGD detectors used as target material. Three dimensional tracks of charged particles produced in neutrino interactions in the FGDs or elsewhere in the near detector can thus be reconstructed accurately through the TPCs. Moreover the TPCs allow to measure the momenta and energy loss of the particles, and therefore to determine the different types of charged particles.

Each TPC is made of an inner box filled with an argon-based drift gas, contained in an outer box that holds CO_2 as an insulating gas. A uniform electric drift field of around 280 V/cm is produced between the central cathode panel and the external planes. This is illustrated on a simplified drawing in Fig. 2.15. Charged particles from interactions elsewhere in the near detector that go through the TPC ionise the gas, producing electrons that drift away from the cathode towards the readout planes. Those electrons are then amplified and sampled with micromegas modules [107]. Each of these module planes is $342 \times 359 \text{ mm}^2$ large and consists of 1728 anode pad segmentations, providing a point spatial resolution of around 0.7 mm. Six front-end electronics cards digitise and collect the charge and time information, allowing a high resolution readout in order to make accurate track measurements. Fig. 2.16 shows an event display example, for instance a neutrino interaction event with deep inelastic scattering. More technical details can be found in [108].

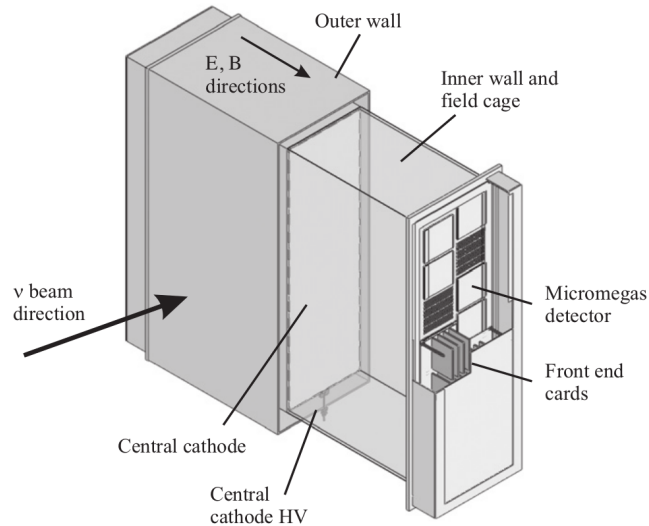


Figure 2.15: Schematic representation of one Time Projection Chamber. Source: [108]

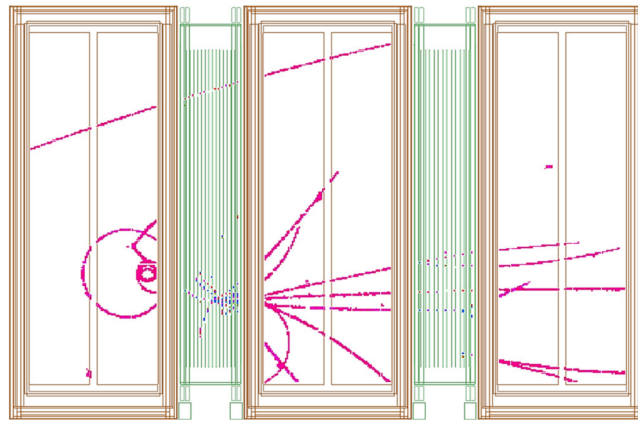


Figure 2.16: Event display of a neutrino interaction event where a second neutrino undergoes a deep inelastic scatter in FGD1. Source: [108]

The very good imaging capabilities of the TPCs allow to determine easily the number of charged particles that go through the detector and their orientations. Selections of high-purity samples of various types of neutrino interactions are thus enabled. Moreover, as already mentioned briefly, TPCs operate in a 0.2 T magnetic field (see Sec.2.3.5). Trajectories of charged particles in an electromagnetic field are curved with respect to their momentum (and charge). Therefore the momenta of charged particles that are created in a neutrino interaction can be determined with good accuracy. The amount of ionisation left by each particle can also be measured. This energy deposit measurement can be combined with the momentum information, allowing particle identification. Indeed, as can be seen in Fig. 2.17, the shape of the energy loss versus momentum distribution depends on the particle type. In order to identify a particle from a given track, a dE/dx^1 pull is computed, corresponding to the deviation of the measurement with respect to the expected value at the observed momentum for each type of particle. An example of dE/dx pull distribution is shown in Fig. 2.18 for the electron hypothesis as a function of the momentum. Details on the TPC particle identification method are given in [109].

¹energy loss per unit of length

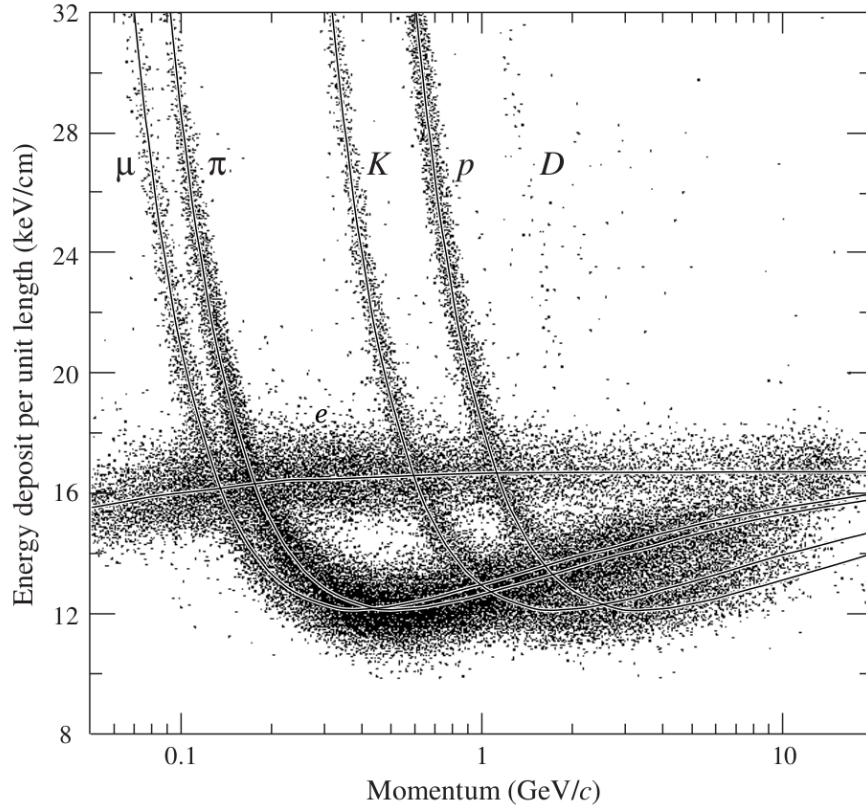


Figure 2.17: Energy loss as a function of the momentum compared to the expected curves for muon, pion, kaon, proton, deuterium and electron. Source: [109]

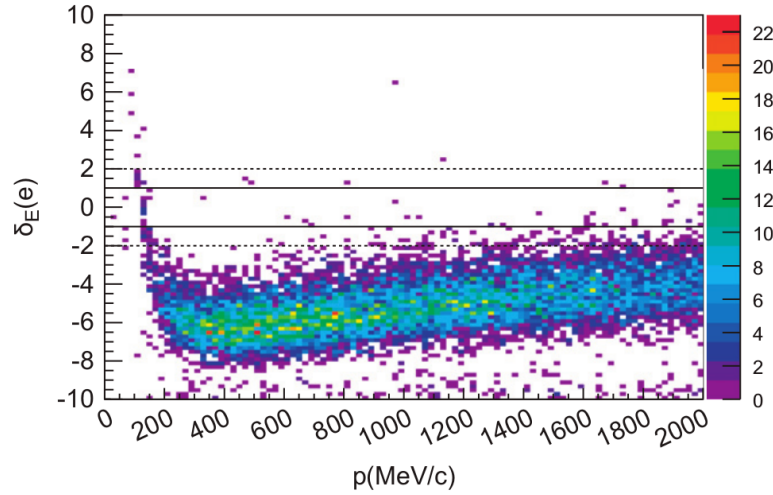


Figure 2.18: Distribution of the energy loss pull in the electron hypothesis for a sample of going-through muons. The solid lines indicate a pull value < 1 and the dashed lines < 2 . Source: [108]

2.3.5 The UA1 Magnet

In order to determine the momentum with a good resolution and the sign of charged particles produced by neutrino interactions the near detector operates in a magnetic field orthogonal to the neutrino beam direction. The 0.2 T dipole magnetic field is provided by the UA1/NOMAD

2. The T2K Experiment

magnet, reused from a CERN experiment. The magnet is made of aluminium coils that are distributed in C-shaped iron yokes. The coils are cooled down thanks to water flowing through the middle of the coils. The nominal current is 2900 A. The dimensions of the inner volume are $7.0\text{ m} \times 3.5\text{ m} \times 3.6\text{ m}$ and the yoke total weight is 850 tons. The magnet yoke is built in two movable halves that surround the ND280 tracker and can be opened in order to access the different sub-detectors inside the magnet.

2.3.6 The Side Muon Range Detector (SMRD)

The Side Muon Range Detector (SMRD) covers different functions. Firstly it allows to trigger on muons from interactions happening outside the ND280 basket, for instance muons coming from cosmic rays or muons from neutrino interactions anywhere in the cavern walls. The second role is to detect muons escaping the inner detector with high angles with respect to the neutrino beam direction.

The SMRD is made up of 440 scintillator modules read out by MPPCs (see Section 2.3.1) that are connected to miniature PCBs. The module layers are placed on the detector sides in the radial direction in the air gaps of the magnet yokes.

2.3.7 The Electromagnetic Calorimeter (ECal)

The ND280 Electromagnetic Calorimeter (ECal) consists of 13 independent active scintillator modules that surround the inner detectors. The modules are made of layers of polystyrene scintillator bars glued to lead absorbers sheets; light is read out by MPPCs (see Section 2.3.1). With an almost full coverage of all particles exiting the detector basket, the ECal helps the inner detector doing a full event reconstruction.

The ECal is very useful in particular in the measurement of π^0 produced in neutrino interactions within the detector volume. The π^0 are actually reconstructed in the P0D detector. However the P0D-ECal modules are required to complement measurements in the case of events that are not fully contained. The ECal modules are also used as a veto for incoming backgrounds, complementing the SMRD (see Section 2.3.6), and they also provide a particle identification tool (ECal PID).

2.4 The INGRID on-axis near detector

The Interactive Neutrino GRID detector is designed to monitor the T2K neutrino beam direction and intensity [110]. 14 identical modules are arranged as a cross that is centered on the neutrino beam axis at 0° . Moreover 2 additional modules are placed in the off-axis directions outside of the main cross in order to check the axial symmetry of the neutrino beam. A schematic representation of the modules is shown in Fig. 2.19.

The modules have a sandwich structure of 9 iron plates and 11 tracking scintillator planes, made of scintillator bars in the x and y directions. Each module is surrounded by veto scintillator plates. The total mass of target iron is 7.1 tons per module.

An extra module, called Proton Module, is added in order to measure neutrino interactions. This module contains finer scintillator bars than the other modules, allowing to track muons alongside with protons with a better efficiency. It has no iron plates. Published cross-section results from INGRID can be read in [111, 112].

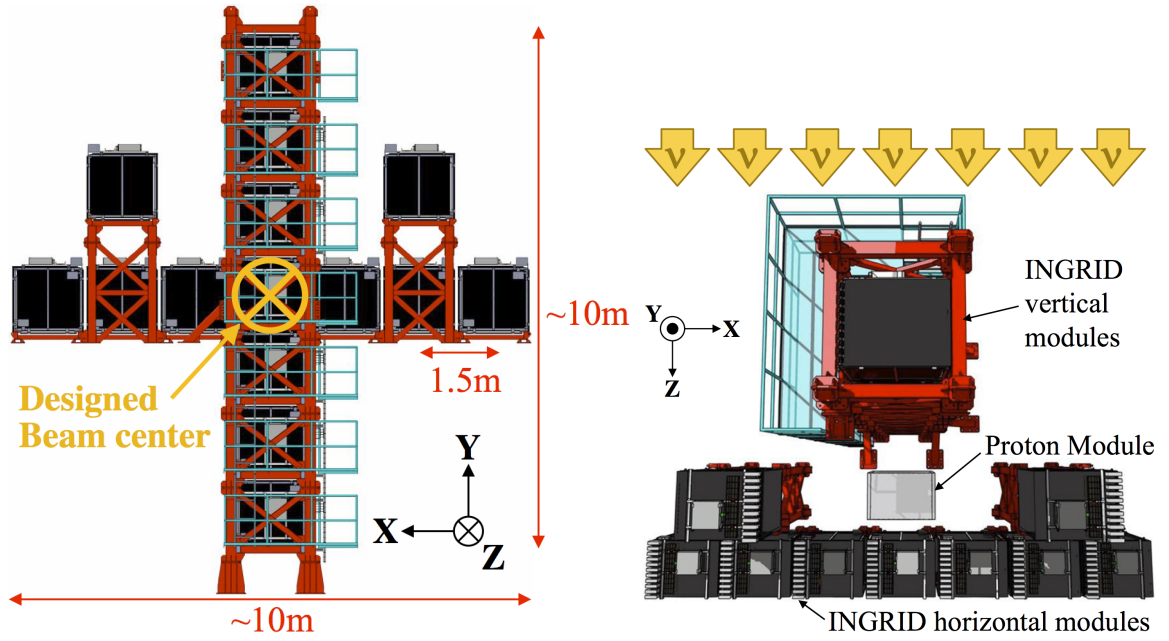


Figure 2.19: Schematic representation of the INGRID detector. Source: [53]

2.5 The ND280 software

The ND280 software is a C++ framework based on ROOT [113]. It contains many different packages, the main ones being in charge of event simulations, calibration of real data and event reconstruction. After the reconstruction stage information is stored in a specific format inheriting from the class `oaEvent`. The size and complexity of these files are not suitable for an analysis. Other packages are used in order to reduce the data size, `oaAnalysis`, and in order to perform an event selection and evaluate the detector uncertainties, `Highland2` (HIGH Level ANalysis Development). `Highland2` is able to perform various types of event selections, applying corrections to some reconstructed variables to correct for MC to real data discrepancies. Associated systematic uncertainties are propagated using toy experiments.

Motivations, strategy and inputs for the cross-section extraction

3.1 Motivations

As discussed in Section 1.4 a good neutrino cross-section knowledge is essential for accurate oscillation measurements, as it is crucial to compare interaction rates at the near and far detectors. In the T2K Experiment the comparison is not obvious as the far detector target mass is water and the near detector contains mainly hydrocarbon scintillators. Therefore it is also important to measure neutrino interactions with water targets in ND280, which is made possible by the second Fine-Grained Detector (FGD2, see Section 2.3.3) that contains interleaved water layers. In addition to the neutrino cross sections on water and on carbon the FGDs allow measurements of the oxygen over carbon cross-section ratio. The cross-section ratio is useful while comparing neutrino event rates at the near and far detectors given in Eq. (1.30). In this introductory part of the chapter the advantage of utilising both FGDs in a joint fit in order to extract neutrino cross sections on carbon and on oxygen will be discussed in Section 3.1.1. Then, as such measurement has already been done in the past [114], the benefits and improvements of this analysis will be exposed in Section 3.1.2.

3.1.1 Benefits of a FGD1 + FGD2 joint analysis

The alternating scintillator and water layers of FGD2 allow the reconstruction of interactions in a water layer from which the first hit is detected in a x layer. This is illustrated in Fig. 3.1. However interactions in the water and in the x layers are strongly anti-correlated, because of event migration due to mis-reconstructions of the neutrino interaction vertex. To palliate this effect we combine FGD1 samples with the FGD2 measurements. Since the FGD1 detector consists mainly of plastic scintillator bars its additional information constrains the neutrino interaction rate on carbon. As a consequence the statistical uncertainty on carbon measurements is reduced and the anticorrelations between interactions in the two elements is decreased too. This is demonstrated in the studies presented in Appendix B.3.

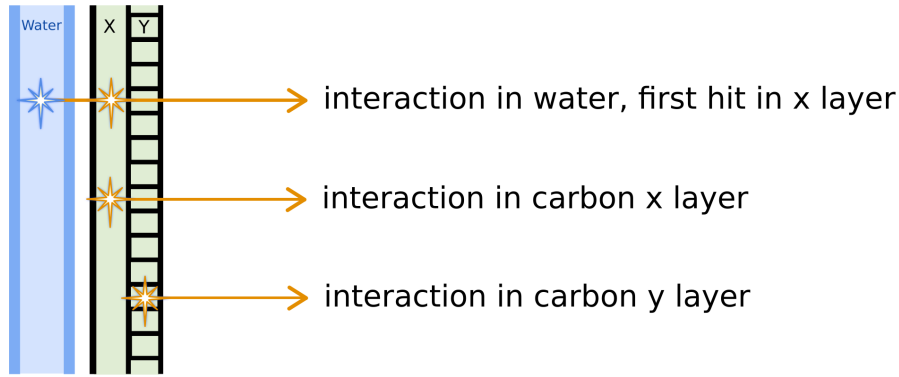


Figure 3.1: Sketch of the FGD2 layers with symbolic representation of interactions in the water and in the x and y scintillator layers.

3.1.2 Improvements with respect to previous T2K analyses

A previous joint measurement of the neutrino cross section on carbon and oxygen has already been made with FGD1 and FGD2 and is related in T2K-TN-338 [114]. However it does not include the full T2K data that are currently available and many developments have been done in the ND280 particle selection and in the fitter framework since then. For these reasons it is important to update such measurement with recent improvements and bug fixes.

First of all the data statistics is increased with the new T2K run period 8, doubling the number of Protons On Target (POT). An updated flux tuning is used with a lower flux uncertainty compared to previous analyses. A new control sample is added to the fitter for an additional control of background events with pion production ($\text{CC-}1\pi^+$) with the help of Michel electron measurements. Moreover backward migration of events in the FGD2 have been studied more deeply [115], therefore the associated systematic uncertainty is improved. Studies conducted on the ND280 selection of muon neutrino charged-current interactions with no pion in the final state ($\nu_\mu \text{ CC-}0\pi$) [116] showed few bugs, which have now been fixed for this analysis, and the most recent software version is used for the event selection. The method used to separate events between x and y layers of FGD2 has been improved in order to accept events with a reconstructed start position in the water, which were previously rejected. Finally many major developments have been done on the cross-section fitter framework and in particular the method used to propagate the systematic uncertainties has been improved. Such developments have made possible to fit up to about a thousand parameters.

3.2 Analysis strategy

This section defines more precisely the type of cross section that is measured and gives an overview of the method used in order to extract the neutrino interaction rates. Note that in this analysis we talk about *topologies*, which are associated to events according to information about particles leaving the nucleus *after* interaction. Following criteria define the topologies:

- **CC- 0π :** one true negative muon and no pion in the final state;
- **CC- $1\pi^+$:** one true negative muon, one positive pion and no negative or neutral pions in the final state;
- **CC-Other:** one true negative muon and at least one neutral or negative pion or more than one positive pion (it corresponds to all $\nu_\mu \text{ CC}$ events that are not associated to one of the two latter categories);

- **Background (BKG):** anti-neutrino, electron neutrino and neutral current (NC) interactions;
- **Out Of Fiducial Volume (OOFV):** interaction vertex outside of FGD1 or FGD2 fiducial volume.

3.2.1 Cross section and signal definition

We search for muon neutrino (ν_μ) charged-current (CC) interactions with no pion in the final state (0π) and producing possibly one or more protons. The flux-integrated double-differential ν_μ CC- 0π cross section on carbon and oxygen is measured in the FGD1 and FGD2 detectors. Interactions on other targets are treated as backgrounds. Choices for this measurement have been made in order to reduce as much as possible model dependencies. First, the cross section is extracted as a function of the muon momentum and angle (double differential). The choice of outgoing muon kinematic variables avoids a large model dependency coming from measurements in neutrino energy or transferred momentum Q^2 . Second, the signal definition also allows to reduce the dependency to cross-section modelling since it is defined in terms of the particles that exit the nucleus, which are the ones that we measure. CC- 0π interactions include not only CCQE events ($\sim 80\%$) but also resonant interactions (RES) in which a pion is produced and reabsorbed within the nucleus ($\sim 7\%$), 2p2h ($\sim 12\%$) or Deep Inelastic Scattering (DIS) ($\sim 0.3\%$). This can be seen in Fig. 3.2 where the distribution of all true CC- 0π events is plotted stacked by interaction modes. Last considering the flux integrated over the whole energy range allows to get rid of the neutrino energy dependency.

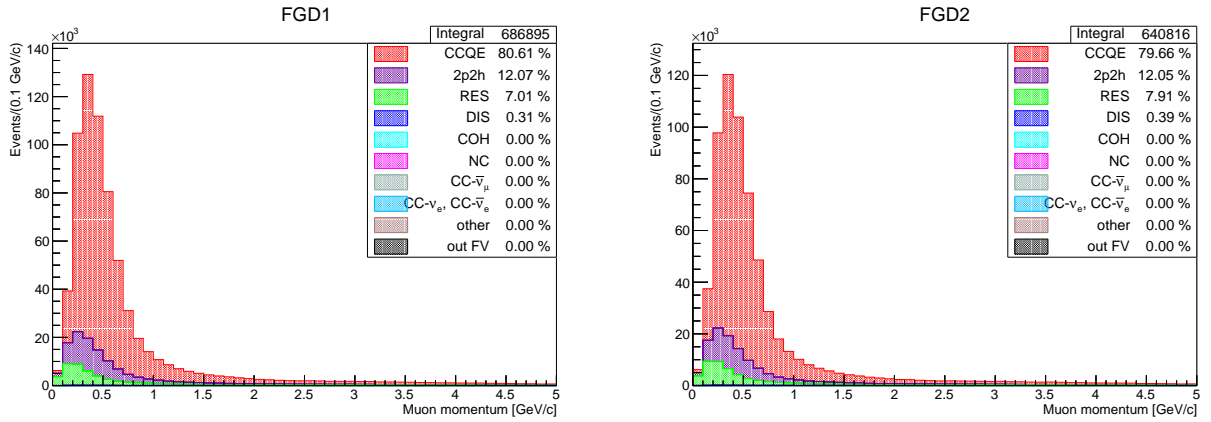


Figure 3.2: True muon momentum distributions from NEUT Monte Carlo prediction in FGD1 (left) and FGD2 (right) of true CC- 0π events stacked by their true interaction mode.

The double differential cross section is defined as

$$\frac{d\sigma_i^\alpha}{dp_\mu^i d\cos\theta_\mu^i} = \frac{N_i^{\text{signal } \alpha}}{\epsilon_i^\alpha \Phi N_t^\alpha \Delta p_\mu^i \Delta \cos\theta_\mu^i} \quad (3.1)$$

where α corresponds to neutrino interactions with either carbon or oxygen targets. $p_\mu^i \cos\theta_\mu^i$ is the true analysis bin i with bin width $dp_\mu^i d\cos\theta_\mu^i$ (see Section 3.3.2), ϵ_i^α is the bin-by-bin efficiency correction in analysis binning, Φ is the integrated flux and N_n^α the number of nucleon targets in the fiducial volume (see Section 5.4.2). $N_i^{\text{signal } \alpha}$ is the number of signal events in true bin i extracted by the likelihood fit. Its expression is given later on in Eq.3.11.

3. Motivations, strategy and inputs for the cross-section extraction

We also measure the cross-section ratio,

$$\frac{d\sigma_i^O}{d\sigma_i^C} = \frac{N_i^{\text{signal } O}}{N_i^{\text{signal } C}} \times \frac{N_t^C}{N_t^O} \times \frac{\epsilon_i^C}{\epsilon_i^O} \quad (3.2)$$

The advantage of the ratio is the cancellation of the flux and therefore of its uncertainty, as it does not depend on the target. Moreover, some of the systematic uncertainties cancel due to correlations. The ratio is useful for measurements that require the use of detectors made of multiple targets as discussed in Section 3.1, it provides a more natural way to propagate the results to the oscillation analysis.

3.2.2 Cross-section extraction

Unfolding

Comparing measurements to theory and generator predictions is not obvious as measured quantities are smeared due to the detector resolution effects. The process of deconvolving the detector smearing effects from data in order to make them comparable at the truth level is called *unfolding* and is represented schematically in Fig. 3.3.

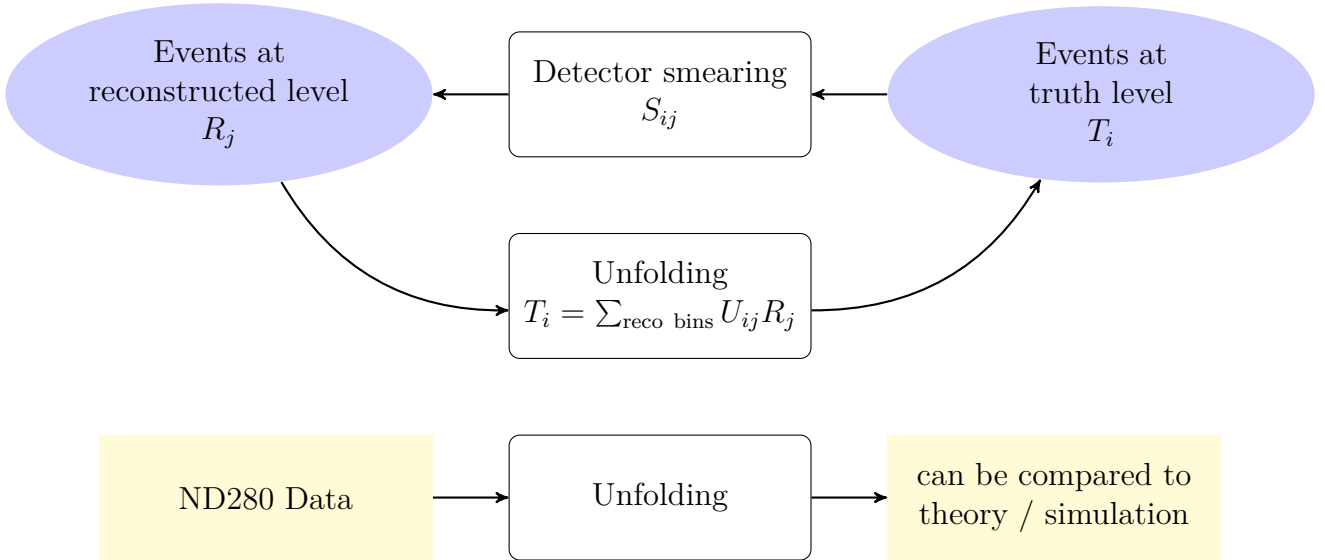


Figure 3.3: Schematic representation of the deconvolution of detector smearing effects.

As can be seen on the diagram from Fig. 3.3 if one wants to compare data to model predictions in the true space, one has to *unfold* the data, for instance find the matrix U_{ij} . A simple and naive way to proceed is to invert the smearing matrix S_{ij} . However this problem is ill-posed and requires a reliable statistical treatment. Several statistical tools propose ways to resolve these degeneracies. In T2K the commonly used methods are the D’Agostini iterative unfolding method [117] and the binned likelihood fit. The first method is based on Bayes’ theorem to form the unfolding matrix with iterations, knowing that the number of iterations can introduce biases and change the physics conclusion. The second method is chosen for this analysis as the likelihood fit offers more clarity on model dependency and result interpretation. This method will be detailed in the following sections.

Binned likelihood fit

The idea of the likelihood fit is to vary the input simulation in true bins via a set of parameters until the simulation best describes the data in reconstructed bins. The parameters describe the signal but also the backgrounds. To do so the following likelihood is maximised:

$$L = L_{\text{stat}} \times L_{\text{syst}} \quad (3.3)$$

which is, in the limit of zero bin width, equivalent to minimising twice the negative logarithm of the likelihood,

$$-2 \log(L) = -2 \log(L_{\text{stat}}) - 2 \log(L_{\text{syst}}) \quad (3.4)$$

The term $-2 \log(L_{\text{stat}})$, where L_{stat} is the Poisson likelihood, yields how well data and simulation agree in the reconstructed bins. It can be translated into a p -value that measures the goodness of the fit [118]. According to Wilks' theorem [119] and in the limit of an infinite sample size, the minimum of $-2 \log(L_{\text{stat}})$ follows a χ^2 distribution for a number of degrees of freedom equal to the number of bins minus the number of fitted parameters. We can write it as [120]

$$-2 \log(L_{\text{stat}}) = \sum_j^{\text{reco bins}} 2 \left(N_j^{\text{sim}} - N_j^{\text{obs}} + N_j^{\text{obs}} \log \frac{N_j^{\text{obs}}}{N_j^{\text{sim}}} \right) \approx \chi_{\text{stat}}^2 \quad (3.5)$$

where N_j^{sim} and N_j^{obs} are the simulated and observed numbers of events in the reconstructed bin j .

The term $-2 \log(L_{\text{syst}})$ allows to add prior knowledge into the fit, from theory and external data fits. It can be written as a χ^2 describing the agreement between sets of parameters while taking their correlations into account via the covariance matrix:

$$-2 \log(L_{\text{syst}}) \approx \chi_{\text{syst}}^2 = (\vec{a}_{\text{syst}} - \vec{a}_{\text{syst}}^{\text{prior}})^T (V_{\text{syst}}^{\text{cov,prior}})^{-1} (\vec{a}_{\text{syst}} - \vec{a}_{\text{syst}}^{\text{prior}}) \quad (3.6)$$

where $\vec{a}_{\text{syst}}^{\text{prior}}$ and \vec{a}_{syst} are vectors containing the prior and fitting systematic parameters respectively, and $V_{\text{syst}}^{\text{cov,prior}}$ is the associated covariance matrix.

The method of template weights

The method described above is model dependent since we allow parameters to vary only within the chosen model. Results should not be dependent on the input signal model though, since neutrino-nucleus interactions are not well known. A solution is to assign a *template weight* on the nominal number of signal events in each true analysis bins. We allow the template weights to vary in the fit with no prior constraint: template weights are changed in true bins, inducing changes in the reconstructed distribution. They are written as c_i and o_i to alter the number of simulated interactions in carbon and oxygen respectively in true bin i , giving reweighted predicted number of events:

$$\begin{aligned} N_{i,\text{true}}^{\text{signal C}} &= c_i N_{i,\text{true}}^{\text{sim signal C}} \\ N_{i,\text{true}}^{\text{signal O}} &= o_i N_{i,\text{true}}^{\text{sim signal O}} \end{aligned} \quad (3.7)$$

3. Motivations, strategy and inputs for the cross-section extraction

The total new predicted number of signal events in reconstructed bin j can be written as

$$N_{j,\text{reco}}^{\text{signal}} = \sum_i^{\text{true bins}} \left(c_i N_{i,\text{true}}^{\text{sim signal C}} + o_i N_{i,\text{true}}^{\text{sim signal O}} \right) U_{ij} \quad (3.8)$$

where U_{ij} is the detector smearing matrix from true bin i to reconstructed bin j . The number of reconstructed background events in bin j is

$$N_{j,\text{reco}}^{\text{bkg}} = \sum_i^{\text{true bins}} N_{i,\text{true}}^{\text{sim bkg}} U_{ij} \quad (3.9)$$

Background events are constrained by fitting simultaneously sideband regions. One can now rewrite the total number of events in reconstructed bin j that is used to compute the χ_{stat}^2 in Eq.(3.5):

$$\begin{aligned} N_{j,\text{reco}} = & \sum_i^{\text{true bins}} \left[c_i \left(\prod_a^{\text{model}} \omega(a)_i^{\text{signal C}} \right) N_{i,\text{true}}^{\text{sim signal C}} + o_i \left(\prod_a^{\text{model}} \omega(a)_i^{\text{signal O}} \right) N_{i,\text{true}}^{\text{sim signal O}} \right. \\ & \left. + \left(\prod_a^{\text{bkg}} \omega(a)_i^{\text{bkg}} \right) N_{i,\text{true}}^{\text{sim bkg}} \right] \\ & \times U_{ij} r_j^{\text{det}} \sum_n^{E_\nu} \omega_n^i f_n \end{aligned} \quad (3.10)$$

where not only the variation of template parameters c_i and o_i is allowed but also the variation of systematic parameters:

- **Interaction model parameters a :**

$\prod_a^{\text{model}} \omega(a)_i$ is the product of weights that account for the effect of theoretical modeling parameters a for signal and backgrounds. The model parameters have pre-fit prior values and covariances given by fits to external data. The so-called *response functions* $\omega(a)$ are calculated using the **T2KReWeight** software (more details given later on in Section 4.3).

- **Detector parameters r_j^{det} :**

r_j^{det} is the parameter describing the detector systematic uncertainty on the number of events in reconstructed bin j . The prior value is unity. The covariance matrix is computed propagating weights within the selection process using toy experiments.

- **Neutrino flux parameters f_n :**

ω_n^i is the relative contribution from neutrino energy in E_ν in bin n to true analysis bin i . f_n are the flux weights, distributed around unity. The prior covariance matrix is provided by the T2K beam group.

More details on prior parameter values and associated covariance matrices will be provided later on in Section 4. The final result can be written as the truth-level distribution of selected events, which is in true analysis bin i ,

$$\begin{aligned} N_i^{\text{signal}} = & \left[c_i \left(\prod_a^{\text{model}} \omega(a)_i^{\text{signal C}} \right) N_{i,\text{true}}^{\text{sim signal C}} + o_i \left(\prod_a^{\text{model}} \omega(a)_i^{\text{signal O}} \right) N_{i,\text{true}}^{\text{sim signal O}} \right] \\ & \times \sum_j^{\text{reco bins}} r_j^{\text{det}} (U_{ij}^{-1}) \sum_n^{E_\nu} \omega_n^i f_n \end{aligned} \quad (3.11)$$

Singular-Value Decomposition and Principal Component Analysis

As we will see in the next sections the number of detector parameters is very large ($\sim 10^3$) hence the matrix in (3.6) becomes huge and one has to fit more than a thousand parameters. Not only the fitter becomes extremely slow but exploring such a large and highly-correlated parameter space leads to instabilities and non-convergence. One solution is to reduce the number of fit parameters by utilising reduced binnings or combining samples. However this technique can lead to underestimating the detector uncertainties with the method that we are using to propagate the uncertainties from the fit to the final cross section (see Section 4.5) and the sensitivity of the fit would be reduced as the number of parameters is already quite small compared to the number of systematics. Another solution to overcome this problem is to perform a singular-value decomposition to de-correlate the parameter space and identify the most important parameters using Principal Component Analysis (PCA). It consists in factorising a matrix into a form represented by its eigenvalues and eigenvectors. Then PCA tools can be used, showing which parameters contribute the most to the variance and keeping only the latter to perform the fit. We thus reduce the complexity of the fit and the number of parameters to be fitted. This technique is already used within the T2K oscillation analysis fit for some subsets of the parameters.

3.3 Event selection and other inputs for cross-section extraction

Within this section we discuss the inputs to the cross-section fitter and how they are produced. After relating about the simulated and real data samples, as well as the analysis binning in kinematic variables used in this work, we describe how events are selected and distributed among different signal and background regions. We aim to select events from neutrino interactions with carbon and oxygen targets in the FGD1 and FGD2 detectors that produce one muon, no pion, and possibly one or more protons in the final state (ν_μ CC- 0π). Finally an overview of selected event distributions with their selection efficiency will be shown.

3.3.1 Monte Carlo and data samples

In this work we analyse ND280 data collected between 2010 and 2017 within the T2K forward horn current (neutrino mode) run periods 2, 3, 4 and 8. The first T2K run period was excluded for some calibration reasons and because the amount of statistics is negligible. Runs 5, 6 and 7 were operated in reverse horn current (antineutrino mode) and therefore only have very few neutrino statistics. The real data and Monte Carlo statistics used within this work are reported in Table 3.1.

The Monte Carlo (MC) samples used as a reference were generated with the **NEUT** 5.3.2 generator [72, 73]. The simulation takes into account the beam conditions during corresponding run periods using the T2K flux predictions (see Section 5.4.1 later on), as well as the detector conditions. Other MC samples have been produced with **GENIE** 2.8.0 [74] under the same flux and detector conditions in order to probe the reliability and stability of the fit method. The same detector reconstruction is applied, the difference to **NEUT** lies in the interaction predictions. More details on neutrino event generators were given in Section 1.3.5 and the differences between the nuclear models used by each generator are listed in Table 1.1.

3. Motivations, strategy and inputs for the cross-section extraction

Table 3.1: List of samples used in this analysis from the different T2K run periods and associated numbers of Protons On Target (POT) for real data and Monte Carlo samples. Runs are splitted according to whether the P \emptyset D detector was filled with water or with air but this has no impact onto this analysis.

T2K Run	Data POT ($\times 10^{20}$)	MC POT ($\times 10^{20}$)
Run 2 air	0.359	9.329
Run 2 water	0.433	5.198
Run 3	1.582	30.83
Run 4 air	1.783	34.91
Run 4 water	1.643	16.36
Run 8 air	1.581	36.26
Run 8 water	4.149	26.47
Total	11.53	159.34

To perform the fit MC samples are normalised to the corresponding real data POT. They are also reweighted to the flux tuning provided by the beam group [90, 121]. Moreover corrections are applied to both data and simulated events in order to reduce the discrepancies between them that are due to misreconstructions of the detector effects in simulations. The corrections are estimated either based on known hardware failures or as a result of precise studies using control samples. Those corrections are summarised in Table 3.2 and more details are given in T2K-TN-212 [122]. Corrections are applied within the Highland2 framework while performing the event selection (see Section 2.5).

Data Quality: In some of the run periods the FGDs and TPCs had defective parts, therefore we correct data quality for these periods.

dE/dx and PID corrections: The detector performances are expected to be constant over the different run periods and the three TPCs are supposed to behave all the same. However this is not the case in practice as external factors may vary between the run periods (gas density, temperature, etc). For instance observations have shown that the dE/dx pull distributions are slightly biased. A set of corrections accounting for calibrations and variations over time are applied to the events in order to adjust pulls to be centered at zero.

Momentum resolution: Momentum resolution discrepancies are observed between real data and simulated events. A smearing factor is applied in the x direction to the global momentum resolution of each TPC track in the MC to correct for this difference.

Table 3.2: List of the corrections applied to neutrino events in the Highland2 framework.

Corrections
Data Quality
dE/dx data correction
dE/dx MC correction
TPC expected dE/dx correction
TPC PID pull MC correction
FGD PID pull MC correction
FGD PID correction
Momentum resolution MC correction

3.3.2 Analysis binning

The analysis variables are the outgoing muon momentum p_μ and cosine angle $\cos\theta_\mu$ with respect to the neutrino trajectory. The binning was optimised for an analysis where similar sample selection and statistics were used (see T2K-TN-337 [123]), to keep an internal consistency within T2K we choose to use the same binning. The momentum and cosine angle values of the 58 bins are listed in Table 3.3.

In the $\mu\text{FGD}+p\text{TPC}$ and μFGD regions many bins are slightly populated or even empty in the angle bins for forward going muons. For the stability and convergence of the fit a minimum bin population is required. Therefore an adapted binning is used for those two regions with larger bins at low angles and more bins at high angles, aiming at having at least 10 MC events per bin. The two different binnings are shown on Table 3.4.

3. Motivations, strategy and inputs for the cross-section extraction

Table 3.3: List of the bins in muon momentum and cosine angle used in the fit.

Bin	$\cos \theta_\mu$	p_μ (GeV)
0	-1.0 – 0.2	0 – 30
1	0.2 – 0.6	0 – 0.3
2		0.3 – 0.4
3		0.4 – 0.5
4		0.5 – 0.6
5		0.6 – 30.0
6	0.6 – 0.7	0 – 0.3
7		0.3 – 0.4
8		0.4 – 0.5
9		0.5 – 0.6
10		0.6 – 0.8
11		0.8 – 30.0
12	0.7 – 0.8	0 – 0.3
13		0.3 – 0.4
14		0.4 – 0.5
15		0.5 – 0.6
16		0.6 – 0.8
17		0.8 – 30.0
18	0.8 – 0.85	0 – 0.3
19		0.3 – 0.4
20		0.4 – 0.5
21		0.5 – 0.6
22		0.6 – 0.8
23		0.8 – 1.0
24		1.0 – 30.0
25	0.85 – 0.9	0 – 0.3
26		0.3 – 0.4
27		0.4 – 0.5
28		0.5 – 0.6
29		0.6 – 0.8
30		0.8 – 1.0
31		1.0 – 1.5
32		1.5 – 30.0

Bin	$\cos \theta_\mu$	p_μ (GeV)
33	0.9 – 0.94	0 – 0.4
34		0.4 – 0.5
35		0.5 – 0.6
36		0.6 – 0.8
37		0.8 – 1.25
38		1.25 – 2.0
39		2.0 – 30.0
40	0.94 – 0.98	0 – 0.4
41		0.4 – 0.5
42		0.5 – 0.6
43		0.6 – 0.8
44		0.8 – 1.0
45		1.0 – 1.25
46		1.25 – 1.5
47		1.5 – 2.0
48		2.0 – 3.0
49		3.0 – 30.0
50	0.98 – 1.0	0 – 0.5
51		0.5 – 0.7
52		0.7 – 0.9
53		0.9 – 1.25
54		1.25 – 2.0
55		2.0 – 3.0
56		3.0 – 5.0
57		5.0 – 30.0

Table 3.4: List of the bins in muon momentum and angle used for the μ FGD+pTPC region (left) and for the μ FGD region (right).

Bin	$\cos \theta_\mu$	p_μ (GeV)
0	-1.0 – 0.0	0 – 0.3
1		0.3 – 0.5
2		0.5 – 0.7
3		0.7 – 30.0
4		0 – 0.3
5	0.0 – 0.6	0.3 – 0.6
6		0.6 – 30.0
7		0 – 0.6
8	0.6 – 0.85	0.6 – 30.0
9		0 – 30.0
10	-1.0 – 0.2	0 – 0.3
11		0.3 – 0.4
12		0.4 – 0.5
13		0.5 – 0.7
14		0.7 – 30.0
15	0.2 – 0.6	0 – 0.4
16		0.4 – 0.8
17		0.8 – 30.0
18	0.6 – 0.7	0 – 0.4
19		0.4 – 0.5
20		0.5 – 0.6
21		0.6 – 1.0
22		1.0 – 30.0
23	0.7 – 0.85	0 – 0.6
24		0.6 – 30.0
25		0 – 0.6
26	0.85 – 1.0	0.6 – 30.0
27		0.6 – 30.0

3.3.3 Event selection

The selection of muon neutrino interactions with no pion in the final state (ν_μ CC-0 π) is performed through a specific package¹ within the **Highland2** framework (see Section 2.5). The Fine-Grained Detectors FGD1 and FGD2 are used as target mass for neutrino interactions with carbon and oxygen and, along with the Time Projection Chambers TPC1, TPC2 and TPC3, as particle trackers. In addition to track reconstruction the TPCs are exploited to provide charged-particle momenta and angles and for particle identification (see Section 2.3.4).

The selection is based on an existing and well-established ν_μ CC-0 π selection that has been developed to constrain ND280 event rates in the oscillation analysis and for other cross-section measurements [67]. Studies with more details are related in T2K-TN-212 [122] and T2K-TN-216 [116] and the cuts applied to ND280 events in order to select signal and background samples will be described later on in this section (see Fig. 3.5). The selection has been optimised for the purposes of this analysis and updated according to certain developments in the software framework requiring adjustments in the selection package. The plots in Fig. 3.4 show the two-dimensional momentum and cosine angle distributions of signal selected events in FGD1, FGD2x and FGD2y in the true variables of the selected events.

¹numuCCZeroPiAnalysis/v2r2

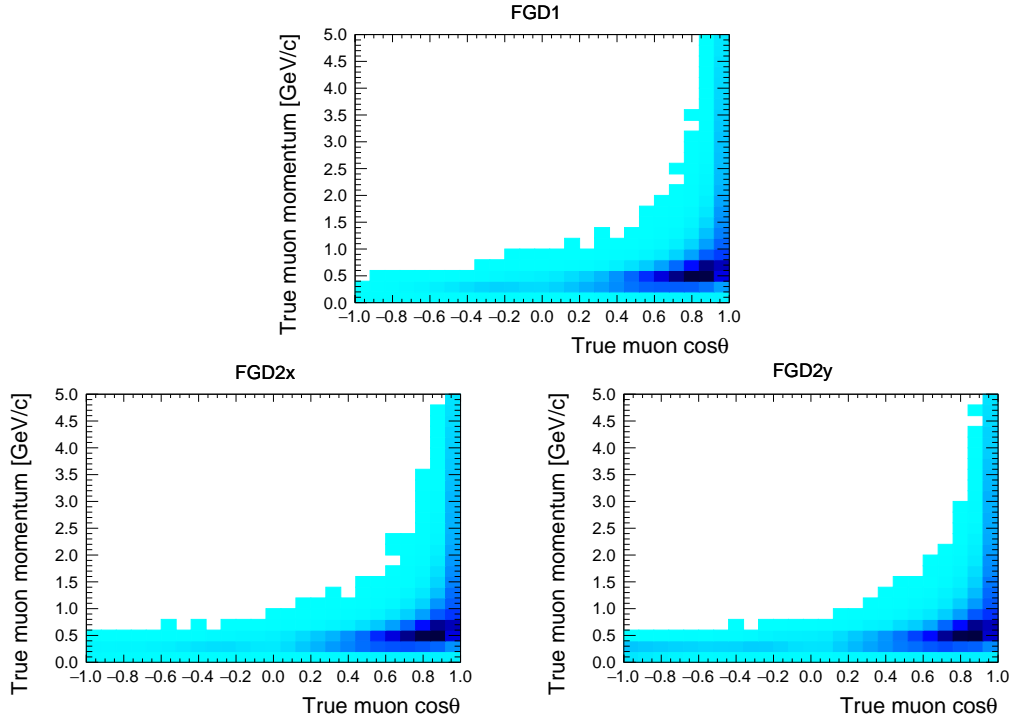


Figure 3.4: Distribution of CC- 0π selected events in true muon momentum and cosine angle in the FGD1 (top), in the FGD2 x layers (bottom left) and in the FGD2 y layers (bottom right).

We look for events with an interaction vertex found in the FGD1 or FGD2 Fiducial Volume (FV) and containing:

- one muon track;
- any number of proton tracks;
- no other identified tracks².

The different cuts of the signal and background event selection are represented on the tree in Fig. 3.5 and a brief description of them is given here.

Selection cuts

Event quality: This cut is determined by a data quality flag telling whether the detector and beam were working correctly or not. The criteria are based on beam spills, ND280 hardware status and a list of checks made with some reconstructed variables to assess the quality of data in each run period. For Monte Carlo simulated events the data quality cut is always passed.

HMN vertex: The Highest Momentum Negative track is chosen as muon candidate.

Muon PID: The muon Particle IDentification cut selects tracks for which the dE/dx pull value is consistent with the muon hypothesis (see Section 2.3.4).

1 negative track: Reject events with more than one negative track in order to reduce the background from interactions with muon and other charged particles in the final state.

²Other identified tracks would be typically charged pions and electrons from γ produced in π^0 decays.

Only muon and proton tracks: Reject other particles according to the PID algorithm in order to reduce the background.

No Michel electron / At least one Michel electron (CC-1 π Michel): Discriminate between CC-0 π and CC-1 π^+ interactions by identifying pion production through its decay into a muon that will then produce an electron, known as *Michel electron*. Because of the decay time a Michel electron is recognisable due to its vertex that is separated in time from the primary interaction vertex.

No proton / One proton / Multi-protons: Break down into the different signal samples according to the number of protons seen.

One TPC proton / One FGD proton: This cut selects events for which the proton track from the previous cut is starting in the FGD and ending in the TPC / contained in the FGD.

Stopping proton / Stopping muon: This cut is selecting proton / muon tracks that are fully contained in FGD1 or FGD2. The end position is required to be in the fiducial volume in order to ensure an accurate momentum by range reconstruction (see Section 2.3.3).

HMP track is pion: The Highest Momentum Positive track is selected as pion candidate and a TPC PID cut is done in order to ensure that a pion is selected.

Multi-TPC track: All the tracks are reconstructed in the TPC.

Two tracker tracks in TPC: The HMN and HMP tracks from previous cuts are both in the TPC.

HMP vertex: We associate the Highest Momentum Positive track to a proton candidate. For events with a muon stopping in one of the FGD detectors we use the TPC proton track as TPC PID is more precise, while the Highest Momentum Negative track was associated to the muon candidate in the case of FGD-TPC muon tracks as described above in the HMN vertex cut.

Leading proton TPC track: The HMP track is going into the TPC.

Long FGD track: This cuts selects only events with a track length above a certain size in the FGD. It ensures that the muon candidate track will have accurate information to estimate the muon kinematics. This cut also helps to discriminate between muons and pions as muons, which usually have higher momenta in CC-0 π interactions, have longer tracks than pions.

Common vertex: The common vertex is a safety cut to ensure that the muon and the proton come from the same vertex. There is only a tiny risk of measuring two particles coming from different interactions, but this cut helps with bad kinematics reconstruction too.

Muon candidate is a HA candidate: This cut is passed if the muon candidate track is a High-Angle track with respect to the neutrino beam direction.

ECal PID: This cut selects events according to the ECal PID algorithm.

Cuts removed from the T2K official selection

π^0 veto cut: If a charge deposition in the ECal is consistent with a photon from a π^0 decay this cut will reject the event, which belongs to backgrounds.

The ECal π^0 veto cut is problematic. First of all the benefit of this cut as it is implemented now does not seem worth since the product purity \times efficiency does not change if this cut is used and the ECal-related uncertainties have an important contribution to detector systematic uncertainties. Moreover the use of this cut would require an extra control sample for the events rejected by this cut. Such control sample has been investigated and it would contain around 50% and 30% of CC- 0π events for FGD1 and FGD2 respectively. Therefore the use of this cut requires improvements in the ECal reconstruction that are underway and are beyond the scope of this work.

Time of Flight (ToF) cut: This cut eliminates OOFV events based on the calculated particle time of flight.

During the data taking of Run 8 the measurement of the time of flight failed for some of the runs because of a hardware problem. About 30% of the data has to be rejected if one utilises the ToF cut, resulting in a total loss of about 15% of the total statistics. However, not using the ToF cut leads to a reduction from $\sim 85\%$ to $\sim 65\%$ of the muFGD sample purity, which is the only sample using that cut. This leads to a small increase in the detector systematic uncertainty associated to that sample. Moreover, as can be seen on the efficiency plotted as a function of $\cos\theta_\mu$ in Fig. 3.17 the muFGD sample is not dominating in any of the phase-space region. For these reasons we decide not to use the ToF cut for this analysis and keep the whole statistics. As a consequence of removing this cut the μ FGD region has quite a large Out Of Fiducial Volume (OOFV) background (see Fig. 3.10). Further developements of this cut are likely to improve the selection purity in future analysis of this kind and are already ongoing.

Signal events

The selected signal events are broken down into five regions according to the location of the reconstructed tracks within the different subdetectors. The separation into different regions is essential as the detector response, detector acceptance, interaction modes and topologies differ in each of these categories. Signal events are splitted into following regions:

- **Region 1 (μ TPC)**
 - One muon candidate with FGD-TPC track
 - No proton candidate
- **Region 2 (μ TPC + p TPC)**
 - One muon candidate with FGD-TPC track
 - One proton candidate with FGD-TPC track
- **Region 3 (μ TPC + p FGD or μ TPC + Np)**
 - One muon candidate with FGD-TPC track
 - One proton candidate stopping in FGD or multi-protons reconstructed
- **Region 4 (μ FGD + p TPC or μ FGD + p TPC + Np or μ FGD + Np)**
 - One muon candidate with FGD track (fully contained or not)
 - One proton candidate with FGD-TPC track and/or multi-protons reconstructed
- **Region 5 (μ FGD)**
 - One muon candidate with FGD track (fully contained or not)
 - No proton candidate

Figures 3.6, 3.7, 3.8, 3.9 and 3.10 show the CC- 0π selected event distributions in reconstructed p_μ and $\cos \theta_\mu$ for each signal region described above. The distributions of simulated events are stacked in event topology based on true MC information and compared to the distribution of real data. The purity corresponds to the fraction of events with a certain topology indicated in the plot legends. The events are associated to the different topologies described in Section 3.2.

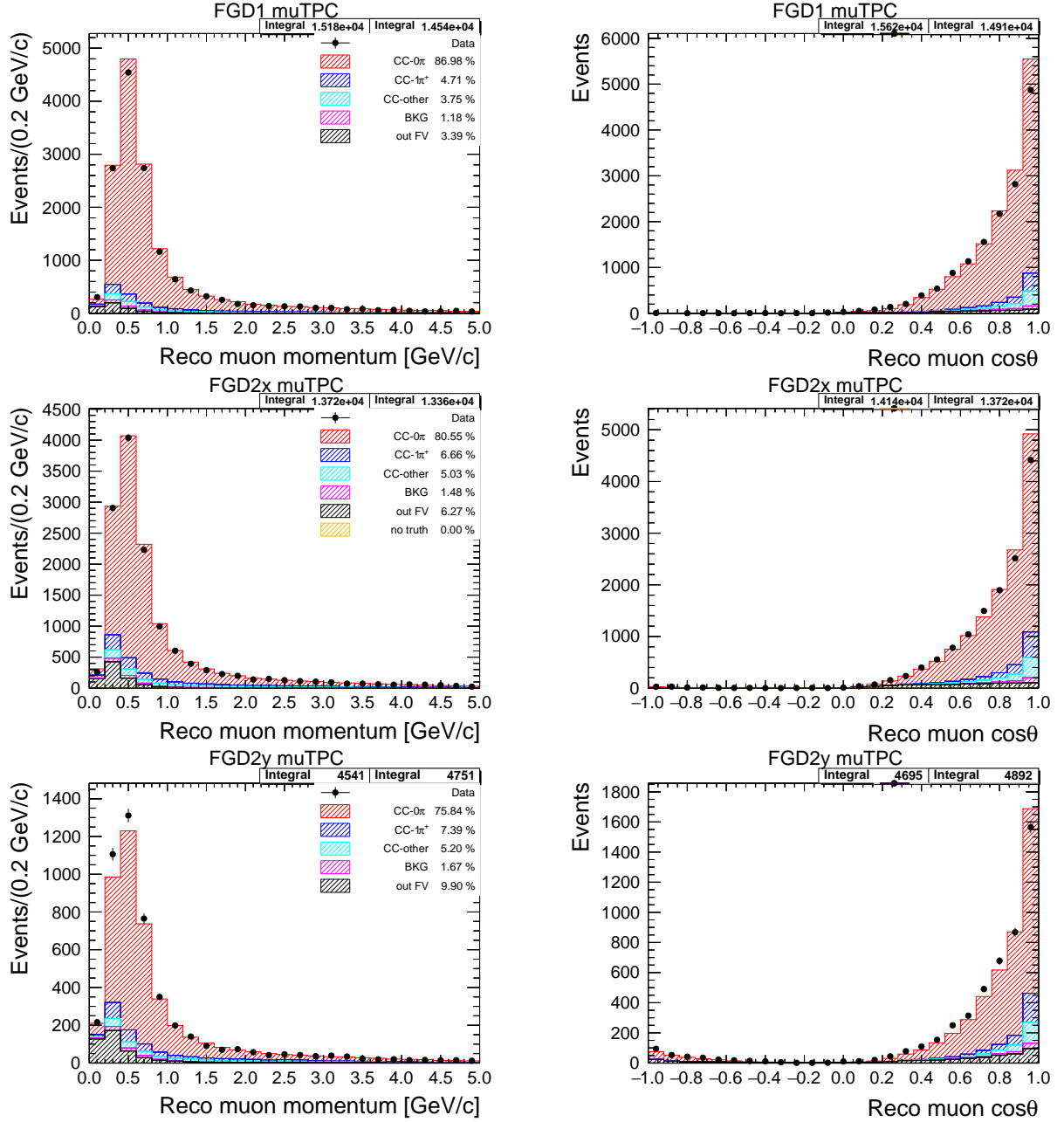


Figure 3.6: Reconstructed momentum (left) and cosine angle (right) distributions of the reconstructed muon of the CC- 0π selection for region 1 in the FGD1 (top), in the FGD2 x-layers (middle) and in the FGD2 y-layers (bottom). Histograms are stacked by event topology.

3. Motivations, strategy and inputs for the cross-section extraction

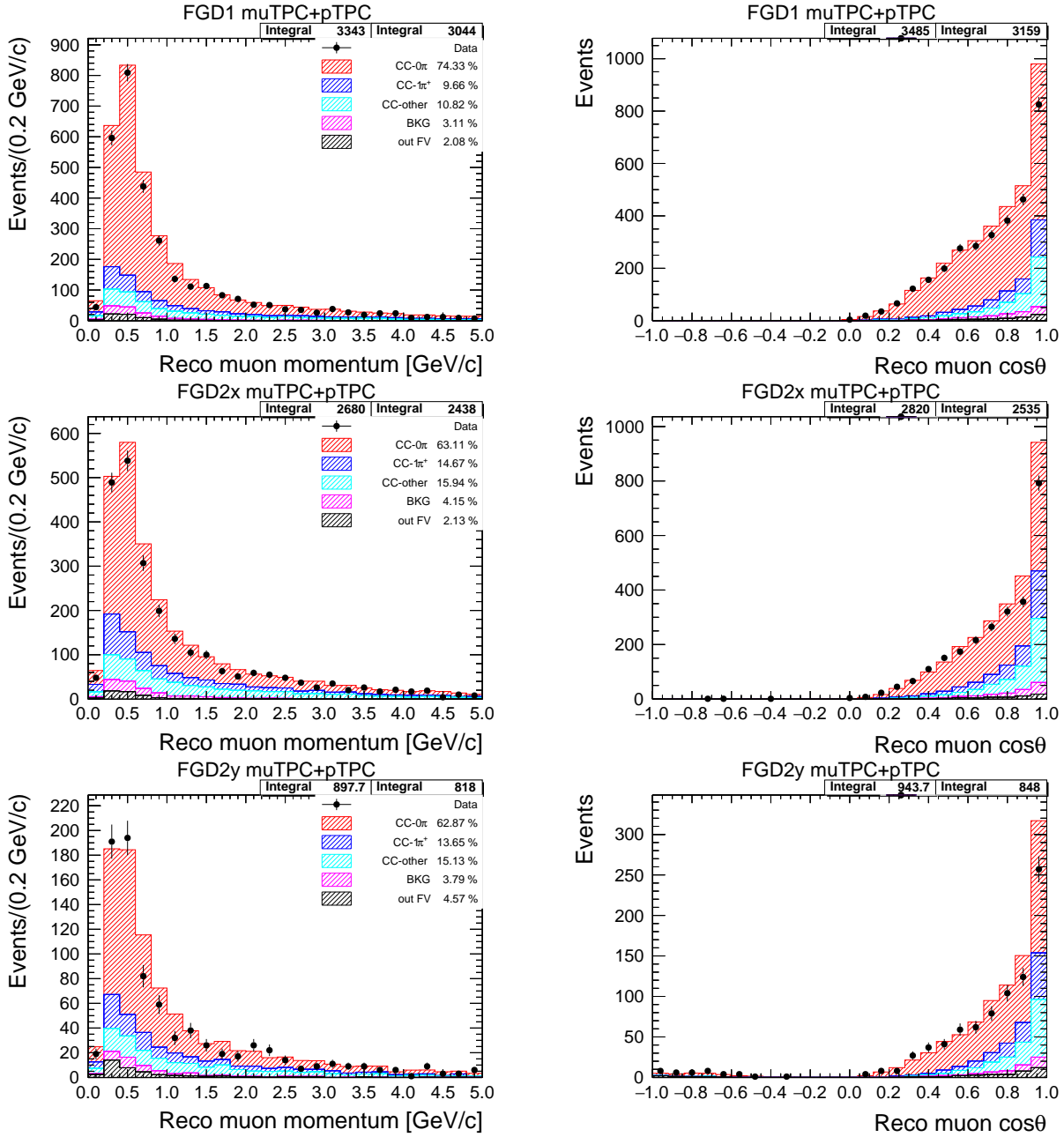


Figure 3.7: Reconstructed momentum (left) and cosine angle (right) distributions of the reconstructed muon of the CC-0 π selection for region 2 in the FGD1 (top), in the FGD2 x-layers (middle) and in the FGD2 y-layers (bottom). Histograms are stacked by event topology.

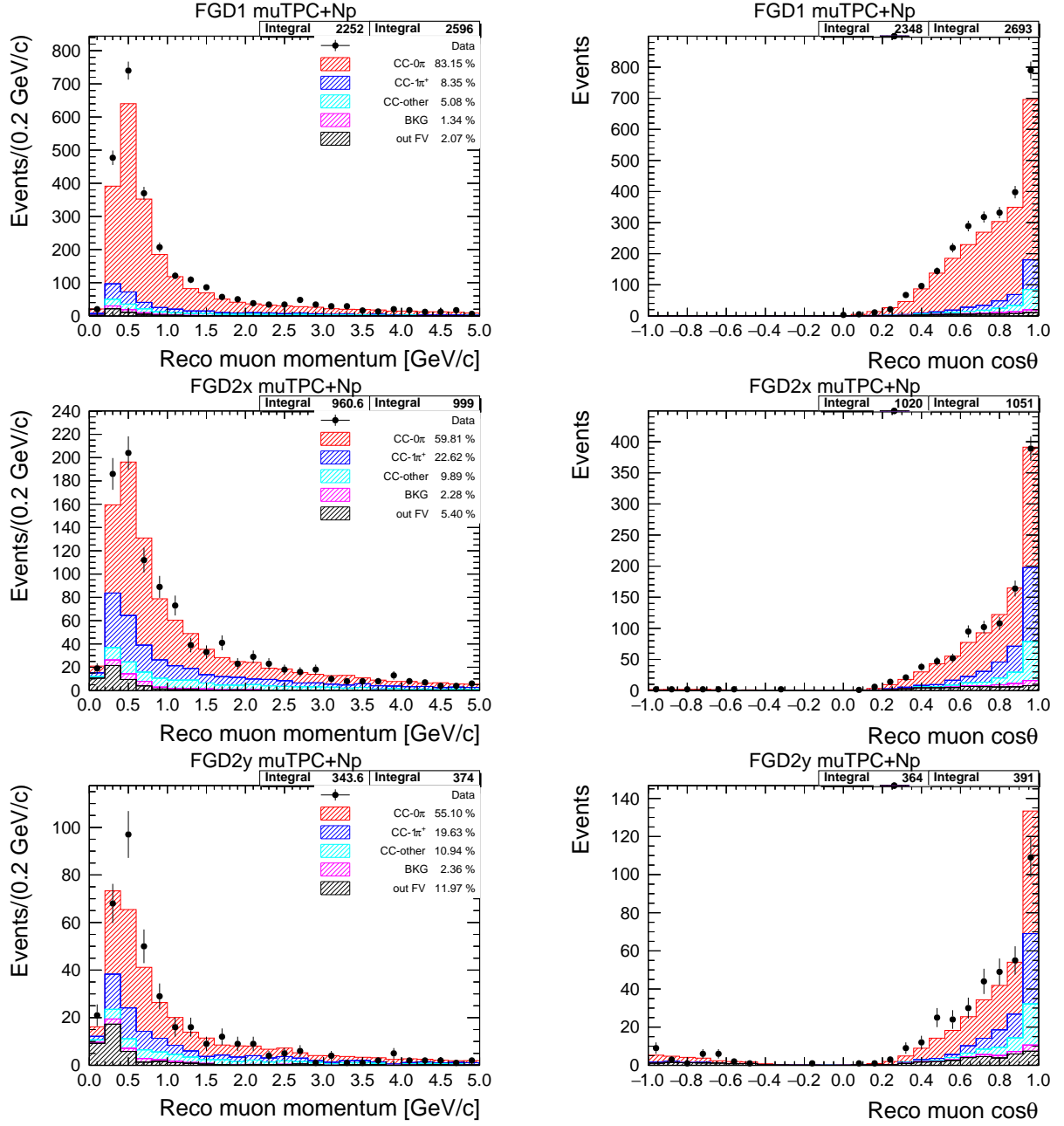


Figure 3.8: Reconstructed momentum (left) and cosine angle (right) distributions of the reconstructed muon of the CC- 0π selection for region 3 in the FGD1 (top), in the FGD2 x-layers (middle) and in the FGD2 y-layers (bottom). Histograms are stacked by event topology.

3. Motivations, strategy and inputs for the cross-section extraction

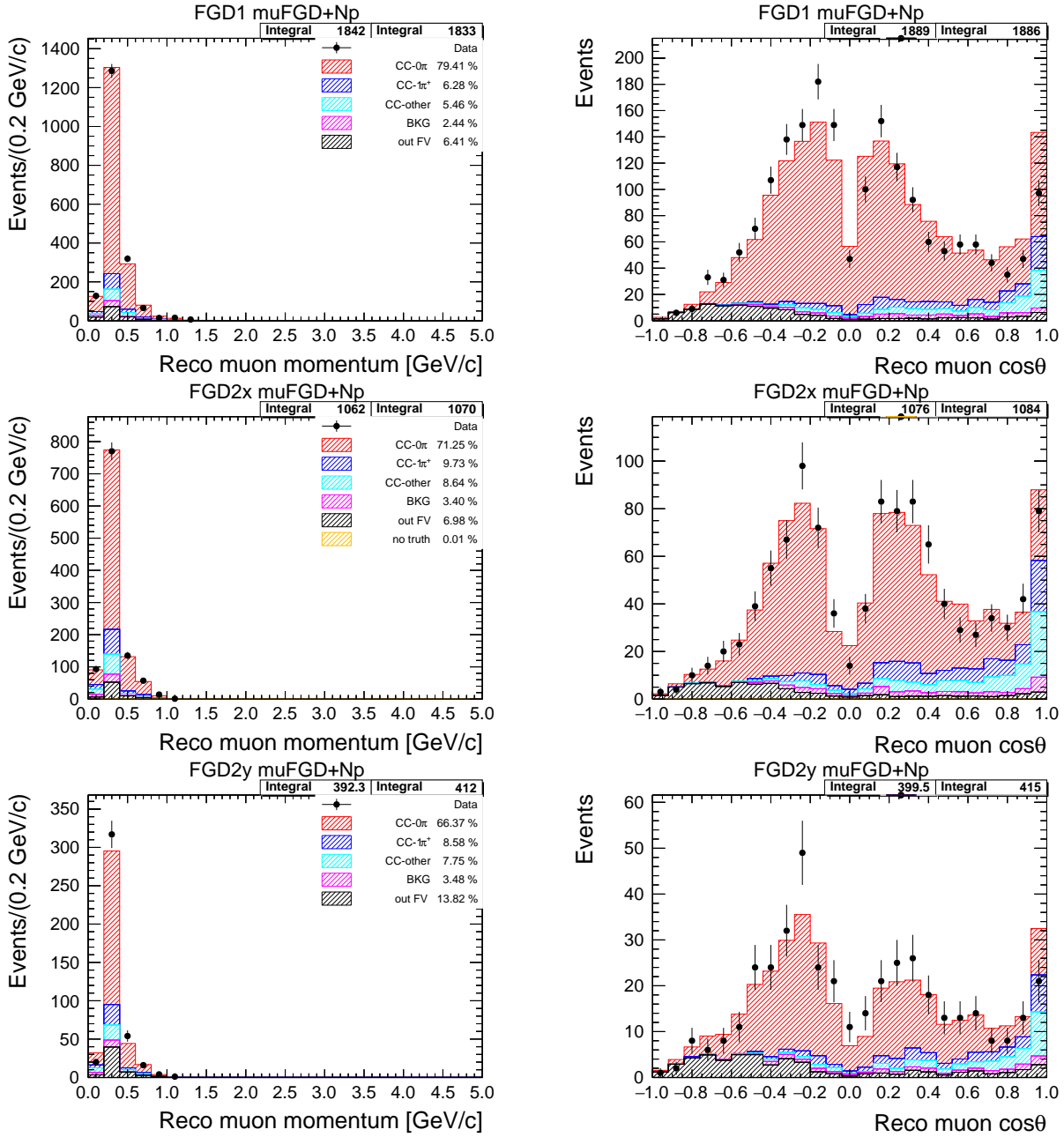


Figure 3.9: Reconstructed momentum (left) and cosine angle (right) distributions of the reconstructed muon of the CC- 0π selection for region 4 in the FGD1 (top), in the FGD2 x-layers (middle) and in the FGD2 y-layers (bottom). Histograms are stacked by event topology.

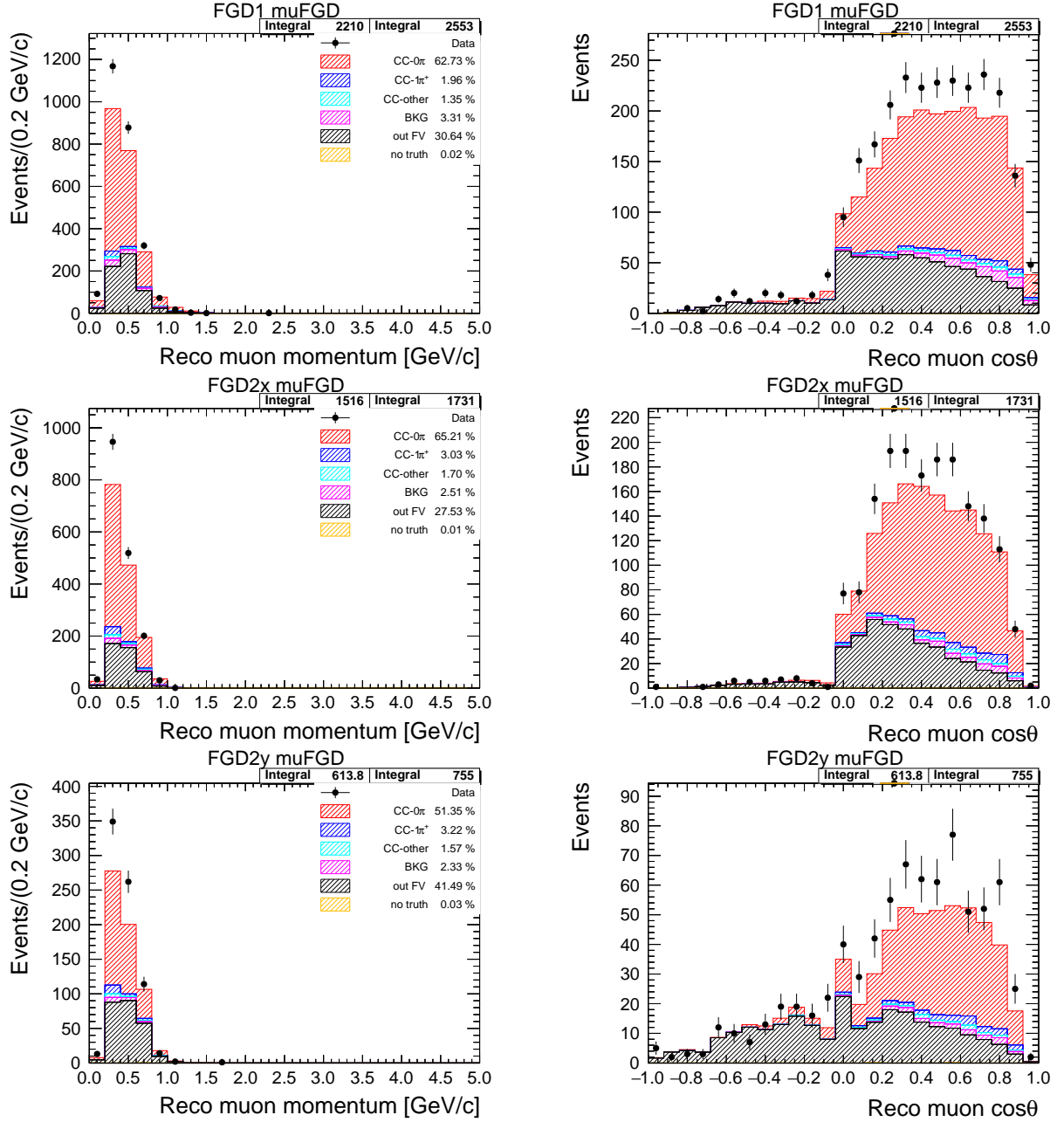


Figure 3.10: Reconstructed momentum (left) and cosine angle (right) distributions of the reconstructed muon of the CC-0 π selection for region 5 in the FGD1 (top), in the FGD2 x-layers (middle) and in the FGD2 y-layers (bottom). Histograms are stacked by event topology.

Background events

It can be observed in the signal selection plots shown above that the background contamination is not negligible. Particle identification is made referring to the dE/dx curve. However, at low momentum, pion and proton curves are not so distinguishable. Therefore a π^+ can be mis-reconstructed as a proton. Deep Inelastic Scattering (DIS) can even produce more than one pion. Moreover Michel electrons³ are used to tag pions, but a pion can be missed by Michel electron tag failure. In order to constrain those backgrounds, we use three control samples, also called *sidebands*:

³We call *Michel electron* the electron coming from the decay of a muon produced by an outgoing pion.

3. Motivations, strategy and inputs for the cross-section extraction

- **Control sample 1** CC- $1\pi^+$

This sideband is constraining events with resonant interactions in which a π^+ is produced

- One muon candidate with FGD-TPC track
- One positive pion candidate with FGD-TPC track

- **Control sample 2** CC-Other

Here we constrain Deep Inelastic Scattering events producing more than one pion.

- One muon candidate with FGD-TPC track
- More than one pion candidate in the final state

- **Control sample 3** CC- $1\pi^+$ with Michel electron

We constrain events that are rejected by the Michel electron cut.

- One muon candidate with FGD-TPC track
- At least one Michel electron is detected

This is important to check that the phase space covered by a control sample is similar to the phase space covered by the background events contained in the signal, since we use the control samples to constrain the background in the signal. We therefore want the sidebands to mimic the background that cannot be removed in the signal sample. To verify this assumption we look at the CC- $1\pi^+$ and CC-Other composition of the associated sidebands and we compare it to the background events contained in the signal sample. The normalised distributions for the two CC- $1\pi^+$ sidebands are shown in Fig. 3.11 in the true muon and pion momentum. The shapes of the muon momentum distributions are very similar. In the pion momentum distribution however, one can see that the first CC- $1\pi^+$ control sample does not cover the low pion momentum region. To overcome this issue, this analysis updates the selection including a new control sample with Michel electron, covering this region. The distribution for the CC-Other background are shown in Fig. 3.12. The angular distributions are similar while the momentum distributions show some deviation. This control sample is not perfect, but this is the best that we can achieve.

Distributions of the three background samples stacked by topology are shown in Figures 3.13, 3.14 and 3.15.

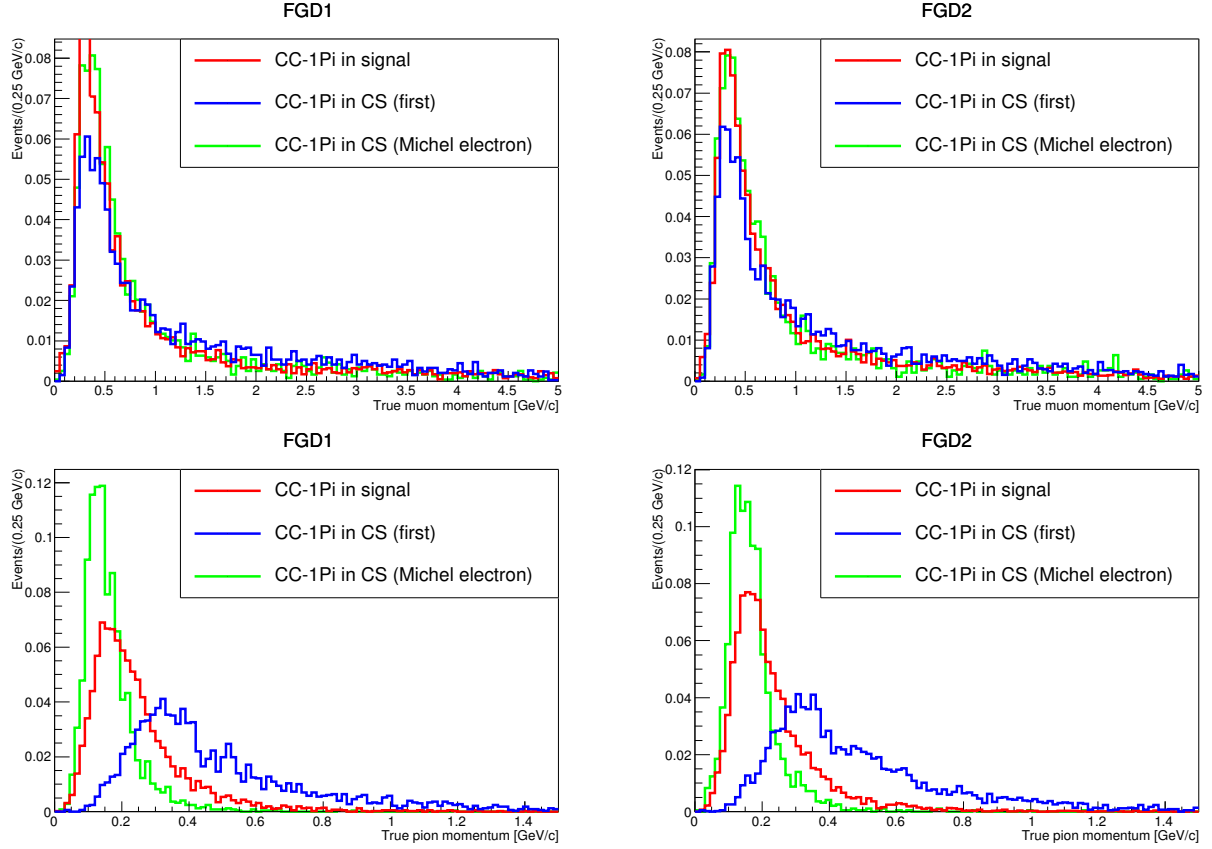


Figure 3.11: CC-1 π^+ background events contained in the signal, in the first CC-1 π^+ control sample and in the second CC-1 π^+ control sample with Michel electron, distributed in true muon momentum (top) and in true pion momentum (bottom) for FGD1 (left) and FGD2 (right). Distributions are normalised to unit.

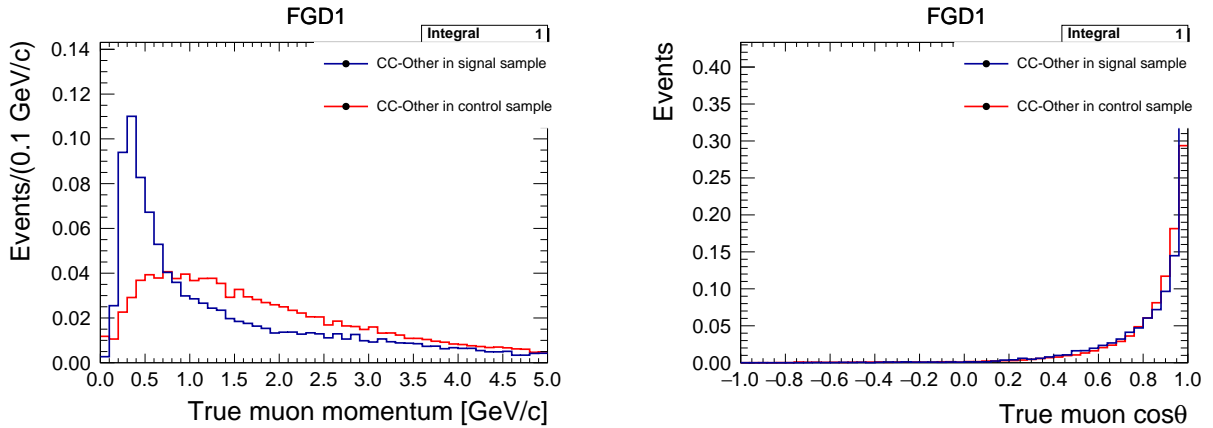


Figure 3.12: CC-Other background events contained in the signal and in the control samples distributed in true muon momentum (left) and cosine angle (right) for FGD1. Distributions are normalised to unit.

3. Motivations, strategy and inputs for the cross-section extraction

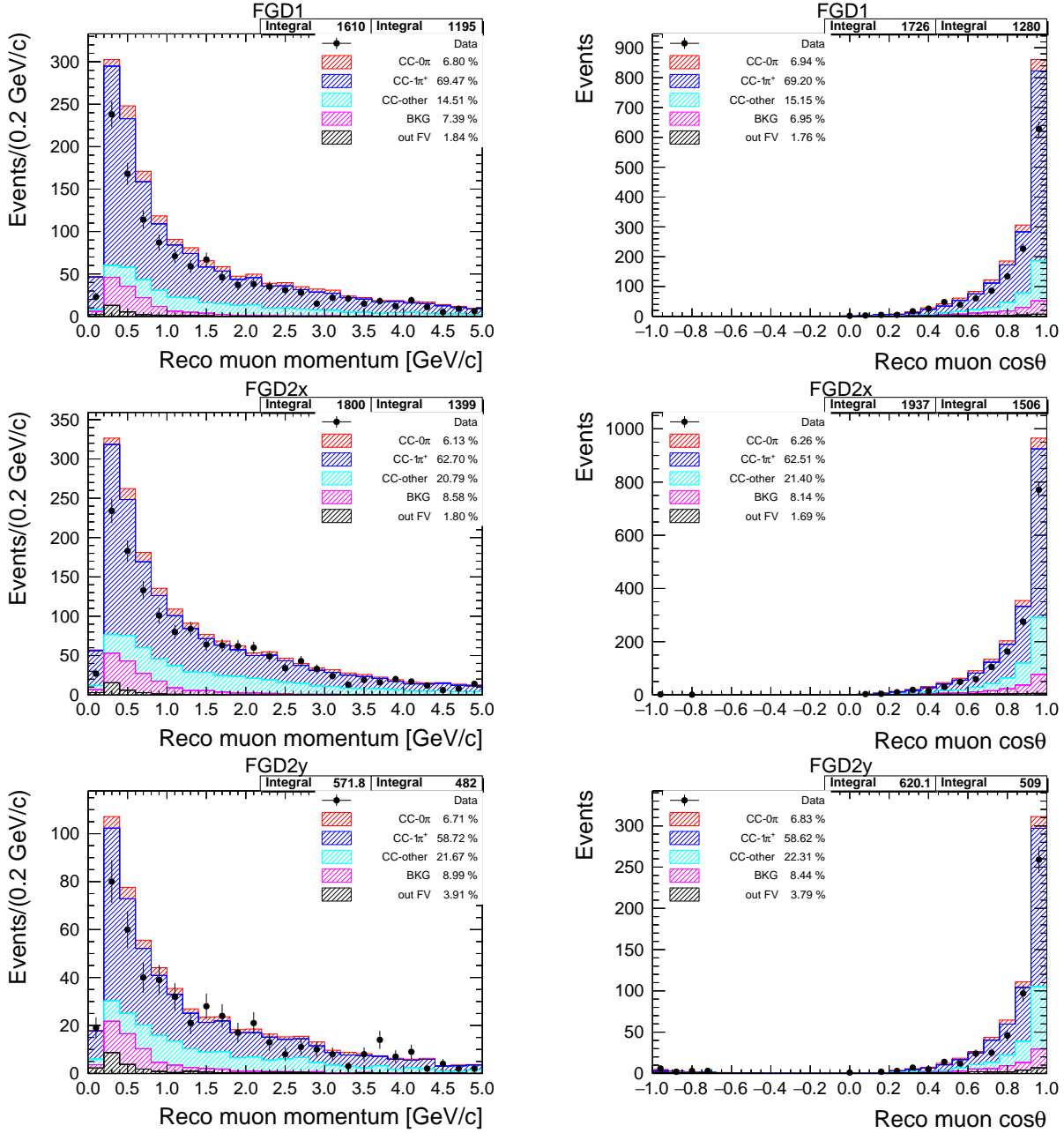


Figure 3.13: Reconstructed momentum (left) and cosine angle (right) distributions of the reconstructed muon of the CC- $1\pi^+$ sideband in the FGD1 (top), in the FGD2 x-layers (middle) and in the FGD2 y-layers (bottom). Histograms are stacked by event topology.

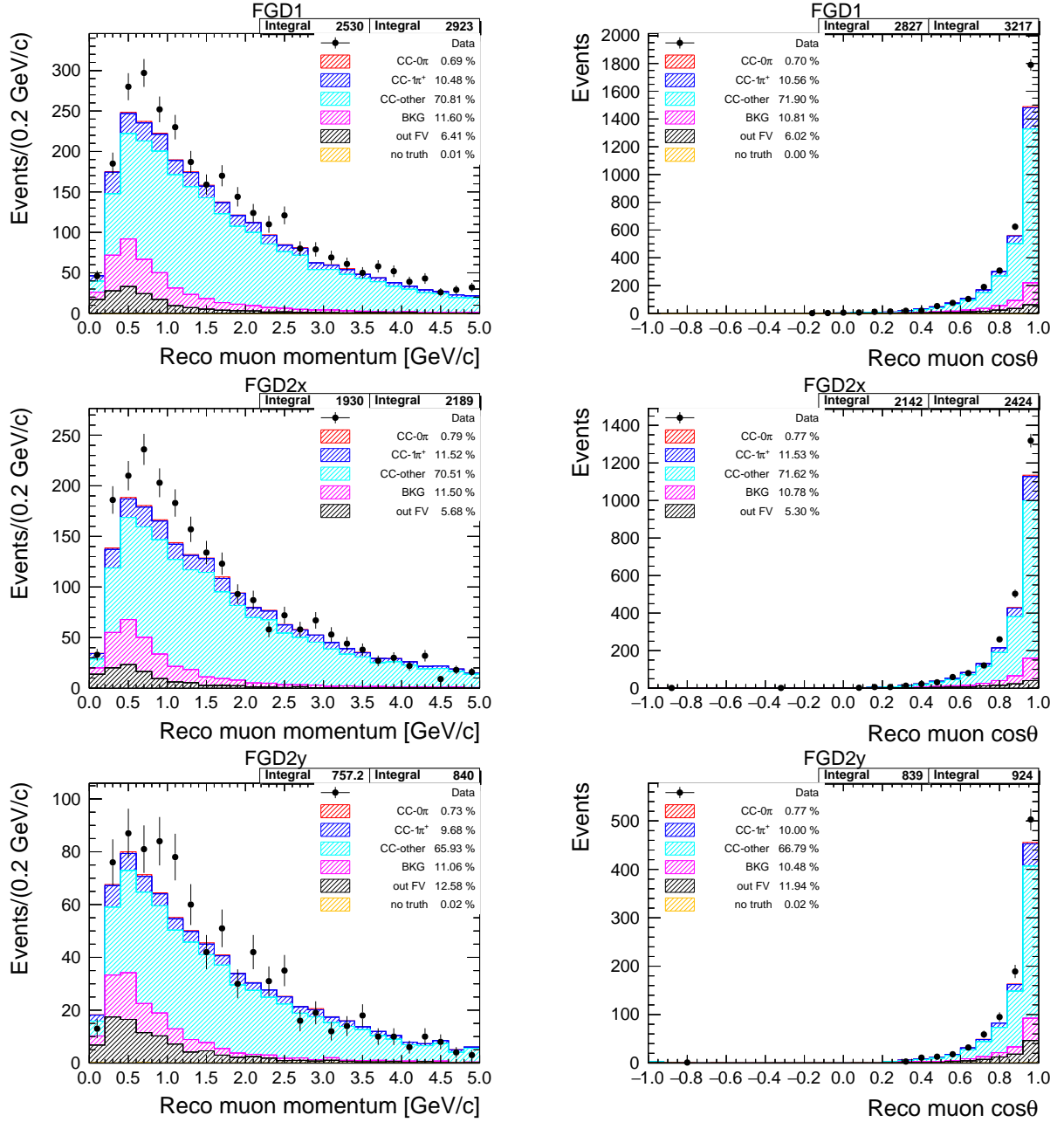


Figure 3.14: Reconstructed momentum (left) and cosine angle (right) distributions of the reconstructed muon of the CC-Other sideband in the FGD1 (top), in the FGD2 x-layers (middle) and in the FGD2 y-layers (bottom). Histograms are stacked by event topology.

3. Motivations, strategy and inputs for the cross-section extraction

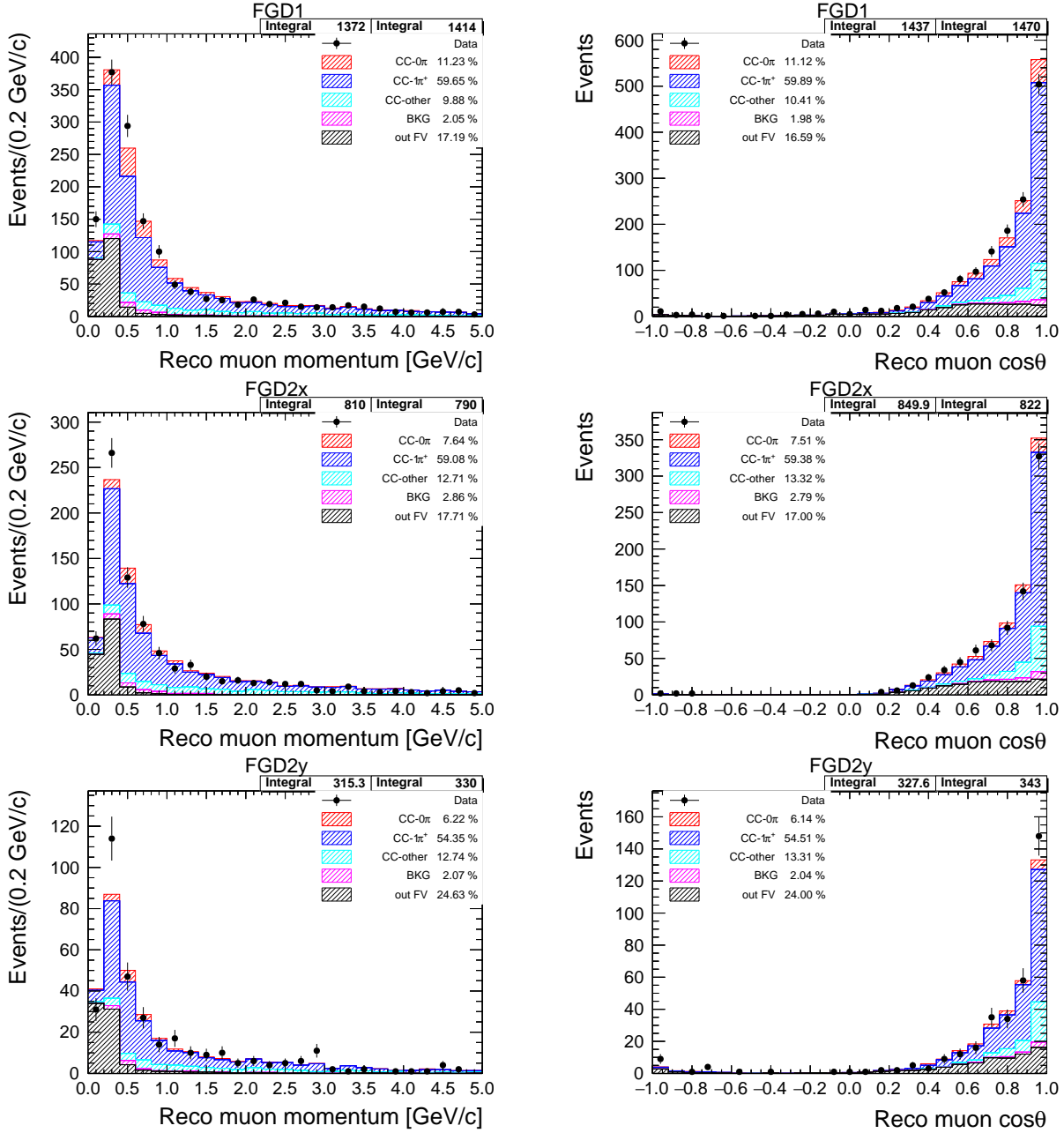


Figure 3.15: Reconstructed momentum (left) and cosine angle (right) distributions of the reconstructed muon of the CC-1 π -Michel sideband in the FGD1 (top), in the FGD2 x-layers (middle) and in the FGD2 y-layers (bottom). Histograms are stacked by event topology.

We end up with 5 signal samples and 3 control samples. These 8 samples are splitted again into interactions in FGD1, FGD2 x layers and FGD2 y layers, giving a total of 24 samples to be fitted. A summary of the samples is shown in Table 3.5 and Fig. 3.16 shows the event distribution among the samples with their composition in true event topologies.

Table 3.5: Summary of the samples to be fitted. The numbers refer to the associated sample in the fit.

		FGD1	FGD2x	FGD2y
Signal 1	$\mu_{\text{TPC, no p}}$	0	8	16
Signal 2	$\mu_{\text{TPC} + \text{PTPC}}$	1	9	17
Signal 3	$\mu_{\text{TPC} + \text{pFGD}}$	2	10	18
	$\mu_{\text{TPC} + \text{Np}}$	2	10	18
Signal 4	$\mu_{\text{FGD} + \text{PTPC}}$	3	11	19
	$\mu_{\text{FGD} + \text{PTPC} + \text{Np}}$	3	11	19
	$\mu_{\text{FGD} + \text{Np}}$	3	11	19
Signal 5	$\mu_{\text{FGD, no p}}$	4	12	20
Sideband 1	CC- $1\pi^+$	5	13	21
Sideband 2	CC-Other	6	14	22
Sideband 3	CC- 1π -Michel	7	15	23

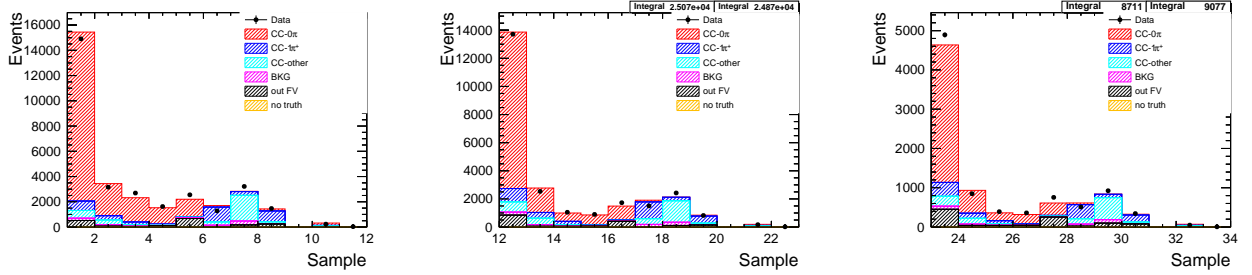


Figure 3.16: Distribution of the analysis samples stacked by topologies, for FGD1 (left) and for FGD2 x layers (middle) and y layers (right). The sample number mapping is given in Table 3.5, numbers on the x axis on this plot correspond to numbers given in the table.

Selection efficiency

The fitted number of events needs to be efficiency corrected in order to extract a cross section. The selection efficiency is calculated as the number of selected signal events divided by the total number of true signal events, using Monte Carlo simulated events. The NEUT efficiency of the different signal regions is shown in Fig. 3.17 as a function of true muon momentum and cosine angle. The total signal efficiency is drawn in black and the contributions from each of the five signal regions described in the beginning of the section are plotted in colors. A comparison of the NEUT, GENIE and NuWro efficiencies in $p_\mu, \cos\theta_\mu$ analysis binning is shown in Fig. 3.18 and 3.19. Total signal efficiencies by target are summarised in Table 3.6 for each neutrino generator.

3. Motivations, strategy and inputs for the cross-section extraction

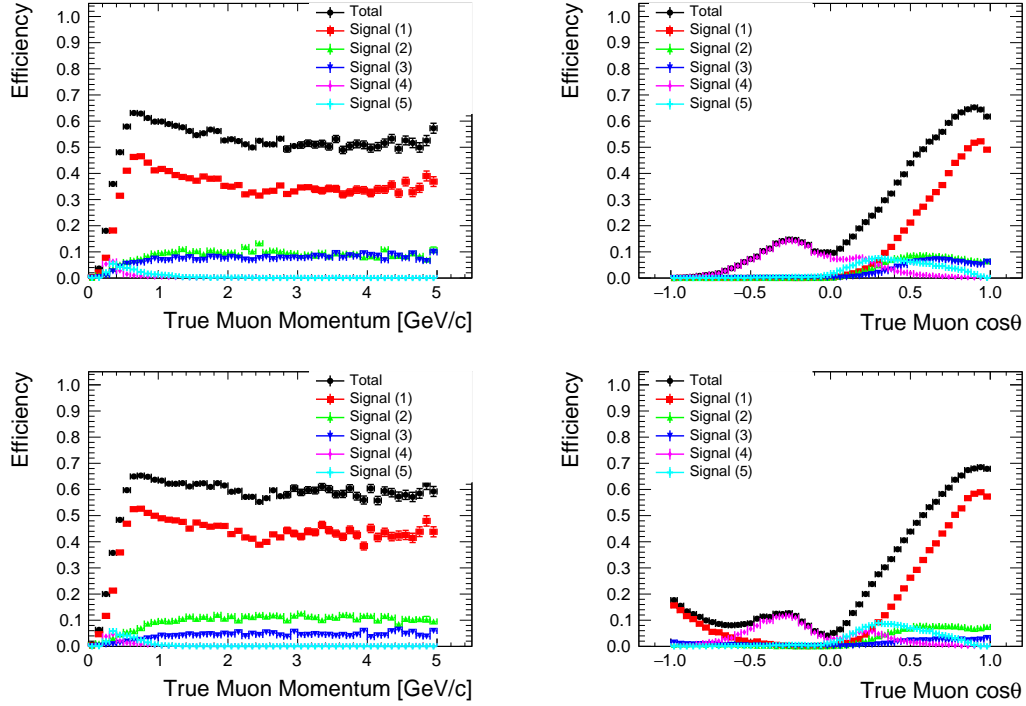


Figure 3.17: Selection efficiency of the CC- 0π selection in the FGD1 (top), in the FGD2 (bottom) for true muon momentum (left) and angle (right). The signal region numbers correspond to the description in Sec.3.3.3.

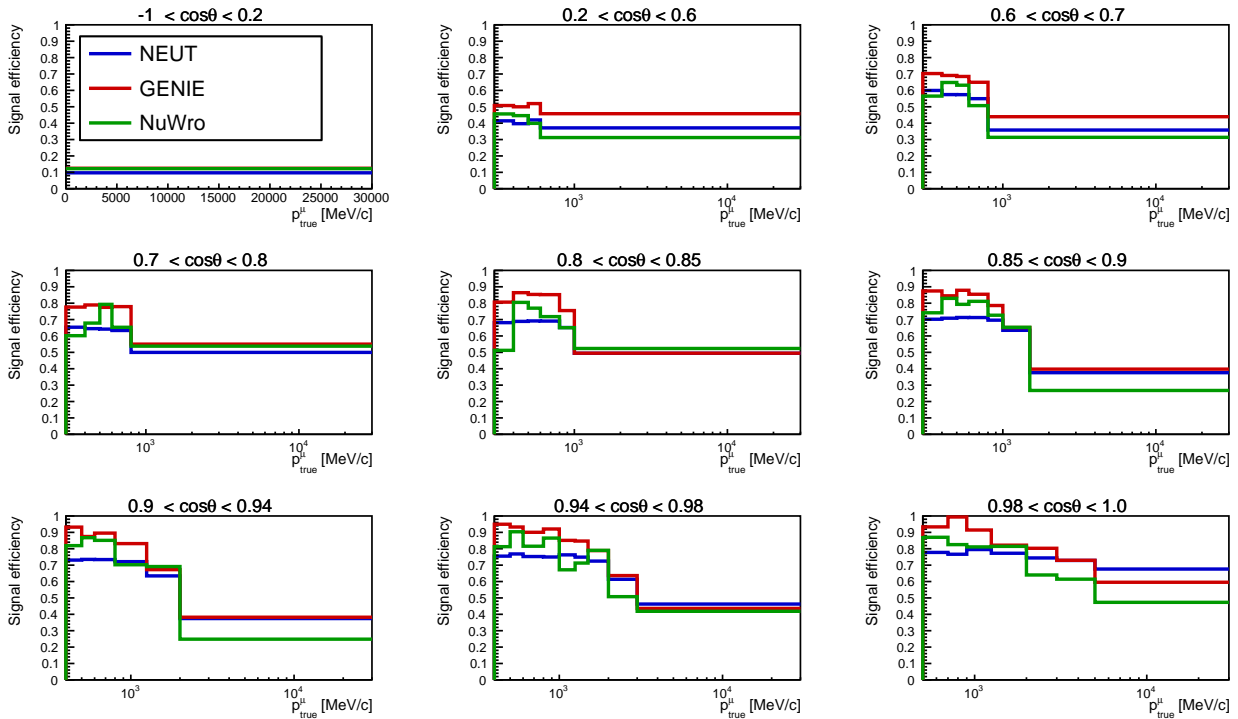


Figure 3.18: Signal efficiency in $p_{\mu}, \cos\theta_{\mu}$ analysis bins (as defined in Section 3.3.2) of events with neutrino interactions with carbon generated by different neutrino generators.

3.3 Event selection and other inputs for cross-section extraction

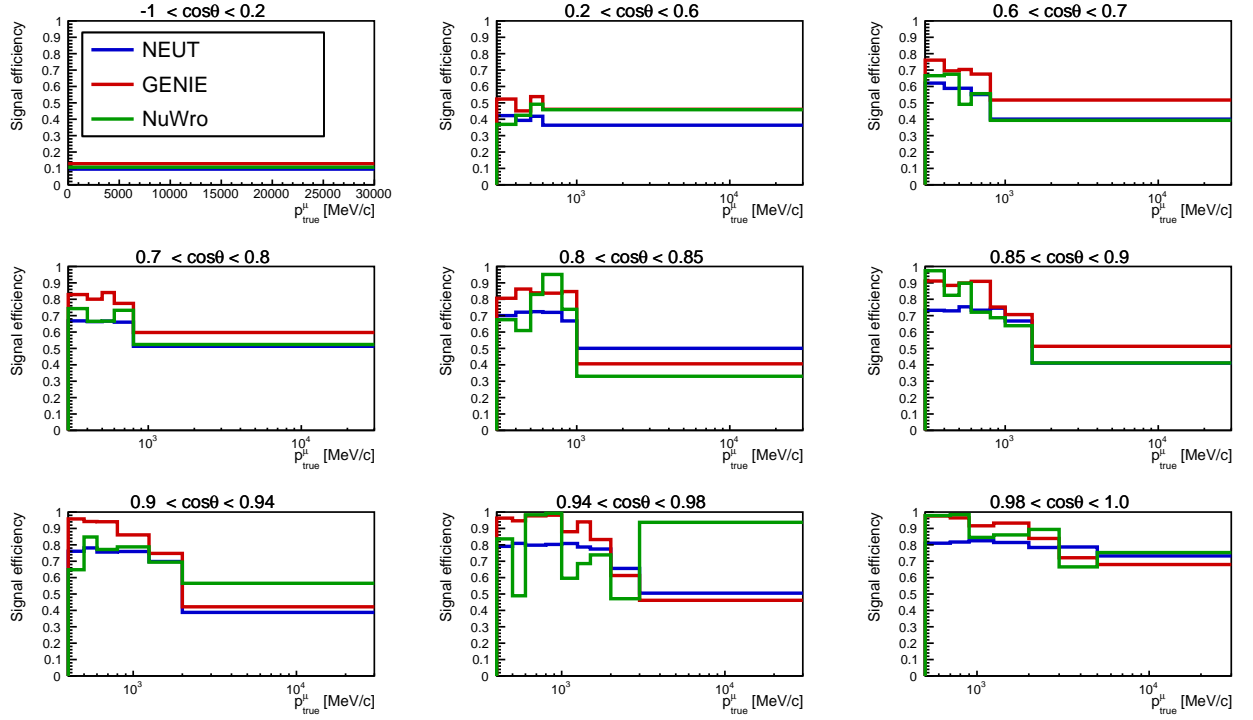


Figure 3.19: Signal efficiency in $p_{\mu}, \cos\theta_{\mu}$ analysis bins (as defined in Section 3.3.2) of events with neutrino interactions with oxygen generated by different neutrino generators.

Table 3.6: Summary of the total signal efficiency for each target and for the different neutrino generator samples.

Generator	Carbon	Oxygen
NEUT	43.7%	45.1%
GENIE	46.8%	48.2%
NuWro	49.1%	50.8%

Evaluation of the uncertainties on cross-section measurement

Several kinds of uncertainties affect the cross-section measurement. A delicate part of the measurement is the estimation of the systematic uncertainties. Detector effects, flux prediction and cross-section modeling affect the number of events and their errors need to be propagated through the fit. The number of targets and efficiency uncertainties have a direct impact on the final cross section, they also need to be taken into account. In addition to the systematic uncertainties, the statistical uncertainty is included directly in the post-fit output provided by MINUIT [124], which is a minimisation method provided by ROOT [113]. The MINUIT package acts on a multiparameter function and is therefore ideal to minimise the χ^2 in a multiparameter space. In this section we review the evaluation and propagation of each kind of systematic uncertainty.

The systematic detector, flux and cross-section model uncertainties are estimated prior to the fit and a covariance matrix used for the uncertainty propagation is built according to these uncertainty values and their correlations. This pre-fit covariance matrix is given as input to the fitter¹. The uncertainties thus can be propagated through the fit via associated *nuisance parameters* that affect the predicted number of events (r_i^{det} , f_n and $\omega(a)$ in Eq.(3.10)) and the prior covariance matrix is considered in the systematic penalty term ($V_{\text{syst}}^{\text{cov,prior}}$ in Eq.(3.6)). The evaluation of the detector, flux and cross-section model prior covariances will be described in the following sections.

The statistical contribution to the total uncertainty on the fit result cannot be separated from the systematic uncertainty. If the statistics are varied then all the systematic constraints would also change and hence the background subtraction, flux normalisation and efficiency uncertainties would be different. A method will be proposed in Section 4.6 to estimate the statistical contribution in the overall uncertainty.

4.1 Detector systematic uncertainties

The particle propagation through ND280 with GEANT4 [125] and the detector response are obviously not perfectly modelled in the simulations. These model uncertainties must be accounted for while performing a cross-section extraction. Such detector uncertainties have been studied deeply for both previous ND280 cross-section measurements and T2K oscillation analyses using near detector constraints [122, 116]. The detector uncertainties associated with the selection

¹Each matrix index corresponds to a systematic parameter of the fit

4. Evaluation of the uncertainties on cross-section measurement

used for this cross-section measurement come from several sources:

- **Particle kinematics:** The reconstruction of outgoing particle kinematics is affected by different modelling issues. The FGDs and TPCs have a limited momentum resolution, which differ in the simulated and real data measurements. Moreover the absolute momentum scale has plausible biases, in the TPC from magnetic field distortions and in the FGD from imprecisions in the track start and end positions, as well as the energy loss readings. Finally the momentum is biased by possible migration of the interaction vertex, which also requires an uncertainty to account for.
- **Charge and particle Identification (PID):** The charge of a particle is determined by the sign of the curvature measured in the TPC. In addition particle types are identified in the TPC, FGD and ECal by PID algorithms. Both the charge and the particle identifications are subject to failures and potential misidentifications need to be accounted for by associated uncertainties.
- **Tracking efficiencies:** The TPC and FGD detectors sometimes fail to reconstruct tracks accurately. Tracks may be misidentified or missing hits.
- **Other FGD and TPC uncertainties:** Matching FGD-TPC tracks is performed by an algorithm, which can potentially miss hits or fail completely. More specifically the FGD needs a special uncertainty to account for variations in the Michel electron tagging efficiency. The TPC has some uncertainty associated to the probability of finding a cluster of TPC pads for a given track.
- **FGD2 vertex backward migration:** If an interaction vertex is reconstructed in an FGD layer located upstream from the layer in which the true interaction happened, it can impact the signal samples. For this analysis a specific study has been conducted to have a deeper knowledge of backward migration in FGD2 and is presented in details in a dedicated appendix (see App. A).
- **GEANT4 modelling of pion and proton SI:** When pions and protons leave the nuclear medium after a neutrino interaction they may undergo further interactions within the detector. Such secondary interactions are modelled by GEANT4 and potential failures may affect the event reconstruction.
- **External backgrounds:** Finally uncertainties are needed to account for backgrounds coming from events with interactions out of fiducial volume (OOFV) and from event pile-up, as they impact the selection efficiency.

4.1.1 Uncertainty evaluation

The detector effects on the event selection are evaluated within the **Highland2** framework. Toy experiments are thrown through the selection process and parameters associated to the different sources of systematic uncertainty are varied according to prior knowledge. Three different methods [122, 116] are used depending on the type of uncertainty that needs to be propagated:

- **Weight systematics**

This method applies for systematic uncertainties that affect the total normalisation. In this case each events is reweighted according to a prior variation suggested by systematic error studies.

- **Efficiency-like systematics**

They are computed based on studies comparing data and MC predictions in well-known control samples. One can easily compute the efficiency in the MC sample by using the truth information. The efficiency in the data can be predicted by reweighting the MC efficiency by the ratio of the efficiencies in the control samples, $\epsilon_{\text{data}} = \frac{\epsilon_{\text{data}}^{\text{CS}}}{\epsilon_{\text{MC}}^{\text{CS}}} \epsilon_{\text{MC}}$.

- **Observable-variation systematics**

This method applies when the variables can have different mean values or resolution in data and MC. The propagation consists in smearing the observables before running the event selection on the new observable.

A list of the detector systematic uncertainties enabled for the measurement presented in this document is given in Table 4.1.

Table 4.1: Detector systematic uncertainties propagated through the Highland2 selection process.

Efficiency-like systematics	
0	Charge ID efficiency
1	TPC cluster efficiency
2	TPC tracking efficiency
3	TPC-FGD matching efficiency
4	FGD hybrid tracking efficiency
5	Michel electron efficiency
Weight systematics	
6	Event pile-up
7	OOFV
8	ECal PID
9	Pion SI (Secondary Interactions)
10	Proton SI
11	FGD2 backward migration

Variation systematics	
12	Magnetic field distorsions
13	Momentum scale
14	Momentum resolution
15	Momentum range resolution
16	Momentum bias from vertex migration
17	TPC PID
18	FGD PID

4.1.2 The covariance matrix

The uncertainties and covariances resulting from the selection are stored into matrix. Each covariance matrix index is associated to a bin at the reconstructed level, i.e. one bin corresponds to a kinematic bin for one of the signal or control samples as listed in Table 3.5. The detector covariance matrix element ij is defined as

$$V_{\text{det}, ij}^{\text{cov}, \text{prior}} = \sum_{t=1}^{N_{\text{toys}}} \left(\frac{(1 - n_i^t)(1 - n_j^t)}{\bar{n}_i \bar{n}_j} \right) / N_{\text{toys}} \quad (4.1)$$

where n_i^t is the content of the i th bin for toy t and \bar{n}_i its mean over all toys, calculated as $\bar{n}_i = \sum_t n_i^t / N_{\text{toys}}$. Here we use a number of toys $N_{\text{toys}} = 500$. In general correlation matrix elements are the covariance elements normalised by the errors, that is

$$V_{ij}^{\text{corr}} = \frac{V_{ij}^{\text{cov}}}{V_{ii}^{\text{cov}} V_{jj}^{\text{cov}}} \quad (4.2)$$

It is more convenient to show correlation matrices as the correlation values are between -1 and 1 , which makes the interpretation of results easier. Note that negative values correspond to anticorrelations.

4.1.3 Resulting pre-fit detector uncertainty inputs

The pre-fit detector covariance matrix is shown in Fig. 4.1 and the total pre-fit uncertainties in muon momentum are shown in Fig. 4.2 for the signal samples and in Fig. 4.3 for the sidebands. The detector uncertainty is significantly higher for the y layers of FGD2. This difference comes from the contribution of the backward migration systematics in FGD2², which is shown within the appendix dedicated to backward migration studies in Figures A.22 and A.23.

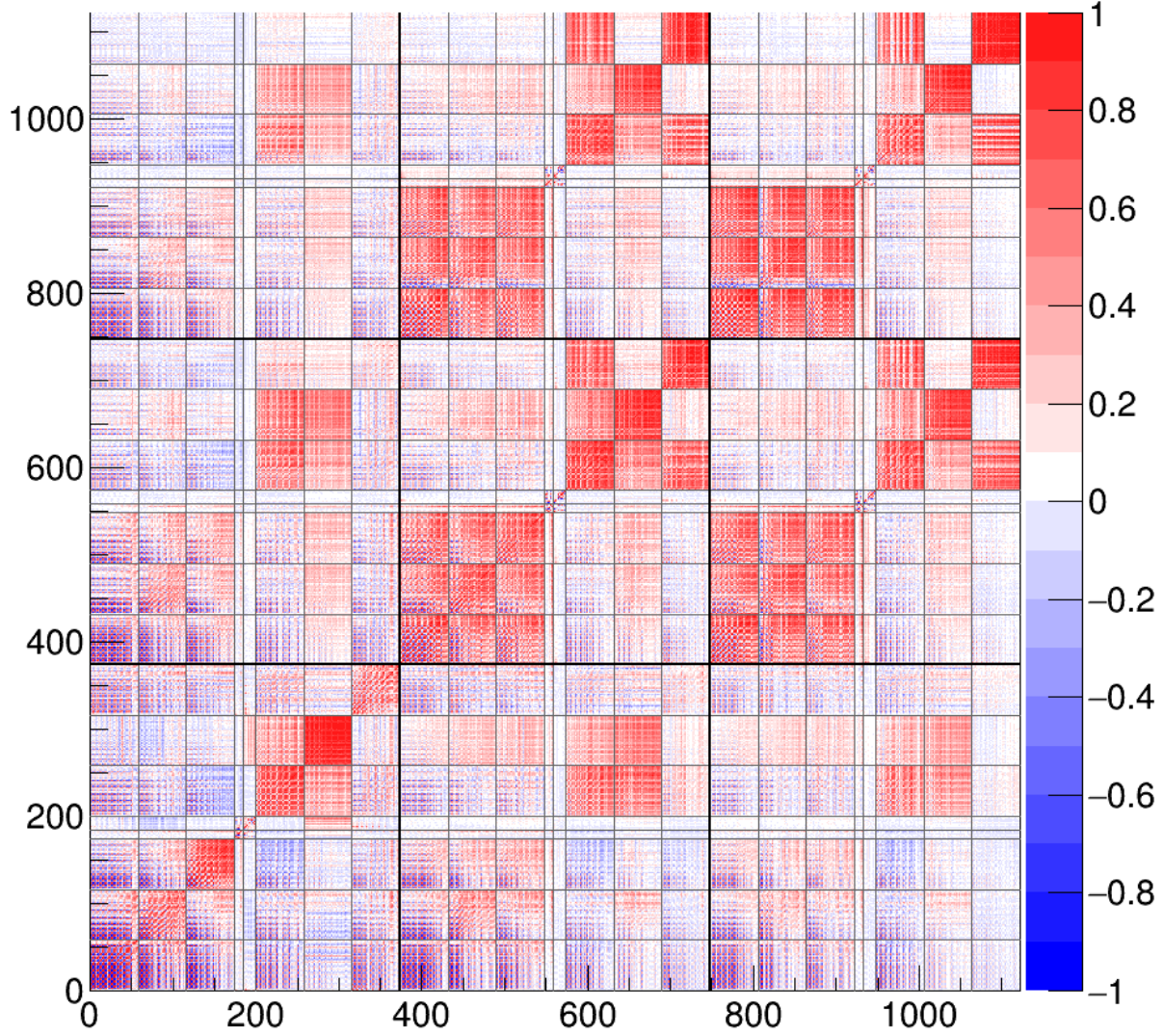


Figure 4.1: Pre-fit detector correlation matrix for each analysis bin in each signal and control sample. The first large block corresponds to FGD1 samples, the second and third blocks to FGD2x and FGD2y samples respectively. Small blocks correspond to the 5 signal and 3 control samples as listed in Table 3.5.

²This uncertainty is calculated only for FGD2, where migration between x and y layers has an impact on the separation between water and carbon layers, although it is also plotted for FGD1 and is equal to 0 in that case.

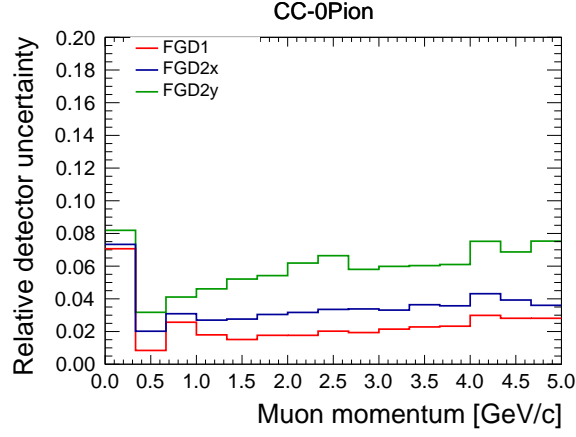


Figure 4.2: Total detector systematic uncertainties for FGD1 (red), FGD2x (blue) and FGD2y (green) signal samples.

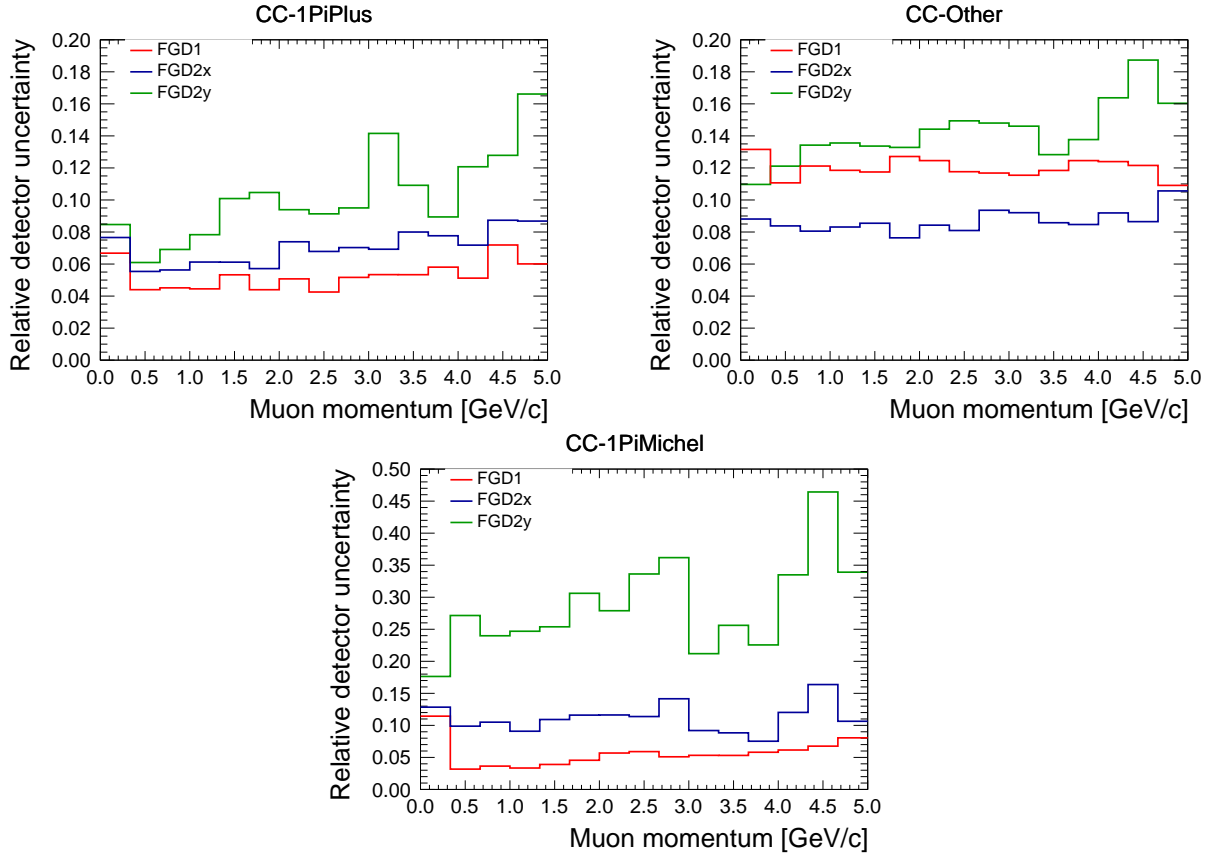


Figure 4.3: Total detector systematic uncertainties for FGD1 (red), FGD2x (blue) and FGD2y (green) control samples CC- $1\pi^+$ (top left), CC-Other (top right) and CC- 1π -Michel (bottom).

4.2 Flux systematic uncertainties

The uncertainty on the flux prediction affects the number of events but also the integrated flux in the denominator of the cross-section formula in Eq. (3.1). The flux covariance matrix that is used in the penalty term of the χ^2_{sys} in Eq.(3.6) is shown in Fig. 4.4 and comes from the T2K

4. Evaluation of the uncertainties on cross-section measurement

flux release 13av4 [90, 121]. Each matrix index, associated to one flux parameter, corresponds to a neutrino energy bin. The energy binning that is used is reported in Table 4.2.

Table 4.2: Neutrino energy binning used for the flux parameters.

	ν energy [GeV]
0	0.0 – 0.1
1	0.1 – 0.2
2	0.2 – 0.3
3	0.3 – 0.4
4	0.4 – 0.5
5	0.5 – 0.6
6	0.6 – 0.7
7	0.7 – 0.8
8	0.8 – 1.0
9	1.0 – 1.2
10	1.2 – 1.5
11	1.5 – 2.0
12	2.0 – 2.5
13	2.5 – 3.0
14	3.0 – 3.5
15	3.5 – 4.0
16	4.0 – 5.0
17	5.0 – 7.0
18	7.0 – 10
19	10 – 30

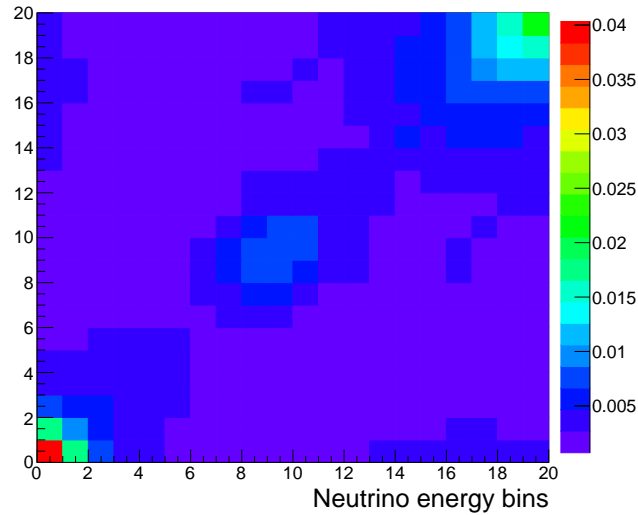


Figure 4.4: Flux covariance matrix for ND280 FHC ν_μ , T2K run periods 1 to 8, with neutrino energy binning described in Table 4.2.

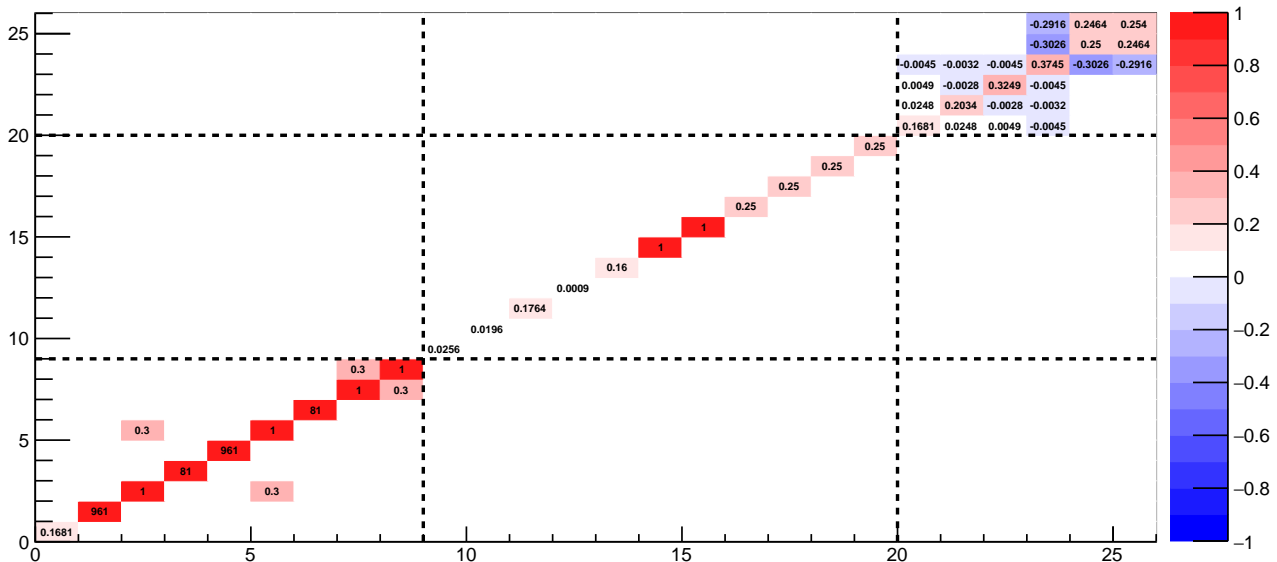
4.3 Model systematic uncertainties

The prior values, errors and covariances of the cross-section model parameters are provided by the T2K Neutrino Interaction Working Group (NIWG). Most of the values used come from T2K-TN-315 [126], although some of them have been updated in 2018. Most recent values are taken. The parameters and their associated values and errors used in the fit are summarised in Table 4.3 and the covariance matrix is shown in Fig. 4.5.

Table 4.3: Cross-section model parameters with their nominal values, errors and validity ranges used in this analysis. Their associated covariance matrix is represented in Fig. 4.5.

	Parameter	Prior	Error	Validity	Type
0	M_A^{QE} axial mass, form factor parameter	1.20	0.41	[0, 999]	Signal
1	p_F^{C} Pauli blocking parameter	217.0	31.0	[200, 275]	
2	MEC C multinucleon component normalisation	1.00	1.00	[0, 999]	
3	E_B^{C} binding energy	25.0	9.00	[12, 42]	
4	p_F^{O} Pauli blocking parameter	225.0	31.0	[200, 275]	
5	MEC O multinucleon component normalisation	1.00	1.00	[0, 999]	
6	E_B^{O} binding energy	27.0	9.00	[12, 42]	
7	MEC O multinucleon component shape	1.00	1.00	[0, 999]	
8	MEC C multinucleon component shape	1.00	1.00	[0, 999]	
9	C_A^5 1π form factor parameter	1.01	0.16	[0, 999]	Background
10	M_A^{RES} 1π form factor parameter	0.95	0.14	[0, 999]	
11	Bkg Resonant, isospin= $\frac{1}{2}$ normalisation	1.30	0.42	[0, 999]	
12	CC- ν_e radiative corrections	1.00	0.03	[0, 999]	
13	DIS CC other shape uncertainty	1.00	0.40	[0, 999]	
14	CC-coherent normalisation	1.00	1.00	[0, 999]	
15	NC-other normalisation	1.00	1.00	[0, 999]	
16	CC- $1\pi^+$ normalisation, $p_\pi < 2.5 \text{ GeV}/c$	1.00	0.50	[0, 999]	
17	CC- $1\pi^+$ normalisation, $p_\pi > 2.5 \text{ GeV}/c$	1.00	0.50	[0, 999]	
18	CC multi- π normalisation	1.00	0.50	[0, 999]	
19	CC DIS normalisation	1.00	0.50	[0, 999]	
20	FSI inelastic, $p_\pi < 0.5 \text{ GeV}/c$	1.00	0.41	[0, 999]	Pion FSI
21	FSI Pion absorption	1.10	0.45	[0, 999]	
22	FSI charge exchange, $p_\pi < 0.5 \text{ GeV}/c$	1.00	0.57	[0, 999]	
23	FSI Pion production	1.80	0.61	[0, 999]	
24	FSI inelastic, $p_\pi > 0.5 \text{ GeV}/c$	1.00	0.50	[0, 999]	
25	FSI charge exchange, $p_\pi > 0.5 \text{ GeV}/c$	1.80	0.50	[0, 999]	

4. Evaluation of the uncertainties on cross-section measurement



These model parameters are then allowed to be varied within a 5σ interval by the fitter in order to find their best-fitting values. As one cross-section parameter is changed the number of events need to be reweighted accordingly to the response to variations of this parameter, as in Eq.(3.10). The response function $\omega(a)$ gives a weight as a function of the parameter a . Response functions can be generated within the **T2KReWeight** framework provided by the NIWG. For a given model parameter one response functions needs to be calculated for each kinematic bin and for each event type. Weights are computed for a certain number of parameter values within the 5σ interval around the mean value, producing so-called *splines*. Splines are provided to the fitter for every event topology, interaction target and true neutrino reaction and for each kinematic bin. As an example the M_{A}^{QE} spline is shown in Fig. 4.6 for CC- 0π topology, CCQE interaction on a carbon target in bin number 5.

4.4 Proton FSI systematic uncertainty

Proton Final State Interactions (FSI) are not yet implemented in the T2KReWeight framework. Thus the covariances have to be evaluated separately and added manually to the final covariance matrix. Proton FSI mainly affect the bin-by-bin efficiency. We thus choose the selection efficiency to estimate their contribution to the cross-section uncertainty. Proton FSI are not yet implemented in NEUT so we use a sample of events generated by NuWro [71] that includes FSI. To evaluate the uncertainty we take a second NuWro sample where FSI are not included and use it as a unique variation to estimate the relative covariance between bins i and j assuming a 100% uncertainty on proton FSI:

$$V_{ij} = \frac{(\epsilon_i^{\text{FSI}} - \epsilon_i^{\text{no FSI}})(\epsilon_j^{\text{FSI}} - \epsilon_j^{\text{no FSI}})}{\epsilon_i^{\text{FSI}} \cdot \epsilon_j^{\text{FSI}}} \quad (4.3)$$

The efficiencies of the two samples are plotted in Fig. 4.7 and the correlation matrix associated to the covariances calculated with Eq.(4.3) is drawn in Fig. 4.8. One can see that the bins are either fully correlated or fully anti-correlated, this naturally comes from the definition in Eq.(4.3).

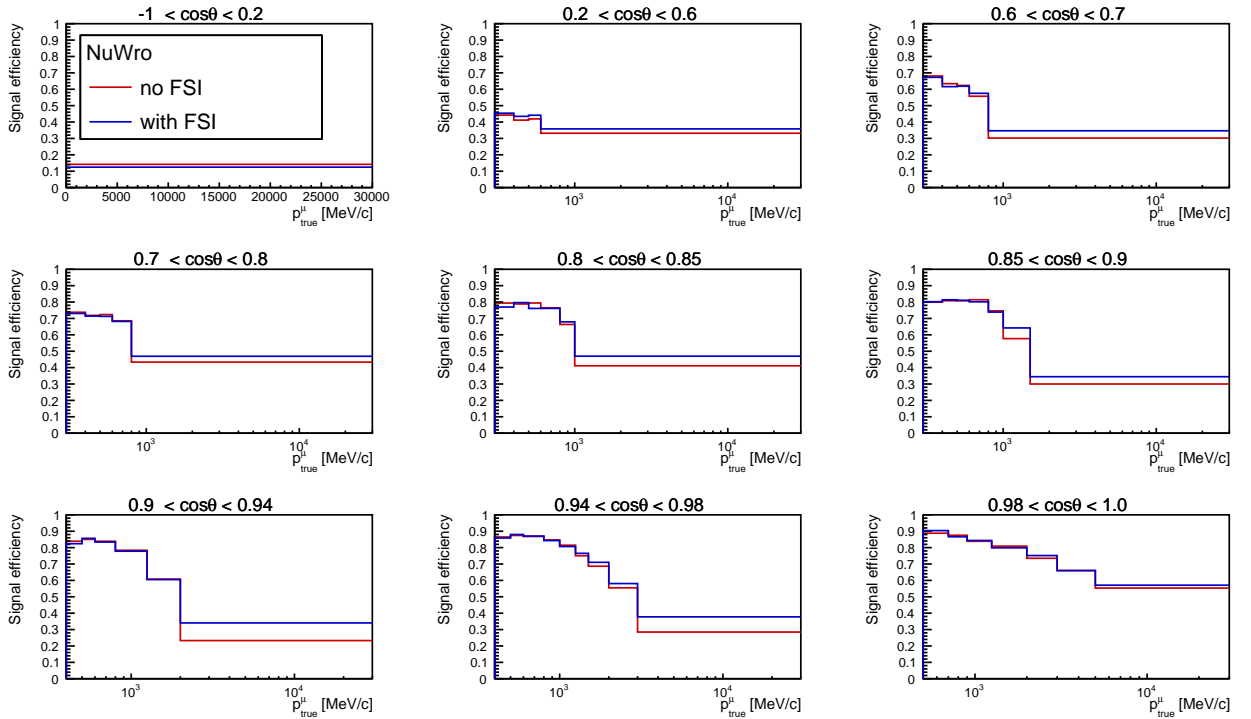


Figure 4.7: Efficiency of the ν_μ CC-0 π selection on carbon in $p_\mu, \cos\theta_\mu$ bins of the two NuWro samples, including (blue) and not including proton FSI (red).

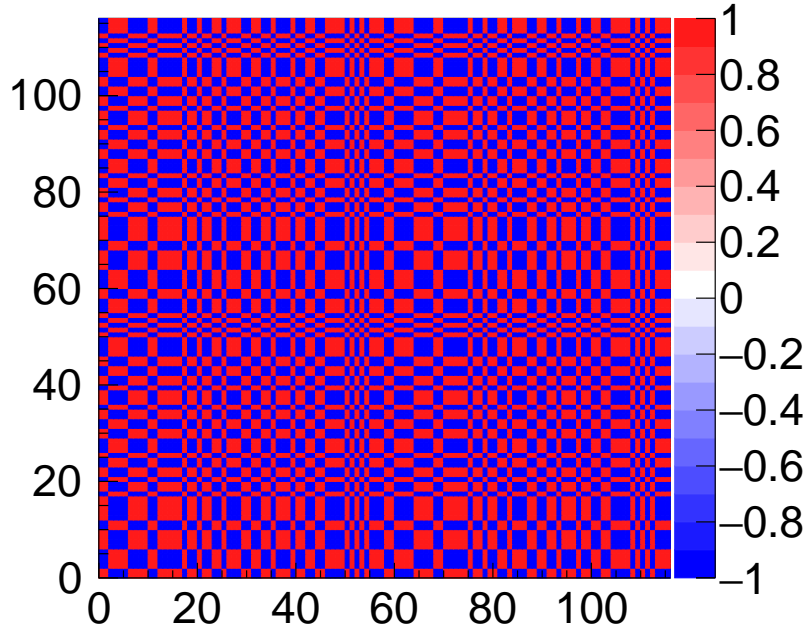


Figure 4.8: Correlation matrix associated to proton FSI efficiency built according to Eq.(4.3). The matrix elements correspond to the analysis binning described in Table 3.3, where the first half corresponds to carbon and the second half to oxygen.

Since no sample has been generated for FGD2 without FSI we can only rate this uncertainty on carbon using FGD1. We use the same values for oxygen, as we expect them to be in the same order. The resulting uncertainty by bin on carbon is shown in Fig. 4.9. The evaluation of the uncertainty on the cross-section ratio is more difficult since we only have the uncertainty on carbon and use the same values for oxygen. Uncertainties on carbon and on oxygen interaction rates could be considered as fully correlated as they are the same. However, the FSI uncertainty are not controlled very well and to be cautious we treat the two uncertainties as fully *uncorrelated*. Thus we estimate the uncertainty on the cross-section ratio as the carbon uncertainty multiplied by a factor two.

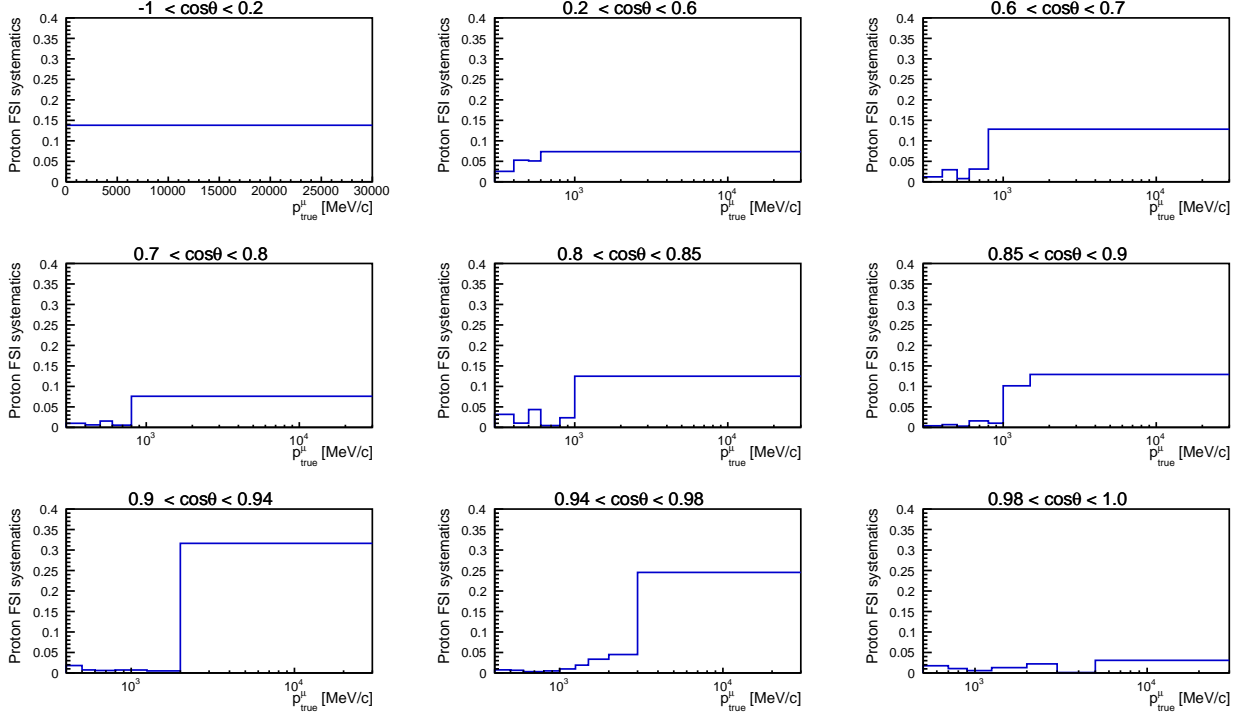


Figure 4.9: Uncertainty on proton FSI in $p_\mu, \cos \theta_\mu$ bins estimated with the selection efficiency calculated with NuWro samples.

4.5 Uncertainties on the final measurement

The estimation of pre-fit systematic uncertainties has been described in Sections 4.1, 4.2 and 4.3. The prior errors are then propagated through the fit, which returns a post-fit covariance matrix including all the systematic and statistical uncertainties for each systematic parameter of the fit. As the indices of the output matrix correspond to fit parameters these uncertainties need to be propagated to the final cross-section measurement in analysis (kinematic) bins. The errors are propagated by generating cross-section toy experiments. In each toy experiment the parameters are varied around their best-fit values. The cross-sections on carbon and on oxygen as well as their ratio are evaluated according to Eq.(3.1) and Eq.(3.2) respectively, where the terms of the formula are calculated as follows:

- $N_i^{\text{signal O or C}}$: throw fit parameters around their best-fit value according to the post-fit covariance matrix and reweight all events to calculate the number of events in each analysis bin;
- $N_{\text{O or C}}^t$: throw number of targets according to a Gaussian error around nominal value and prior error (see Section 5.4.2);
- Φ : calculate the integral using the current toy throw flux parameters to reweight the nominal flux;
- ϵ_i : calculate the efficiency using the selected and true events after reweighting using the current toy throw fit parameters;
- $\Delta p_\mu^i \Delta \cos \theta_\mu^i$: take the width of each analysis bin.

Finally the variations over the toy experiments are used to calculate a covariance matrix in the analysis binning, from which the uncertainty on final measurements can be extracted.

4.6 Estimation of the contribution from each source to the total uncertainty

One cannot separate the statistical from the different systematic contributions to the total cross-section uncertainty. However a method is used to give an estimation of the contributions. This should not be considered as the exact contribution but as a rough approximation. An Asimov fit³ is performed fitting only the template parameters while all the systematic parameters have fixed (prior) values. This cross-section error yields the statistical uncertainty since in this case the only uncertainty comes from the data statistics. Second an Asimov fit is performed allowing only one set of systematic parameters to vary while the other sets are fixed. The difference in quadrature with the error evaluated in the first case gives an estimation of the contribution to the uncertainty from that set of parameters.

The uncertainties for each of these Asimov fits are shown in Fig. 4.10 for neutrino interactions on carbon, in Fig. 4.11 for interactions on oxygen and in Fig. 4.12 for the cross-section ratio. Even though they are only estimations and should not be considered as the exact contributions, they confirm that the fit uncertainty is statistics dominated.

Note that the fit with only template and cross-section parameters does not properly explore the parameter space and small values were added to the Hesse matrix diagonal by the fit method in order to make it invertible. This is due to the fact that only fitting template and cross-section parameters leads to over-constraining the cross-section parameters. This degeneracy is solved once more degrees of freedom are added through other systematic parameters. The cross-section parameter contribution is not shown on these plots as the error is underestimated because of the Hessian matrix diagonal being modified in order for the fit to converge.

³An Asimov fit consists in fitting the simulated event distribution to itself, i.e. using the same Monte Carlo sample as data and nominal inputs. More details are given in Appendix B.2.

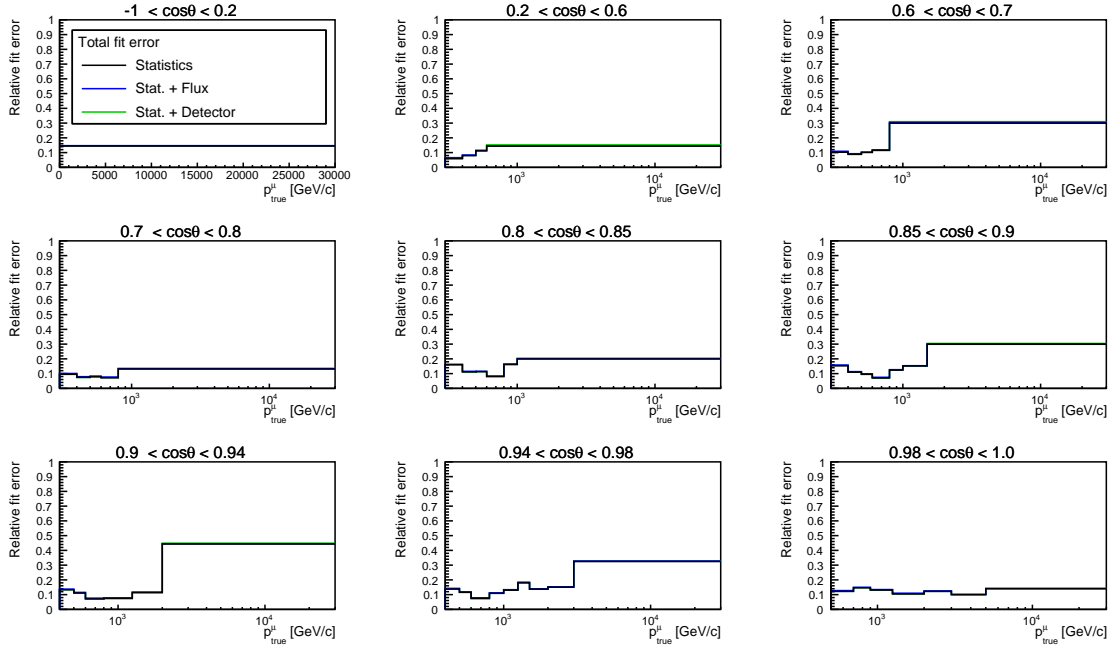


Figure 4.10: Estimation of the different contributions to the total fit uncertainty on carbon interactions. The black line is the uncertainty of an Asimov fit performed by allowing only template parameters to vary, which represent the statistical error. The colored lines are the errors of Asimov fits where only one type of systematic parameters is varied (flux in blue, cross-section model in red and detector in green).

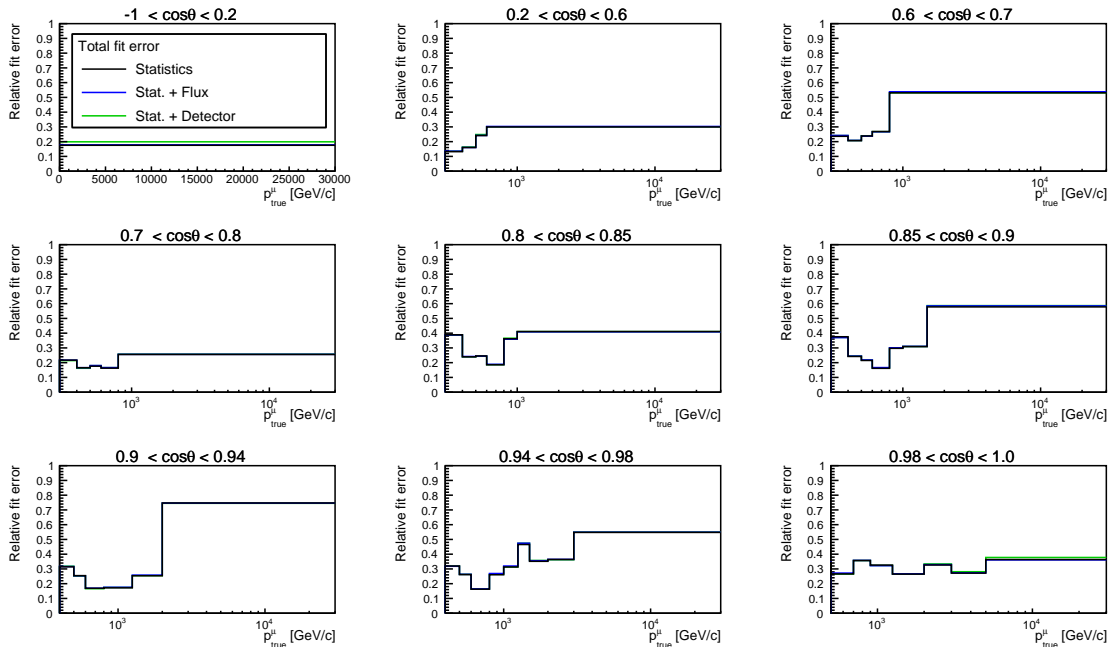


Figure 4.11: Estimation of the different contributions to the total fit uncertainty on oxygen interactions. The black line is the uncertainty of an Asimov fit performed by allowing only template parameters to vary, which represent the statistical error. The colored lines are the errors of Asimov fits where only one type of systematic parameters is varied (flux in blue, cross-section model in red and detector in green).

4. Evaluation of the uncertainties on cross-section measurement

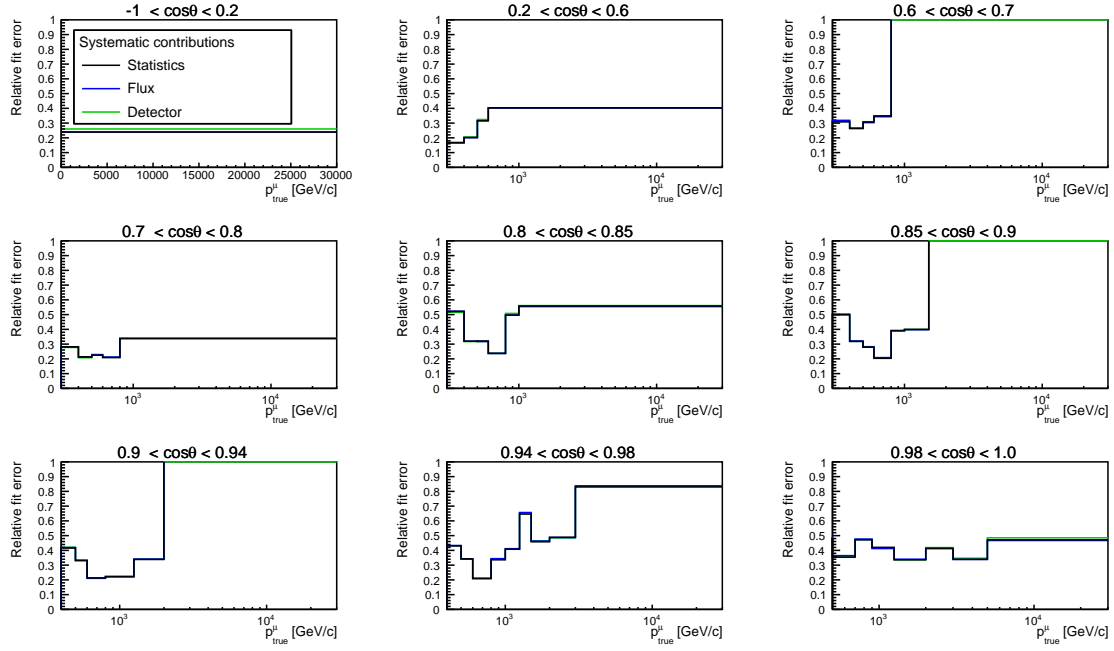


Figure 4.12: Systematic uncertainty on oxygen over carbon cross-section ratio of fits performed by allowing only template parameters to vary (black) and also one type of systematic parameters, flux (blue), cross-section model (red) and detector (green).

Final cross-section results

The complete process for generating inputs to the fitter has been explained in the previous sections. Section 3.3 has described the event selection methods in details, as well as the samples and binning used. Section 4 has explored all sources of uncertainty and detailed their evaluation. This section will now present the results from the fit performed according to the likelihood method described in Section 3.2.2, after giving an overview of the specificities of the fit in the particular case of this analysis. Eventually we explain how to obtain the integrated neutrino flux and the number of nucleon targets in order to evaluate a cross section and present the extracted cross-sections.

5.1 Fitter specific features

Before showing the fit results, the specific tools used to perform the fit and to analyse results are explained in this short section.

5.1.1 Fit parameters

The main feature of the binned likelihood fit is the use of template parameters that reweight the predicted number of events in each true analysis bin, as written in Eq.(3.7). Therefore the fit has two sets of 58 template weights, one set for parameters reweighting number of events with interactions on carbon (c_i 's) and a second set for interactions on oxygen (o_i 's). Moreover, as described in Section 3.2.2 and written in Eq.(3.11), the fit also has the ability to vary systematic parameters for the neutrino flux, detector and cross-section model. Flux parameters are associated to neutrino energy bins (see Section 4.2). Detector parameters correspond to kinematic bins at the reconstructed level (see Section 4.1). Finally cross-section parameters give some freedom to several interaction modes for signal and background events (see Section 4.3). Table 5.1 summarises the fit parameter correspondance to physics observables and systematic uncertainties.

5. Final cross-section results

Table 5.1: Summary of the fit parameters used in this analysis and their correspondence to physics observables or uncertainties.

Parameters	Nb.	Range	Physical quantity
Template par. on carbon (c_i)	58	0 – 57	$p_\mu, \cos \theta_\mu$ bins in Table 3.3
Template par. on oxygen (o_i)	58	58 – 115	$p_\mu, \cos \theta_\mu$ bins in Table 3.3
Flux parameters	20	116 – 135	Flux weights in E_ν bins in Table 4.2
Cross-section model parameters	26	136 – 161	Model parameters as listed in Table 4.3
Detector parameters	1122	162 – 1283	$p_\mu, \cos \theta_\mu$ bins in each signal and control sample
Total fit parameters	1284	0 – 1283	

5.1.2 χ^2 definitions and goodness of fits

In order to estimate the goodness of the fit, χ^2 values are evaluated. Several χ^2 's are computed with different methods associated to the different results that are presented.

The pre-fit and post-fit χ^2 's shown with the event distributions are the values returned by the MINUIT fit method. They yield the difference in the number of events at the reconstructed level between the nominal MC values and the (fake) data values according to Eqs.(3.5)-(3.6). When showing the post-fit event distributions a simplified χ^2 is written on top of each plot by region. This χ^2 gives a simple estimation of the data - post-fit discrepancy by summing up the difference square of data and post-fit numbers of events divided by the data number of events in each bin of the specific region,

$$\chi_{\text{simpl.}}^2 = \sum_i^{\text{bins}} \frac{|N_{\text{data}} - N_{\text{post-fit}}|}{N_{\text{data}}} \quad (5.1)$$

The final cross-section χ^2 that carries the difference in the true analysis binning is rated according to a Gaussian approximation, namely

$$\chi_{\text{xsec}}^2 = (\vec{\sigma}_{\text{best fit}} - \vec{\sigma}_{\text{prior}})^T (V_{\text{xsec}}^{\text{cov}})^{-1} (\vec{\sigma}_{\text{best fit}} - \vec{\sigma}_{\text{prior}}) \quad (5.2)$$

where $\vec{\sigma}_{\text{best fit}}$ is a vector containing cross-section values in each analysis bin for the best-fit parameters, $\vec{\sigma}_{\text{prior}}$ is the vector of nominal cross-section values and $V_{\text{xsec}}^{\text{cov}}$ is the final covariance matrix in the analysis binning.

For normal distributions the χ^2 is distributed as a χ^2 -distribution with mean equal to the number of degrees of freedom. More details and χ^2 's studies are reviewed in Appendix B.5.

5.2 Fit validation

To test the robustness and reliability of the fit method, a series of studies are conducted. In order to avoid biases, sets of *mock data* are used instead of the *real data*. In other words fits are performed where various Monte Carlo samples are used as "fake" data inputs. These "fake" data samples are either the nominal MC events with artificially altered content or events simulated with other neutrino interaction generators. Before revealing results coming from real data measurements, the fake data studies have been reviewed internally within the T2K Collaboration in order to approve the methods developped for this measurement. Fit validation results are detailed in Appendix B.

5.3 Post-fit parameters and event distributions

After the fit against the data sample, we have a look at the post-fit parameters, in other words the *best-fit* parameters, compared to their prior values. The template parameters are plotted in Fig. 5.1, the flux parameters in Fig. 5.2, the interaction model parameters in Fig. 5.3 and the detector parameters in Fig. 5.4. In each case the associated relative uncertainties are plotted in the bottom plot and the associated post-fit correlation matrix is shown in Fig. 5.5.

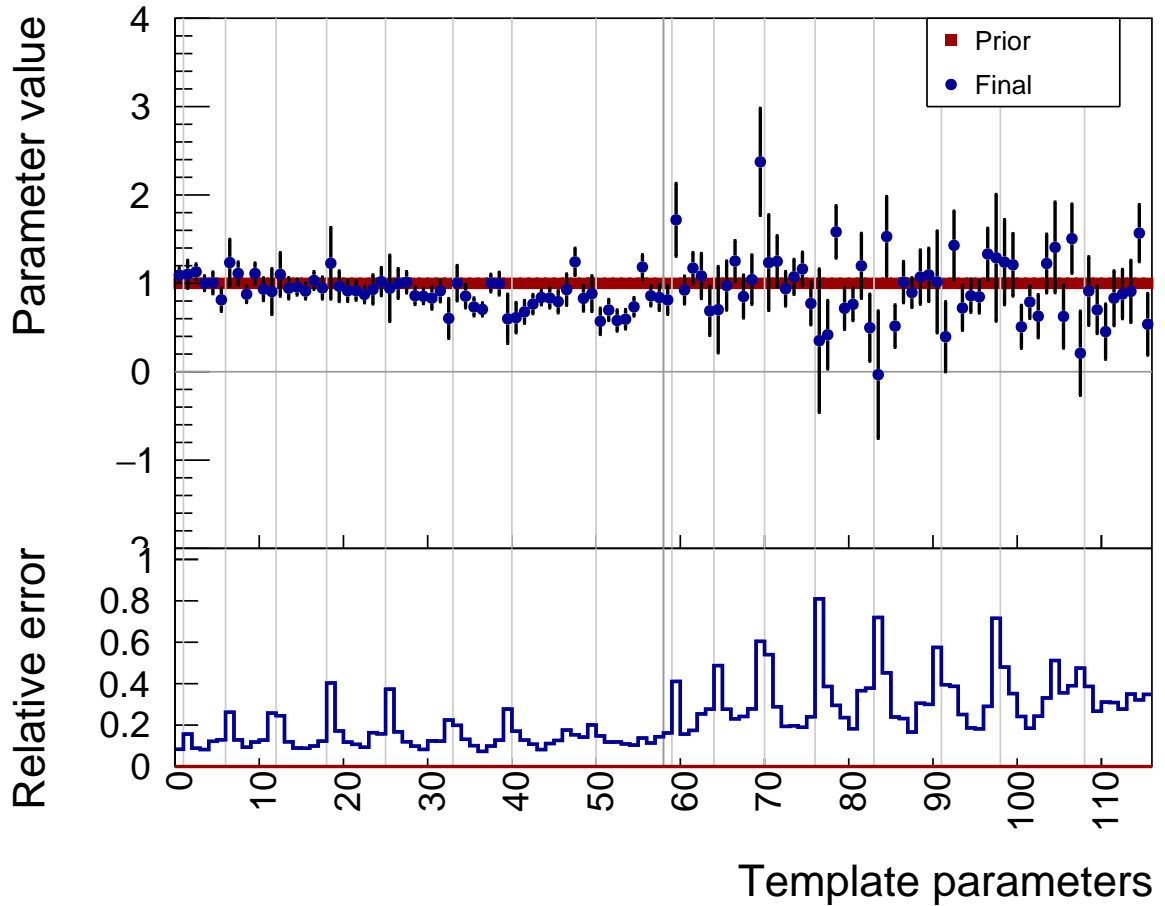


Figure 5.1: Prior and post-fit template parameter values and their associated uncertainty. The first 58 parameters correspond to the carbon parameters (c_i) and the next 58 parameters are the ones for oxygen (o_i). Gray lines demarcate the different $\cos\theta_\mu$ bins.

As expected, it can be seen in Fig. 5.1 that the parameters associated to interactions on carbon (c_i 's) have lower uncertainties than the ones for interactions on oxygen (o_i 's), and the o_i 's fluctuate more. This is due to higher statistics of events with interactions in the scintillating layers, thus reducing the statistical uncertainty on the parameters associated to carbon. Template parameters associated to carbon tend to take values slightly below 1 in the three slices associated to low muon angle tracks. This effect will be reflected in the final cross section and will be discussed later on.

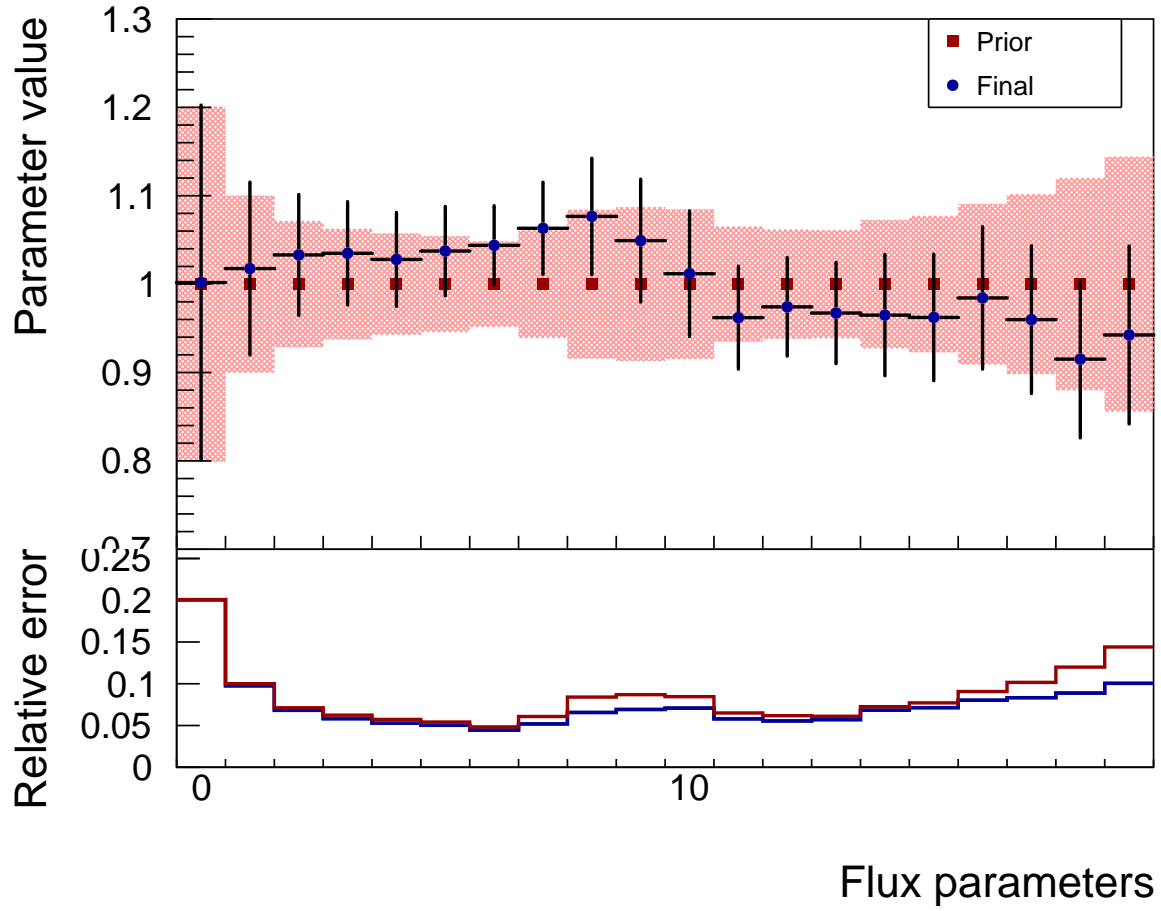


Figure 5.2: Prior and post-fit flux parameter values and their associated uncertainty. We remind that each flux parameter is a weight in neutrino energy bin, see Table 4.2. Prior weight values are equal to unity.

The flux parameters, shown in Fig. 5.2, fluctuate a bit around their nominal values, but it is nice to observe that post-fit values are compatible with prior flux weights within 1σ uncertainty intervals. The post-fit errors do not change much with respect to their prior values.

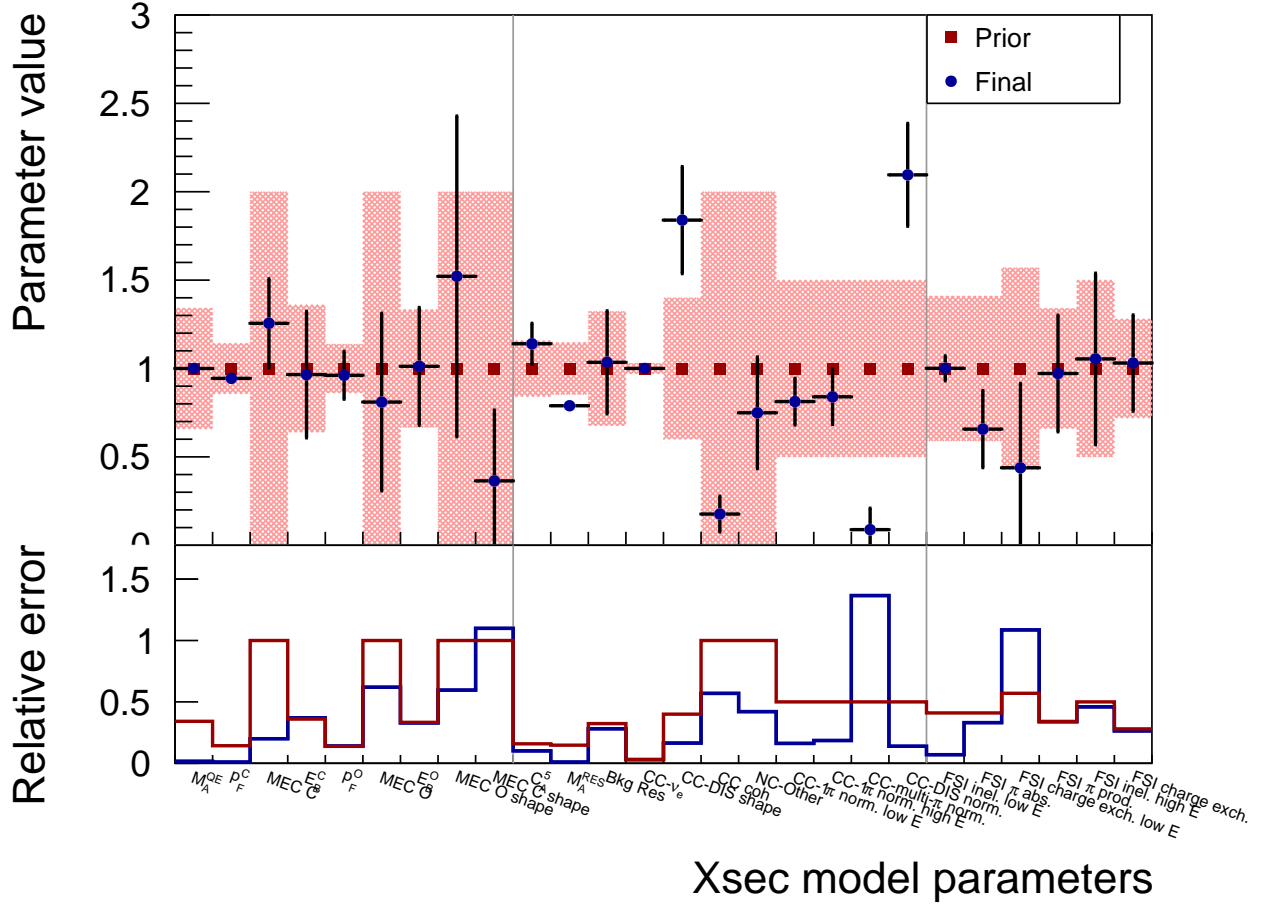


Figure 5.3: Prior and post-fit cross-section model parameter values and their associated uncertainty. We remind that signal parameters are going from 0 to 8, background parameters from 9 to 19 and FSI parameters from 20 to 25. Their values are normalised to the parameter prior values as given in Table 4.3.

The cross-section model parameters, plotted in Fig. 5.3, are compatible with prior values within the 1σ uncertainty intervals, except certain background parameters. In particular the CC-DIS shape (13), CC multi- π normalisation (18) and CC DIS normalisation parameters (19) are pushed close to their boundaries. Obviously the fit struggles to fit the CC-Other region. It is trying to compensate through the model parameters for the data excess over MC prediction seen in the CC-Other event distributions in Fig. 3.14. Moreover, there is a quite strong anti-correlation between the multi- π and the DIS normalisation parameters, as can be observed in the correlation matrix in Fig. 5.5, which is not a surprise since they both contribute to the CC-Other sideband.

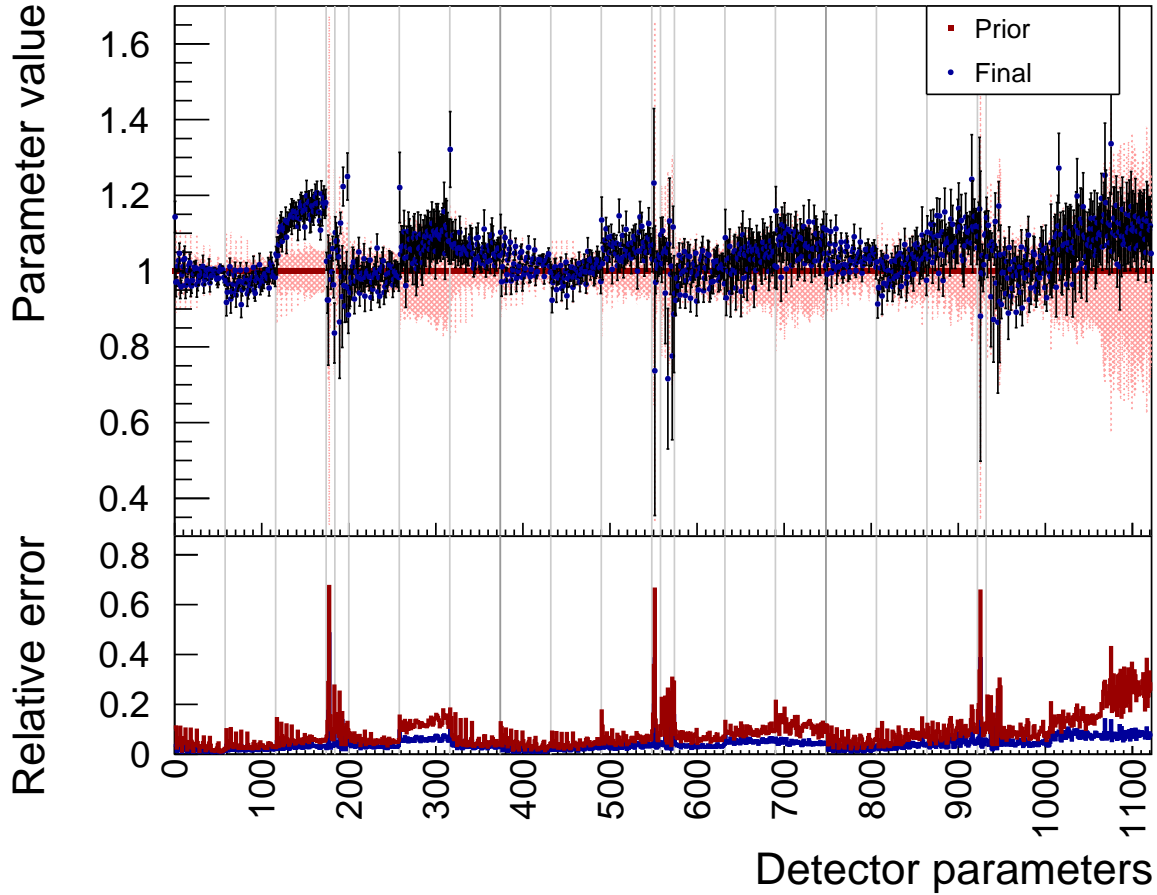


Figure 5.4: Prior and post-fit detector parameter values and their associated uncertainty. Each parameter is a weight associated to a bin at the reconstructed level, that is the kinematic bins for each signal and control sample. The first third is for FGD1 events, the second third to FGD2 x events and the last one for FGD2 y. Regions demarcated by gray lines correspond to the 5 signal and 3 control samples as defined in Section 3.3.3.

We observe in Fig. 5.4 that detector parameters corresponding to the CC- 1π -Michel sideband in the FGD2 y layers (on the right side of the x axis) have large prior uncertainties, due to low statistics and probably also to the large OOFV background contamination in this sample, as can be seen in the data and MC event distributions in Fig. 3.15. However, the fit reduces drastically these uncertainties. The parameters corresponding to signal sample (3) ($\mu_{\text{TPC}} + \text{pFGD}$ and $\mu_{\text{TPC}} + \text{Np}$) in FGD1 are pushed up outside the error bars. We can see indeed in the selected event distribution for that region, in Fig. 3.8, that there is a small excess of data with respect to the MC predicted number of events, likely the fitter is compensating for this excess by increasing the detector parameters associated to this sample. Physically, this may be due to event migration between the different μ_{TPC} -like signal samples. There is no freedom given for event migration between the signal samples and we know that protons FSI are not well reconstructed.

This effect can also be observed in the number of event distributions by sample at the reconstructed level in Fig. 5.6, where we observe quite large discrepancies in the μ_{TPC} -like signal samples, reflected by the sample χ^2 's. This is why in Fig. 5.7 the μ_{TPC} -like samples have been grouped together in order to better visualise the result, avoiding confusion due to event migration between the signal samples. In this case we recover a very low χ^2 value associated to the μ_{TPC} samples.

The discrepancies are quite large for the sideband regions, as can be seen by their associated χ^2 values, expected to be around the number of bins, i.e. 58. Again, this shows some difficulties of the fit to accomodate for background regions. The reasons could be the data / MC discrepancy in the CC-Other sideband, as already mentioned above, and the fact that the CC- 1π -Michel sample is hard to fit and may also affect the original CC- $1\pi^+$ sample.

Otherwise the post-fit numbers of events in the signal regions show very good agreement to data and the individual χ^2 's by region have reasonable values, that is, lower or about the number of bins. The overall post-fit χ^2 returned by MINUIT is

$$\chi^2_{\text{post-fit}} = 1321 \tag{5.3}$$

which is a bit high for a 1284 parameter fit (the associated probability is 23.1%), however we explained the large contribution coming from the disagreement in the μ_{TPC} samples with protons and from the sideband regions.

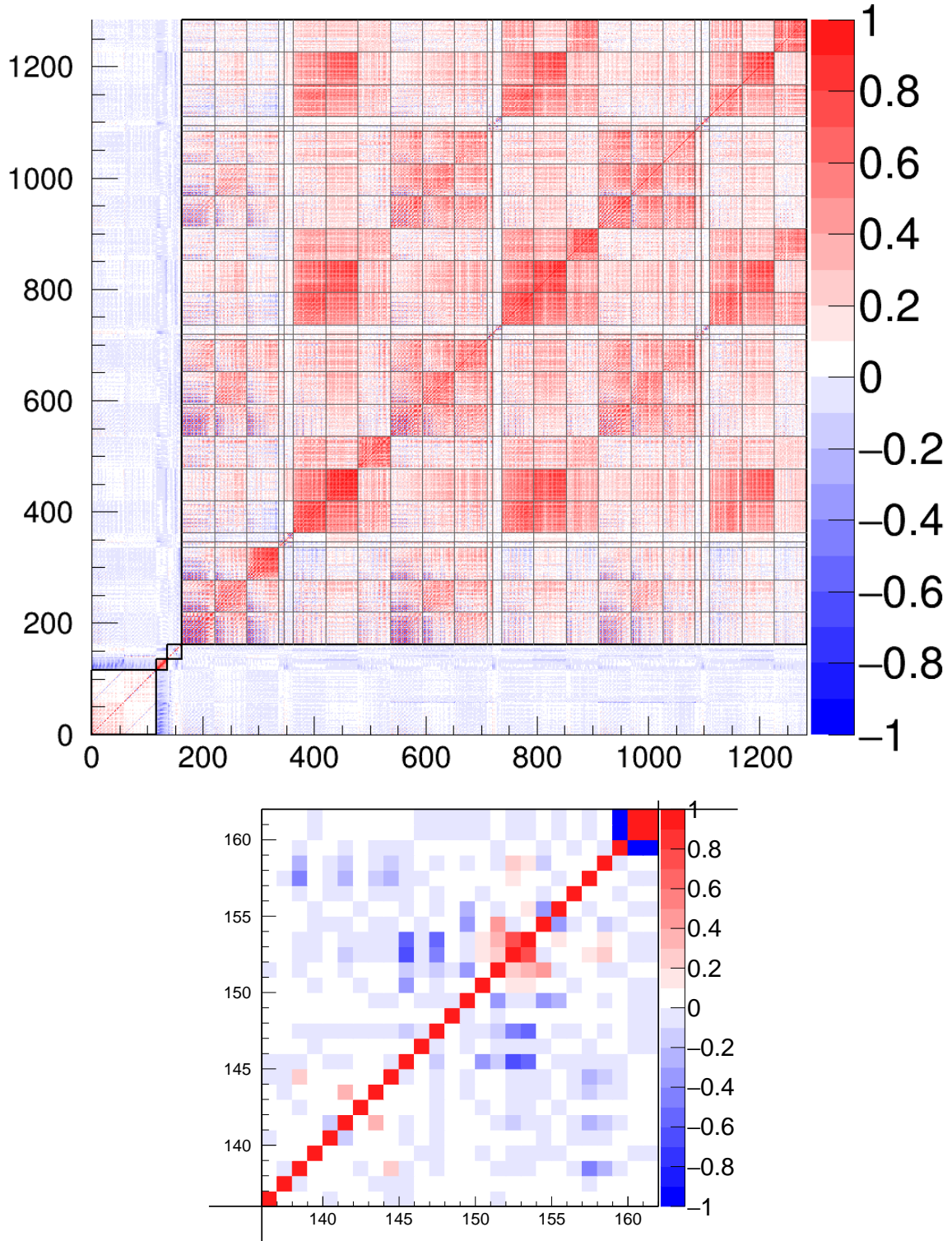


Figure 5.5: Post-fit correlation matrix of all the fit parameters (top) and zoom into the cross-section model parameter sub-matrix (bottom). The sub-matrices for the different types of parameters are separated by black lines. Parameters with bins from 0 to 57 corresponds to the c_i 's, from 58 to 115 o_i 's, from 116 to 135 flux, from 136 to 161 cross-section model and from 162 to 1283 detector parameters. Each small submatrix in the detector parameter matrix (separated by gray lines) relates to the kinematic bins of one signal or control sample. Notice that the two cross-section parameters that are anti-correlated, numbers 154 and 155, correspond to the CC multi- π and CC DIS normalisation parameters, which are pushed to their limits by the fitter.

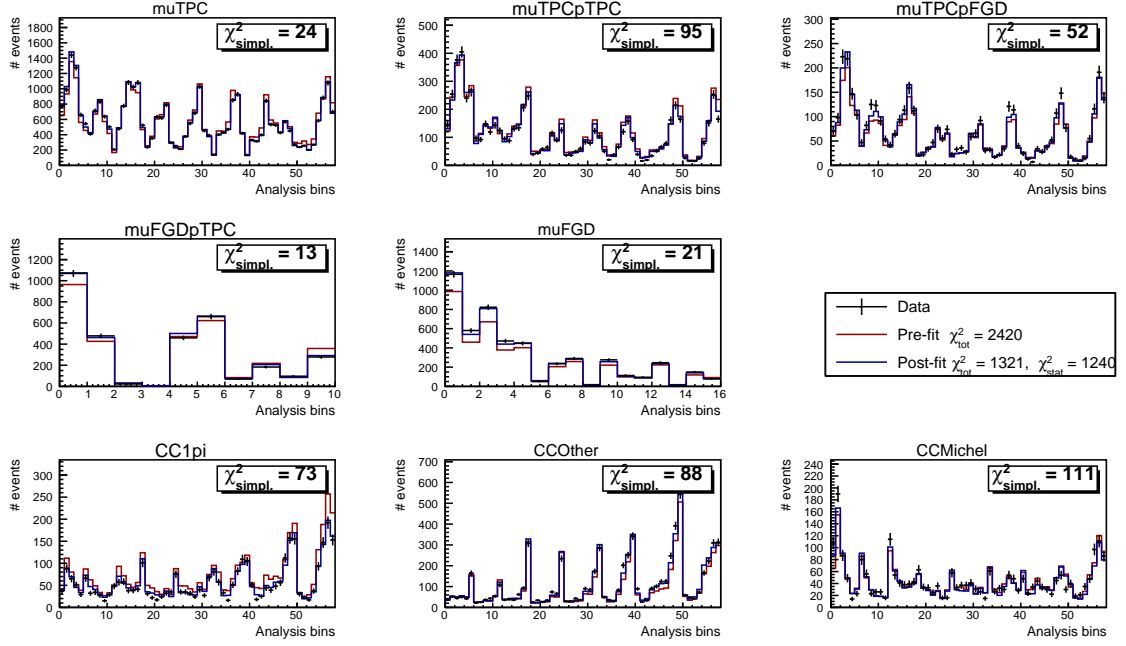


Figure 5.6: Prior (blue) and post-fit (red) signal events compared to data (black) distributed in $p_\mu, \cos \theta_\mu$ analysis bins. Each plot is for a specific signal or sideband region according to its title. The $\chi^2_{\text{simpl.}}$ on top of each region plot is a simplified χ^2 , calculated according to Eq. (5.1). The total pre-fit and post-fit χ^2 's are the values given by MINUIT.

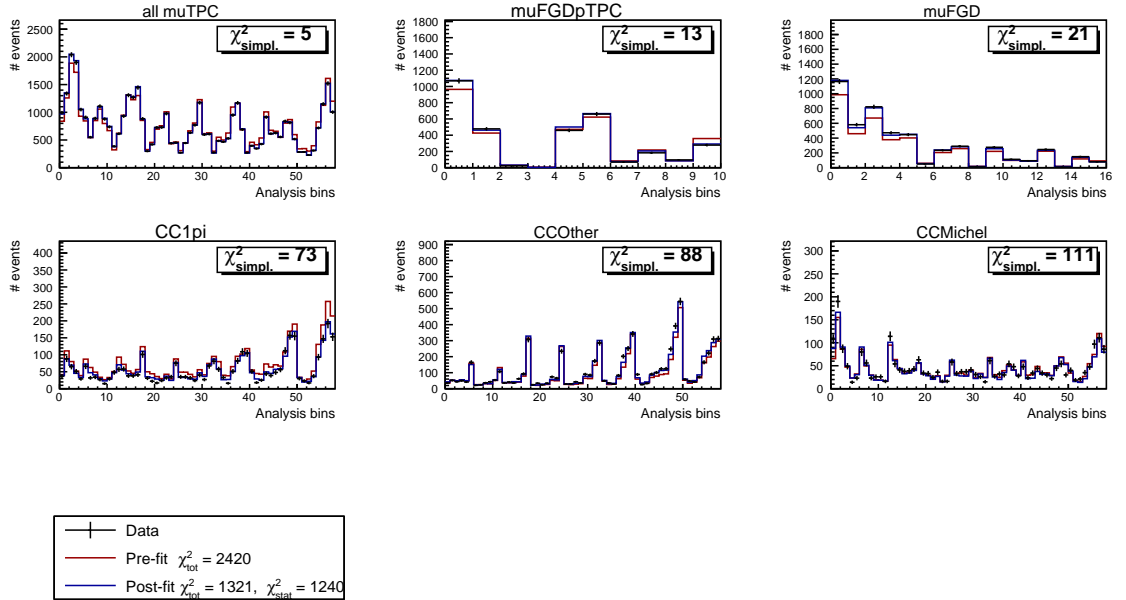


Figure 5.7: Prior (blue) and post-fit (red) signal events compared to data (black) distributed in $p_\mu, \cos \theta_\mu$ analysis bins. Each plot is for a specific signal or sideband region according to its title ; all the μTPC topologies are grouped together in the top left plot. The $\chi^2_{\text{simpl.}}$ on top of each region plot is a simplified χ^2 , calculated according to Eq. (5.1). The total pre-fit and post-fit χ^2 's are the values given by MINUIT.

5.4 Cross-section measurement

We now have a prediction of the number of events in each kinematic bin from the fit and the selection efficiency was shown in a previous chapter (see figures 3.18 and 3.19). In order to have all the ingredients that are necessary to evaluate the neutrino cross section with carbon and oxygen nuclei which are, we remind:

$$\begin{aligned}\frac{d\sigma_i^C}{dp_\mu^i d\cos\theta_\mu^i} &= \frac{N_i^{\text{signal } C}}{\epsilon_i^C \Phi N_t^C \Delta p_\mu^i \Delta \cos\theta_\mu^i} \\ \frac{d\sigma_i^O}{dp_\mu^i d\cos\theta_\mu^i} &= \frac{N_i^{\text{signal } O}}{\epsilon_i^O \Phi N_t^O \Delta p_\mu^i \Delta \cos\theta_\mu^i}\end{aligned}\quad (5.4)$$

we need to evaluate the integrated flux Φ and the numbers of nucleon targets N_t^C and N_t^O . This will be done in the next sections. Finally resulting differential cross sections in kinematic bins and integrated cross sections will be presented, as well as their oxygen over carbon ratio $\frac{d\sigma_i^O}{d\sigma_i^C}$.

5.4.1 Integrated neutrino flux

To compute the integrated flux we use the flux tuning from the latest release **13av4** [121, 90] (see Section 2.1.2). The flux prediction is provided in neutrino energy bins for each T2K run period. It needs to be normalised to the POT corresponding to each run period and then integrated over the energy. The total muon neutrino flux for run periods 2-3-4-8 is

$$\Phi = 2.1316 \times 10^{13} \text{ cm}^{-2} \quad (5.5)$$

5.4.2 Number of target nucleons

In order to extract the cross section on single nucleon, the measured carbon (oxygen) number of events need to be divided by the total number of carbon (oxygen) target nucleons inside the fiducial volume. Such number is computed as:

$$N_t^\alpha = N_A \sum_i^{\text{module}} f_\alpha^i M_{TOT}^i \frac{N_\alpha}{M_\alpha^A} \quad (5.6)$$

where we sum over the water and scintillator modules i , for a target chemical element $\alpha = \text{C}$ or O . f_α^i is the fraction of element α in the fiducial volume depending on the module, N_α the number of nucleons, M_α^A the standard atomic mass, M_{TOT}^i the total mass of the fiducial volume of a module and $N_A = 6.022 \times 10^{23}$ is the Avogadro number. The total mass of one module i can be written as:

$$M_{TOT}^i = \rho^i V_{FV} = \rho_{\text{areal}}^i \Delta X \Delta Y \quad (5.7)$$

where V_{FV} is the Fiducial Volume and $\rho^i = \rho_{\text{areal}}^i \Delta Z$ is the total density averaged over the areal density of each module component. $\Delta X = \Delta Y = 174.902 \text{ cm}$ is the total length of the fiducial volume in the X and Y directions. We can now rewrite the number of target nucleons as

$$N_t^\alpha = N_A \Delta X_{FV} \Delta Y_{FV} (n^{\text{scint}} \rho_\alpha^{\text{scint}} + n^{\text{water}} \rho_\alpha^{\text{water}}) \frac{N_\alpha}{M_\alpha^A} \quad (5.8)$$

where n^{scint} and n^{water} are the total numbers of XY -scintillator modules and water modules respectively. FGD1 consists of 15 XY -scintillator supermodules (polystyrene) and FGD2 consists

of 7 XY -scintillator modules and 6 water modules. A more detailed description was given in Section 2.3.3. The values of the areal density, atomic mass and averaged number of nucleons for each element are summarised in table 5.2. Note that interactions on other targets than carbon and oxygen are negligible and they are treated as backgrounds, although they are not directly constrained by a control sample.

Table 5.2: Values of areal density in a scintillator module and in a water module, atomic mass and averaged number of nucleons for each element.

Element	$\rho_{\alpha}^{\text{scint}}$ (g/cm ²)	$\rho_{\alpha}^{\text{water}}$ (g/cm ²)	M_{α}^A	N_{α}
C	1.849 ± 0.0092	0.4187 ± 0.007	12.01074	12
O	0.0794 ± 0.0048	2.0639 ± 0.005	15.9994	16
H	0.1579 ± 0.0021	0.2928 ± 0.001	1.00794	1
Mg	0.0355 ± 0.0059	0.007 ± 0.001	47.8671	48
Si	0.0218 ± 0.0043	0.011 ± 0.001	28.0855	28
N	0.0031 ± 0.0012		14.00672	14

The uncertainty on the number of target nucleons comes from the error on the measurement of the areal densities of each elements. To compute this uncertainty, toys are thrown for Eq. 5.8. In each toy the areal density is randomly thrown according to the covariance matrix built from the correlations in Table 5.4.

Table 5.3: Correlation matrices for the areal densities of a scintillator module (left) from T2K-TN-091 [103] and a water module (right) from T2K-TN-198 [104].

Table 5.4: Correlation matrices for the areal densities of a scintillator module (left) from T2K-TN-091 [103] and a water module (right) from T2K-TN-198 [104].

	C	O	H	Mg	Si	N
C	1	0.210	0.587	-0.193	-0.161	0.226
O		1	0.115	0.830	0.068	-0.033
H			1	-0.121	-0.879	0.875
Mg				1	0.074	-0.097
Si					1	-0.972
N						1

	C	O	H	Mg	Si
C	1	0.791	0.976	0.748	0.748
O		1	0.697	0.988	0.988
H			1	0.678	0.678
Mg				1	1.000
Si					1

The resulting distributions of the number of nucleons in carbon N_C^t and in oxygen N_O^t for 10^5 toys are shown in Fig. 5.8. The relative uncertainty on the number of nucleons is taken as the RMS over the mean of such distribution. We obtain the following values, which are going to be propagated to the cross-section result (see Section 4.5),

$$N_C^t = (7.439 \pm 0.036) \times 10^{29} \rightarrow 0.5\% \text{ error}$$

$$N_O^t = (2.581 \pm 0.019) \times 10^{29} \rightarrow 0.7\% \text{ error}$$

5. Final cross-section results

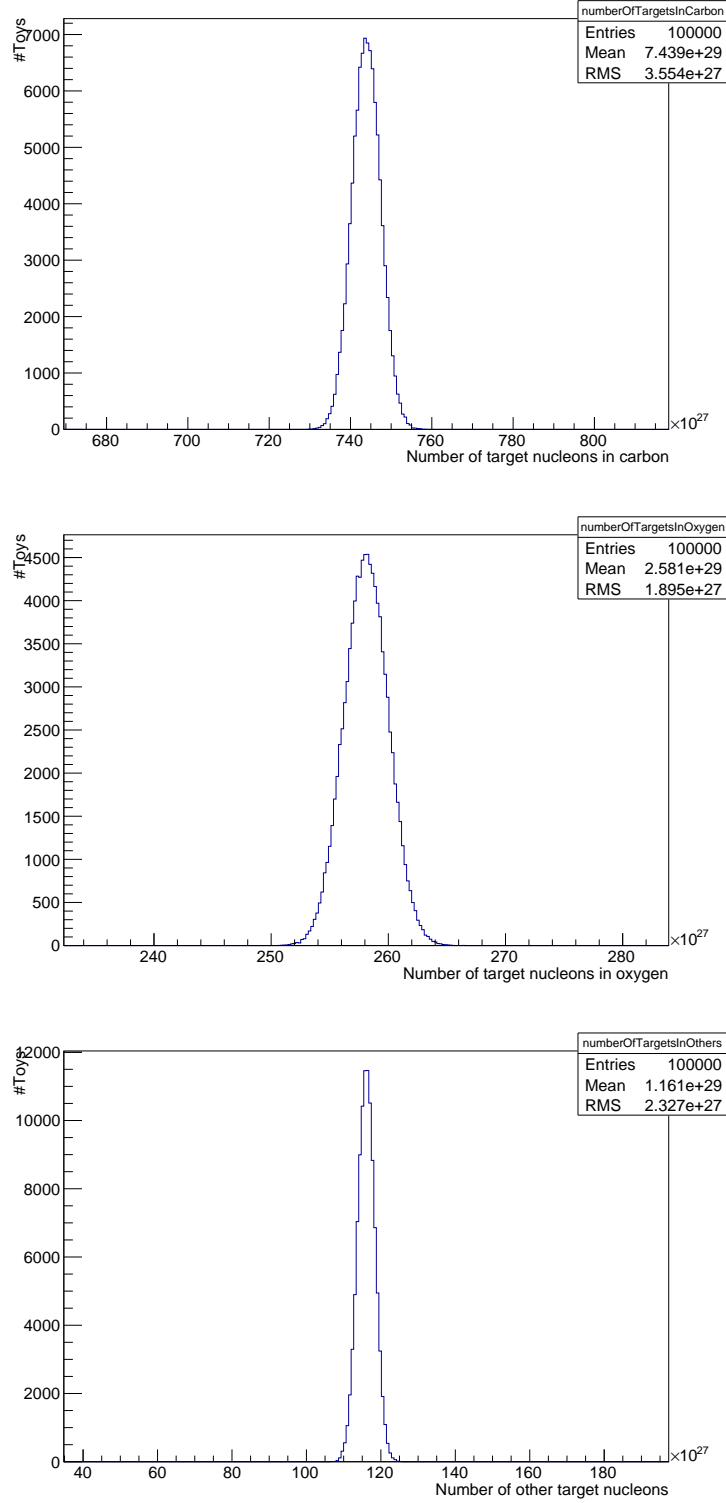


Figure 5.8: Distribution of number of nucleons for 10^5 toys obtained varying the areal density of the various elements composing the FGD1 and FGD2 fiducial volumes following the covariance matrix built from Table 5.4.

5.4.3 Cross-section results in kinematic bins

The double differential cross section in kinematic bins can now be evaluated, as well as its uncertainties propagated as explained in Section 4.5 using the post-fit covariance matrix

represented in Fig. 5.5. The final correlation matrix for the differential cross section in analysis binning is represented in Fig. 5.9. The extracted cross-sections compared to the nominal NEUT predictions are shown in Fig. 5.10-5.11 for neutrino interactions on carbon and in Fig. 5.13-5.14 on oxygen. In each case the result is shown first in linear scale omitting the high-momentum bins for an easier reading and in logarithmic scale including high-momentum bins. Their associated relative uncertainties are plotted in Figures 5.12 and 5.15 respectively.

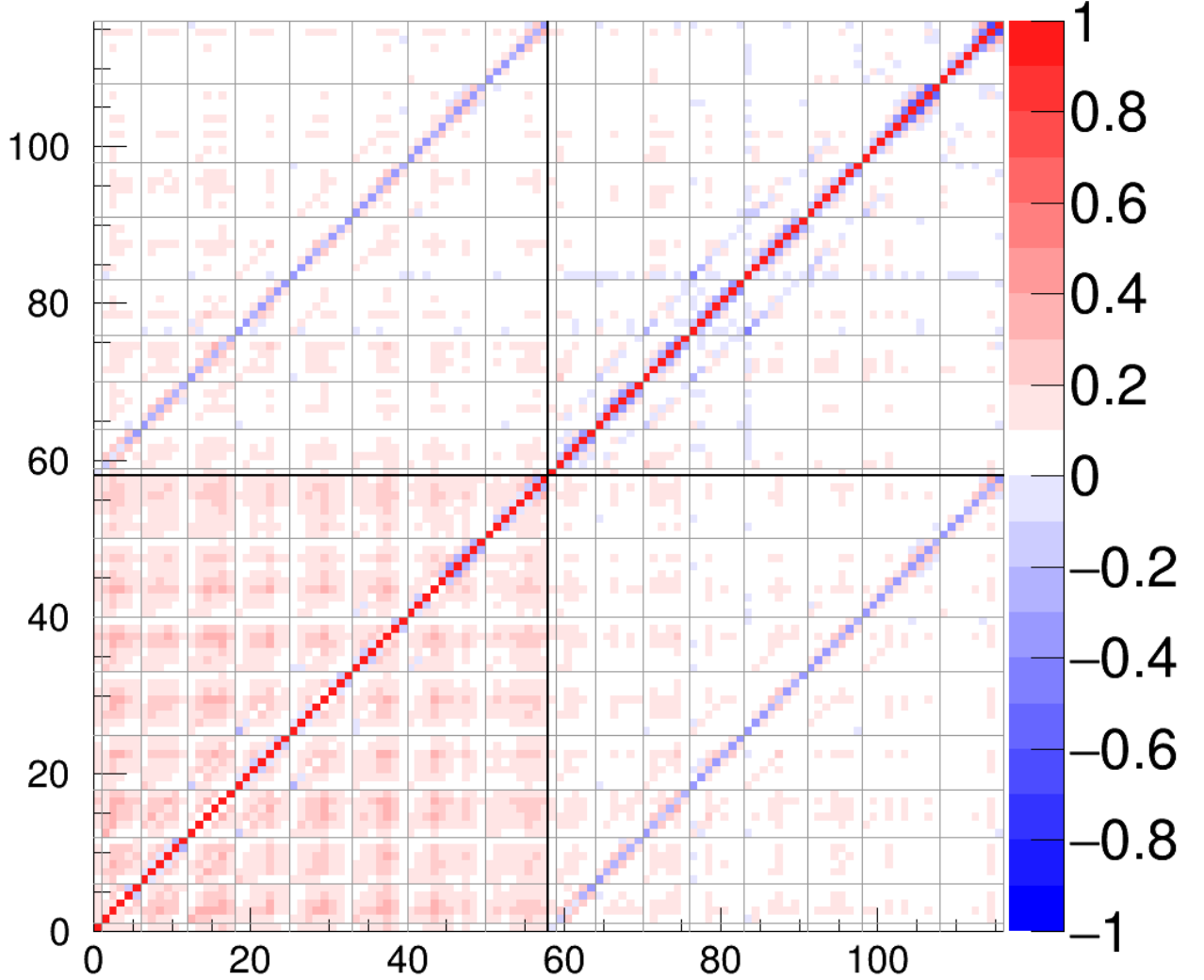


Figure 5.9: Final correlation matrix associated to the cross section results. The sub-matrices for the different $\cos\theta_\mu$ slices are separated by grey lines. Bins from 0 to 57 corresponds to neutrino interactions on carbon, from 58 to 115 to neutrino interactions on oxygen.

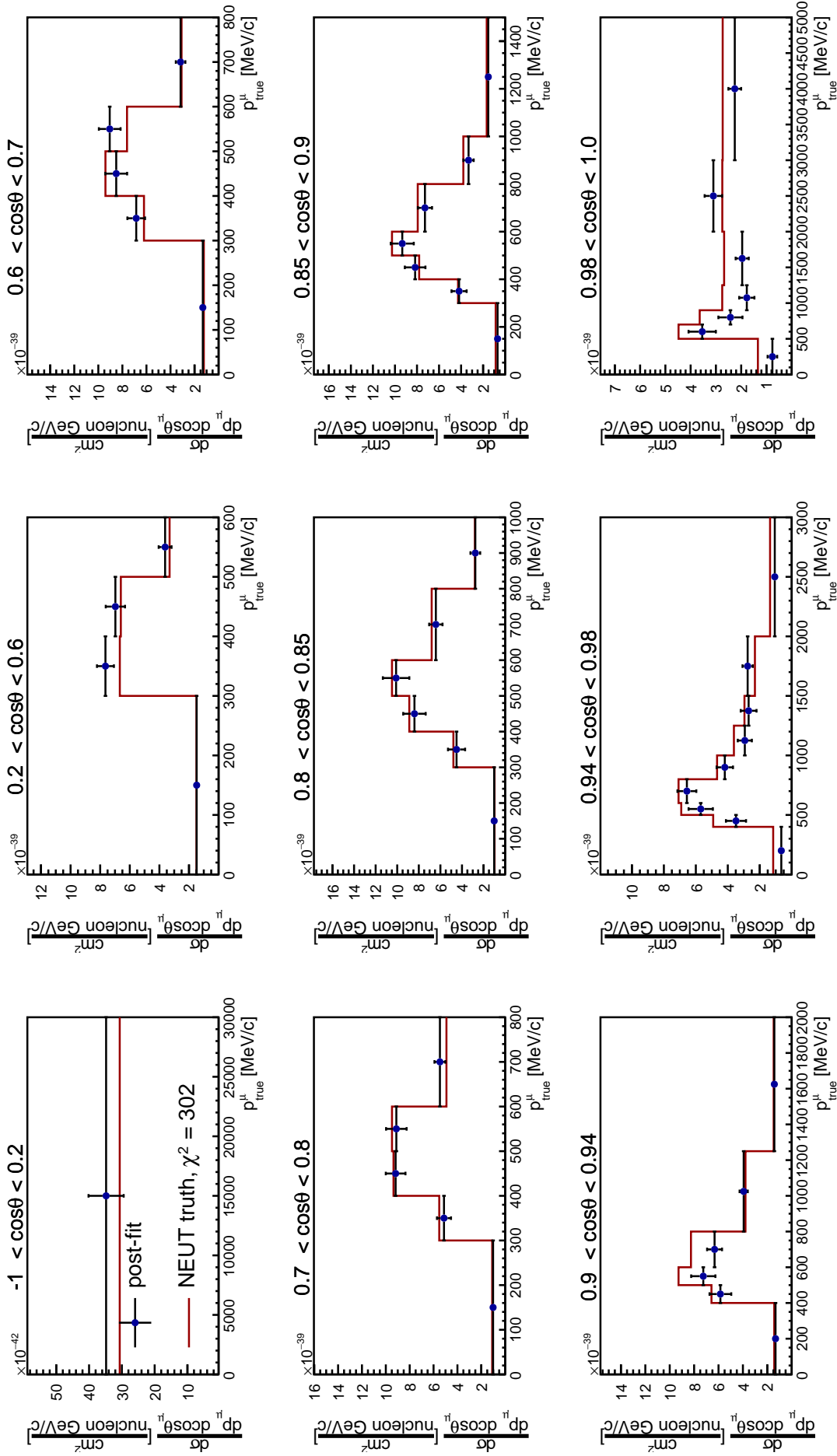


Figure 5.10: Flux integrated ν_μ cross section on carbon in true muon kinematics. Each plot shows the distribution in muon momentum for a given muon angle bin.

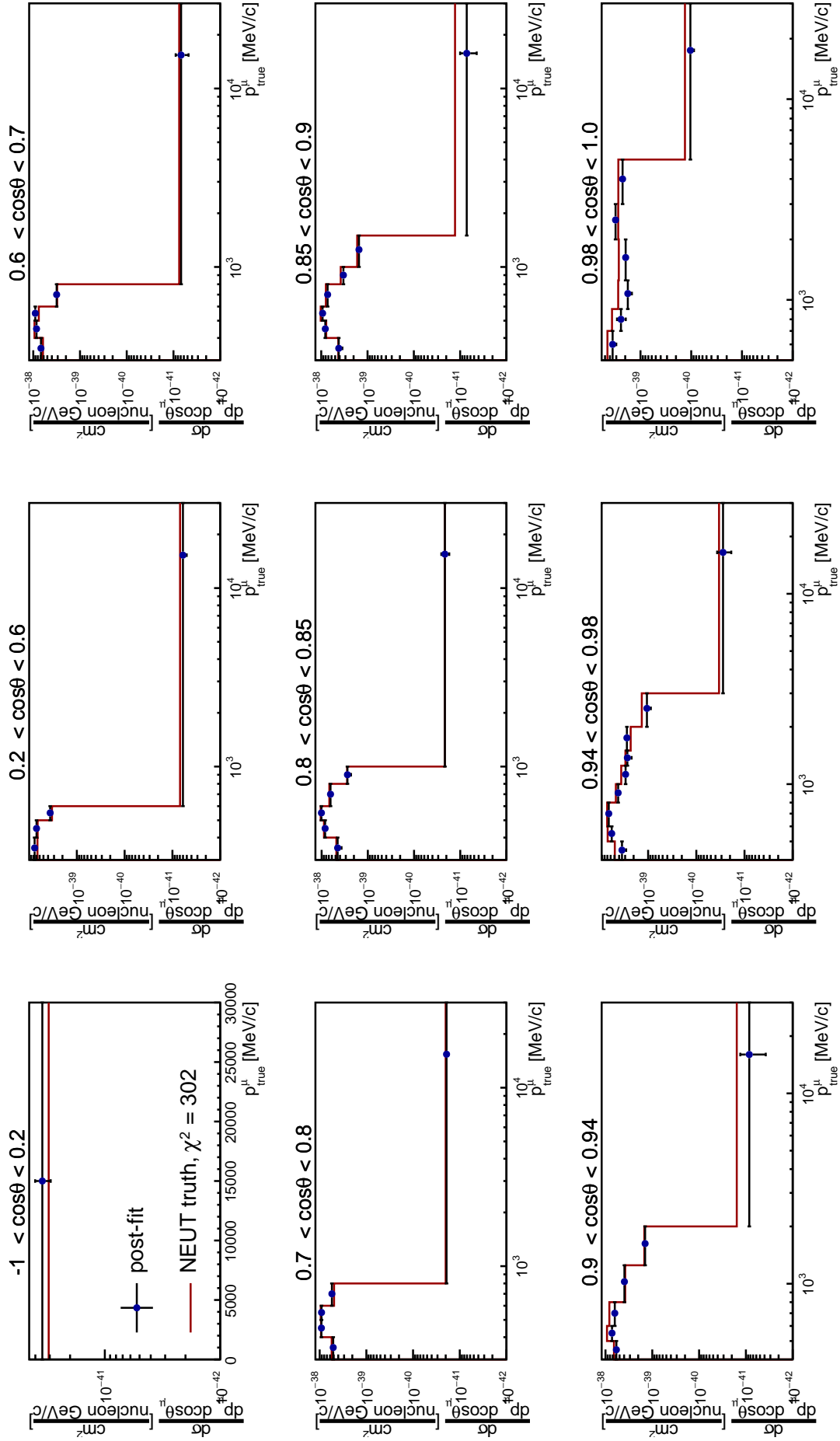


Figure 5.11: Flux integrated ν_μ cross section on carbon in true muon kinematics in logarithmic scale including the last momentum bins. Each plot shows the distribution in muon momentum for a given angle bin.

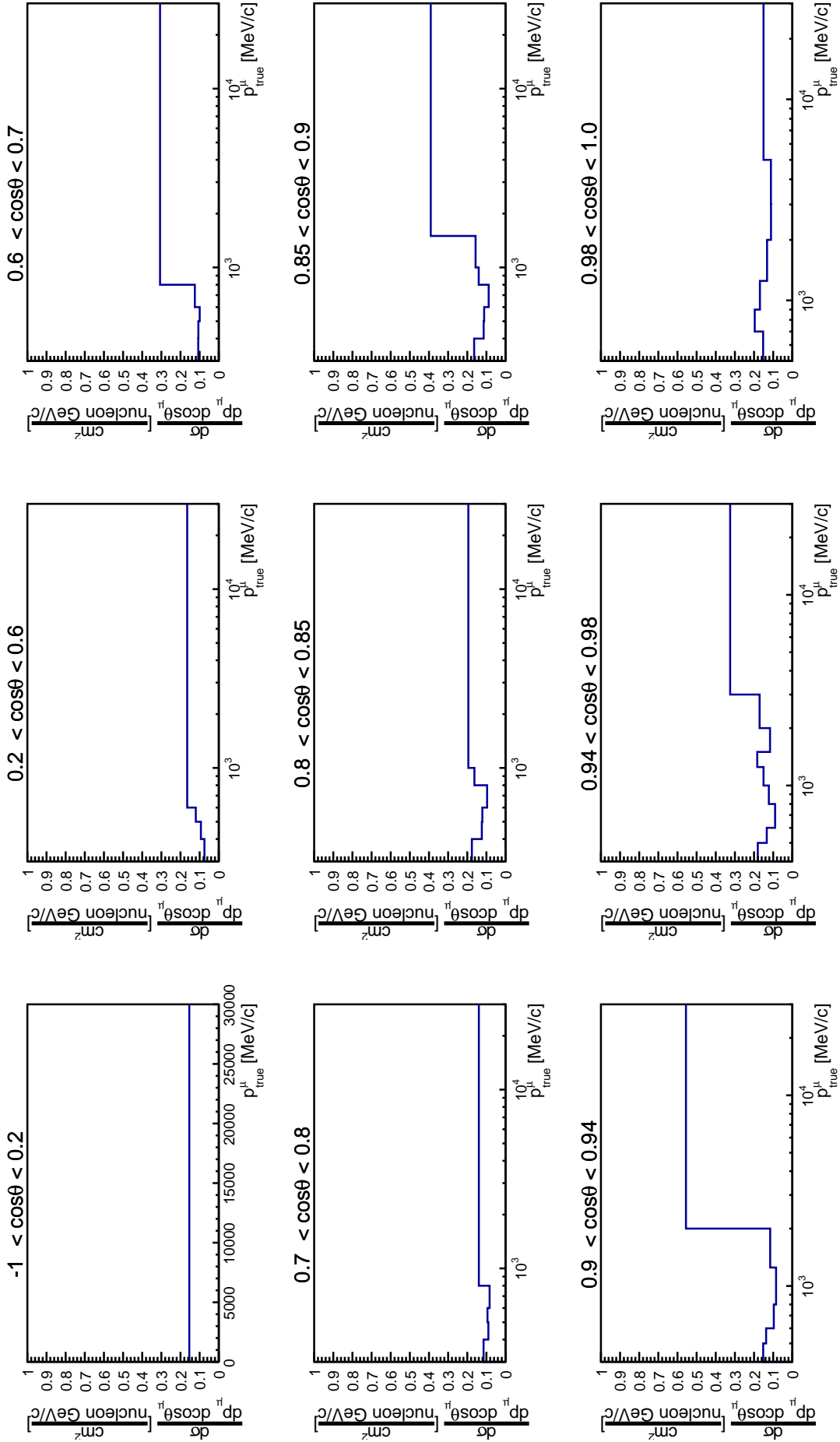


Figure 5.12: Relative uncertainty on the cross section on carbon in true muon kinematics. Each plot shows the distribution in muon momentum for a given muon angle bin.

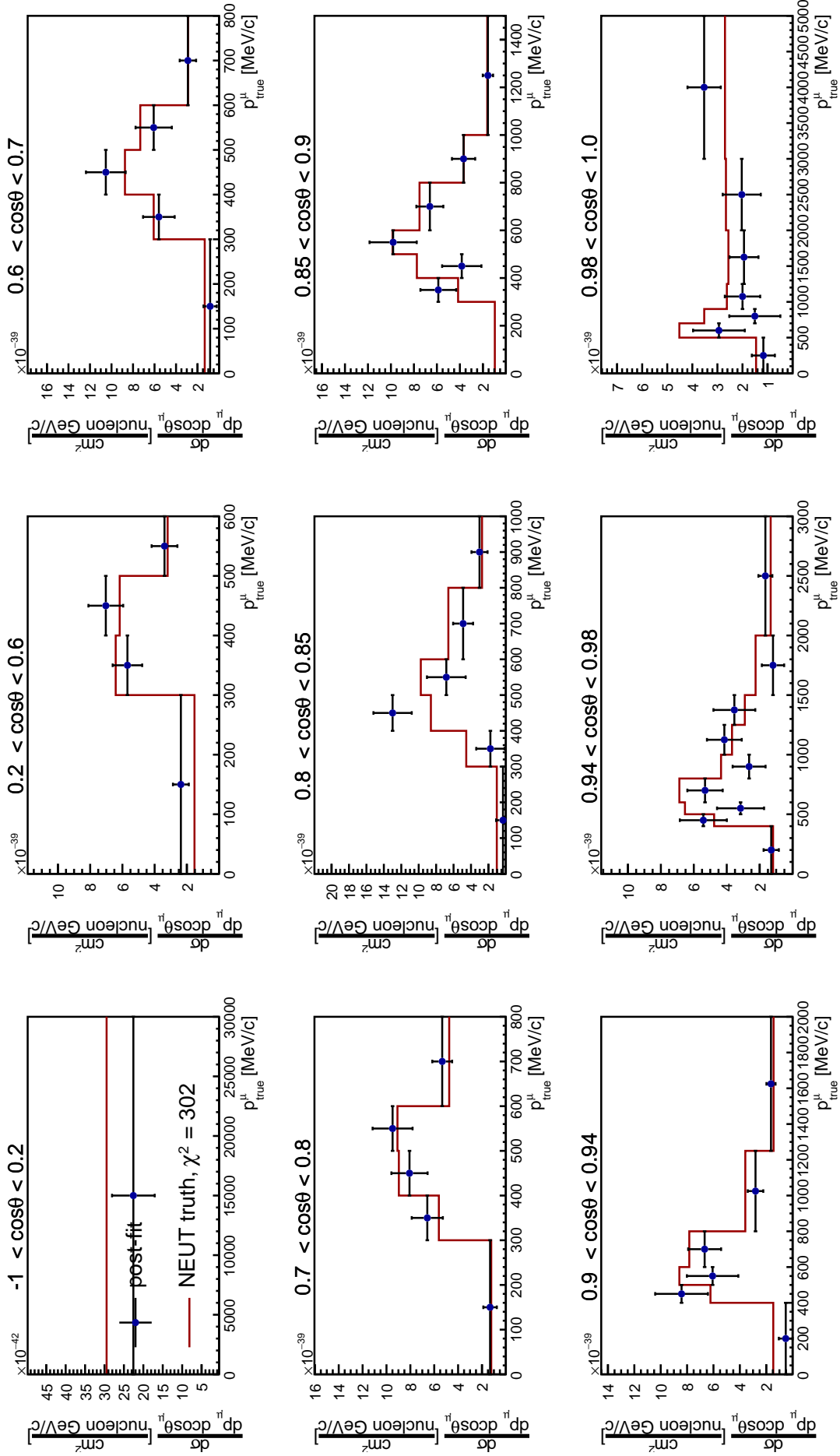


Figure 5.13: Flux integrated ν_μ cross section on oxygen in true muon kinematics. Each plot shows the distribution in muon momentum for a given muon angle bin.

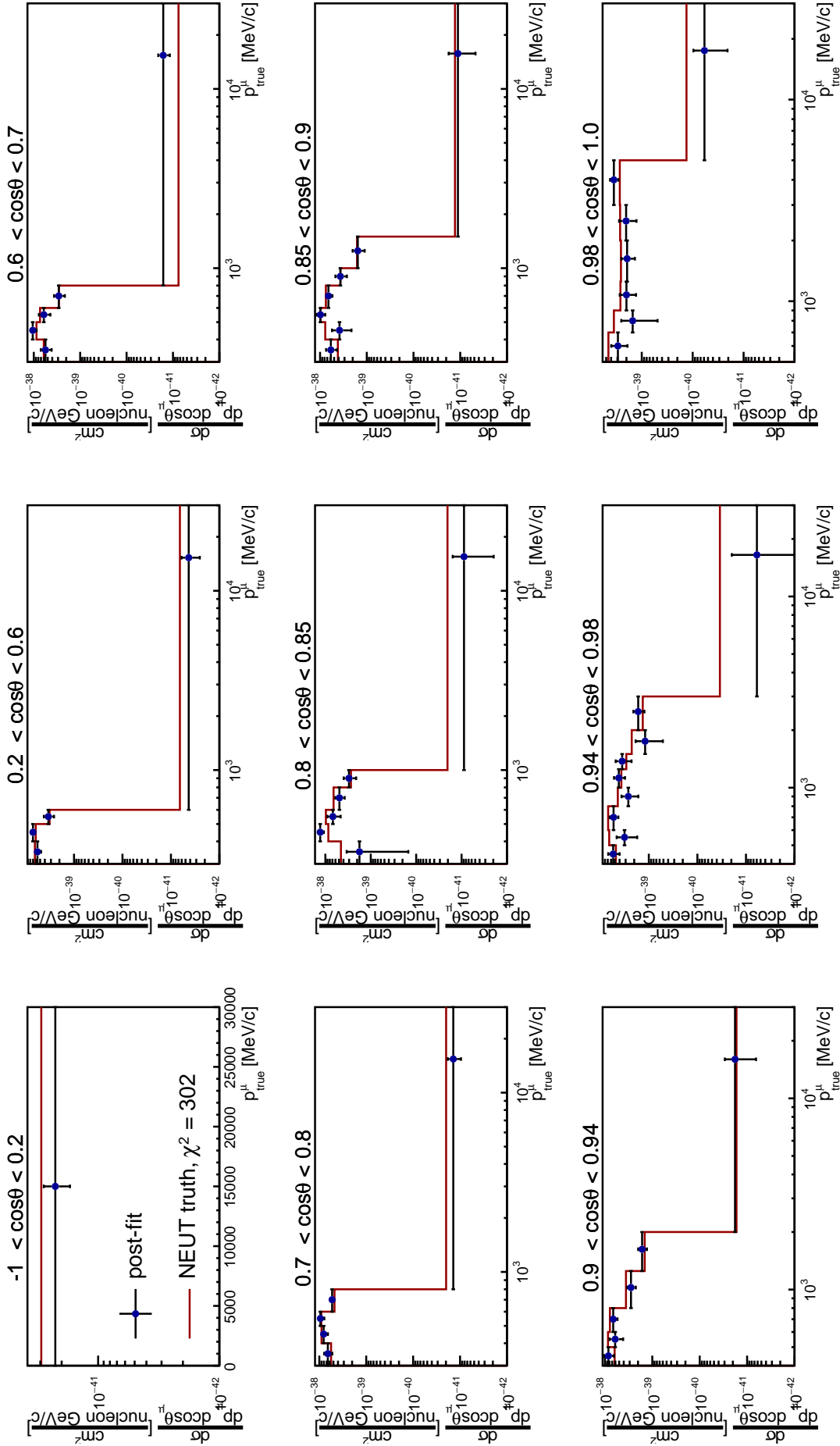


Figure 5.14: Flux integrated ν_μ cross section on oxygen in true muon kinematics in logarithmic scale including the last momentum bins. Each plot shows the distribution in muon momentum for a given muon angle bin.

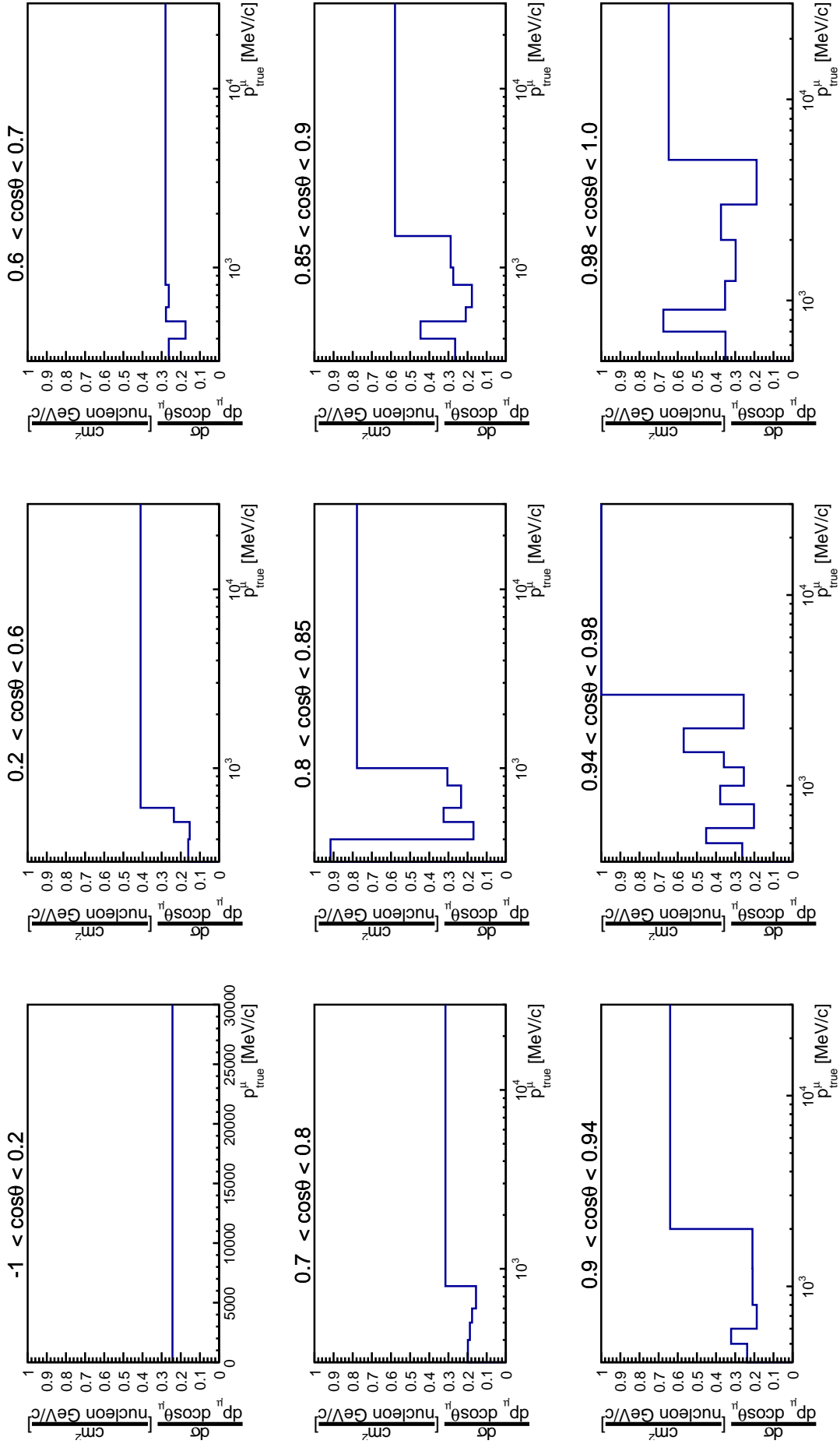


Figure 5.15: Relative uncertainty on the cross section on oxygen in true muon kinematics. Each plot shows the distribution in muon momentum for a given muon angle bin.

5. Final cross-section results

Overall the data extracted cross sections on carbon and on oxygen show a good agreement with NEUT predicted cross sections, except in the very forward-going muon region. In other regions data and Monte Carlo cross sections are compatible within the 1σ uncertainty intervals in all the bins or very close as it fluctuates a bit. In the regions of low muon angles with respect to the neutrino track ($\cos\theta_\mu$ between 0.9 and 1.0) the Monte Carlo prediction overestimates the CC- 0π cross-section on carbon and on oxygen. The discrepancy starts to be observed for $0.90 < \cos\theta_\mu < 0.94$ and $0.94 < \cos\theta_\mu < 0.98$ and becomes really clear in the last angle region $0.98 < \cos\theta_\mu < 1.0$ for both, cross sections on carbon and on oxygen. This low muon angle region corresponds to low momentum transfer (q^2), as can be seen in Figures 5.16 and 5.17 where the event distributions are drawn in true muon momentum vs. momentum transfer q^2 for carbon and oxygen interactions respectively. Lots of nuclear effects occur in this region which are not implemented in the Monte Carlo generator and therefore some physically non-allowed transitions are seen in the prediction. A similar data / MC discrepancy has been observed already in other T2K CC- 0π cross-section measurements, for instance in [127] for the cross section on carbon and in [100] for the cross section on oxygen.

The final cross-section χ^2 , evaluated according to (5.2), is equal to 302. It is large compared to the number of fitted bins (116) but the significant contribution comes from the data / MC discrepancy in the low muon angle region. This large χ^2 has to be seen as a deficit in our MC model and not as a deficit in the analysis.

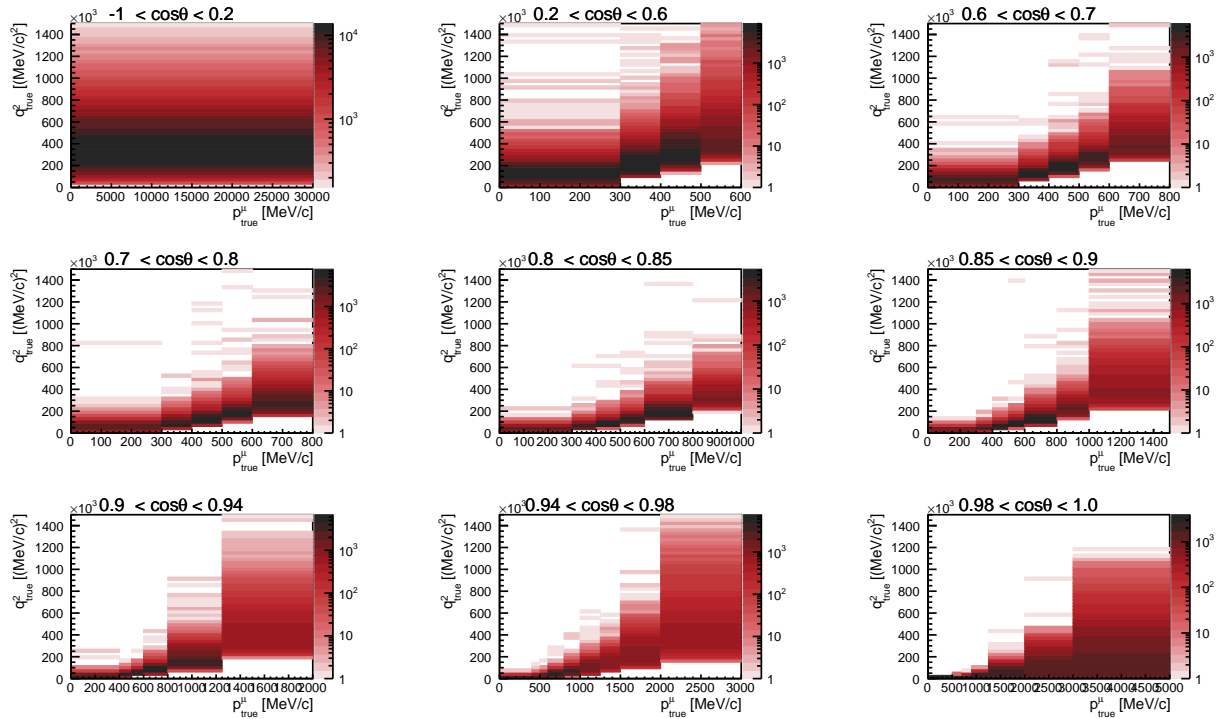


Figure 5.16: Event distributions in muon momentum and momentum transfer q^2 in each $\cos\theta_\mu$ slice for neutrino interactions with carbon. Bins in muon momentum and angle slices correspond to the analysis binning.

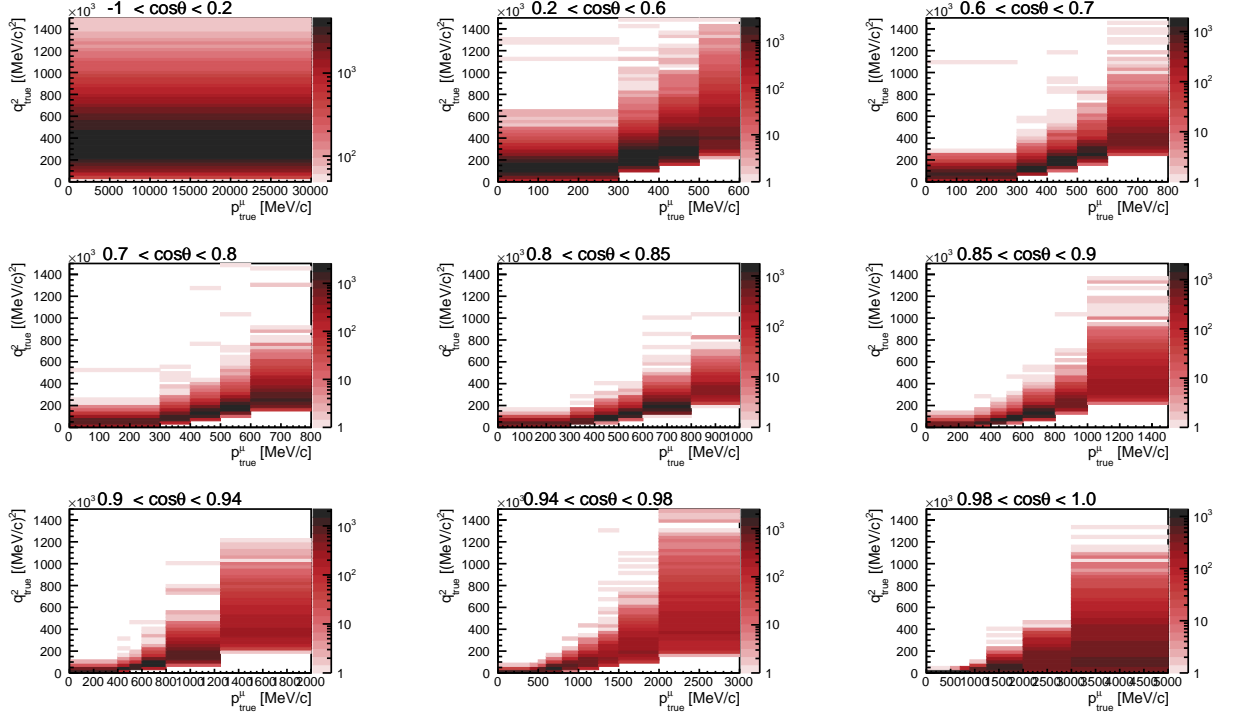


Figure 5.17: Event distributions in muon momentum and momentum transfer q^2 in each $\cos\theta_\mu$ slice for neutrino interactions with oxygen. Bins in muon momentum and angle slices correspond to the analysis binning.

The oxygen over carbon cross-section ratio in kinematic bins is evaluated according to Eq.(3.2) and the post-fit uncertainty is propagated onto the ratio with the same method than for the cross sections themselves (see Section 4.5). Data results in true kinematic bins compared to NEUT predicted values are shown in Fig. 5.18 with associated relative uncertainties in Fig. 5.19 and correlation matrix in Fig. 5.20.

While fluctuating a little bit around unity, data show a good agreement to Monte Carlo predictions. This is reflected in the low χ^2 that is equal to 39. The χ^2 probability for this value and a total of 58 bins is equal to 97%. It is interesting to remark that the ratio recovers from the effect observed in the cross sections on carbon and oxygen at low muon angles. This shows that this effect, appearing in both cross sections on carbon and oxygen, is cancelled out in their ratio and it seems to be a global effect from the Monte Carlo.

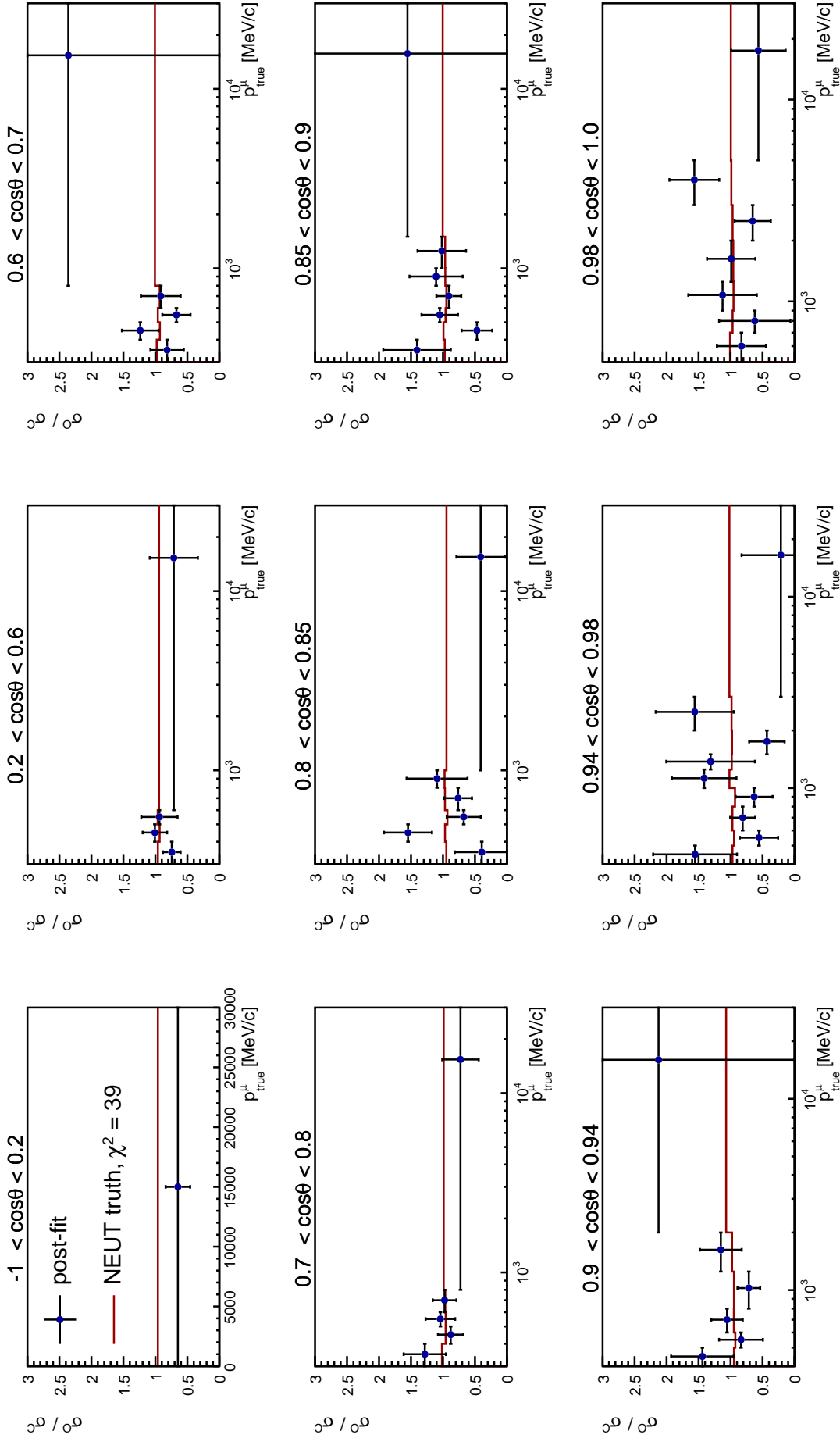


Figure 5.18: Oxygen over carbon cross-section ratio in true muon kinematics. Each plot shows the distribution in muon momentum for a given muon angle bin.

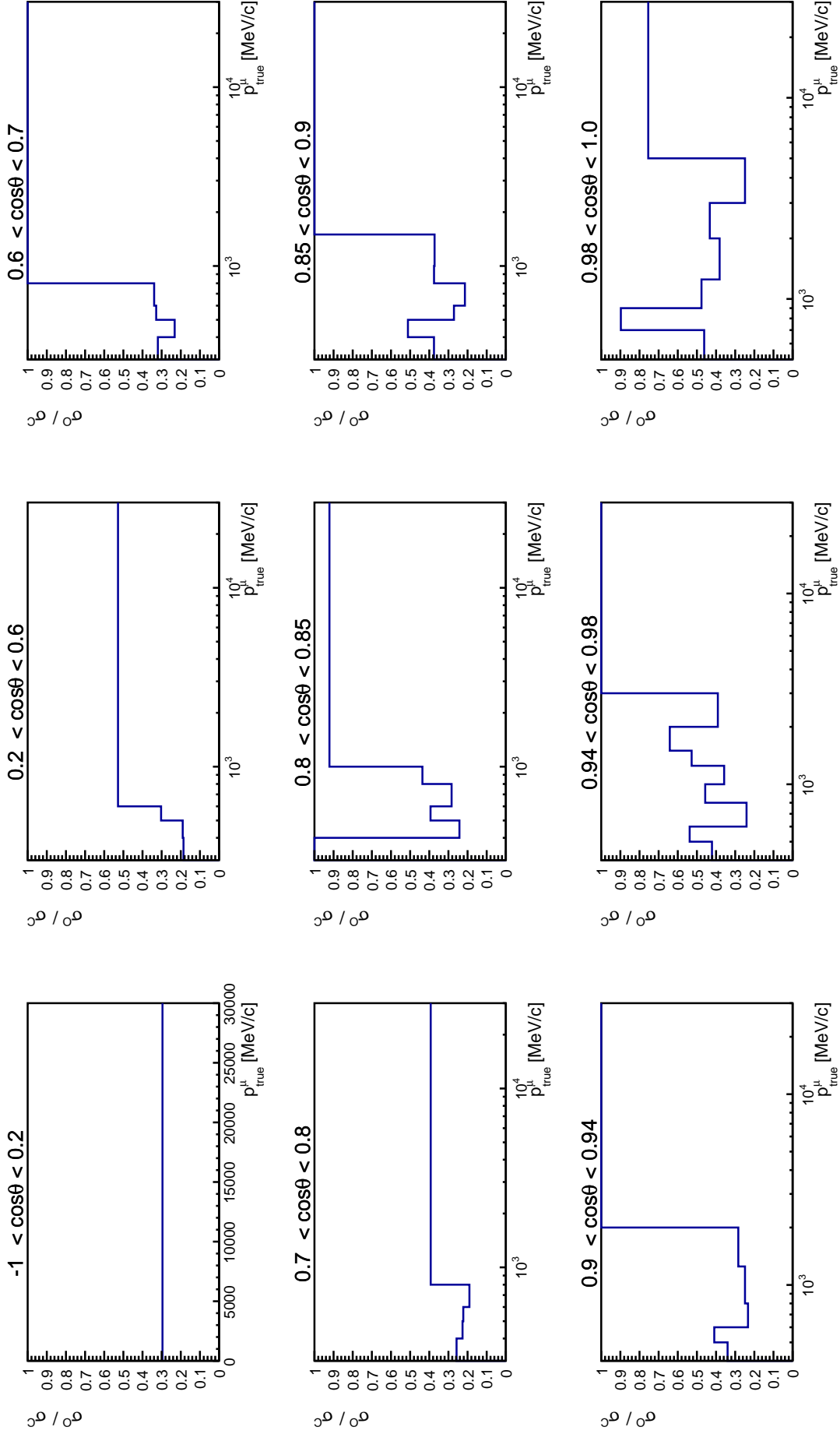


Figure 5.19: Relative uncertainty on the oxygen over carbon cross-section ratio in true muon kinematics. Each plot shows the distribution in muon momentum for a given muon angle bin.

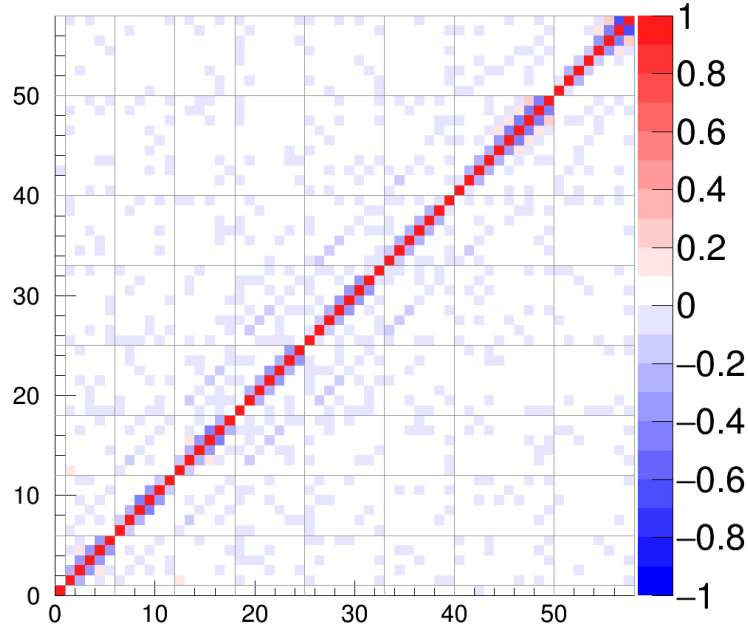


Figure 5.20: Final correlation matrix associated to the cross-section ratio measurement. The sub-matrices for the different $\cos\theta_\mu$ bins are separated by grey lines.

5.4.4 Integrated cross-section results

The total ν_μ CC- 0π cross section on carbon or oxygen is calculated by integrating the double differential cross sections presented above, that is

$$\sigma^\alpha = \sum_{i=1}^{N_{\text{bins}}} \sigma_i^\alpha \Delta p_\mu^i \Delta \cos \theta_\mu^i \quad (5.9)$$

where σ_i^α is the double differential cross section in bin i as defined in Eq.(5.4) for $\alpha = \text{C}$ or O . To evaluate the cross-section ratio we simply divide the two integrals,

$$\sigma^{\text{O}}/\sigma^{\text{C}} = \frac{\sum_{i=1}^{N_{\text{bins}}} \sigma_i^{\text{O}} \Delta p_\mu^i \Delta \cos \theta_\mu^i}{\sum_{i=1}^{N_{\text{bins}}} \sigma_i^{\text{C}} \Delta p_\mu^i \Delta \cos \theta_\mu^i} \quad (5.10)$$

and propagate the uncertainties using the covariance matrix, in order to take into account possible correlations between carbon and oxygen interactions. The obtained results with their associated total uncertainties are the following:

$$\begin{aligned} \sigma^{\text{C}} &= (0.440 \pm 0.029) \times 10^{-38} \text{ cm}^2/\text{nucleon} && \rightarrow 6.6\% \text{ error} \\ \sigma^{\text{O}} &= (0.385 \pm 0.031) \times 10^{-38} \text{ cm}^2/\text{nucleon} && \rightarrow 8.2\% \text{ error} \\ \sigma^{\text{O}}/\sigma^{\text{C}} &= 0.88 \pm 0.070 && \rightarrow 8.1\% \text{ error} \end{aligned}$$

Note that a simple error propagation from the single cross-sections onto the cross-section ratio without correlation gives an uncertainty of 0.092, meaning that the correlation affects the uncertainty and reduces it.

Table 5.5 gives an overview of CC- 0π cross-sections that have been measured with the T2K near detector ND280 and that are comparable to the cross sections extracted within this work. We have measured interactions with isolated carbon and oxygen components, whereas other

analyses have extracted cross sections on C_8H_8 or H_2O . For instance in [127] and in [123] the neutrino cross section with C_8H_8 is measured, we therefore rescale the result by a factor $13/12$, which is equal to the total number of nucleons in CH divided by the number of nucleons in a carbon atom, in order to have a relevant comparison to a result per carbon nucleon. In [100] the number of interactions per neutron in H_2O are measured, hence the result is multiplied by a factor $18/16$ (number of nucleons in H_2O over number of nucleons in O) and a factor of $8/18$ to recover an equivalent result per oxygen nucleon.

Table 5.5: Cross-section results from this analysis compared to other T2K cross-section measurements and to Monte Carlo predictions. Results from other analyses have been re-normalised to the number of target nucleons on C and O respectively in order to make them comparable to the results presented in this analysis.

CC-0 π cross section	$\sigma^{\text{C}}[10^{-38} \text{ cm}^2/\text{nucleon}]$	$\sigma^{\text{O}}[10^{-38} \text{ cm}^2/\text{nucleon}]$	$\sigma^{\text{O}}/\sigma^{\text{C}}$
Present analysis	0.440 ± 0.029	0.385 ± 0.031	0.88 ± 0.070
In paper [127]	0.452 ± 0.051	—	—
In T2K-TN-337 [123]	0.466 ± 0.033	—	—
In T2K-TN-338 [114]	0.474 ± 0.072	0.528 ± 0.060	1.12 ± 0.08
In T2K-TN-305 [128]	—	—	0.93 ± 0.070
NEUT 5.3.2	0.436	0.422	0.97
GENIE 2.8.0	0.374	0.385	1.03

The CC-0 π cross-section on carbon shows a good agreement with the NEUT prediction and the measured value is compatible with other T2K measurement within a 1σ uncertainty interval. On the other hand the cross-section on oxygen is a bit low compared to predictions and the other measured value. It therefore affects the oxygen over carbon cross-section ratio, which is lower as expected too. After investigating the integral it appears that the first bin, containing the full momentum range for backward and high-angle tracks ($-1.0 < \cos \theta_\mu < 0.2$), has a cross section on oxygen that is lower than predicted. This bin gives a significant contribution to the integrated cross sections (about 20%) as it has a very large width. This is a kinematic region in which not only we do not trust very much the reconstruction and with a poor efficiency (about $\sim 10\%$, see Figures 3.18 and 3.19), but also most of the bin content comes from high-angle track contribution, as can be seen in the right plots of Fig. 3.17. Therefore it is worth looking at the measurement over a restricted phase space removing this bin.

Moreover it is surprising that the uncertainties on measurements on carbon and on oxygen are so close. Roughly, events with interactions on carbon make up $3/4$ of the total number of events whereas events on oxygen make up $1/4$ of the total event statistics. We would expect the ratio of the statistical uncertainties to be about $\sqrt{1/3} \approx 0.6$, but the obtained ratio is 0.94. Such similar uncertainties were not to be observed in the differential cross sections. We will see how the uncertainty ratio is affected by restraining the phase space and discuss other factors affecting the uncertainty difference between carbon and oxygen.

5.4.5 Integrated cross-section results in restricted phase space

The first bin covers the full momentum space for an also large cosine angle range, $-1.0 < \cos \theta_\mu < 0.2$. It gives a large contribution to the integral over the kinematic variables, whereas it does not provide a physically sensitive measurement. It is interesting to evaluate the total cross sections and the oxygen over carbon cross-section ratio removing this bin. The integrated cross

5. Final cross-section results

sections and their ratio over this restricted phase space yield

$$\begin{aligned}
\sigma^C(\cos \theta_\mu > 0.2) &= (0.314 \pm 0.016) \times 10^{-38} \text{ cm}^2/\text{nucleon} && \rightarrow 5.2\% \text{ error} \\
\sigma^O(\cos \theta_\mu > 0.2) &= (0.303 \pm 0.020) \times 10^{-38} \text{ cm}^2/\text{nucleon} && \rightarrow 6.4\% \text{ error} \\
\sigma^O/\sigma^C(\cos \theta_\mu > 0.2) &= 0.97 \pm 0.045 && \rightarrow 4.7\% \text{ error}
\end{aligned}$$

Table 5.6 shows these results compared to a published T2K measurement in $\cos \theta_\mu > 0.0$ and Monte Carlo predictions.

Table 5.6: Results of the cross-section integrated over a restricted angular space from this analysis compared to another T2K cross-section measurements and to Monte Carlo predictions. The result from the other analysis has been re-normalised to the number of target nucleons O in order to make it comparable to the results presented in this analysis. However, its phase-space restriction remains different from ours.

CC-0 π cross section	$\sigma^C[10^{-38} \text{ cm}^2/\text{nucleon}]$	$\sigma^O[10^{-38} \text{ cm}^2/\text{nucleon}]$	σ^O/σ^C
Present analysis ($\cos \theta_\mu > 0.2$)	0.314 ± 0.016	0.303 ± 0.020	0.97 ± 0.045
In paper [100] ($\cos \theta_\mu > 0$)	—	0.475 ± 0.067	—
NEUT 5.3.2 ($\cos \theta_\mu > 0.2$)	0.326	0.316	0.97
GENIE 2.8.0 ($\cos \theta_\mu > 0.2$)	0.281	0.288	1.03

The first thing we observe in the restricted phase space is the dramatic reduction of uncertainties. The relative uncertainties on the integrated cross sections is lowered by about 20% and on the cross-section ratio by a bit more than 40%. The two extracted cross sections are compatible with NEUT Monte Carlo predicted values in the 1σ uncertainty interval. A proper comparison with the value measured in [100] is not easy as the phase space is not exactly the same. We also observe that the cross-section ratio for $\cos \theta_\mu > 0.2$ is compatible with other results and predictions within the 1σ uncertainty interval. Moreover, the ratio of oxygen to carbon uncertainties is equal to 0.8, showing an improvement compared to the value obtained in the full phase space. However, this is still higher than the value of ~ 0.6 expected for the statistics that are used. Investigations showed that the expected difference is recovered if the uncertainty is evaluated without taking correlations into account, thus indicating that correlations affect differently the carbon and oxygen cross-section uncertainties.

Conclusion and future prospects

This work details charged-current muon neutrino interactions with carbon and oxygen nucleons with no pion in the final state measured with the T2K near detector ND280. Double differential cross sections in outgoing muon kinematics have been extracted, as well as the oxygen over carbon cross-section ratio, by performing a binned likelihood fit.

The differential CC- 0π cross sections on carbon and on oxygen nuclei both showed an excess of the Monte Carlo prediction compared to the data extracted quantities in the region of forward-going muons (low muon angle with respect to the neutrino track). This is a region of low momentum transfer (q^2) where nuclear interactions are not well modelled in the MC event generator, therefore this effect is not really surprising. Moreover, such effect has been already observed in previous T2K measurements [127, 100]. It is interesting to see that the discrepancy in these low muon angle regions is cancelled out in the oxygen over carbon cross-section ratio, showing that it is affecting both cross sections similarly. In other muon angle regions the measured cross sections agree with predictions within the 1σ uncertainty intervals, although it fluctuates slightly due to event migration between adjacent muon momentum bins.

The integrated cross sections over the full muon kinematics phase space has also been evaluated. The measured muon neutrino CC- 0π cross section on carbon is $\sigma^C = (0.440 \pm 0.029) \times 10^{-38} \text{ cm}^2/\text{nucleon}$ and it is compatible with other T2K measurements and with Monte Carlo predictions within the 1σ uncertainty interval. The extracted cross section on oxygen, $\sigma^O = (0.385 \pm 0.031) \times 10^{-38} \text{ cm}^2/\text{nucleon}$, however, does not show a good agreement with other measurements as it underestimates the total cross section. The total oxygen over carbon cross-section ratio is therefore lower than expected as well, $\sigma^O/\sigma^C = 0.88 \pm 0.070$. In the ratio by bin there is not a region where the deficit is visible. Since the first bin is problematic this might be the cause of the oxygen deficit.

We have also evaluated the integrated cross sections over a restricted phase space, removing the bin containing events with backward and high-angle muon tracks ($-1.0 < \cos \theta_\mu < 0.2$), as this bins gives a large contribution to the total cross sections and the detector is not optimised to reconstruct tracks in this region. It results in a strong reduction of the uncertainties and the oxygen over carbon cross-section ratio recovers a value compatible with other results and Monte Carlo predictions, $\sigma^O/\sigma^C(\cos \theta_\mu > 0.2) = 0.97 \pm 0.045$. The integrated cross sections over a restricted cosine muon angle range are evaluated as $\sigma^C(\cos \theta_\mu > 0.2) = (0.314 \pm 0.016) \times 10^{-38} \text{ cm}^2/\text{nucleon}$ and $\sigma^O(\cos \theta_\mu > 0.2) = (0.303 \pm 0.020) \times 10^{-38} \text{ cm}^2/\text{nucleon}$. It is very interesting to see that a precision of 4.7% was achieved on the cross-section ratio, thus almost reaching a sensitivity that would be able to probe the difference in carbon and oxygen cross sections.

Since the statistical uncertainty dominates, improvements in the precision are expected in

5. Final cross-section results

the future as T2K continues data taking. Moreover the near detector and neutrino beam are going to be upgraded in the upcoming years. 30×10^{20} POT are expected per year, by 2030 we expect to reach about almost 5 times today's integrated POT, thus reducing the statistical uncertainty by a factor ~ 2 . The ND280 upgrade is going to decrease systematic uncertainties but the contribution to carbon and oxygen cross sections is difficult to estimate.

Further improvements could be achieved by giving the fit some freedom to control the proton kinematics, which is not allowed in the currently used fitter. This could be done by adding extra normalisation parameters associated to each sample in order to allow event migration among the signal samples that have different proton topologies.

Vertex backward migration in FGD2

A.1 Introduction

Backward migration is the phenomenon of reconstructing the vertex upstream from its true position, i.e. the true vertex is located in layer N^{true} and reconstructed upstream, i.e. in layer $N^{\text{reco}} < N^{\text{true}}$. Two examples are represented on Fig.A.1 and Fig.A.2 shows the distributions of the difference between the true and reconstructed vertex, that is $N^{\text{true}} - N^{\text{reco}}$. A tail can be observed in the positive values, that correspond to the case of backward migration. This migration induces a bias in the momentum, as can be seen on Fig.A.3, which is treated as a detector systematics through dE/dx [122]. A major consequence for analyses based on X and Y layer separation is the impact on the sample definition, since oxygen interactions are mainly reconstructed in X layers. In this note we study this effect and evaluate the systematical uncertainty due to it.

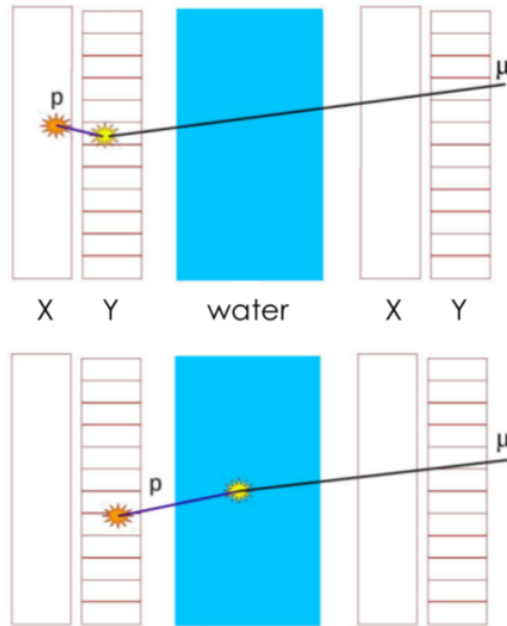


Figure A.1: Examples of backward migration in the FGD2 layers.

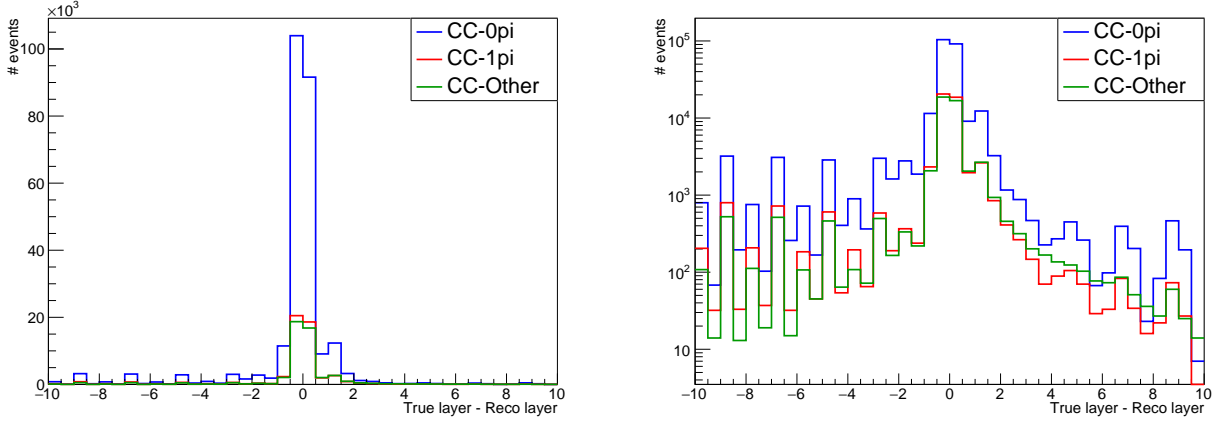


Figure A.2: Distribution of the difference between true and reconstructed layers for the different samples, in linear scale on the left and in logarithmic scale on the right. A difference larger than zero corresponds to a backward migrated tracks (in the case of forward going tracks). A difference of 0.5 (-0.5) corresponds to a true vertex in a water layer that is reconstructed in the y layer upstream (in the x layer downstream).

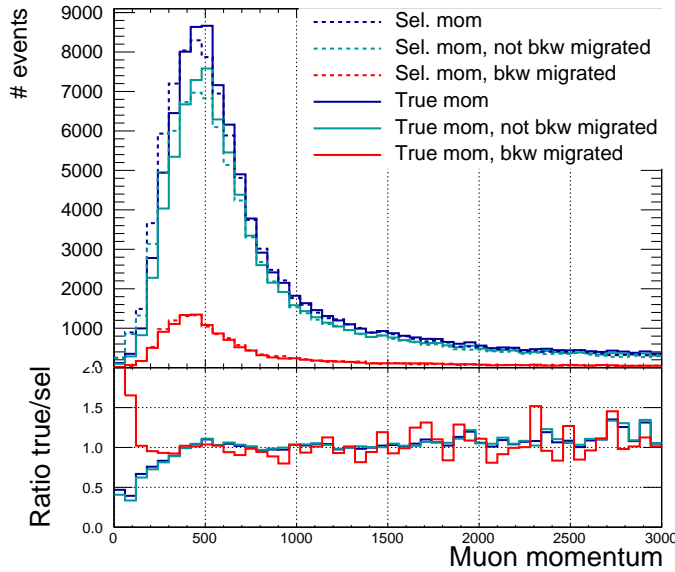


Figure A.3: Comparison of the selected (dashed) and true (solid) muon momentum for all tracks (blue) and for the backward migrated (red) and non-backward migrated (turquoise) contributions in the CC- 0π sample.

A.2 Fit strategy

In order to estimate the uncertainty on the number of backward migrated tracks, we fit the MC fractions of backward migrated and non-backward migrated tracks to the data.

A.2.1 Selection and samples

The selection used in these studies is not *exactly* the same selection used for the cross-section extraction related in the main part of this document. For the purpose of this backward migration

analysis multi- π samples were required. Three samples are selected in FGD2 according to the multi- π topologies, i.e. CC-0 π , CC-1 π and CC-Other with following cuts :

1. Event quality
2. > 0 tracks
3. Quality + fiducial
4. Veto
5. External FGD1 / FGD2
6. Muon PID
7. CC-0 π / CC-1 π / CC-Other

A dedicated package has been created in **Highland2**¹. This selection is also available for FGD1. Samples are produced using data accumulated during run periods 2, 3 and 4 and as for the cross-section extraction NEUT production 6B (96.89²⁰ POT) and production 6M for Data (5.97²⁰ POT) are used.

Table A.1 shows the fractions of backward migrated tracks in the analysis samples of the ν_μ CC-0 π selection.

Table A.1: Fractions of backward migrated and non-backward migrated tracks in the different analysis samples of the ν_μ CC-0 π selection.

Analysis samples	Content	Backward migrated	Not migrated
Signal 1	muTPC muTPC + Np	0.078	0.922
Signal 2	muTPC + pTPC	0.111	0.889
Signal 3	muTPC + pFGD	0.050	0.950
Signal 4	muFGD + pTPC muFGD + pTPC + Np	0.126	0.874
Signal 5	muFGD muFGD + Np	0.141	0.859
Total signal	CC-0 π	0.087	0.913
Sideband 1	CC-1 π^+	0.070	0.930
Sideband 2	CC-Other	0.111	0.889
Sideband 3	CC Michel e $^-$	0.111	0.889

A.2.2 Variables used

To have information about backward migration we use the muon first and second hit variables, that are the following :

- `selmu_1hit_deltapos` :
distance between the 1st hit and the fit position in the Z layer of the 1st hit.
- `selmu_2hit_deltapos` :
distance between the 2nd hit and the fit position in the Z layer of the 2nd hit.

¹nd280Highland2 v2r29 was used and the package can be found under `highland2Systematics/fgdBwdMigrationSystematics (v0r0)`

- `selmu_1hit_charge` :
deposited charge by the closest hit to the reconstructed vertex.
- `selmu_2hit_charge` :
deposited charge by the 2nd closest hit to the reconstructed vertex.

Two methods have been tried to define the fit position. In the first one we approximate the track with a straight line between the start and end points of the reconstructed track. In the second one we use the start point and the direction of the track at that point. We decide to keep the second method since it makes more sense as the muon track can curve and we are interested in the start only. A more detailed description and a comparison of the results are shown in appendix of the T2K-TN-368 [115].

The MC and data distributions of the variables, normalised to the data POT, are shown in Fig.A.4, A.5 and A.6 with their data/MC ratio. Distributions normalised by the area are shown in Fig.A.7, A.8 and A.9 for the three different samples respectively.

As can be seen on the normalised plots A.7, A.8 and A.9, only the 1st hit Δ position shows a significant difference in shape between the two contributions, backward migrated / not-backward migrated. We also look at two-dimensional distributions that carry more information, combining two variables. The differences in shapes is more relevant and one gets more sensitivity on backward migrated events. The 2D histograms are shown on Fig.A.10, A.11 and A.12.

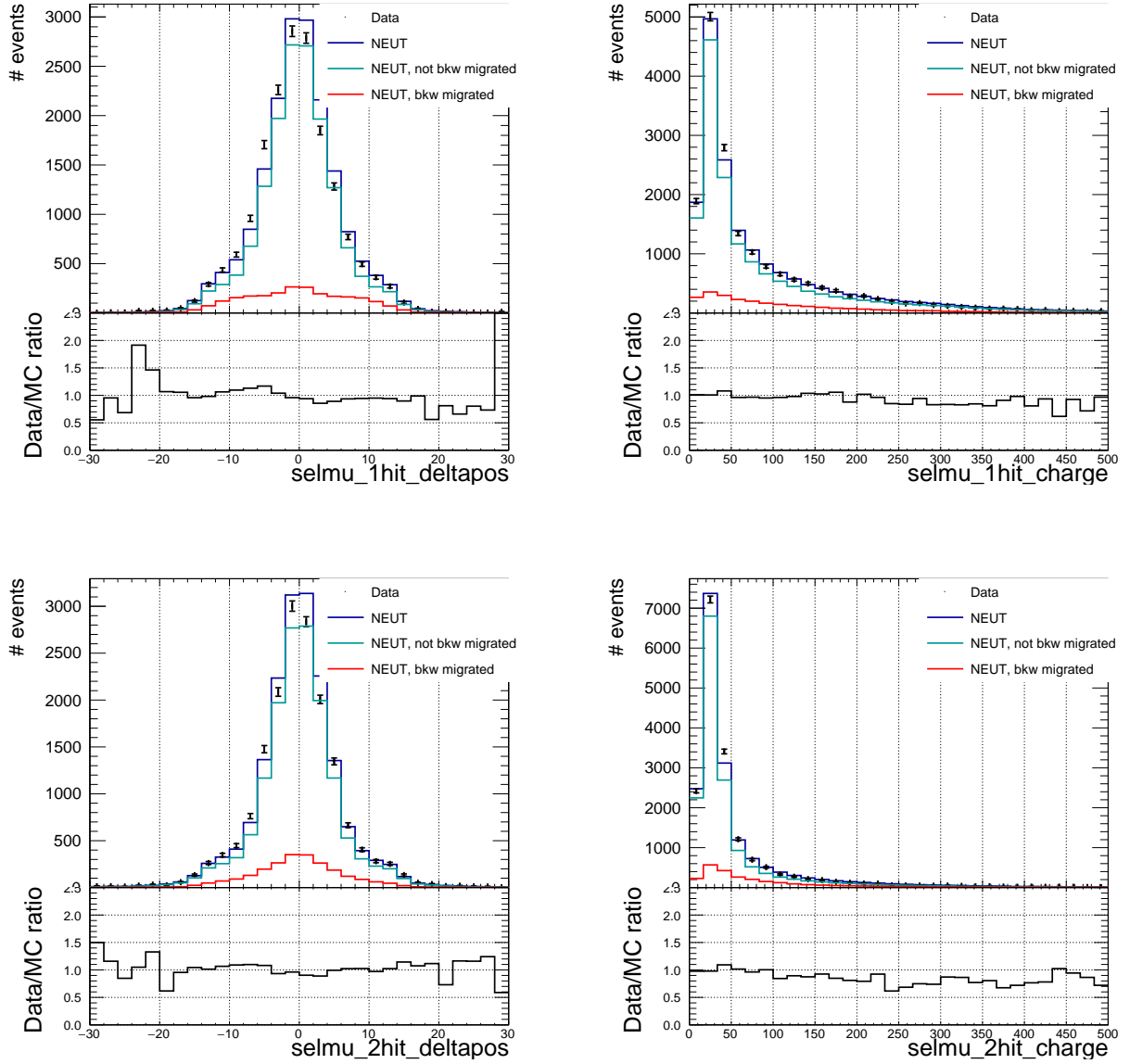


Figure A.4: Distribution of the muon first hit (top) and second hit (bottom) Δ positions (left) and charge (right) in the CC-0 π selection, normalised by data POT. On the bottom of each plot, the ratio between real data and MC number of events is shown.

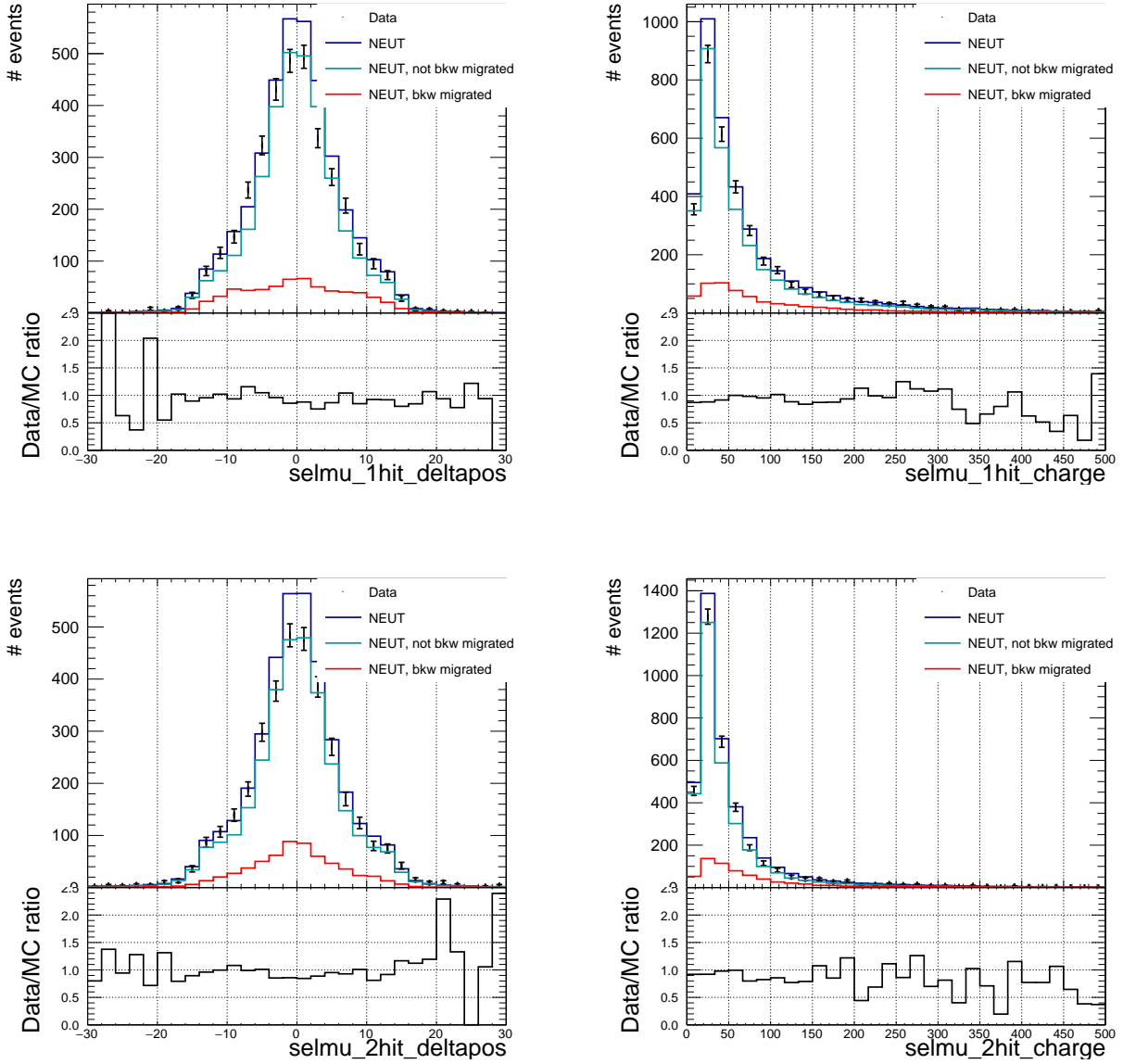


Figure A.5: Distribution of the muon first hit (top) and second hit (bottom) Δ positions (left) and charge (right) in the CC- $1\pi^+$ selection, normalised by data POT. On the bottom of each plot, the ratio between real data and MC number of events is shown.

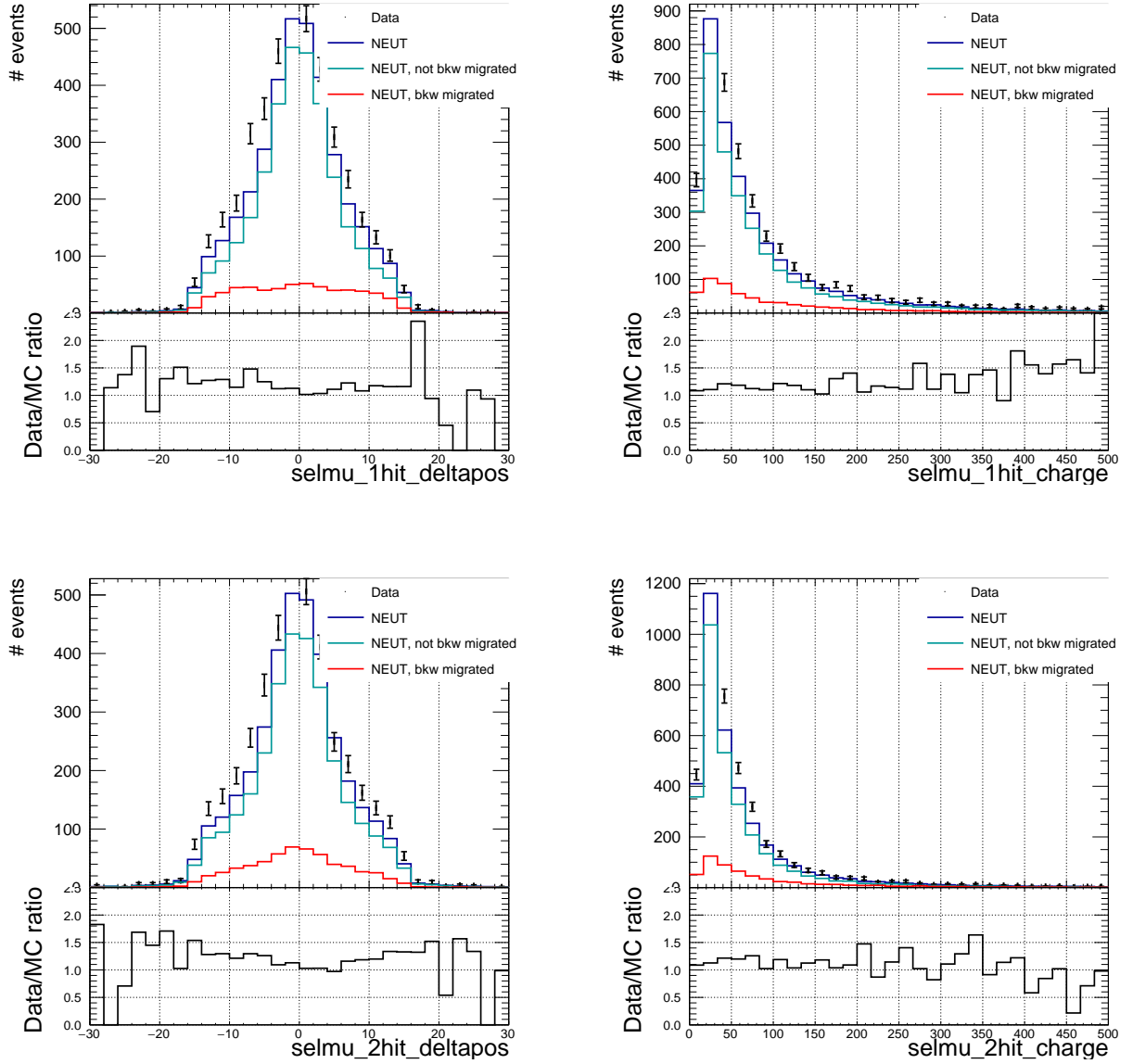


Figure A.6: Distribution of the muon first hit (top) and second hit (bottom) Δ positions (left) and charge (right) in the CC-Other selection, normalised by data POT. On the bottom of each plot, the ratio between real data and MC number of events is shown.

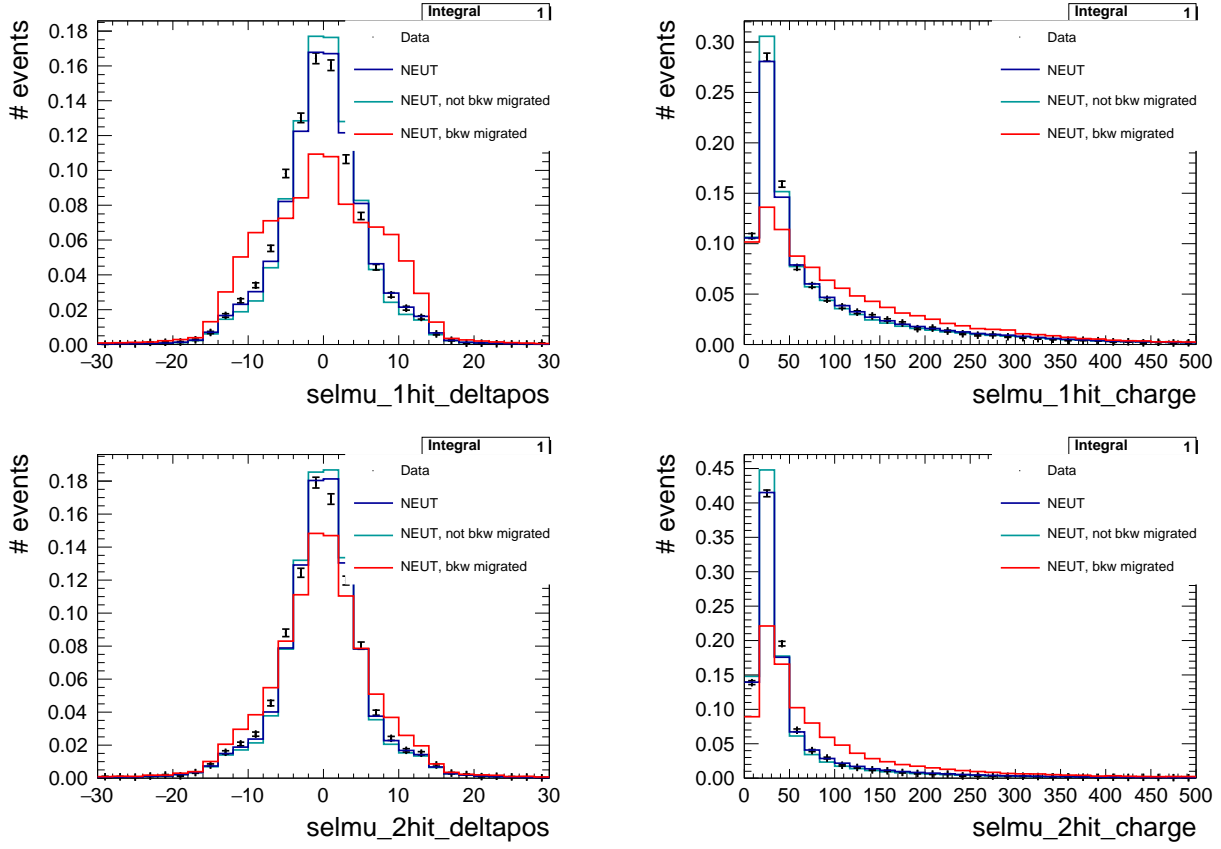


Figure A.7: Distribution of the muon first hit (top) and second hit (bottom) Δ positions (left) and charge (right) in the CC-0 π selection. Distributions are normalised by the area.

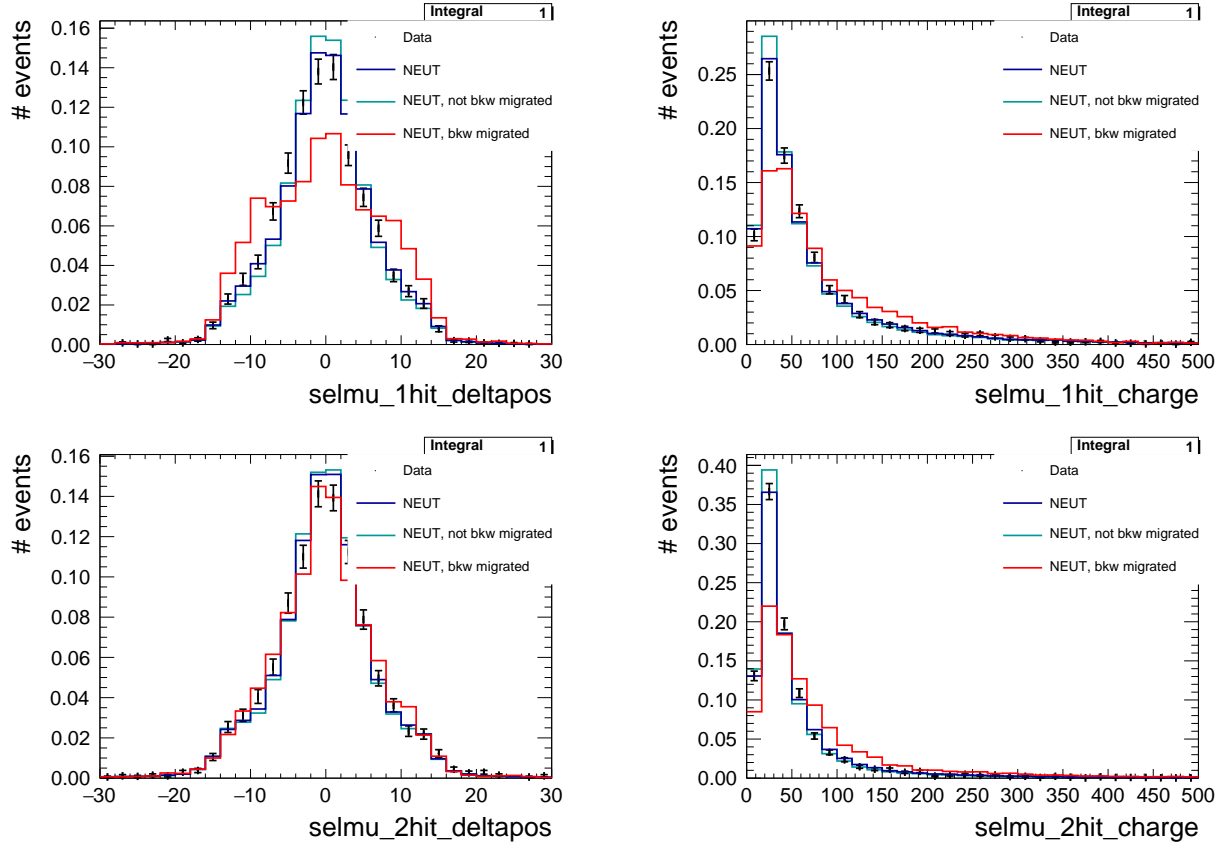


Figure A.8: Distribution of the muon first hit (top) and second hit (bottom) Δ positions (left) and charge (right) in the CC-1 π^+ selection. Distributions are normalised by the area.

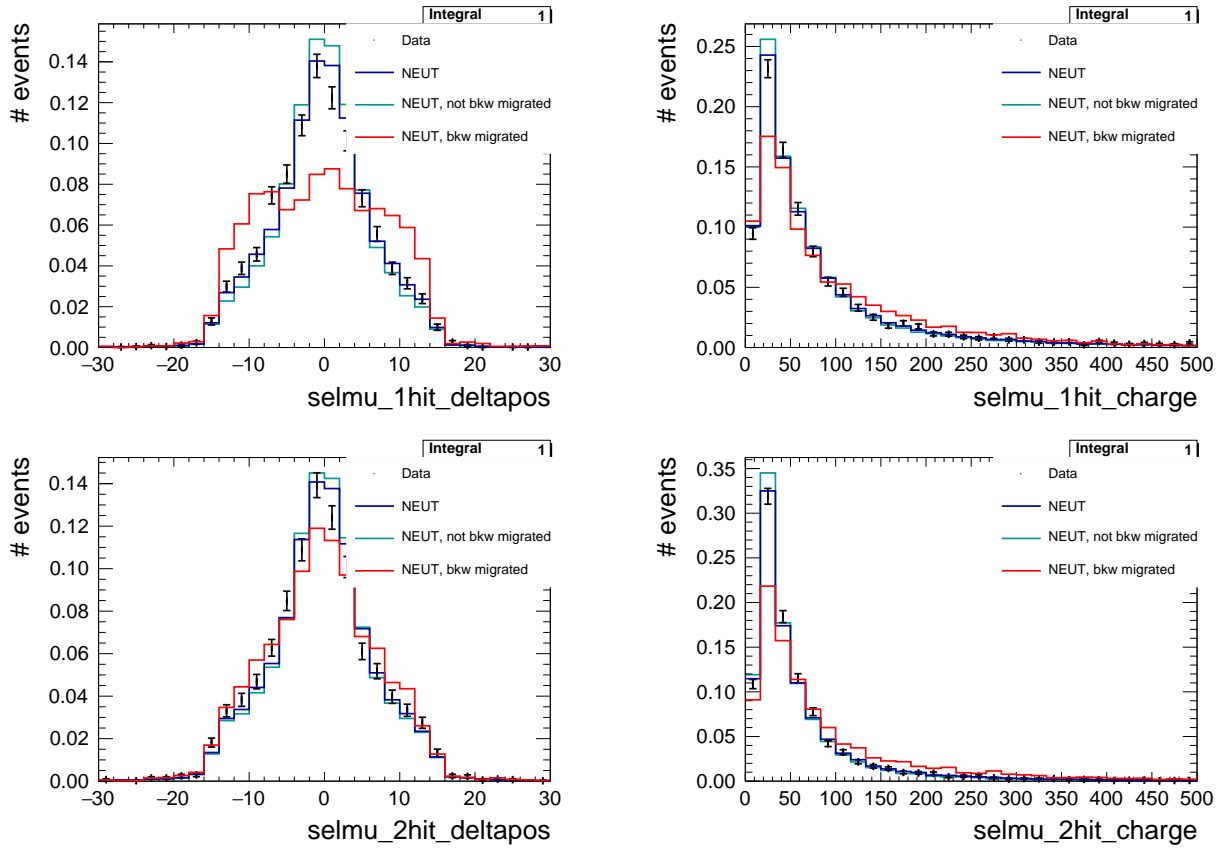


Figure A.9: Distribution of the muon first hit (top) and second hit (bottom) Δ positions (left) and charge (right) in the CC-Other selection. Distributions are normalised by the area.

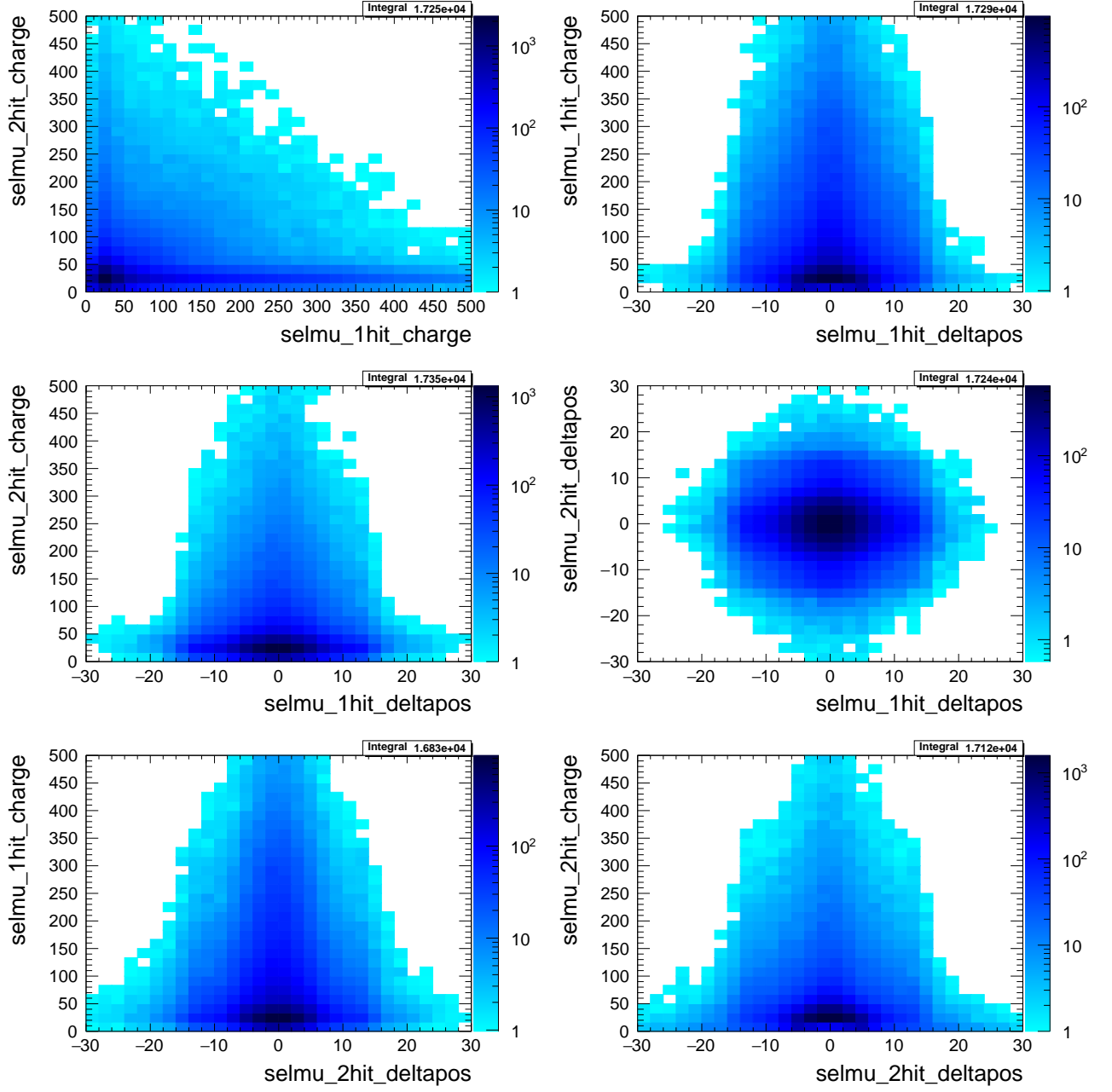


Figure A.10: Two-dimensional MC NEUT distributions of the different variable combinations for CC-0 π .

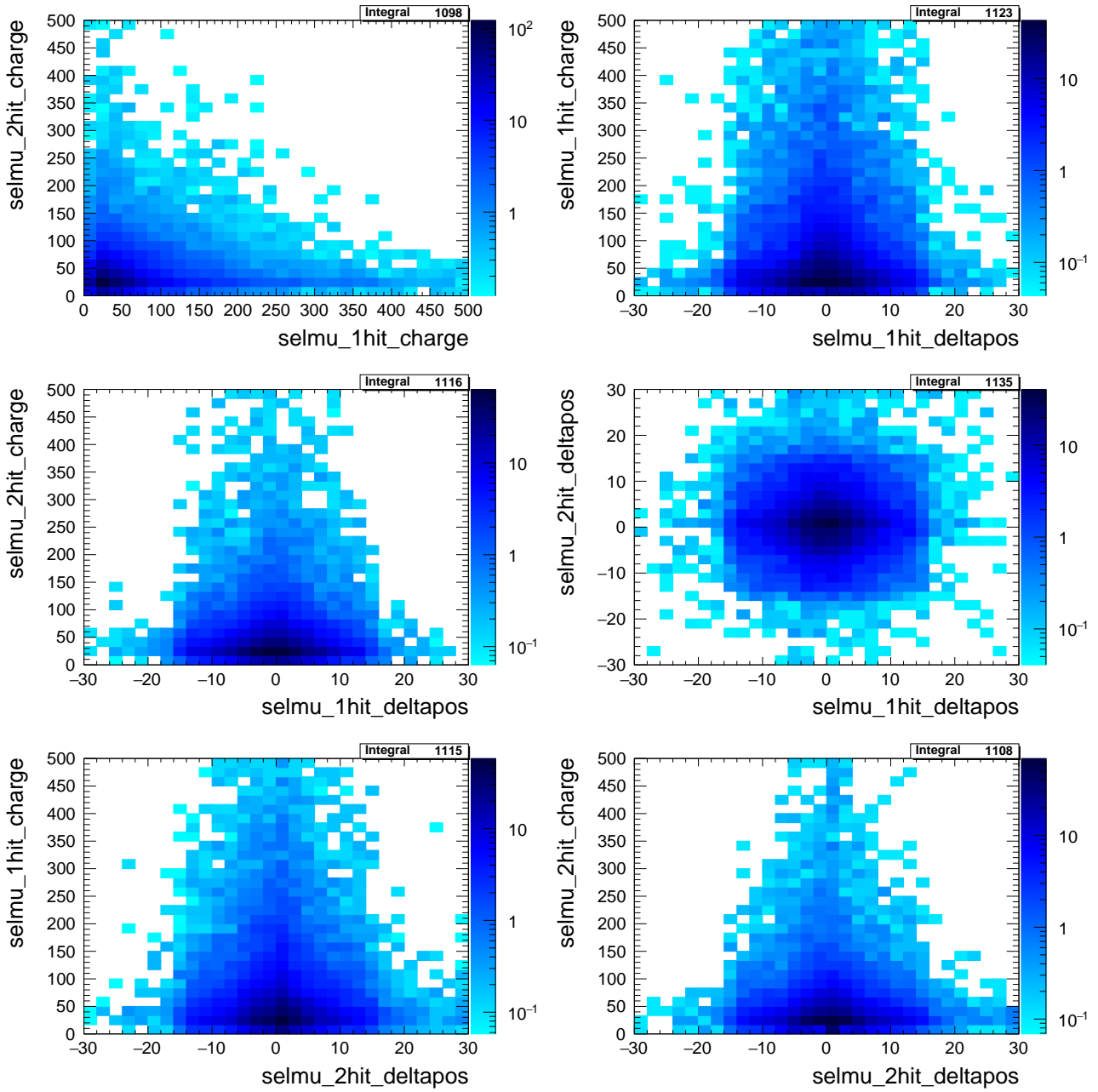


Figure A.11: Two-dimensional MC NEUT distributions of the different variable combinations for CC-1 π^+ .

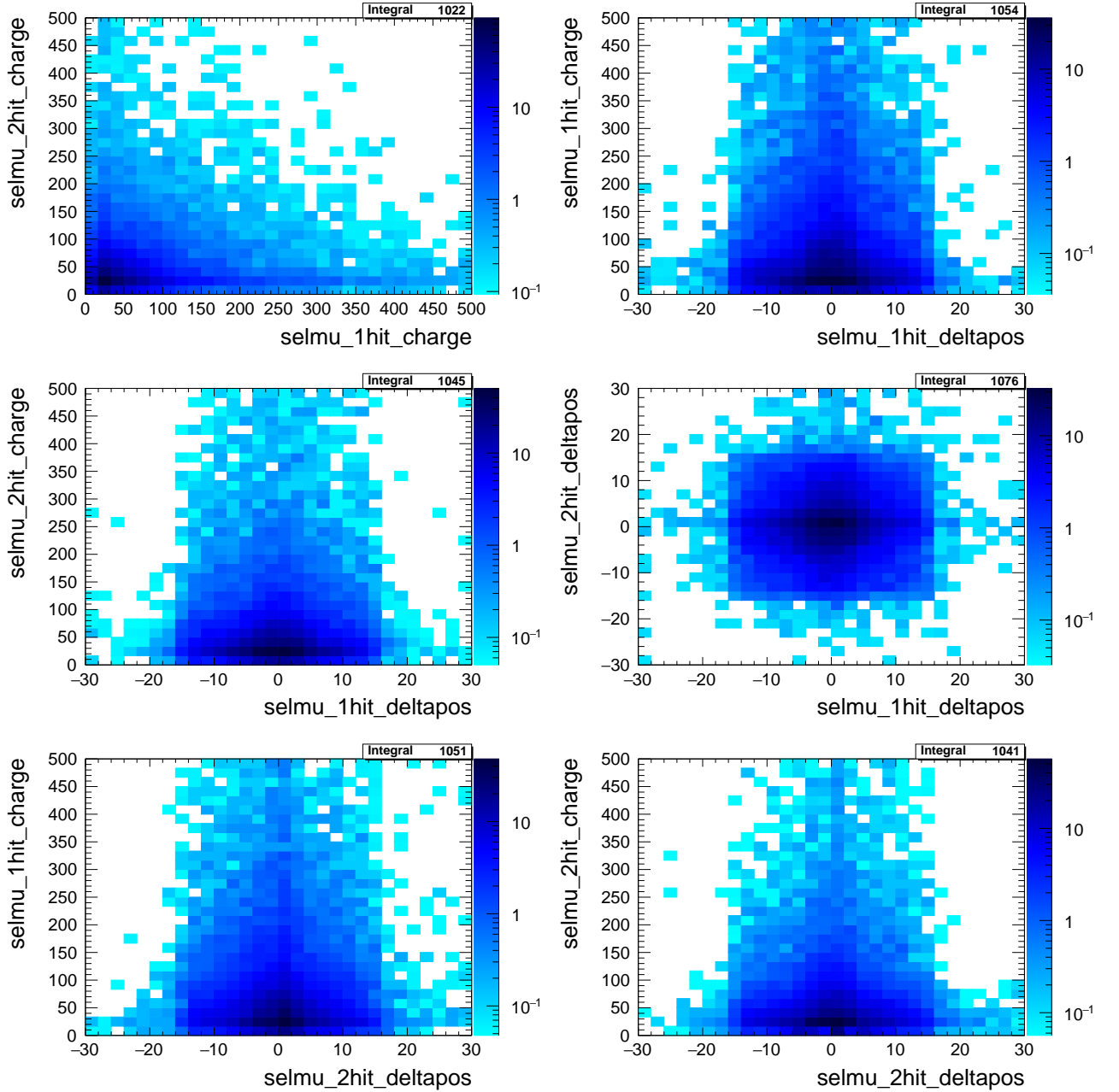


Figure A.12: Two-dimensional MC NEUT distributions of the different variable combinations for CC-Other.

A.2.3 Sensitivity to backward migration

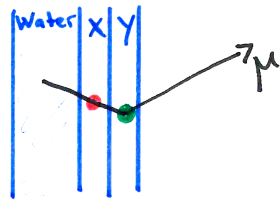
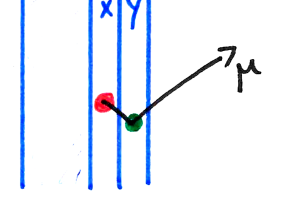
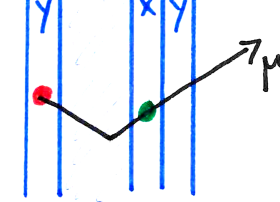
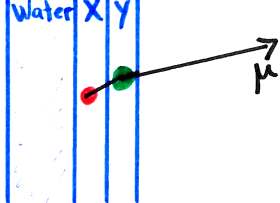
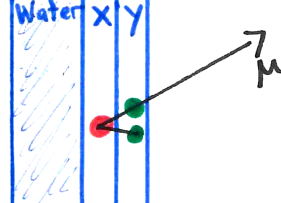
As written in the previous section, the normalised plots A.7, A.8 and A.9 show that only the 1st hit Δ position has a significant difference in shape between the two contributions. We would like to look at the different types of tracks that are selected as backward migrated and the kind of contributions they have to the four variables. A schematic representation of the different tracks and the associated expected behaviour of the variables is summarised in Table A.2.

We consider two-dimensional distributions and look at the projection of some slices from the two-dimensional histograms. This way we can have a look at how the shapes of the contributions in the Δ position vary for different regions of the deposited charge.

We first look for the correlations between 1st hit Δ position and 1st hit charge. In Fig.A.13, we observe that the shapes of the two contributions in the 1st hit Δ position have significant

A. Vertex backward migration in FGD2

Table A.2: Different types of tracks that are selected as backward migrated and expected behaviour of the variables. In case (a) the true vertex is located in layer y, the backward going particle stops in the water layer where lot of energy is deposited and not seen ; the first hit is reconstructed in layer x. In case (b) the true vertex is located in layer y as well but the backward going particle stops in layer x, depositing a lot of energy there. In case (c) the true interaction happens in the water, the backward particle is going to layer y (or y and then x), hence the first hit is in layer y (or x) and the second one in layer x. In case (d) the particle goes in the opposite direction than the muon and therefore does not affect much the reconstructed track. Last case (e) is not a backward migrated track. The track starts in layer x and both the muon and produced proton go in the forward direction and deposit energy in the downstream layer y.

<p>(a)</p>  <p>$N^{\text{true}} - N^{\text{reco}} = 1$</p>	<p>(b)</p>  <p>$N^{\text{true}} - N^{\text{reco}} = 1$</p>	<p>(c)</p>  <p>$N^{\text{true}} - N^{\text{reco}} = 0.5$</p>
<p>Large 1st hit pos Small 1st hit charge</p>	<p>Large 1st hit pos Large 1st hit charge</p>	<p>Large 1st hit pos Large 1st hit charge Small 2nd hit charge</p>
<p>(d)</p>  <p>$N^{\text{true}} - N^{\text{reco}} = 1$</p>	<p>(e)</p>  <p>$N^{\text{true}} - N^{\text{reco}} = 1$</p>	<p>• 1st hit • 2nd hit</p>
<p>Small 1st hit pos Large 1st hit charge</p>	<p>Small 1st hit pos No backward migration</p>	<p>Legend</p>

differences for low values of the 1st hit charge (top left plot), which corresponds to a contribution from case (a). For intermediate values, shapes do not differ too much, which may be associated to case (d). They start to differ again for larger values (bottom right), which could be associated to cases (b) or (c) contributions. The same effects can be observed also when looking at the 2nd hit charge, see Fig.A.14, for low deposited charge (case (a)). But here for larger charge (bottom right) we do not observe case (b) since this is the second hit, which makes sense. The 2nd hit Δ position only shows minor effects if we look at different regions of 1st hit charge, as can be observed in A.15.

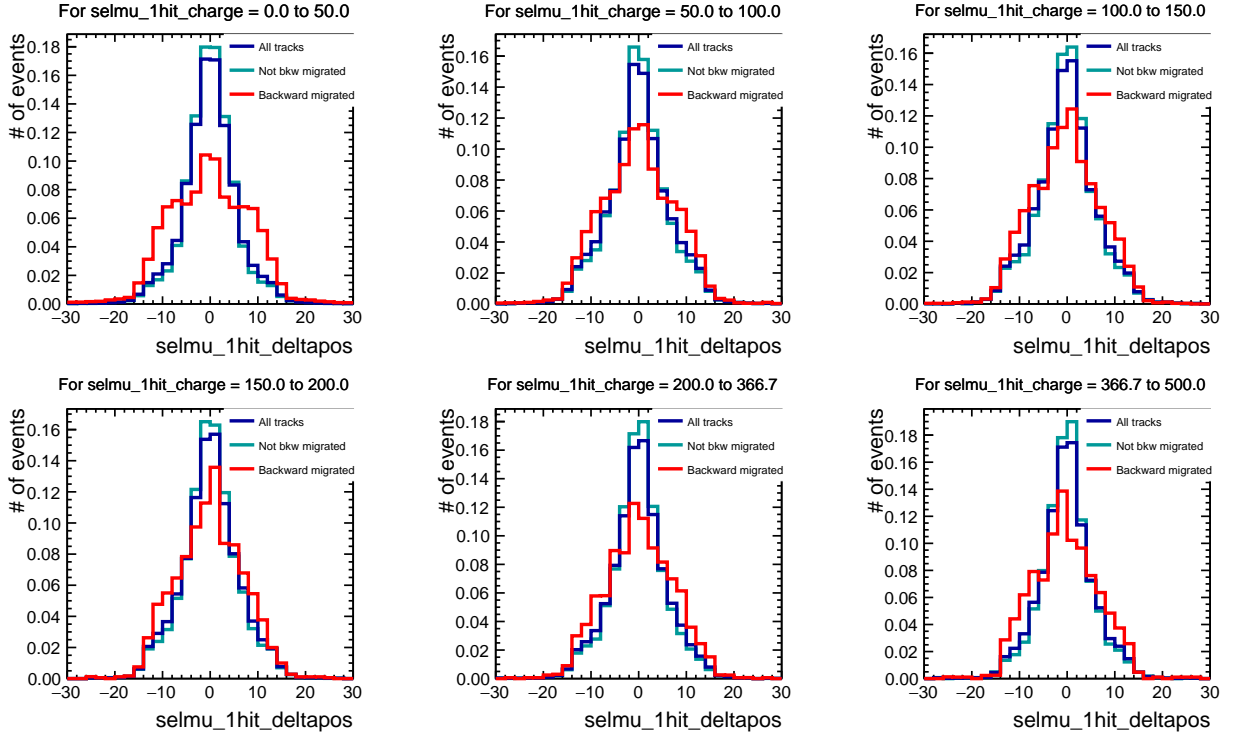


Figure A.13: Slices of the two dimensional 1st hit Δ position VS 1st hit charge distribution, for CC- 0π . A slice is taken between different values of 1st hit charge and projected onto the axis of 1st hit Δ position.

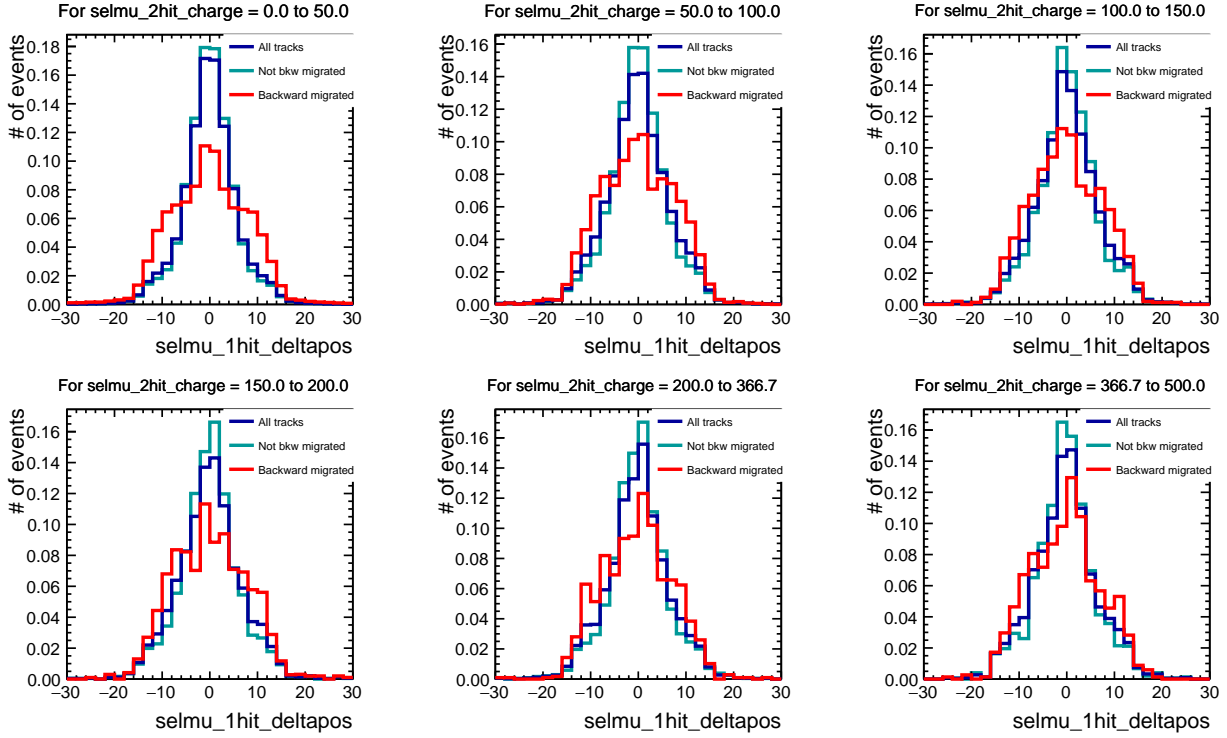


Figure A.14: Slices of the two dimensional 1st hit Δ position VS 2nd hit charge distribution, for CC- 0π . A slice is taken between different values of 2nd hit charge and projected onto the axis of 1st hit Δ position.

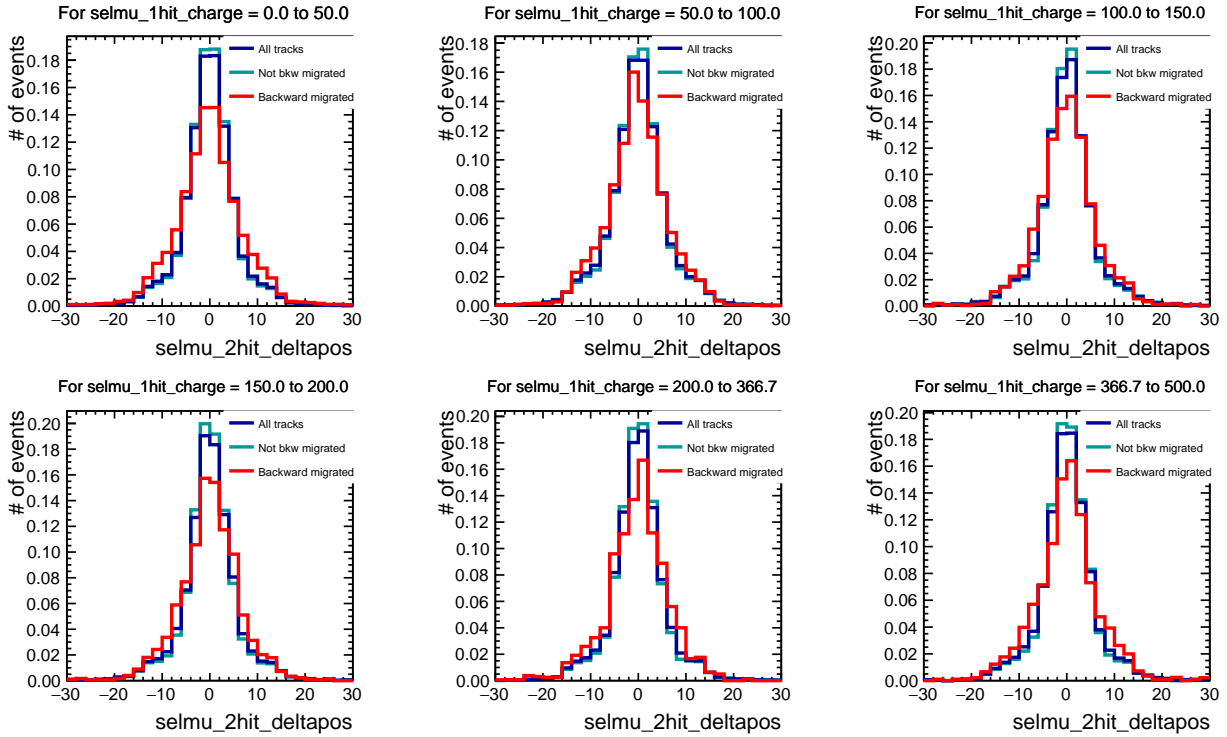


Figure A.15: Slices of the two dimensional 2nd hit Δ position VS 1st hit charge distribution, for CC- 0π . A slice is taken between different values of 1st hit charge and projected onto the axis of 2nd hit Δ position.

A.2.4 Computing the χ^2

The easiest way is to compute a Gaussian χ^2 ,

$$\chi_{\text{Gauss}}^2 = \sum_i^{\text{bins}} \left(\frac{N_{\text{MC}}^i - N_{\text{Data}}^i}{\sigma_{\text{Data}}^i} \right)^2 \quad (\text{A.1})$$

However, bins with too low statistics does not allow to use the Gaussian approximation. A solution is to use a "binned maximum likelihood fit" with a Poissonian χ^2 in the Stirling approximation,

$$\chi_{\text{Poisson}}^2 = 2 \sum_i^{\text{bins}} \left(N_{\text{MC}}^i - N_{\text{Data}}^i + N_{\text{Data}}^i \ln \frac{N_{\text{Data}}^i}{N_{\text{MC}}^i} \right) \quad (\text{A.2})$$

Some studies have first been driven using a Gaussian χ^2 method. Results obtained by the two methods are compatible when using one variable. However, the two-dimensional histograms build from two variables have too low statistics in many bins and the Gaussian approximation can not be used, as the results are not compatible in this case. Therefore we choose the Poisson χ^2 .

Moreover we use the fitter provided by the ROOT method `TFractionFitter` [129, 130]. This method provides a proper treatment of MC statistics, allowing the fit to vary the distributions within the MC errors. The output of the fitter provides estimated values of the fractions f_0^{fit} and f_1^{fit} of not migrated and backward migrated contributions respectively. The postfit distribution of all tracks and the errors on the fractions are given as well by the fitter. We evaluate the fit quality as the χ^2 over the number of degrees of freedom, defined by (number of bins)-(number of parameters).

A.3 Results

A.3.1 One-variable fit

A fit is performed using one of the variables described in section A.2.2 with the ROOT fitter described in section A.2. Results are summarised in table A.3. The prefit and postfit distributions are shown in Fig.A.16 and A.17 for CC-0 π , in Fig.A.18 and A.19 for CC-1 π^+ and in Fig.A.20 and A.21 for CC-Other.

Note that the nominal fraction of backward migrated events f_1^{MC} has not always exactly the same value for each variable. This is due to numerical precision and rounding.

A. Vertex backward migration in FGD2

Table A.3: Comparison of the one-variable fit results. f_1^{MC} is the pre-fit fractions of backward migrated events and f_1^{fit} is the result of the fit, that yields the fraction estimated in the data. The errors are the absolute errors given by the fitter.

Sample	One variable	Best χ^2	Quality	f_1^{MC}	f_1^{fit}	error
CC-0 π	1st hit charge	56.58	2.02	0.15	0.08	0.02
	1st hit Δ pos	158.22	5.65	0.14	0.18	0.01
	2nd hit charge	84.32	3.01	0.14	0.09	0.01
	2nd hit Δ pos	48.42	1.73	0.14	0.32	0.02
CC-1 π^+	1st hit charge	29.69	1.06	0.17	0.25	0.04
	1st hit Δ pos	45.30	1.62	0.16	0.26	0.04
	2nd hit charge	31.25	1.12	0.16	0.10	0.03
	2nd hit Δ pos	33.12	1.18	0.16	0.41	0.07
CC-Other	1st hit charge	29.79	1.06	0.16	0.27	0.05
	1st hit Δ pos	42.09	1.50	0.16	0.25	0.03
	2nd hit charge	26.13	0.93	0.16	0.14	0.03
	2nd hit Δ pos	28.97	1.03	0.16	0.53	0.06

Looking at CC-0 π results, only the result for 1st hit Δ position is compatible with the prefit MC values. This was expected after looking at the variable distributions in section A.2.2 and comparing the shapes of the backward migrated tracks with the shape of all tracks. Indeed the 1st hit Δ position is the only one that shows a relevant difference and hence has a sensitivity to backward migration contribution.

The CC-1 π^+ and CC-Other results are less precise and they do not seem to give results compatible with prefit values.

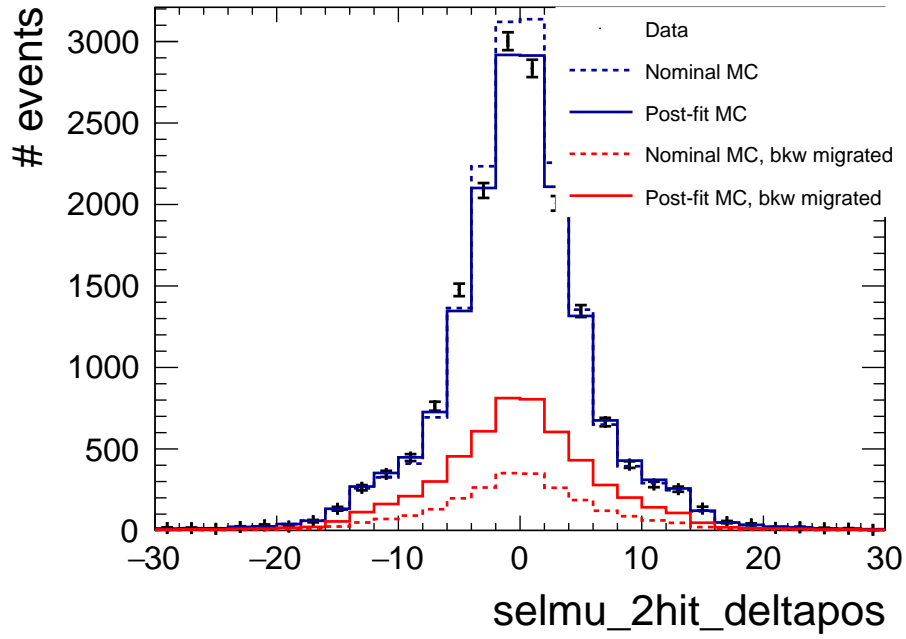
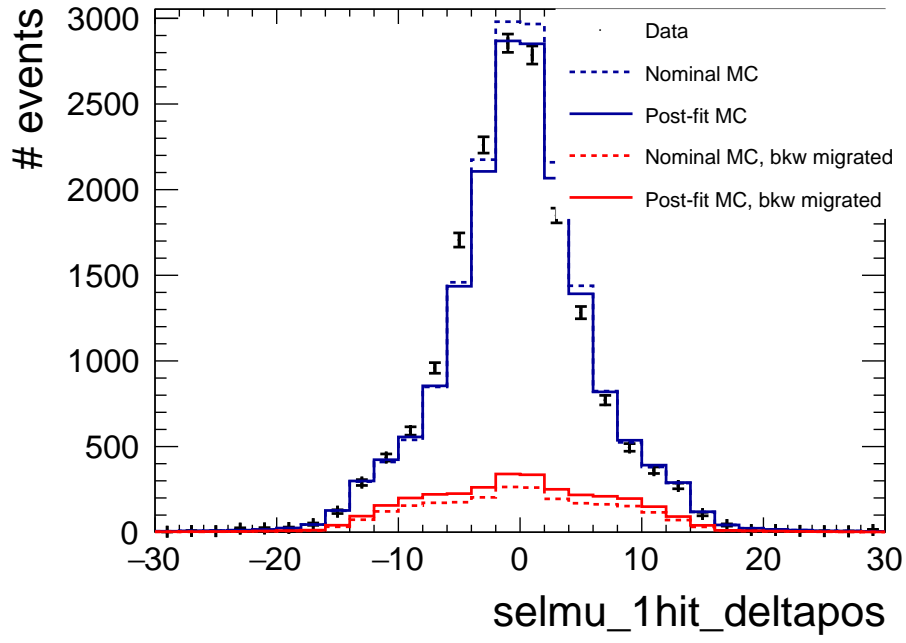


Figure A.16: Comparison of nominal MC and post-fit MC (blue lines), backward migrated contribution (red lines) with data (black) of the 1st hit (top) and 2nd hit (bottom) Δ position distributions, for the CC-0 π sample.

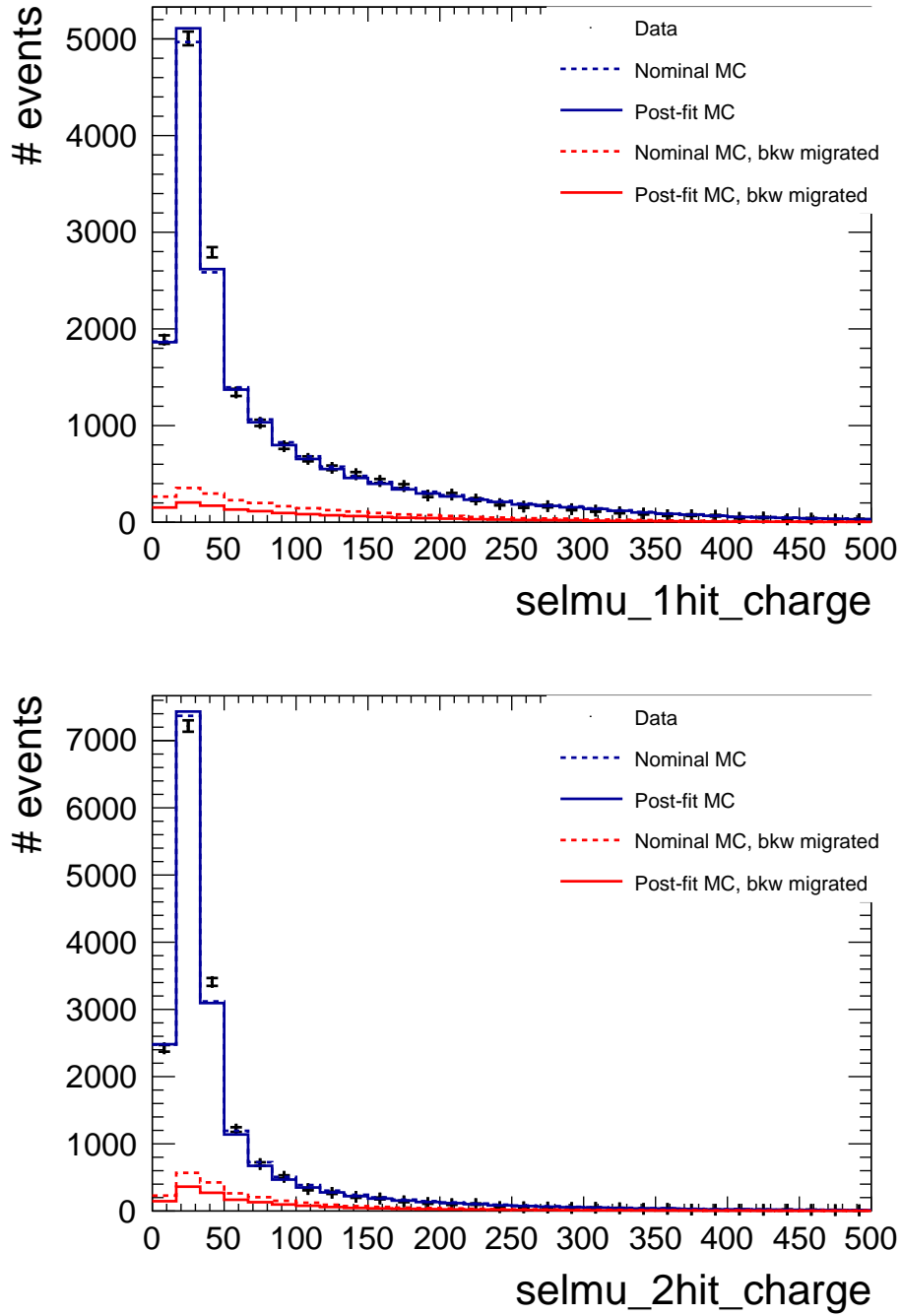


Figure A.17: Comparison of nominal MC and post-fit MC (blue lines), backward migrated contribution (red lines) with data (black) of the 1st hit (top) and 2nd hit (bottom) charge distributions, for the CC- 0π sample.

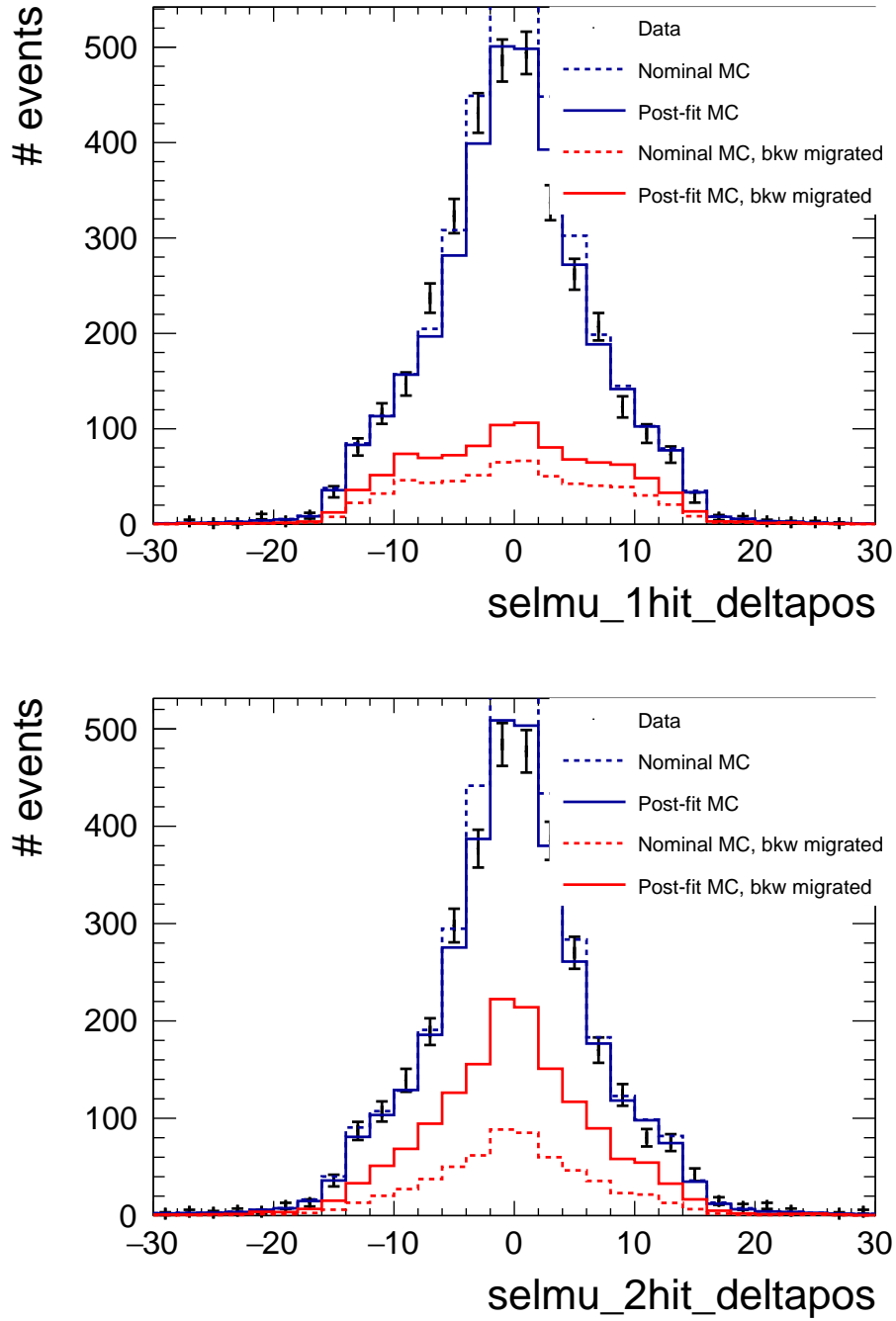


Figure A.18: Comparison of nominal MC and post-fit MC (blue lines), backward migrated contribution (red lines) with data (black) of the 1st hit (top) and 2nd hit (bottom) Δ position distributions, for the CC- $1\pi^+$ sample.

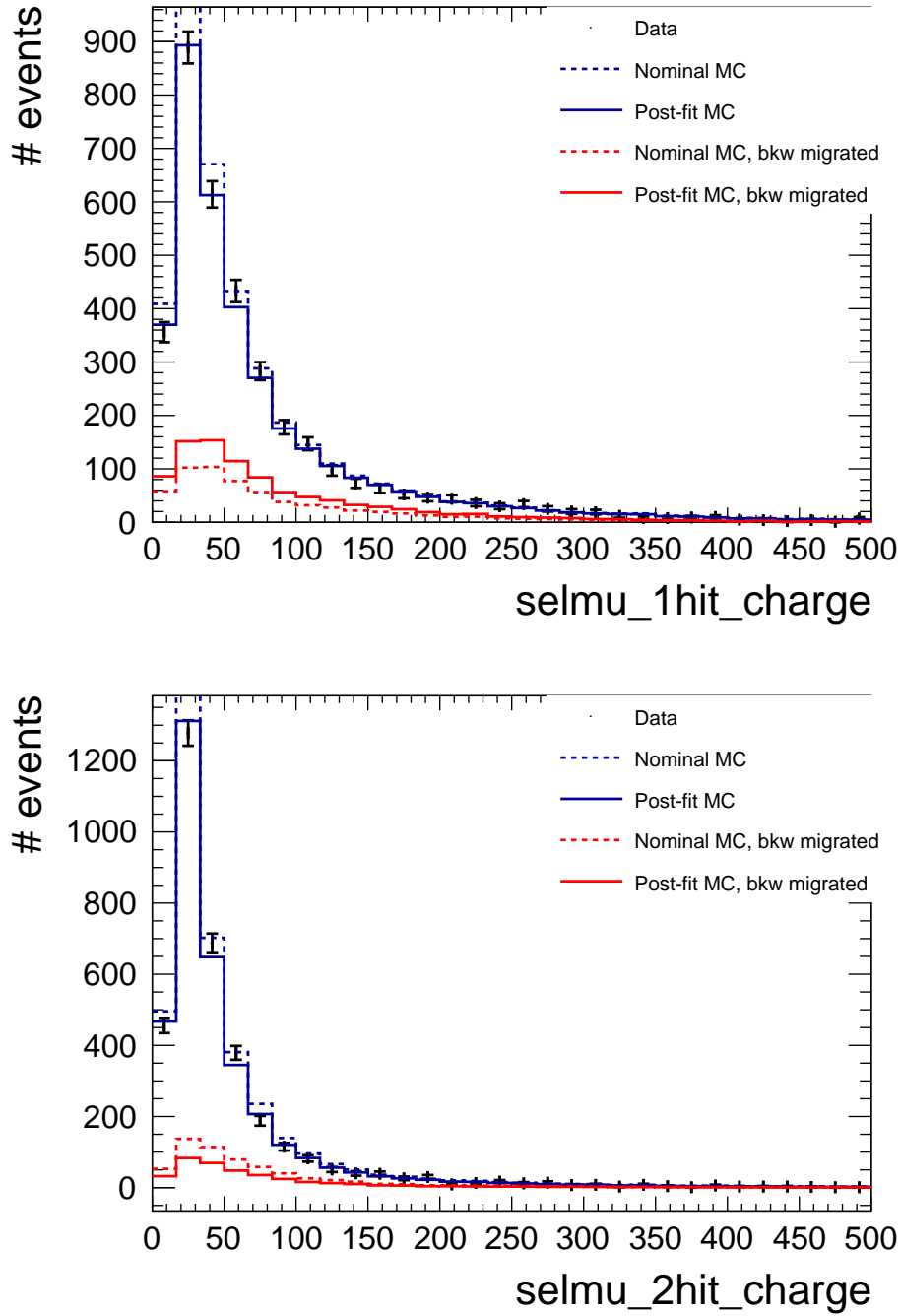


Figure A.19: Comparison of nominal MC and post-fit MC (blue lines), backward migrated contribution (red lines) with data (black) of the 1st hit (top) and 2nd hit (bottom) charge distributions, for the CC- $1\pi^+$ sample.

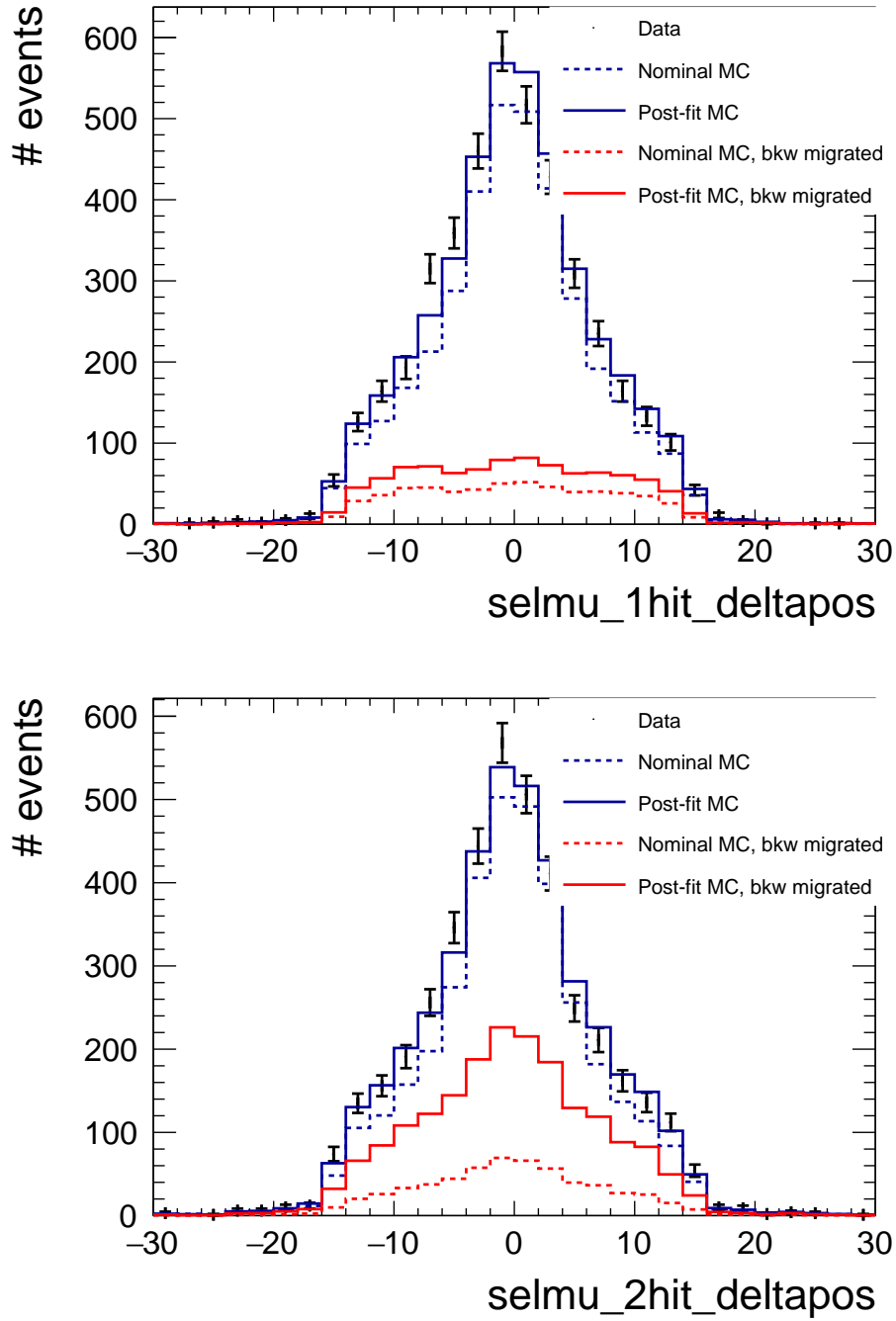


Figure A.20: Comparison of nominal MC and post-fit MC (blue lines), backward migrated contribution (red lines) with data (black) of the 1st hit (top) and 2nd hit (bottom) Δ position distributions, for the CC-Other sample.

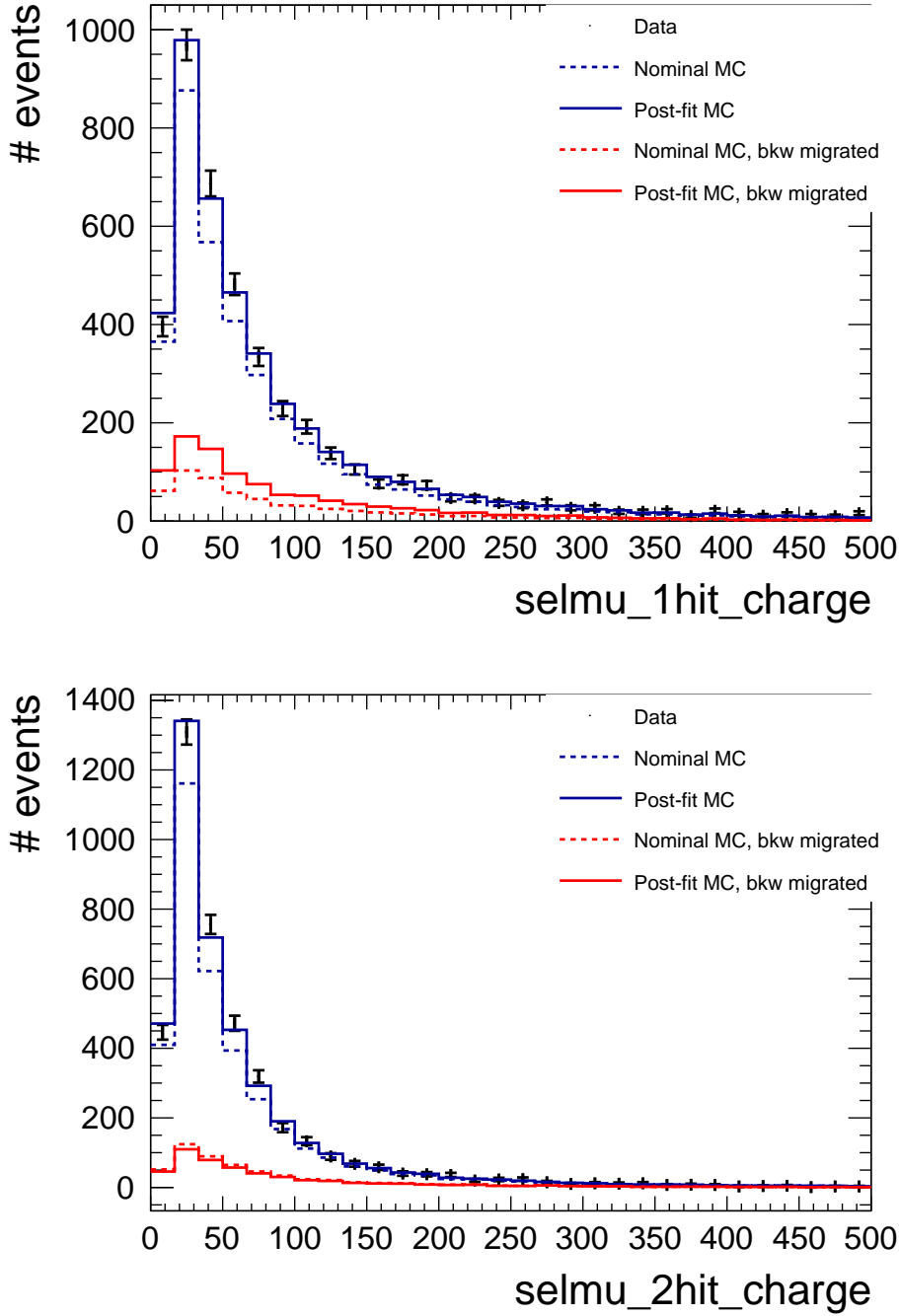


Figure A.21: Comparison of nominal MC and post-fit MC (blue lines), backward migrated contribution (red lines) with data (black) of the 1st hit (top) and 2nd hit (bottom) charge distributions, for the CC-Other sample.

A.3.2 Two-variable fit

The method is exactly the same to fit two variables. A histogram is built in two dimensions for two variables, then this histogram is linearised in order to be used as a 1D histogram input to the fitter. Results are given in Table A.4, A.5 and A.6 for the three samples respectively. The fraction of events that are not backward migrated is not shown in the results, as it is $f_0 = 1 - f_1$, where f_1 is the fraction of backward migrated tracks.

CC-0 π

The 1st and 2nd hit charges are the variables that have the least sensitivity on backward migration and as expected, fitting those two does not give compatible results. However, fitting 1st or 2nd hit Δ positions together with 1st or 2nd hit charge give results that are compatible with prefit MC.

Table A.4: Comparison of the two-variable fit results for CC-0 π . f_1^{MC} is the pre-fit fraction of backward migrated events and f_1^{fit} is the result of the fit, that yields the fraction estimated in the data. The errors are the absolute errors given by the fitter.

Sample	Two variables	Best χ^2	Q	f_1^{MC}	f_1^{fit}	error
CC-0 π	1st hit charge	1011.73	1.13	0.14	0.10	0.01
	2nd hit charge					
	1st hit Δ pos 1st hit charge	1005.93	1.12	0.14	0.15	0.01
	1st hit Δ pos 2nd hit charge	957.32	1.07	0.13	0.11	0.01
	1st hit Δ pos 2nd hit Δ pos	953.51	1.06	0.14	0.19	0.01
	2nd hit Δ pos 1st hit charge	932.21	1.04	0.14	0.15	0.01
	2nd hit Δ pos 2nd hit charge	938.84	1.05	0.13	0.10	0.01

CC-1 π^+

For CC-1 π^+ results are not compatible with prefit values.

Table A.5: Comparison of the two-variable fit results for CC-1 π^+ . f_1^{MC} is the pre-fit fraction of backward migrated events and f_1^{fit} is the result of the fit, that yields the fraction estimated in the data.. The errors are the absolute errors given by the fitter.

Sample	Two variables	Best χ^2	Q	f_1^{MC}	f_1^{fit}	error
CC-1 π^+	1st hit charge	589.31	0.66	0.16	0.16	0.02
	2nd hit charge					
	1st hit Δ pos 1st hit charge	606.69	0.68	0.16	0.26	0.03
	1st hit Δ pos 2nd hit charge	564.46	0.63	0.16	0.15	0.02
	1st hit Δ pos 2nd hit Δ pos	650.62	0.72	0.16	0.30	0.04
	2nd hit Δ pos 1st hit charge	617.13	0.69	0.16	0.28	0.03
	2nd hit Δ pos 2nd hit charge	579.77	0.65	0.16	0.09	0.03

CC-Other

For CC-Other results are not compatible with prefit values.

Table A.6: Comparison of the two-variable fit results for CC-Other. f_1^{MC} is the pre-fit fraction of backward migrated events and f_1^{fit} is the result of the fit, that yields the fraction estimated in the data.. The errors are the absolute errors given by the fitter.

Sample	Two variables	Best χ^2	Q	f_1^{MC}	f_1^{fit}	error
CC-Other	1st hit charge	770.74	0.86	0.16	0.24	0.03
	2nd hit charge					
	1st hit Δ pos	675.43	0.75	0.16	0.22	0.03
	1st hit charge					
	1st hit Δ pos	573.90	0.64	0.16	0.18	0.02
	2nd hit charge					
	1st hit Δ pos	533.99	0.59	0.16	0.30	0.03
	2nd hit Δ pos					
	2nd hit Δ pos	653.63	0.73	0.16	0.33	0.04
	1st hit charge					
	2nd hit Δ pos	567.31	0.63	0.16	0.23	0.03
	2nd hit charge					

A.3.3 Estimated uncertainty

To estimate the uncertainty on backward migrated tracks, we look at the variation of the predicted fraction of their contribution, f_1^{fit} , among the fits for the different variables. We consider the two-variable fit results. For CC- 0π , the absolute variation of the fractions is around 0.05, which gives a relative uncertainty of 30%. For CC- $1\pi^+$ the absolute variation is about 0.15, which gives a relative uncertainty of 90%. For CC-Other we get a 100% uncertainty.

A.4 Backward migration systematic uncertainty propagation

Now that backward migration in FGD2 has been studied and the associated relative uncertainty has been estimated for the three ν_μ charged-current multi-pion selections, it needs to be propagated through the ND280 particle selection. It is implemented in the **Highland2** framework as a weight systematic uncertainty (see Section 4.1) and the resulting values summarised in Section A.3.3 are provided as prior error values. Resulting contribution to the detector uncertainty is shown in Fig. A.22 for the CC- 0π signal sample and in Fig. A.23 for the control samples. Overall the uncertainty on events with interaction in the y layers of FGD2 is large and gives the most important contribution to the total detector uncertainty.

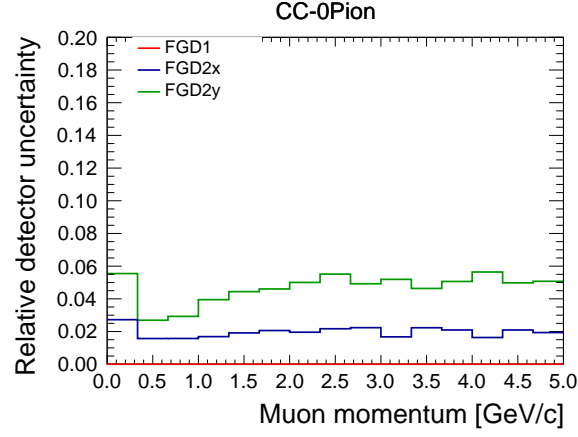


Figure A.22: FGD backward migration systematic uncertainties contribution for FGD1 (red), FGD2x (blue) and FGD2y (green) signal samples.

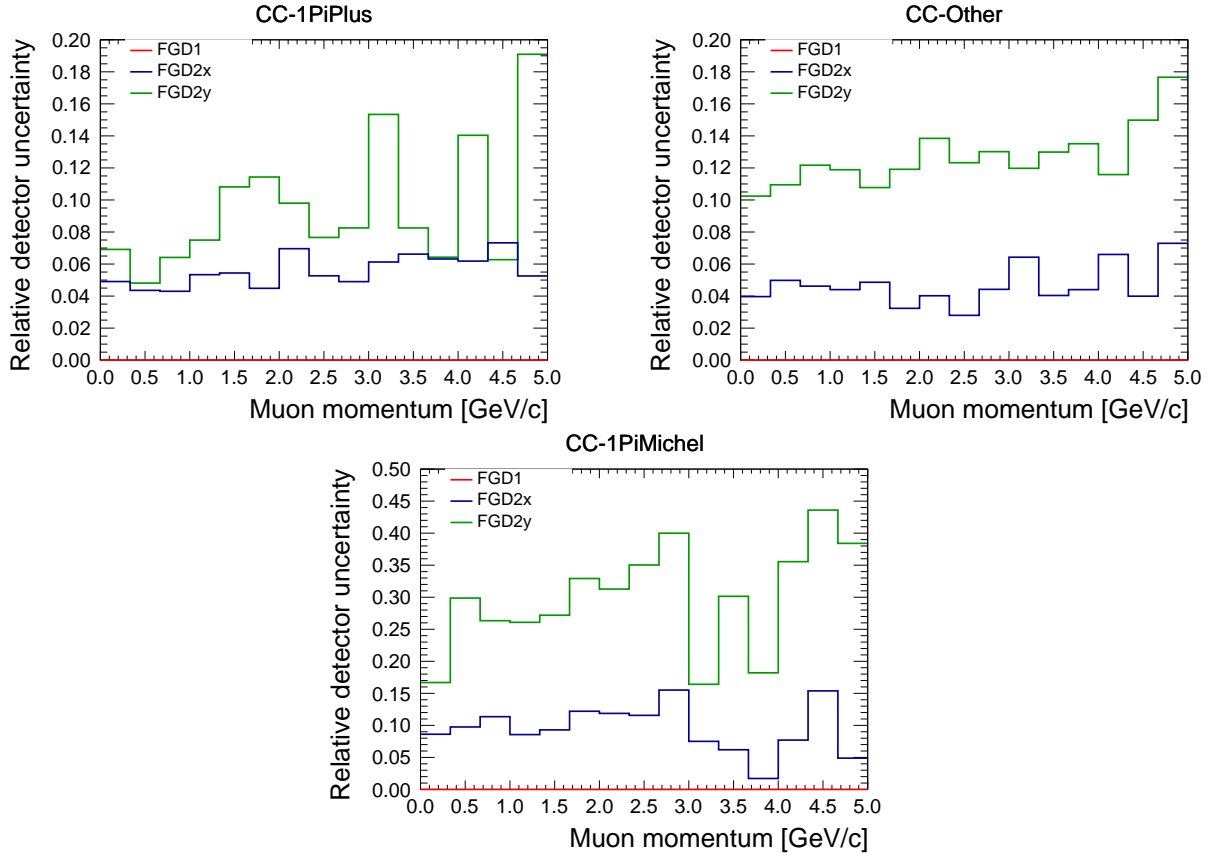


Figure A.23: FGD backward migration systematic uncertainties contribution for FGD1 (red), FGD2x (blue) and FGD2y (green) control samples CC-1 π^+ (top left), CC-Other (top right) and CC-1 π -Michel (bottom).

A.5 Conclusion

In order to estimate the uncertainty on backward migrated tracks in FGD2 layers for multi-pion selections we fit different variables that carry information about the vertex migration. The difference between the fit position and the first hit shows the most sensitivity on backward

migration and fitting this variable gives results that are compatible with prefit distributions for the CC- $1\pi^+$ sample. Other variables are not sensitive enough and for other samples the results are not compatible at all, thus we fit two-dimensional distributions of different variable combinations. As expected the combination of Δ positions with charges variables give sensitive results for CC- 0π and the uncertainty for this sample is 30 %. CC- $1\pi^+$ and CC-Other do not have compatible results with prefit values and have uncertainties of 90 % and 100 % respectively. Those studies give an estimation of the uncertainty on backward migration. We see that fitting two instead of one variable improves the sensitivity. However, further studies would be likely to improve it even more, for example using multi variate analysis (MVA).

B.1 Introduction to fit validation studies

In order to avoid biases this analysis was first conducted in a blind way, i.e. without looking at real data. To validate the fitter framework before unblinding real data a series of studies were conducted with the use of various MC samples as "mock data" input to the fitter, which we call *fake data*. For each of these fits, the Monte Carlo sample that is used as nominal MC input is the full statistic NEUT (see Table 3.1) reweighted to the real data POT¹.

First we fit the nominal NEUT MC to the exact same MC sample used as data to perform what is called an *Asimov fit*, Sec.B.2. Second statistical fluctuations are applied to the event distributions used as fake data, Sec.B.3, and then also initial parameter values are thrown around their prior values, Sec.B.4. A serie of such fits is run with different random seeds in order to perform so-called *coverage study*, looking at parameter pull and χ^2 distributions, Sec.B.5. We then use again the NEUT MC as (fake) data but with an extra bias in the signal or in the background in order to sanity check that template parameters behave as expected, Sec.B.6. Finally, in order to test the model dependency of the fit, fake data studies are conducted with GENIE and NuWro fake data sets, Sec.B.7, as different generators have different specifications depending on the model they are based on.

For an easier reading of the parameter results, we remind that Table 5.1 gives a summary of the fit parameters used in this analysis. The definitions of the different χ^2 's that are calculated and given in the results are presented in Sec.5.1.2.

B.2 Asimov fit

An Asimov fit is performed, giving the exact same MC sample as nominal and data inputs². Fig. B.1, B.2, B.3 and B.4 show the prior and post-fit values of each set of fit parameters with their associated fit errors and Fig. B.6 is the associated post-fit correlation matrix. In Fig. B.1 the separation between the parameters reweighting carbon or oxygen events is indicated by a black line and the separations between the different angle bins by gray lines.

¹Except for the NuWro fake data fit, as there are less statistics available than the data. In that case the nominal MC input is reweighted to the NuWro POT.

²Full Monte Carlo POT is used as fake data, therefore the errors are smaller than what one would expect for the data POT.

B. Fit validation

As expected for an Asimov fit we verify that prior and post-fit parameter values match perfectly. As expected too the errors on the carbon template parameters are smaller than on the oxygen parameters thank to the FGD1 constraint on carbon, see right plot of Fig. B.1. Finally we verify that χ^2 values are

$$\chi_{\text{pre-fit}}^2 = \chi_{\text{post-fit}}^2 = \chi_{\text{xsec}}^2 = 0 \quad (\text{B.1})$$

which can be visualised in Fig. B.5 where the pre-fit and post-fit event distributions are plotted by sample.

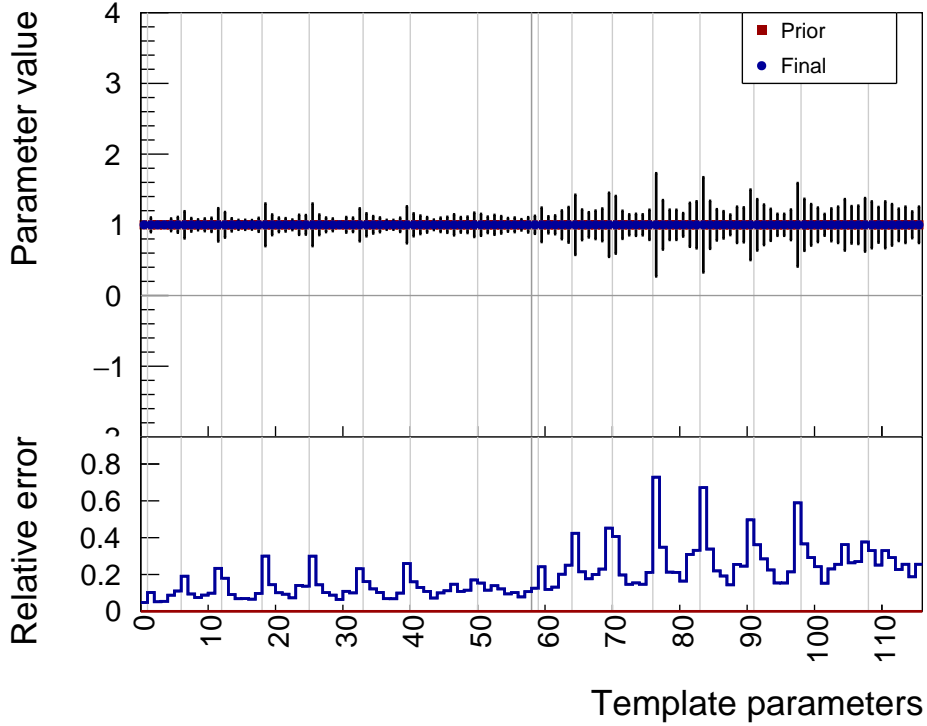


Figure B.1: Prior and post-fit template parameter values and their associated uncertainty for an Asimov fit. The first 58 parameters correspond to the carbon parameters (c_i) and the next 58 parameters are the ones on oxygen (o_i).

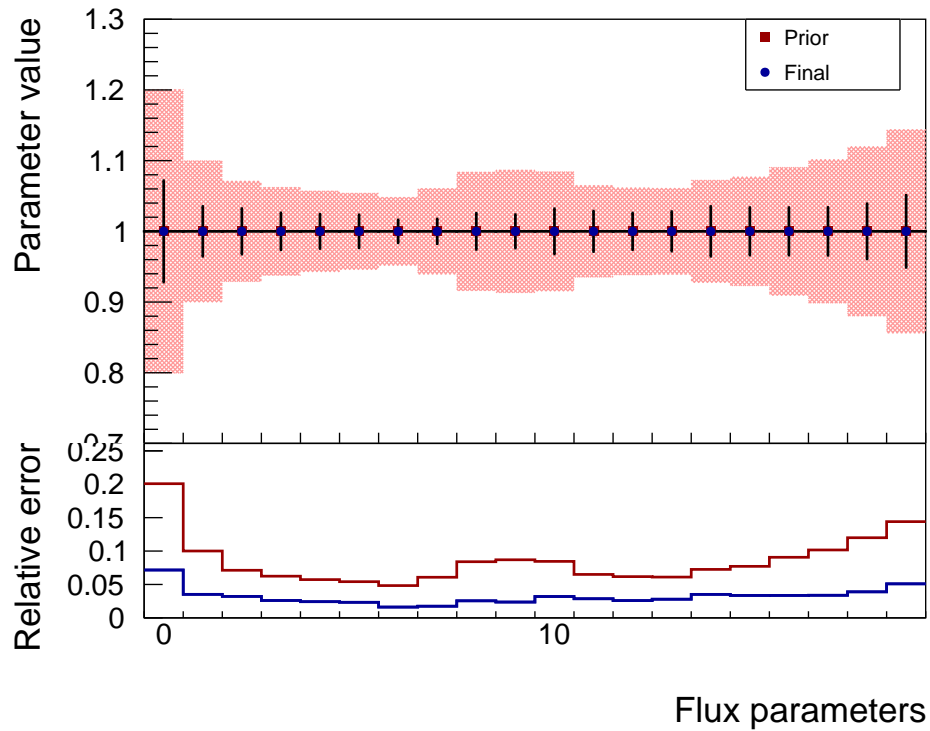


Figure B.2: Prior and post-fit flux parameter values and their associated uncertainty for an Asimov fit.

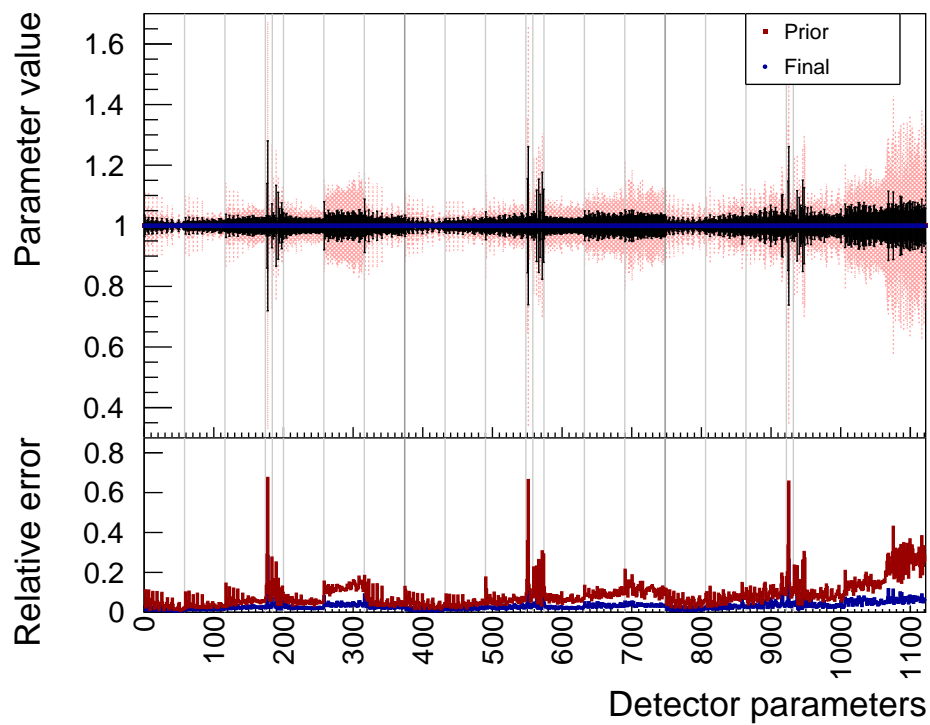
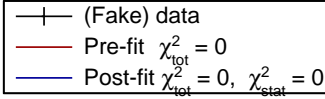


Figure B.3: Prior and post-fit detector parameter values and their associated uncertainty for an Asimov fit.



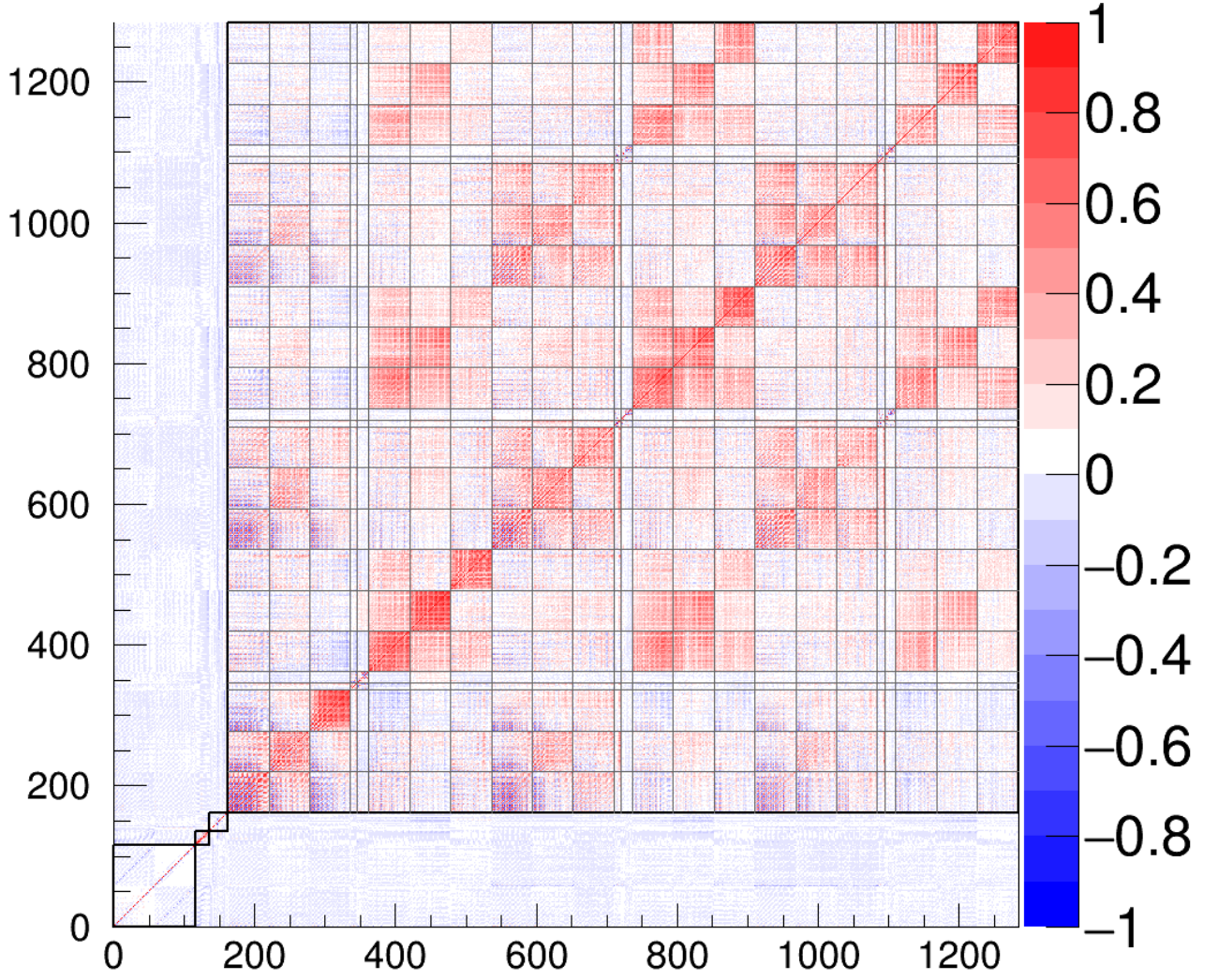


Figure B.6: Post-fit correlation matrix of all the fit parameters for an Asimov fit. The sub-matrices for the different types of parameters are separated by dashed black lines. Parameters with bins from 0 to 57 corresponds to the c_i 's, from 58 to 115 o_i 's, from 116 to 135 flux, from 136 to 161 cross-section model and from 162 to 1283 detector parameters.

B.3 Statistical fluctuations only

Here we fit a (fake) data input that is equal to the nominal MC input as in previous section, except that now statistical fluctuations are applied to the initial event distribution according to a Poisson distribution. The number of events in the inputs are normalised to the real data POT. This kind of fit allows to probe the fitter response to statistical variations in the data input. While performing this fit it often happens that one or more bins with low signal content are statistically fluctuated to negative values. Setting a boundary to zero for template parameters is problematic as MINUIT will return wrong errors for parameters fitted at the boundaries. Errors are then propagated and lead to extremely huge and non sensible final cross-section χ^2 's. We therefore decide to allow template parameters to get negative values. A negative template parameter results in a negative cross section in the associated bin, which is not unphysical because of background subtraction. Such behaviour makes sense in background-dominated regions. However if a result is negative one should make sure that the final result is compatible

with zero, which is the case here.

The final cross-section χ^2 is $\chi^2_{\text{xsec, Fake data}} = \chi^2_{\text{xsec, NEUT}} = 115$, which has a probability of 0.51 for 116 parameters.

The χ^2 per iteration is plotted in Fig. B.7. Fig. B.8, Fig. B.9, B.10, B.11, B.12 show the prior and post-fit parameter values with their fit errors. Their associated post-fit correlation matrix is drawn in Fig. B.13. The pre-fit, post-fit and (fake) data event distributions at the reconstructed level are compared in Fig. B.14 for each signal region and sideband with their χ^2 calculated as explained in Sec.B.5. The χ^2 is quite large in the μ -TPC regions, in fact it makes more sense to group these samples together. This is done in Fig. B.15 where the events for all the regions that have a μ -TPC track are plotted in the same distribution (top left). We see now that the fitter is actually doing a good job in fitting overall those μ -TPC regions. The Michel electron sideband has a large χ^2 . This sideband is not optimal and has a large OOFV background that could be optimised with further studies³. The extracted cross-sections on carbon and oxygen and their ratio are shown in Fig. B.16, B.18 and B.20 respectively with their associated uncertainty in Fig. B.17, B.19 and B.21 and correlation matrices in Fig. B.22 and B.23.

Overall the results show very good agreement between prior and best-fit values. Post-fit and cross-section χ^2 's confirm it with reasonable values.

This fit has also been performed with FGD2 samples only in order to justify the impact of the addition of FGD1 samples to the fit, as discussed in Section 3.1.1. A comparison of the fit uncertainties on carbon and oxygen parameters is shown in Fig. B.9 and it can be observed that the error on carbon parameters is reduced once FGD1 samples are added, because it gives an extra constraint on neutrino interactions in carbon. Even the errors on oxygen parameters become smaller. The strong reduction of anticorrelations between carbon and oxygen can be observed too and is shown in Fig. B.22. The slight noise that seems to appear in the off-diagonal terms of the carbon submatrix are due to the error reduction, since we are showing the correlations, which correspond to covariances normalised by errors.

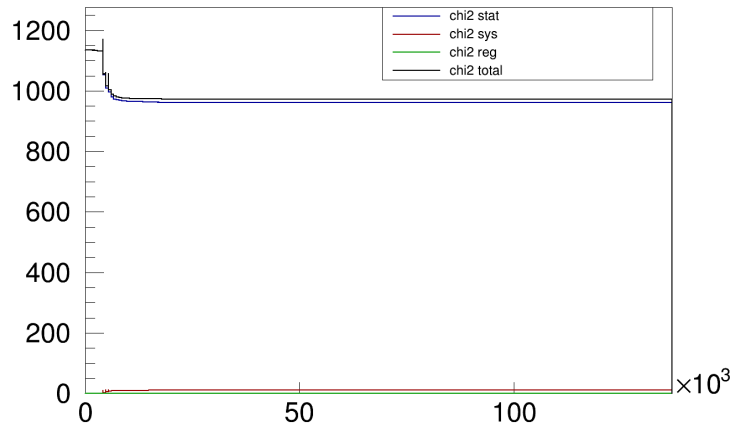


Figure B.7: Evolution of the χ^2 by iteration for a fit to NEUT (fake) data input including statistical fluctuations on the initial number of events.

³For instance the time of flight cut has been removed as explained in Section 3.3.3. Adding it would avoid large OOFV background

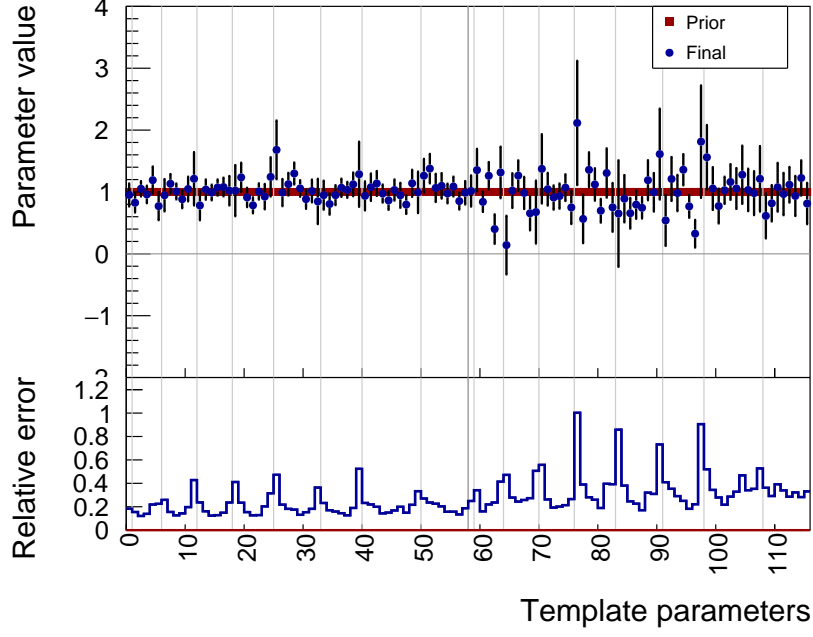


Figure B.8: Prior and post-fit template parameter values and their associated uncertainty for a fit to NEUT (fake) data input including statistical fluctuations on the initial number of events. The first 58 parameters correspond to the carbon parameters (c_i) and the next 58 parameters are the ones on oxygen (o_i).

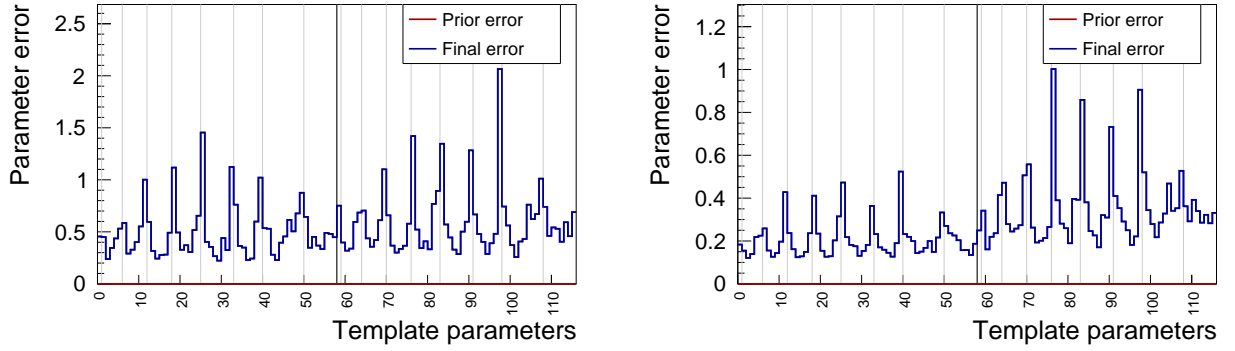


Figure B.9: Total uncertainty on the fit template parameters associated to carbon (analysis bins from 0 to 57) and to oxygen (analysis bins from 58 to 115) for a fit to NEUT (fake) data input including statistical fluctuations on the initial number of events. In the left figure only FGD2 samples are fitted and in the right one FGD1 and FGD2 samples are used.

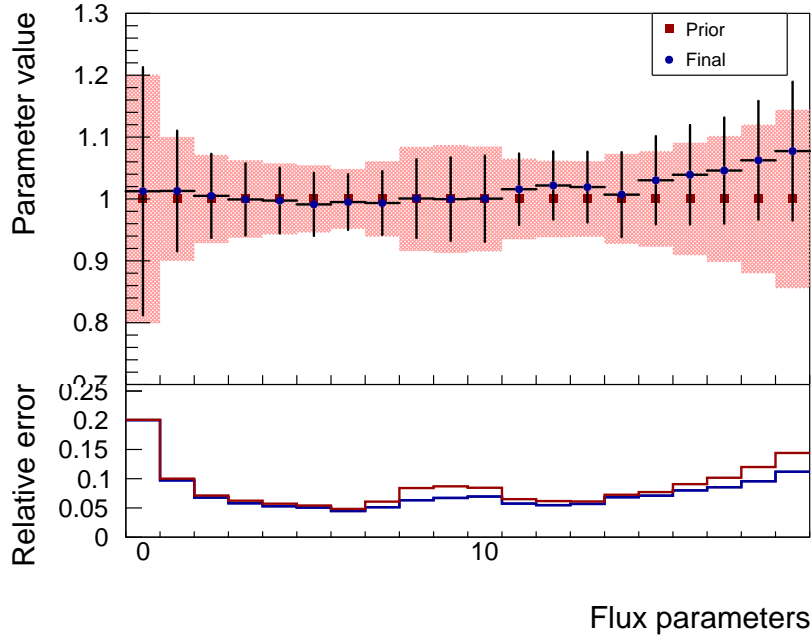


Figure B.10: Prior and post-fit flux parameter values and their associated uncertainty for a fit to NEUT (fake) data input including statistical fluctuations on the initial number of events. The initial thrown parameter values are represented by green triangles.

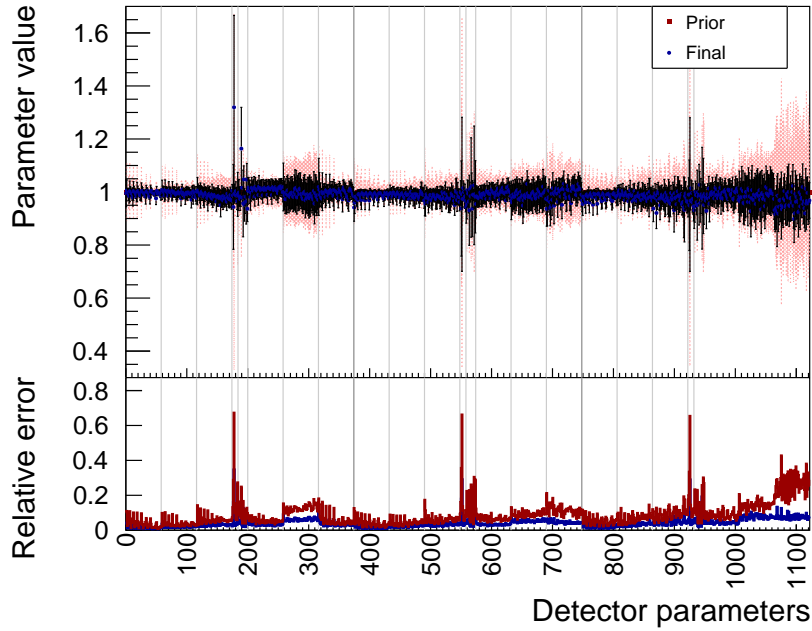


Figure B.11: Prior and post-fit detector parameter values and their associated uncertainty for a fit to NEUT (fake) data input including statistical fluctuations on the initial number of events. The initial thrown parameter values are represented by green triangles.

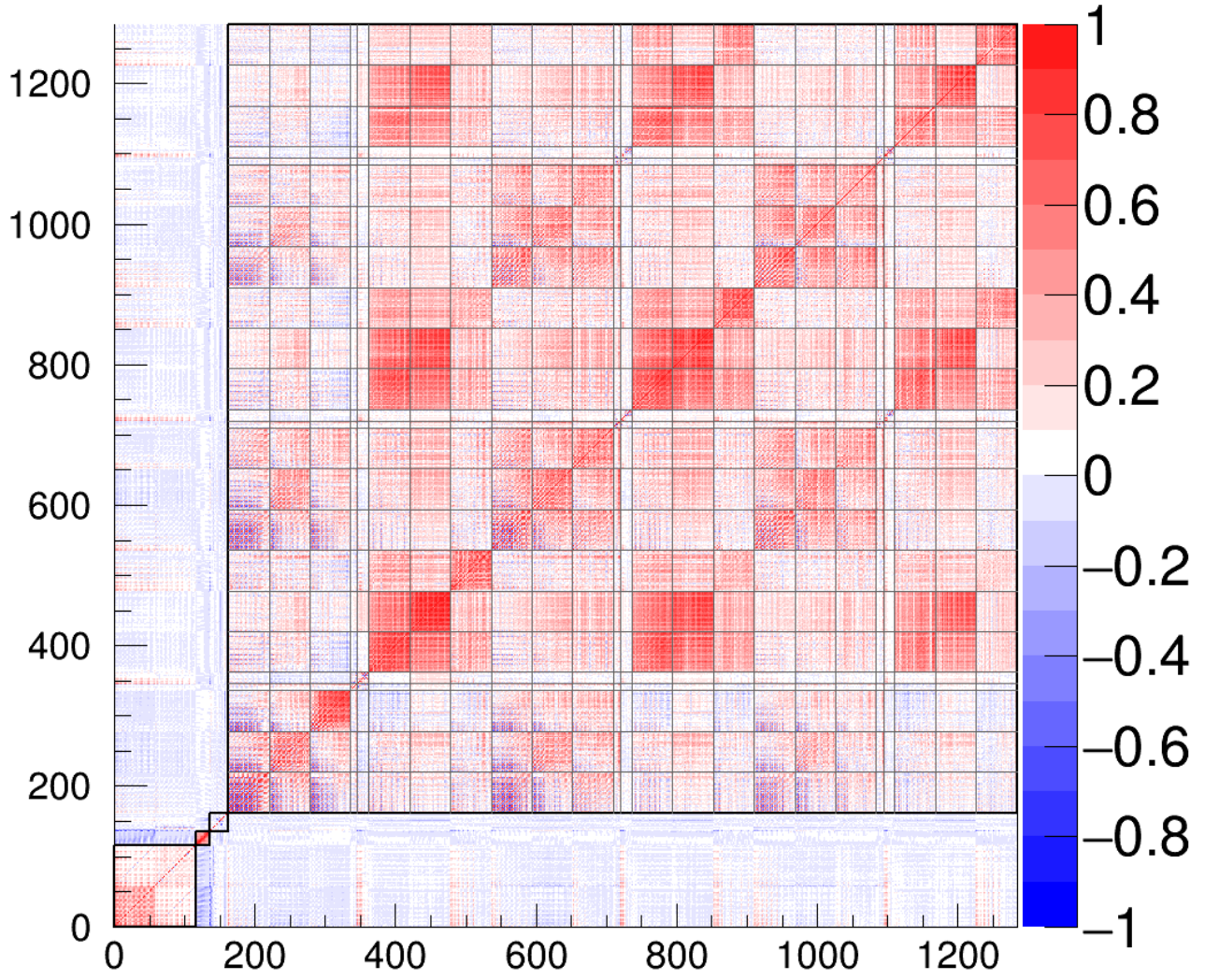


Figure B.13: Post-fit correlation matrix of all the fit parameters for a fit to NEUT (fake) data input including statistical fluctuations on the initial number of events. The sub-matrices for the different types of parameters are separated by dashed black lines. Parameters with bins from 0 to 57 corresponds to the c_i 's, from 58 to 115 o_i 's, from 116 to 135 flux, from 136 to 161 cross-section model and from 162 to 1283 detector parameters.

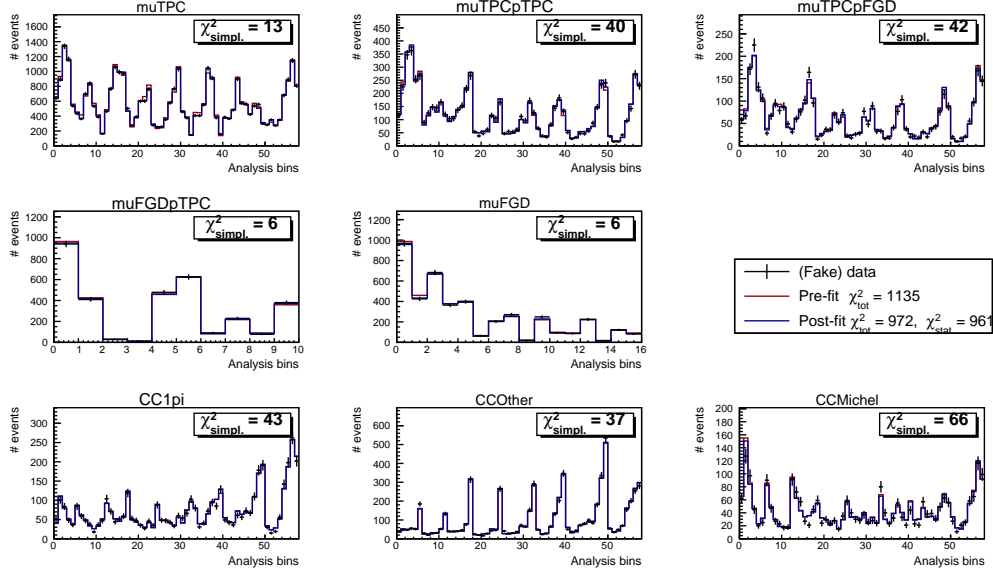


Figure B.14: Prior (blue) and post-fit (red) signal events compared to data (black) distributed in $p_\mu, \cos\theta_\mu$ analysis bins for a fit to NEUT (fake) data input including statistical fluctuations on the initial number of events. Each plot is for a specific signal or sideband region according to its title. The " χ^2 " on top of each region plot is a simple estimation of the data - post-fit discrepancy by summing over the bins the difference square of the data and post-fit numbers of events divided by the data number of events. The total pre-fit and post-fit χ^2 's are the values given by MINUIT.

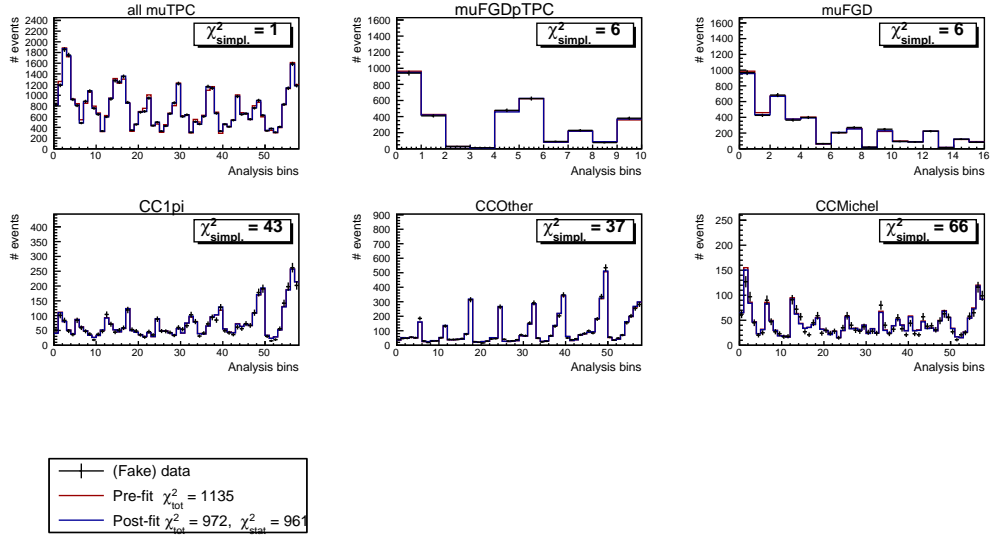


Figure B.15: Prior (blue) and post-fit (red) signal events compared to data (black) distributed in $p_\mu, \cos\theta_\mu$ analysis bins for a fit to NEUT (fake) data input including statistical fluctuations on the initial number of events. Each plot is for a specific signal or sideband region according to its title ; all the muTPC topologies are grouped together in the top left plot.

B. Fit validation

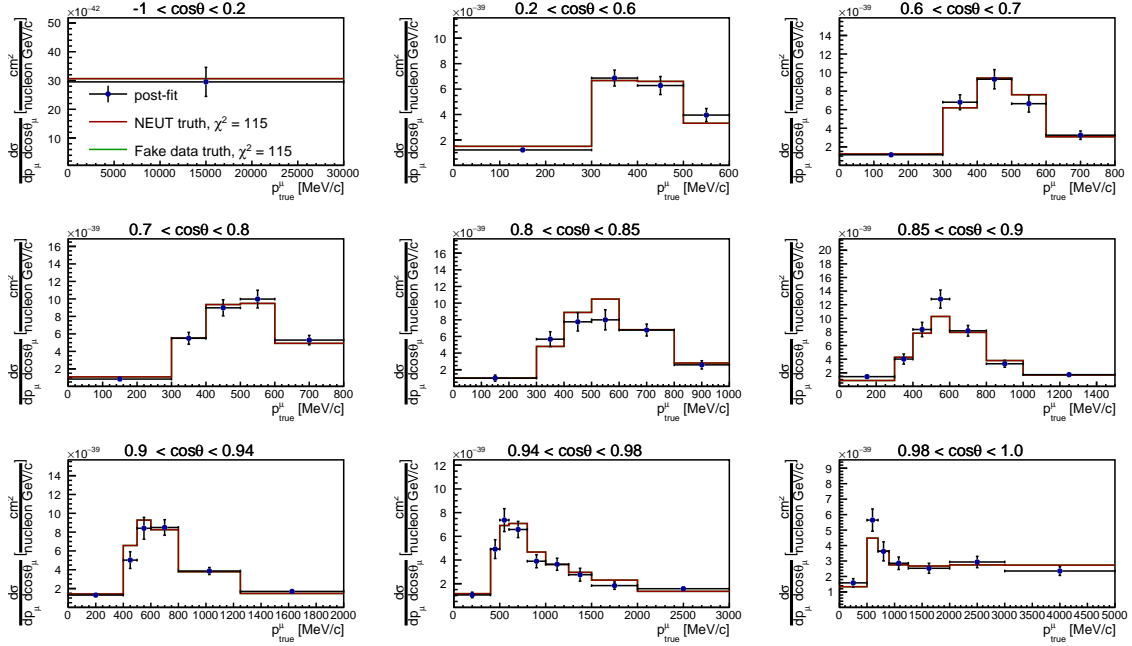


Figure B.16: Flux integrated cross section on carbon, result for a fit to NEUT (fake) data input including statistical fluctuations on the initial number of events. Each plot is for a given angle bin according to its title and the x axis is the muon momentum. Note that the fake data truth is not visible, it is superimposed by the NEUT truth as they are the same.

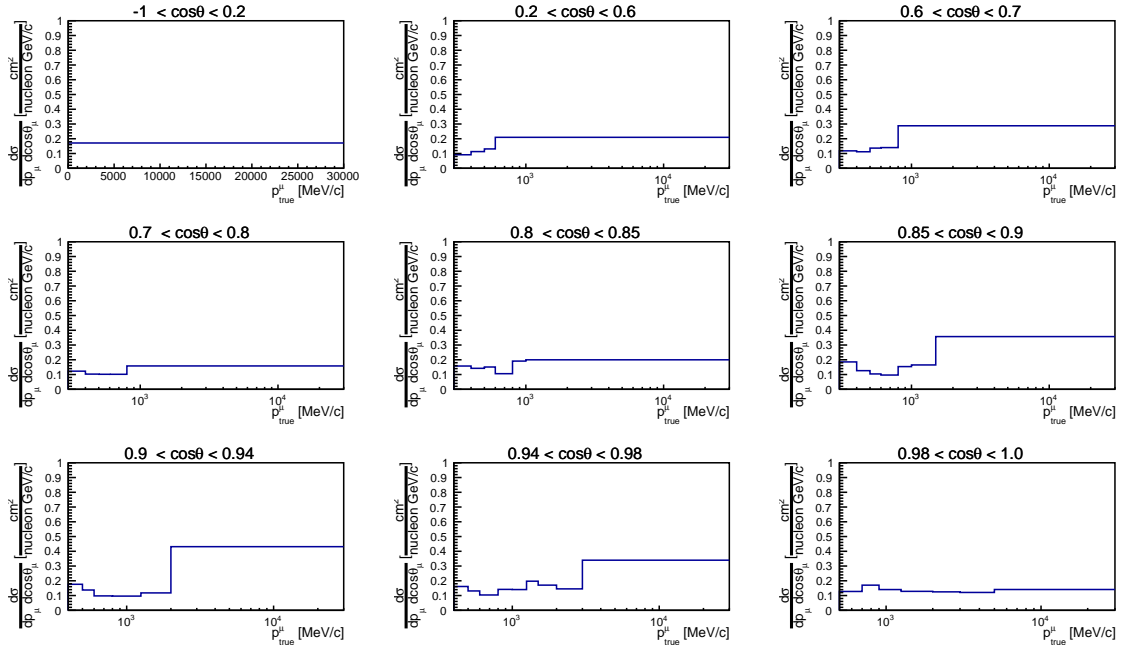


Figure B.17: Relative uncertainty on the cross section on carbon, result for a fit to NEUT (fake) data input including statistical fluctuations on the initial number of events. Each plot is for a given angle bin according to its title and the x axis is the muon momentum.

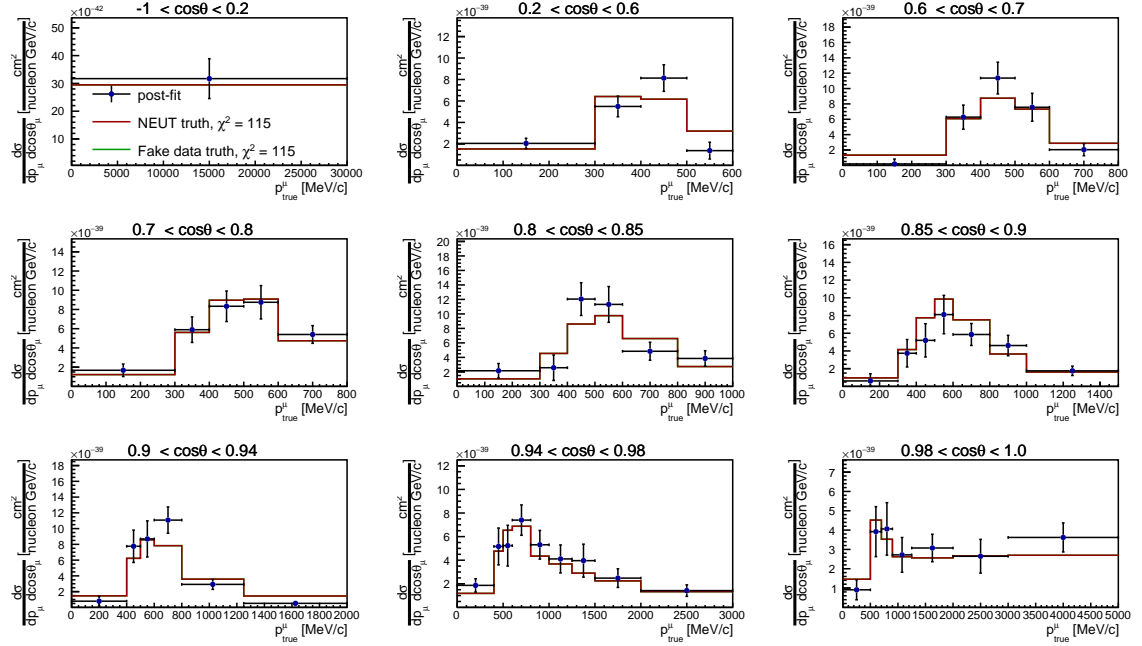


Figure B.18: Flux integrated cross section on oxygen, result for a fit to NEUT (fake) data input including statistical fluctuations on the initial number of events. Each plot is for a given angle bin according to its title and the x axis is the muon momentum. Note that the fake data truth is not visible, it is superimposed by the NEUT truth as they are the same.

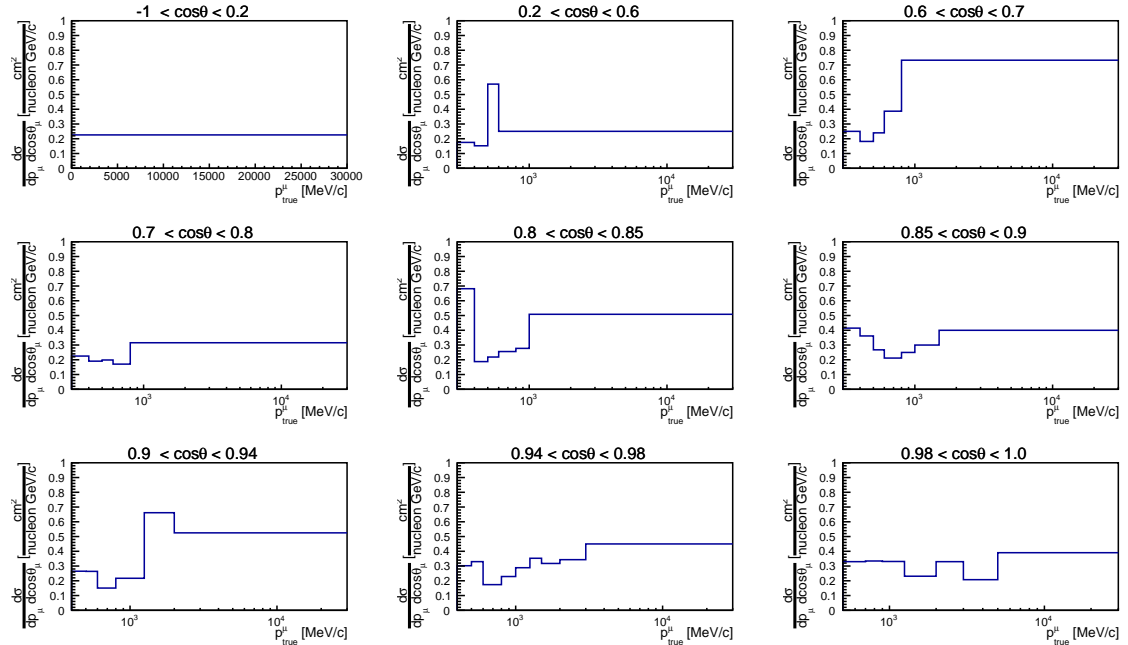


Figure B.19: Relative uncertainty on the cross section on oxygen, result for a fit to NEUT (fake) data input including statistical fluctuations on the initial number of events. Each plot is for a given angle bin according to its title and the x axis is the muon momentum.

B. Fit validation

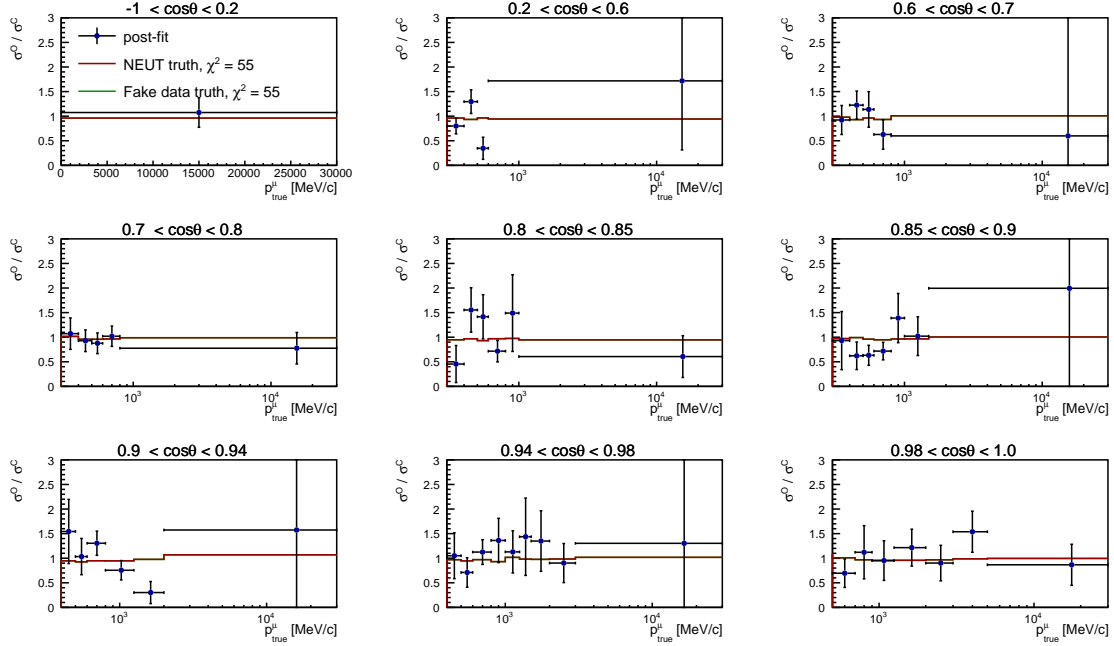


Figure B.20: Oxygen/carbon cross section ratio, result for a fit to NEUT (fake) data input including statistical fluctuations on the initial number of events. Each plot is for a given angle bin according to its title and the x axis is the muon momentum. Note that the fake data truth is not visible, it is superimposed by the NEUT truth as they are the same.

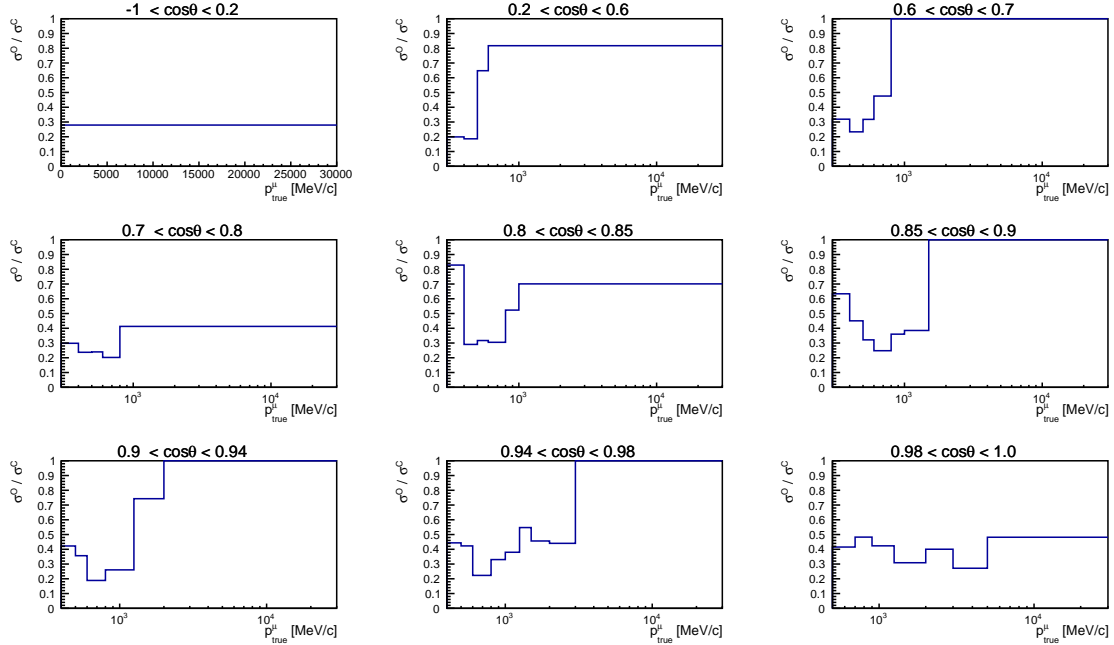


Figure B.21: Relative uncertainty on the oxygen/carbon cross section ratio, result for a fit to NEUT (fake) data input including statistical fluctuations on the initial number of events. Each plot is for a given angle bin according to its title and the x axis is the muon momentum.

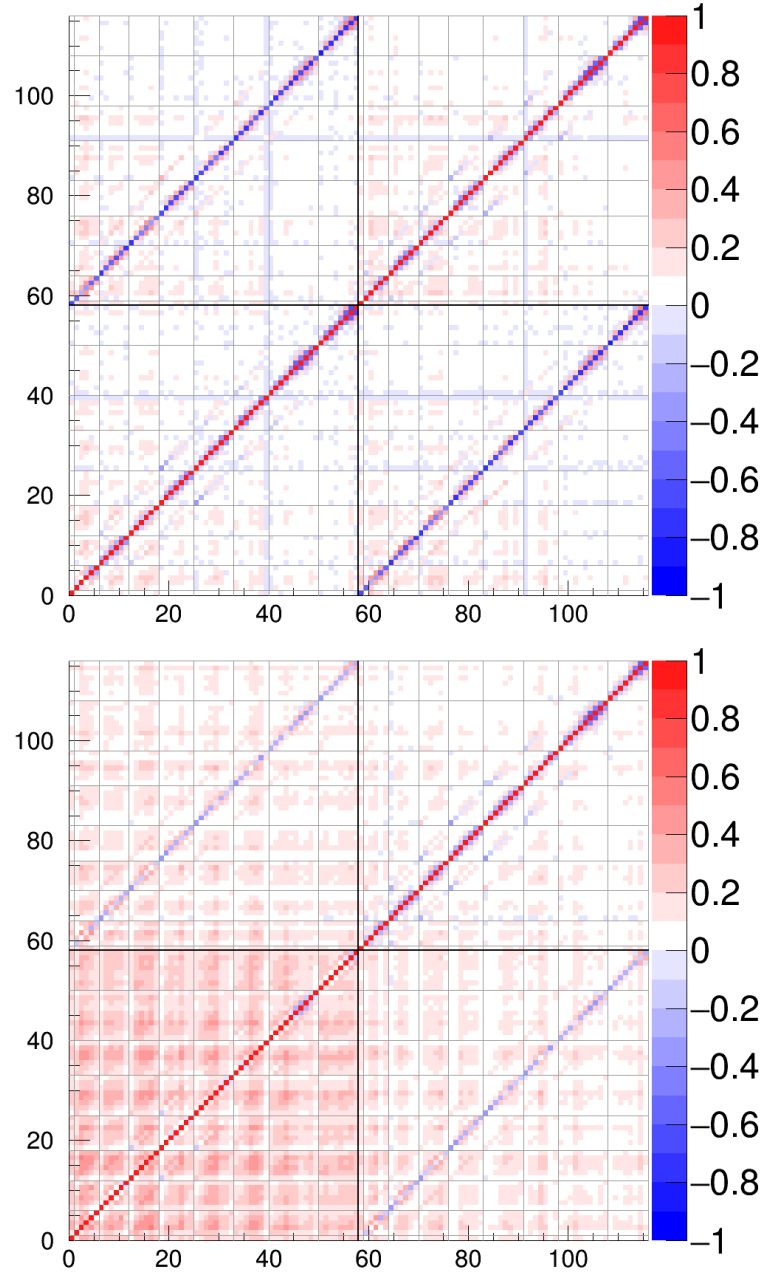


Figure B.22: Final correlation matrix for the cross-section results for a fit to NEUT (fake) data input including statistical fluctuations on the initial number of events. In the top figure only FGD2 samples are fitted and in the bottom one FGD1 and FGD2 samples are used. The sub-matrices for the different $\cos\theta_\mu$ bins are separated by dashed black lines. Bins from 0 to 57 corresponds to carbon interactions, from 58 to 115 to oxygen interactions. The off-diagonal submatrices (top left or bottom right) correspond to carbon to oxygen correlations and their light blue diagonal shows the anticorrelations that were discussed in Section 3.1.1.

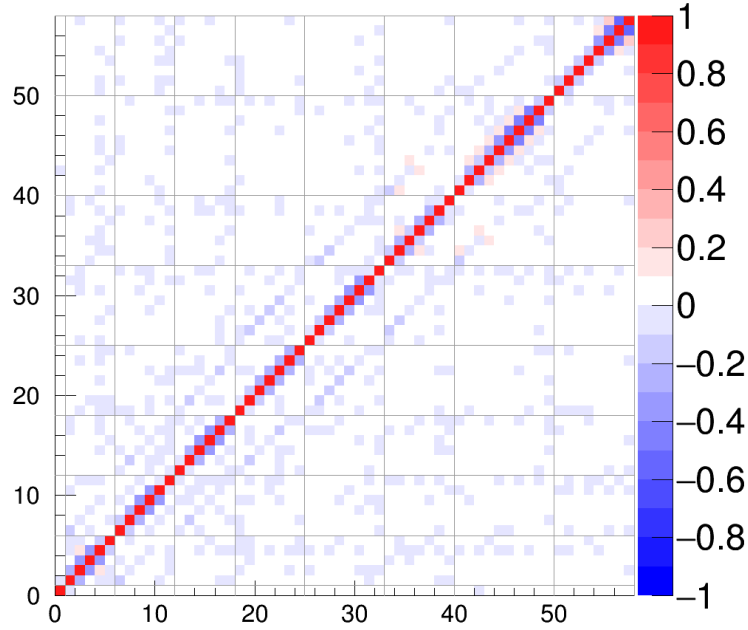


Figure B.23: Final correlation matrix for the cross-section ratio results for a fit to NEUT (fake) data input including statistical fluctuations on the initial number of events. The sub-matrices for the different $\cos\theta_\mu$ bins are separated by dashed black lines.

B.4 Statistical fluctuations and systematic parameter throws

In this case the fake data input is a sub-sample of the NEUT MC, chosen to have a POT of the same order than real data POT. Contrarily to the fit presented in Section B.3 here the input is not the same sample than the nominal MC input, although both of them are events generated with NEUT. Again, statistical fluctuations are applied to the number of events according to a Poisson distribution. Moreover the initial systematic parameters are randomly thrown around their mean values.

The χ^2 per iteration is shown in Fig. B.24. Fig. B.25, B.26, B.27, B.28 show the pre-fit and post-fit parameters with their errors and associated post-fit covariance matrix in Fig. B.29. The event distributions at the reconstructed level are shown in Fig. B.30. Post-fit parameter values are compatible with the prior values and post-fit event distributions at the reconstructed level show a good agreement with distributions of fake data. One should notice that the flux parameters are slightly pushed down, as it will be seen in other kind of fake data fits as well. We do not expect such behaviour as the flux parameters are supposed to be the same for the fake data and nominal inputs. However, the fit probably reduces the flux parameters in order to adjust for the backgrounds. The background parameters likely do not give enough freedom to the fit to alter background contents, therefore it is carried on by flux parameters.

The extracted cross-sections on carbon and oxygen and their ratio are shown in Fig. B.31, B.33 and B.35 respectively with their associated uncertainty in Fig. B.32, B.34 and B.36 and correlation matrices in Fig. B.37 and B.38. Some fluctuations can be seen in the cross-section results, but it is compatible with prior estimations and the χ^2 is reasonable.

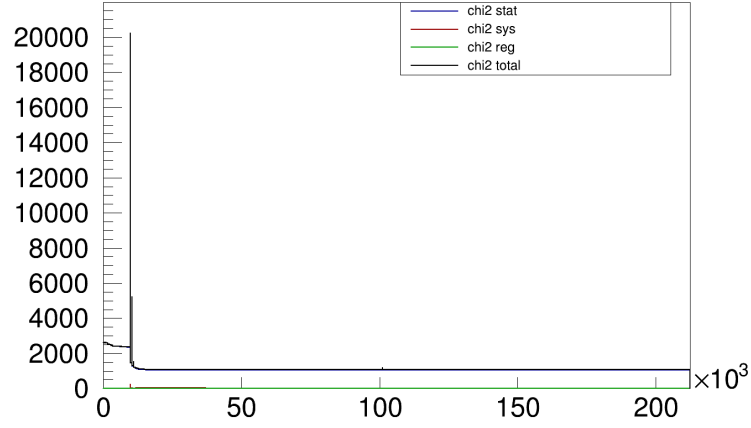


Figure B.24: Evolution of the χ^2 by iteration for a fit to NEUT (fake) data with statistical fluctuations on the number of events and systematic parameter throw.

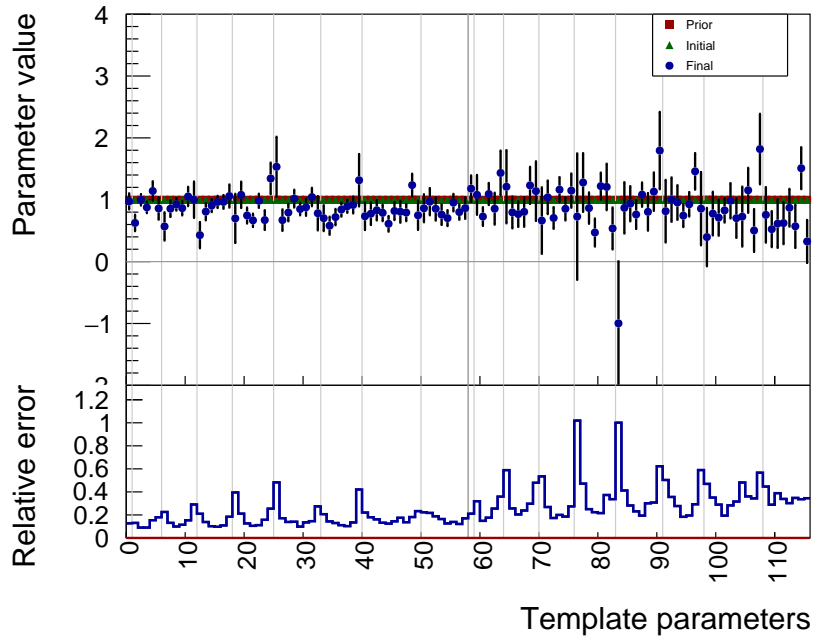


Figure B.25: Prior and post-fit template parameter values and their associated uncertainty for a fit to NEUT (fake) data with statistical fluctuations on the number of events and systematic parameter throw. The first 58 parameters correspond to the carbon parameters (c_i) and the next 58 parameters are the ones on oxygen (o_i).

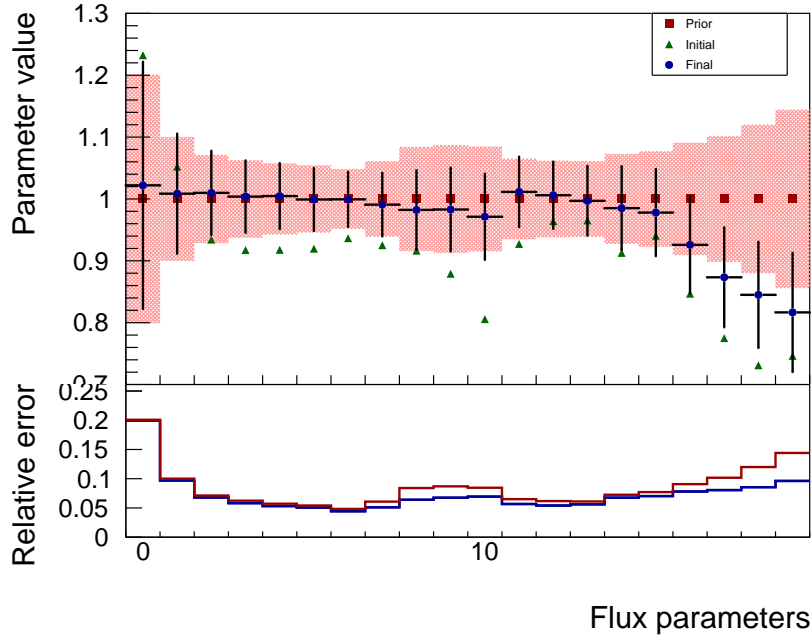


Figure B.26: Prior and post-fit flux parameter values and their associated uncertainty for a fit to NEUT (fake) data with statistical fluctuations on the number of events and systematic parameter throw. The initial thrown parameter values are represented by green triangles.

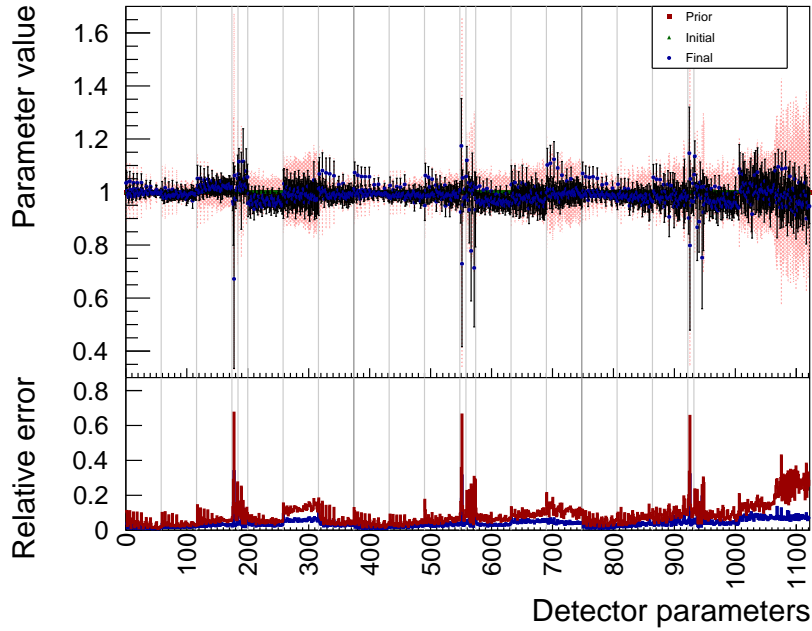


Figure B.27: Prior and post-fit detector parameter values and their associated uncertainty for a fit to NEUT (fake) data with statistical fluctuations on the number of events and systematic parameter throw. The initial thrown parameter values are represented by green triangles.

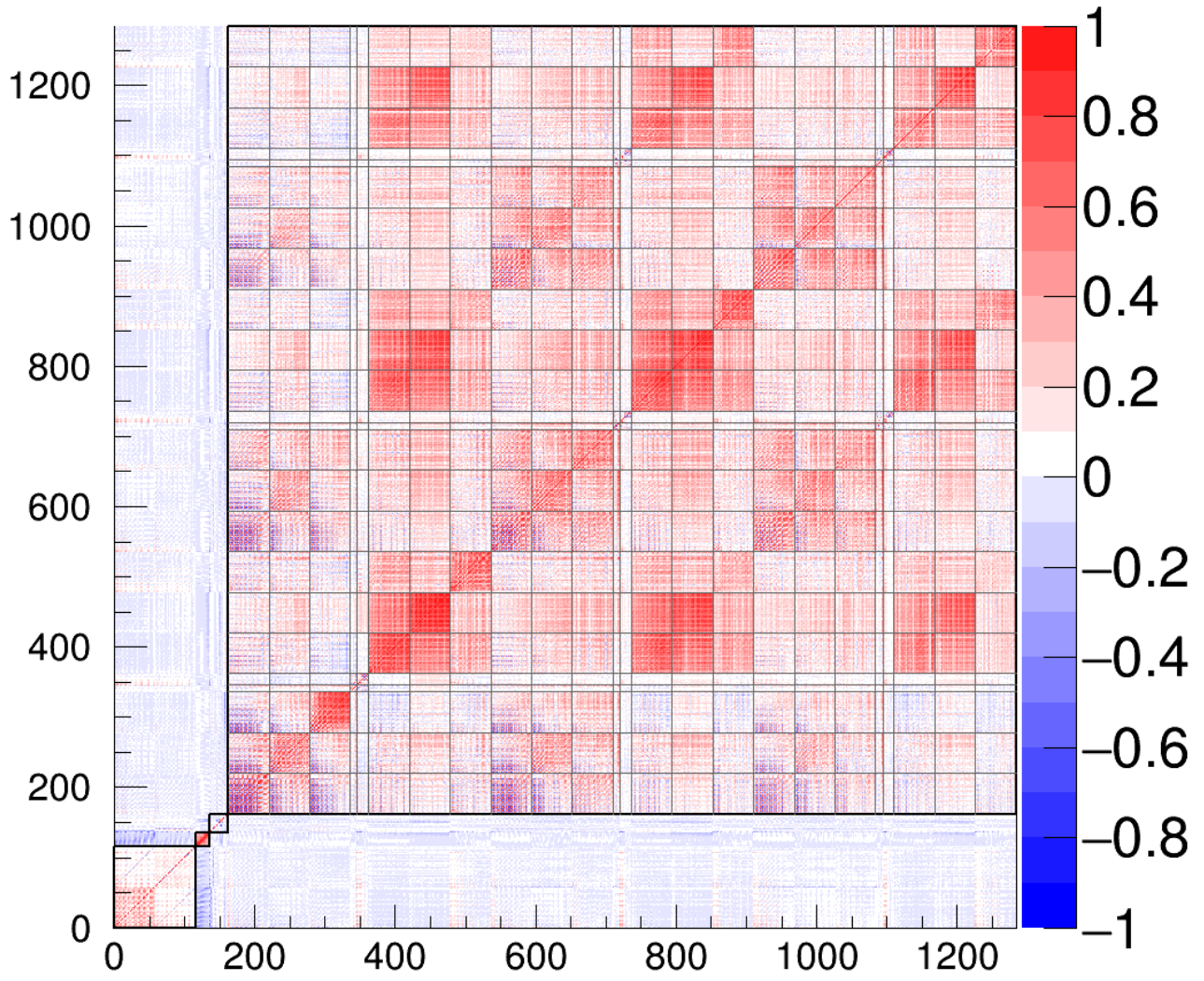


Figure B.29: Post-fit correlation matrix of all the fit parameters for a fit to NEUT (fake) data with statistical fluctuations on the number of events and systematic parameter throw. The sub-matrices for the different types of parameters are separated by dashed black lines. Parameters with bins from 0 to 57 corresponds to the c_i 's, from 58 to 115 o_i 's, from 116 to 135 flux, from 136 to 161 cross-section model and from 162 to 1283 detector parameters.

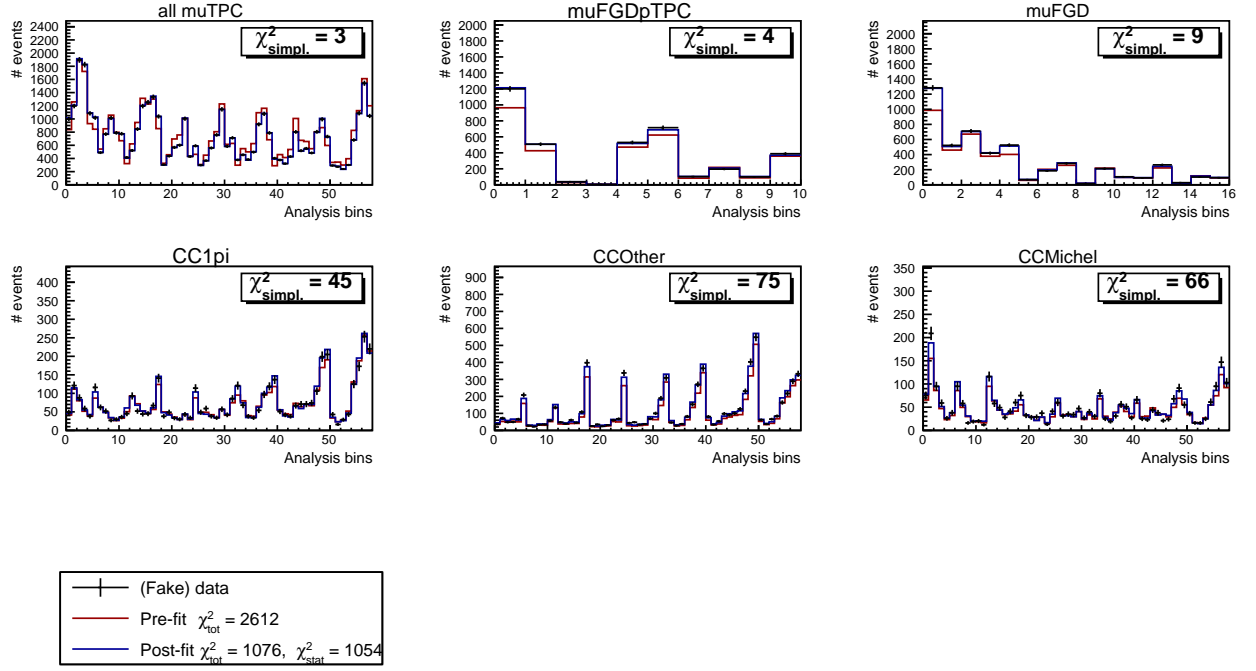


Figure B.30: Prior (blue) and post-fit (red) signal events compared to data (black) distributed in $p_\mu, \cos\theta_\mu$ analysis bins for a fit to NEUT (fake) data with statistical fluctuations on the number of events and systematic parameter throw. Each plot is for a specific signal or sideband region according to its title ; all the muTPC topologies are grouped together in the top left plot.

B. Fit validation

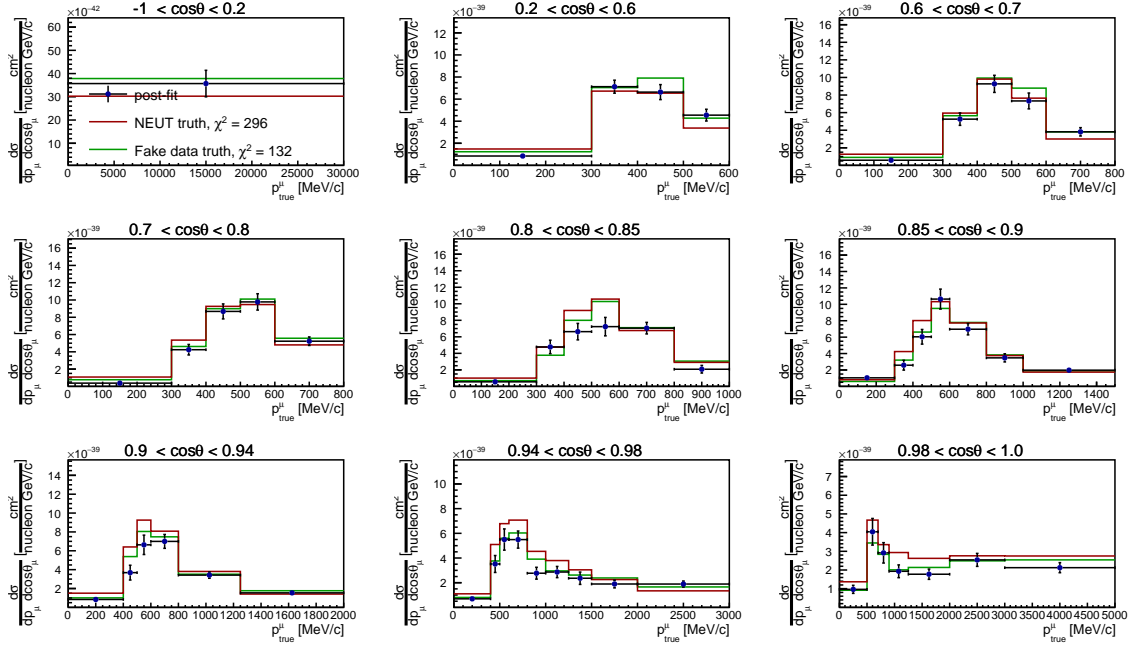


Figure B.31: Flux integrated cross section on carbon, result for a fit to NEUT (fake) data with statistical fluctuations on the number of events and systematic parameter throw. Each plot is for a given angle bin according to its title and the x axis is the muon momentum.

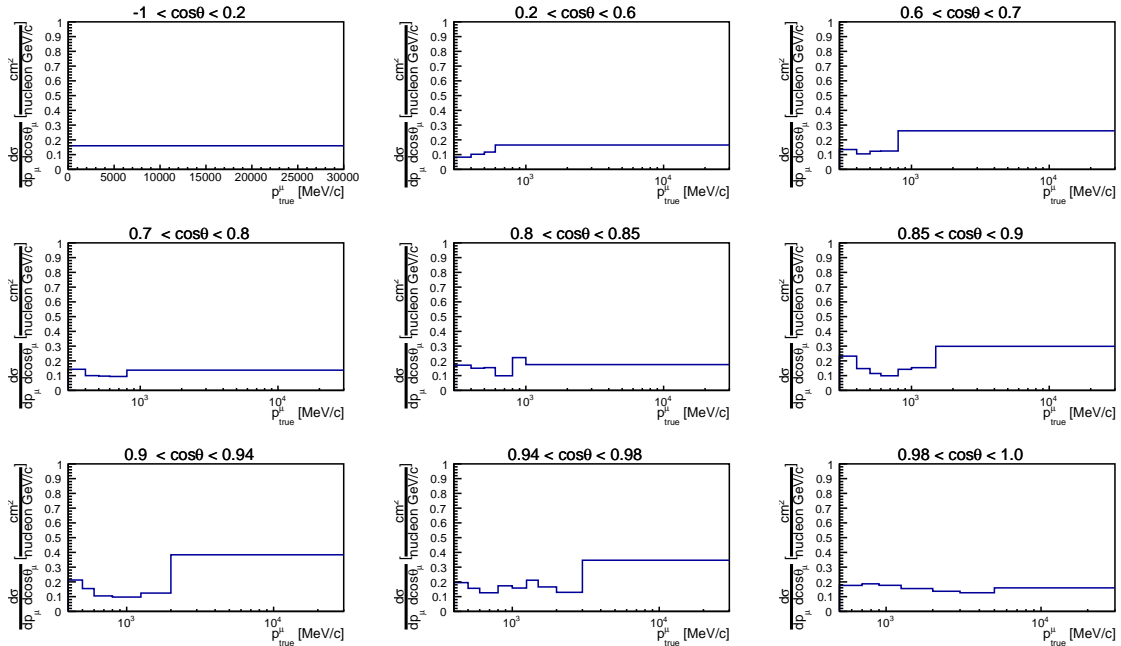


Figure B.32: Relative uncertainty on the cross section on carbon, result for a fit to NEUT (fake) data with statistical fluctuations on the number of events and systematic parameter throw. Each plot is for a given angle bin according to its title and the x axis is the muon momentum.

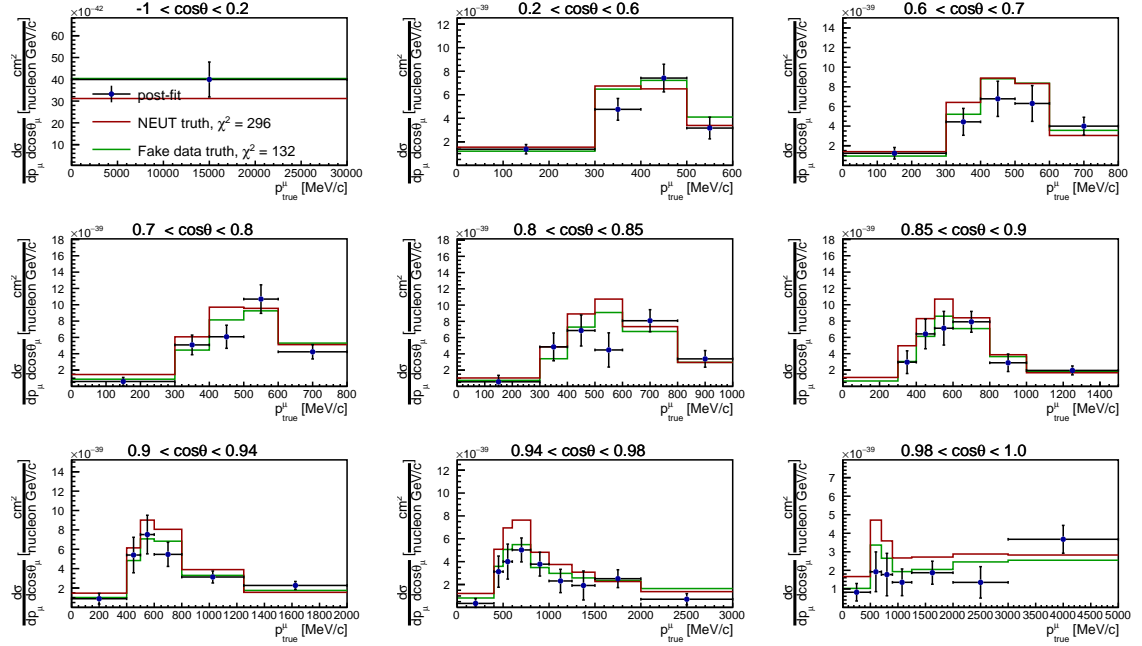


Figure B.33: Flux integrated cross section on oxygen, result for a fit to NEUT (fake) data with statistical fluctuations on the number of events and systematic parameter throw. Each plot is for a given angle bin according to its title and the x axis is the muon momentum.

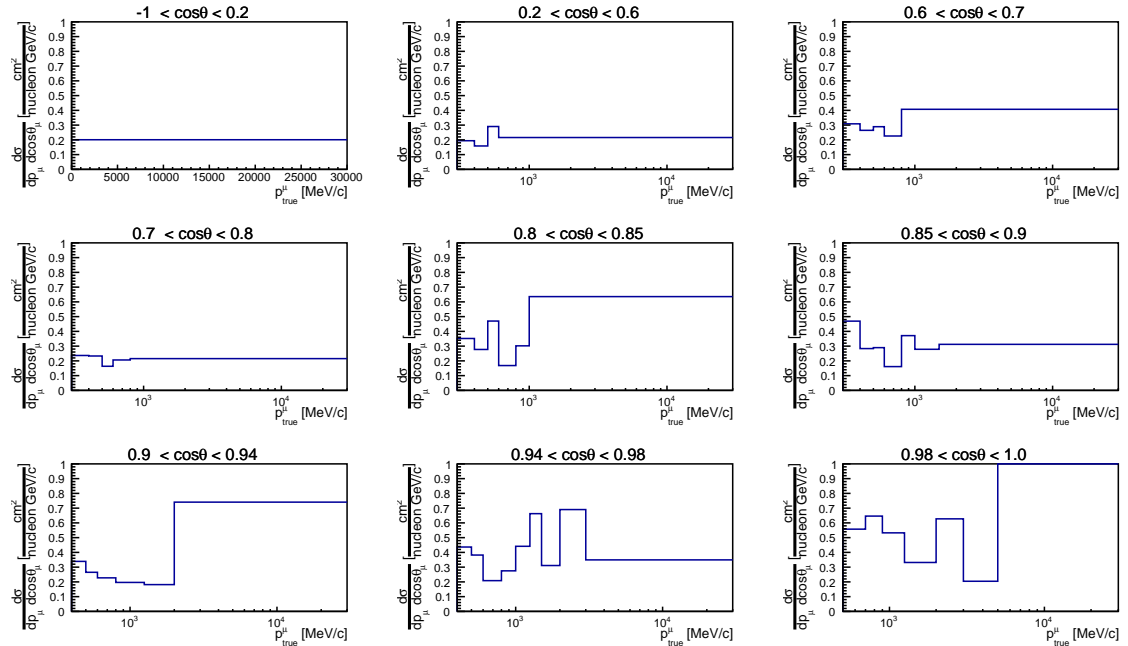


Figure B.34: Relative uncertainty on the cross section on oxygen, result for a fit to NEUT (fake) data with statistical fluctuations on the number of events and systematic parameter throw. Each plot is for a given angle bin according to its title and the x axis is the muon momentum.

B. Fit validation

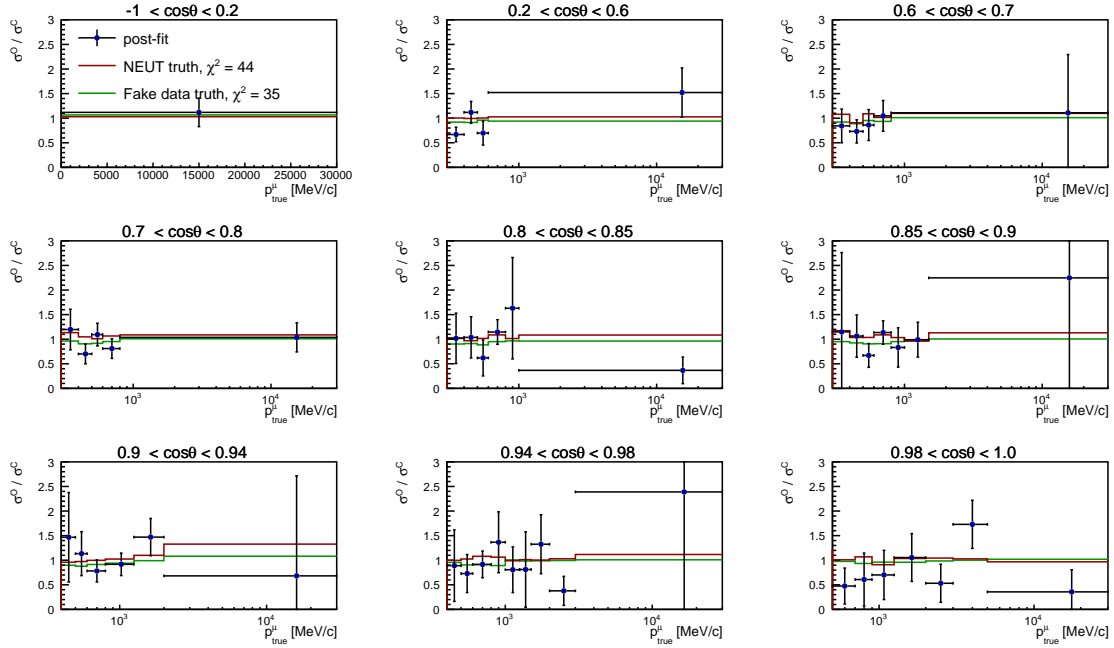


Figure B.35: Oxygen/carbon cross section ratio, result for a fit to NEUT (fake) data with statistical fluctuations on the number of events and systematic parameter throw. Each plot is for a given angle bin according to its title and the x axis is the muon momentum.

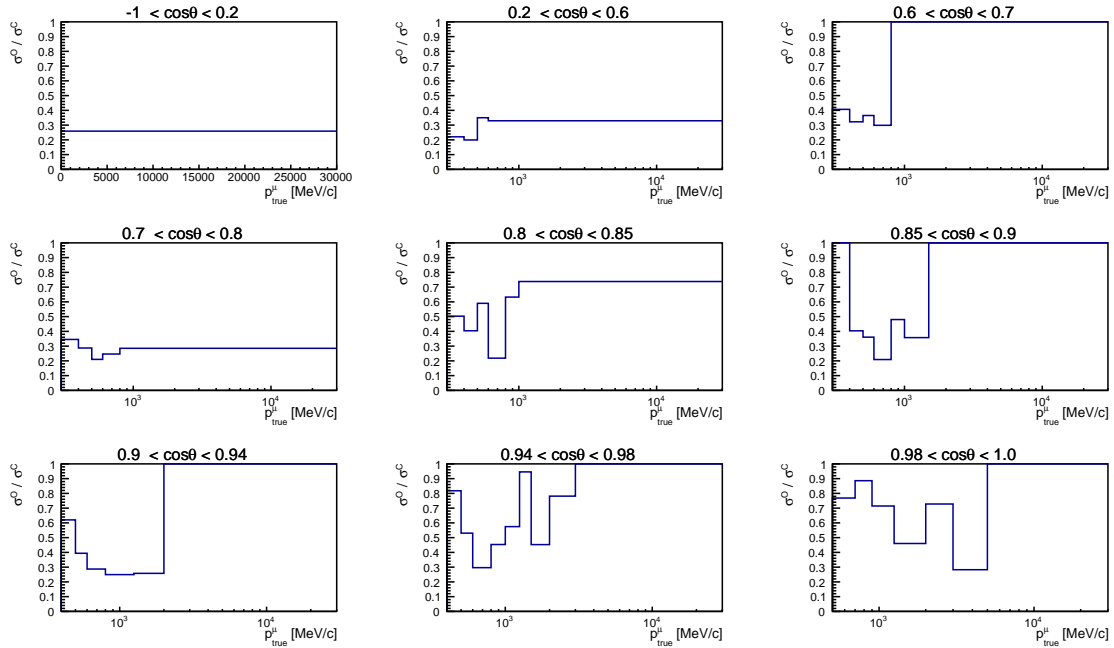


Figure B.36: Relative uncertainty on the oxygen/carbon cross section ratio, result for a fit to NEUT (fake) data with statistical fluctuations on the number of events and systematic parameter throw. Each plot is for a given angle bin according to its title and the x axis is the muon momentum.

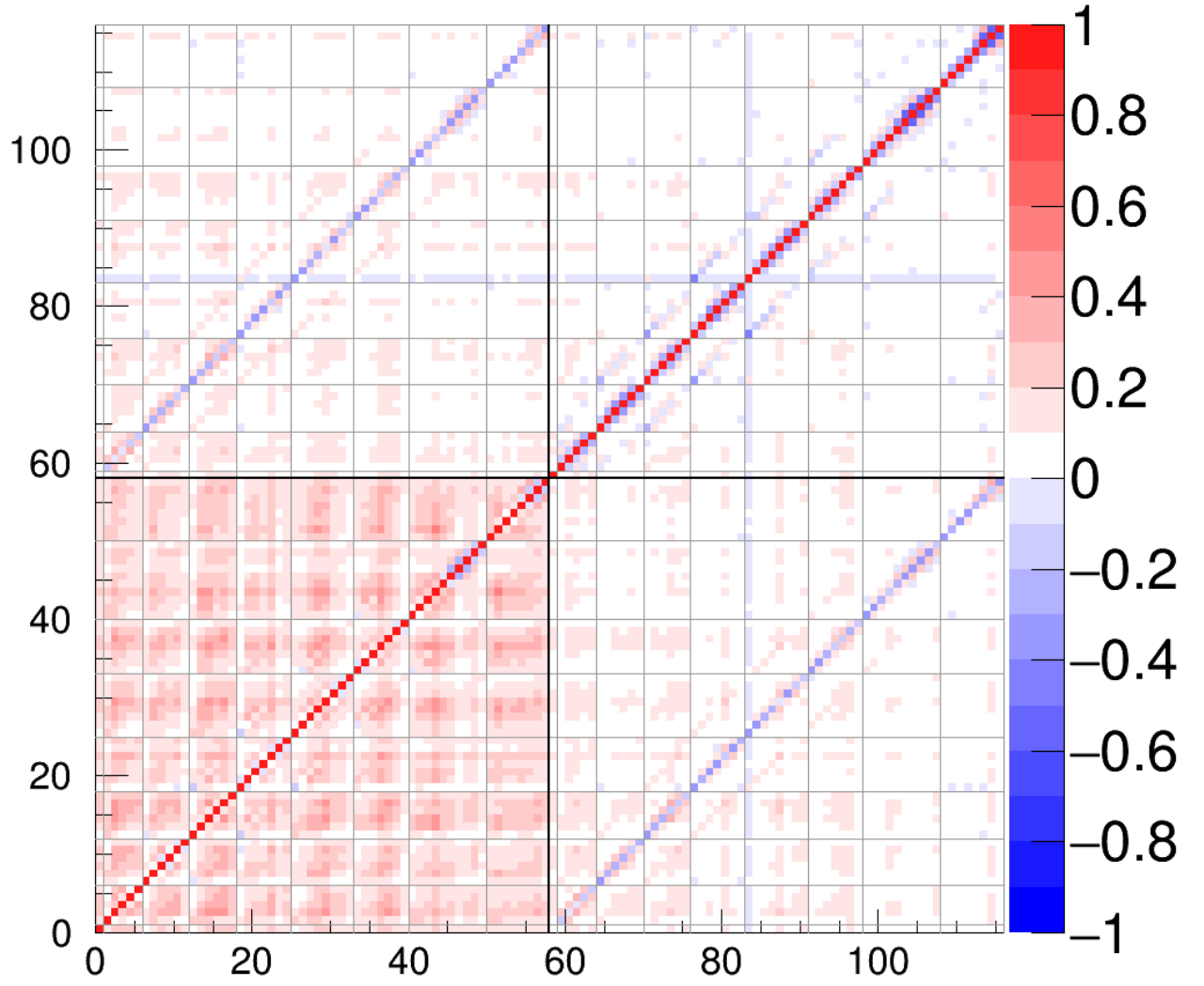


Figure B.37: Final correlation matrix for the cross-section results for a fit to NEUT (fake) data with statistical fluctuations on the number of events and systematic parameter throw. The sub-matrices for the different $\cos \theta_\mu$ bins are separated by dashed black lines. Bins from 0 to 57 corresponds to carbon interactions, from 58 to 115 to oxygen interactions.

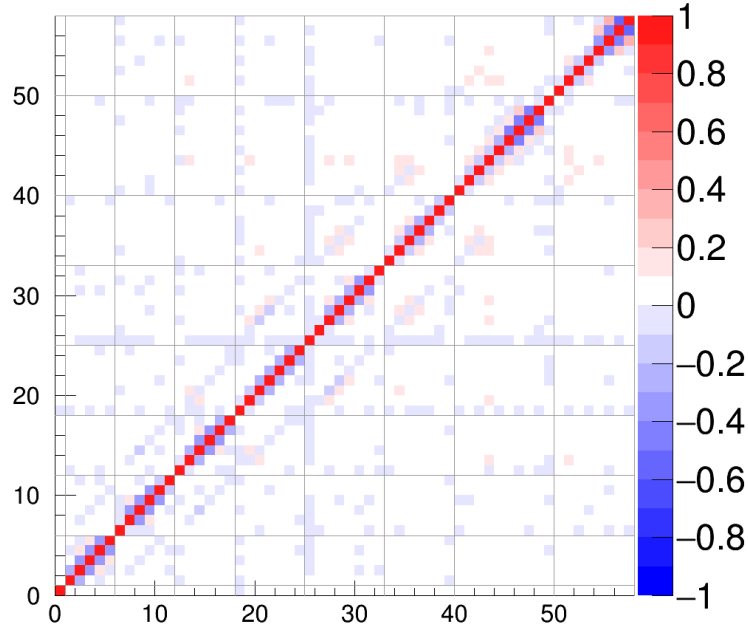


Figure B.38: Final correlation matrix for the cross-section ratio results for a fit to NEUT (fake) data with statistical fluctuations on the number of events and systematic parameter throw. The sub-matrices for the different $\cos\theta_\mu$ bins are separated by dashed black lines.

B.5 Coverage studies

Additional studies are conducted by investigating the fit parameter pulls and χ^2 distributions. For that two series of toy fits are run as described in Sections B.3 and B.4, that is including statistical fluctuations only and then including both, statistical fluctuations and systematic parameter throws.

Coverage studies are an interesting tool to investigate how the fit behaves with statistical variations in the data inputs and in the systematic parameters. The χ^2 distribution of the different toys is expected to behave as the χ^2 probability density function for $N_{\text{d.o.f}}$ equal to the number of reconstructed bins (which is 1122) minus the number of uncorrelated parameters (which we cannot predict before we draw the χ^2 distribution). A deviation in the distribution of the final χ^2 larger than $N_{\text{d.o.f}}$ may show possible under-coverage of the fit results.

B.5.1 Pull definition

We first study the pull, that is the deviation of the fit parameters from their prior values. The pull of one parameter p is defined as

$$\delta p = \frac{p_{\text{prior}} - p_{\text{fit}}}{\epsilon_{\text{fit}}} \quad (\text{B.2})$$

where p_{prior} is the prior value of the parameter, p_{fit} the post-fit value and ϵ_{fit} its associated error.

B.5.2 Results for statistical fluctuations only

Here 100 toy fits are run; 6 of them did not converge and are therefore not taken into account. The pull mean over toys in each bin and associated RMS are shown in the top plots of Fig.

B.39, B.40, B.41 and B.42 for each type of fit parameters. On the bottom plots the distributions of the mean values in each parameter bin is shown. All the pull distributions are centered at values compatible with zero.

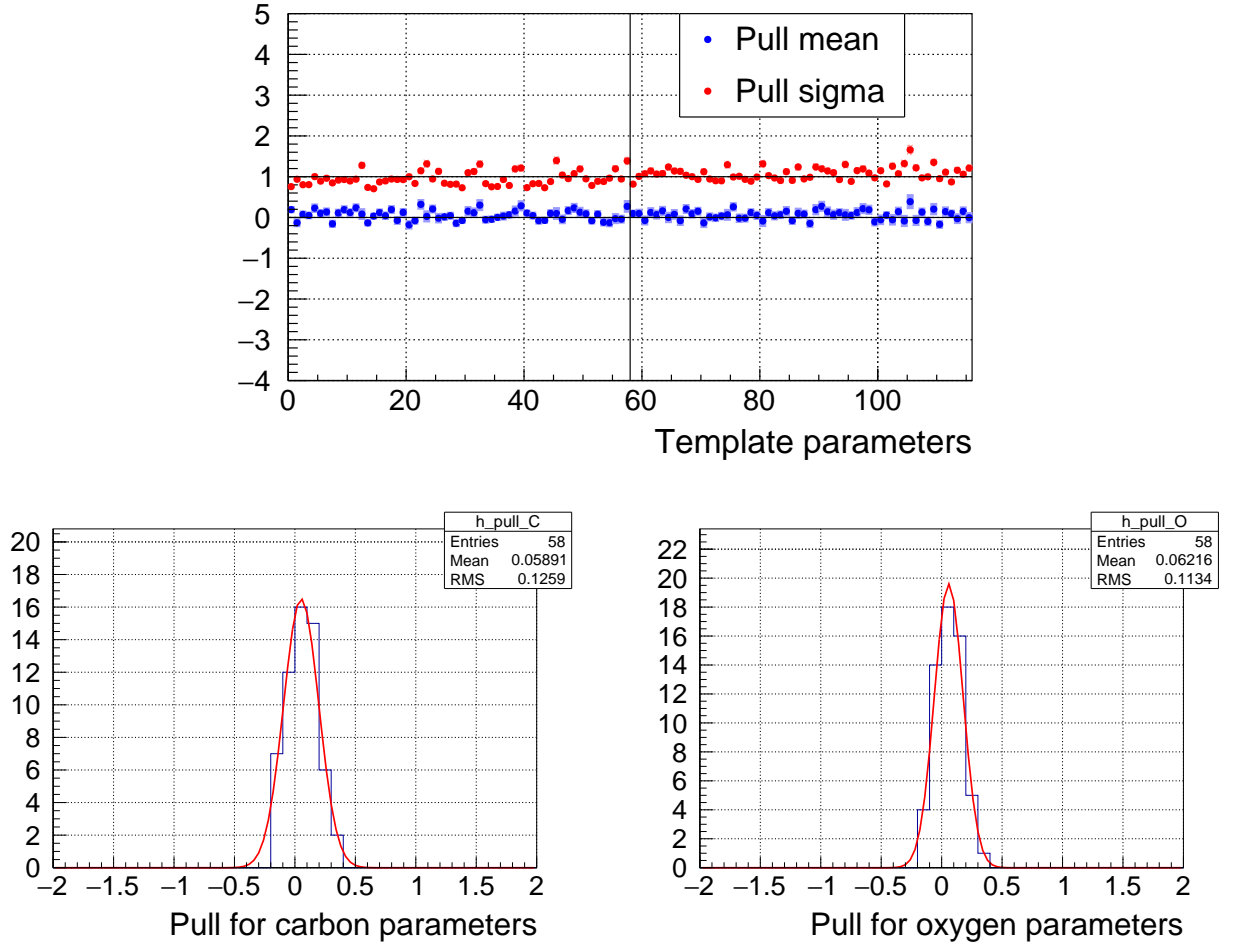


Figure B.39: Pull mean and RMS values of the template parameters (top) and their distributions (bottom). On the top the first 58 bins are the parameters for carbon (c_i 's) and the next 58 bins are for oxygen (o_i 's).

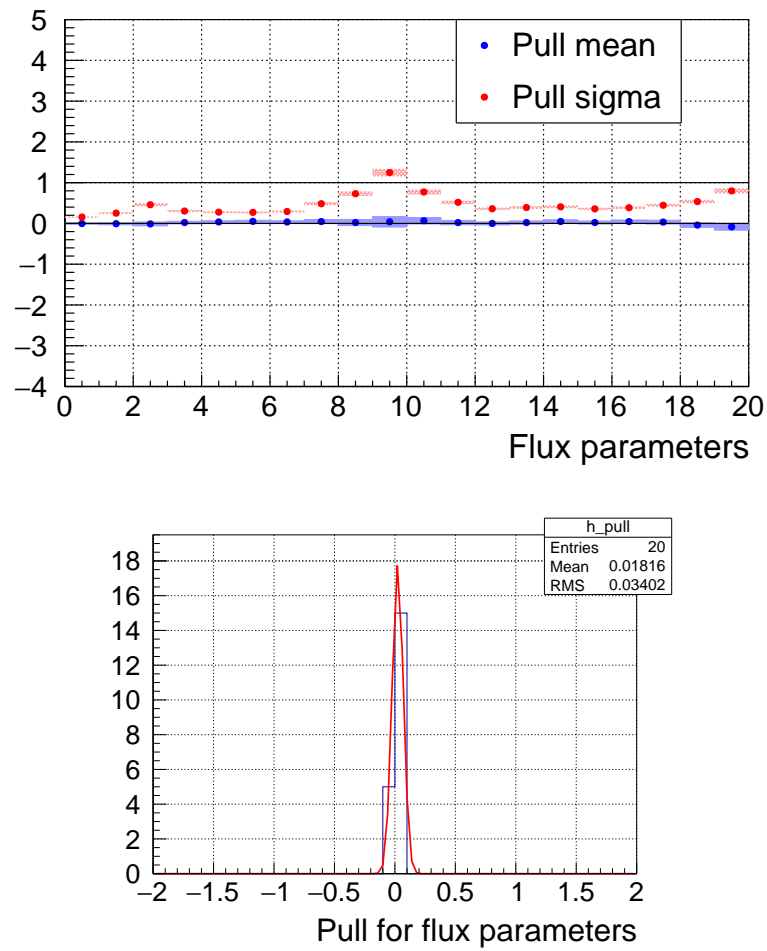


Figure B.40: Pull mean and RMS values of the flux parameters (top) and their distributions (bottom).

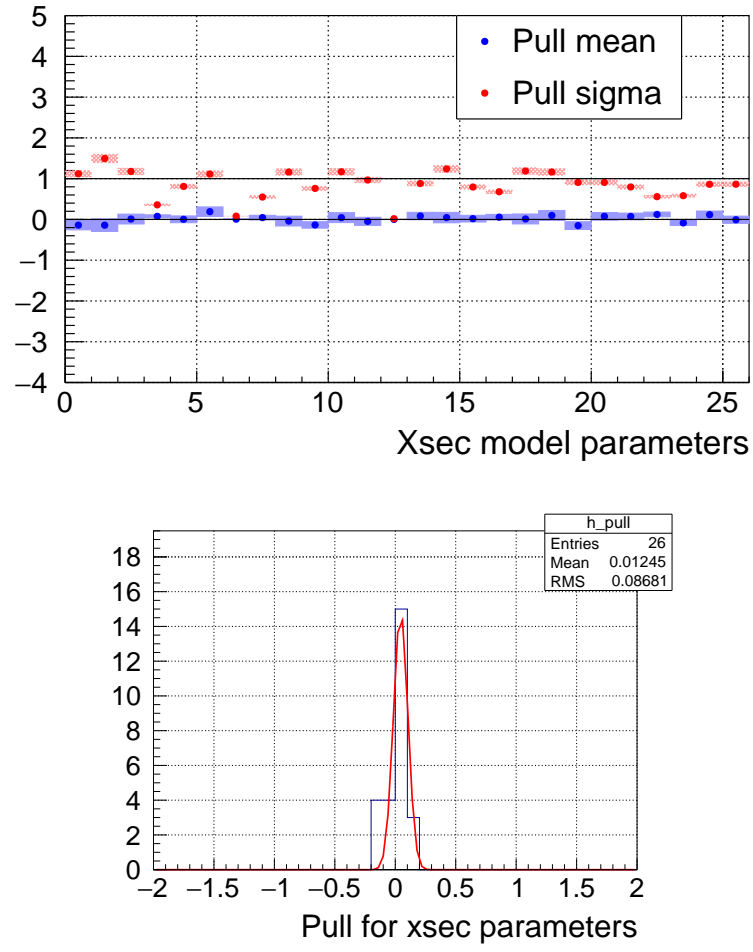


Figure B.41: Pull mean and RMS values of the cross-section model parameters (top) and their distributions (bottom).

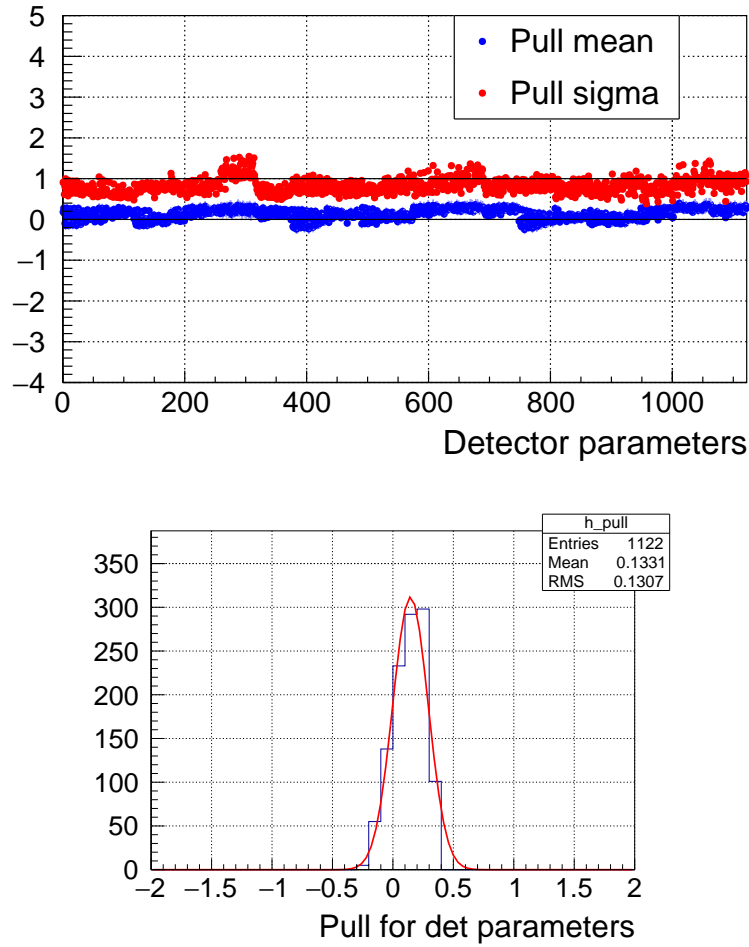


Figure B.42: Pull mean and RMS values of the detector parameters (top) and their distributions (bottom).

The $\chi^2_{\text{post-fit}}$ distribution with normalised area is shown in Fig. B.43. It is interesting to see that the post-fit distribution is centered at 987 which tells us information about the number of uncorrelated fit parameters, being in this case slightly higher than 100 (the difference to the number of reconstructed bins that is 1122).

The χ^2_{xsec} distribution is plotted in Fig. B.44. The distribution is centered around 100 which is lower than the number of template parameters, showing an expected behaviour of the fit including statistical fluctuations only.

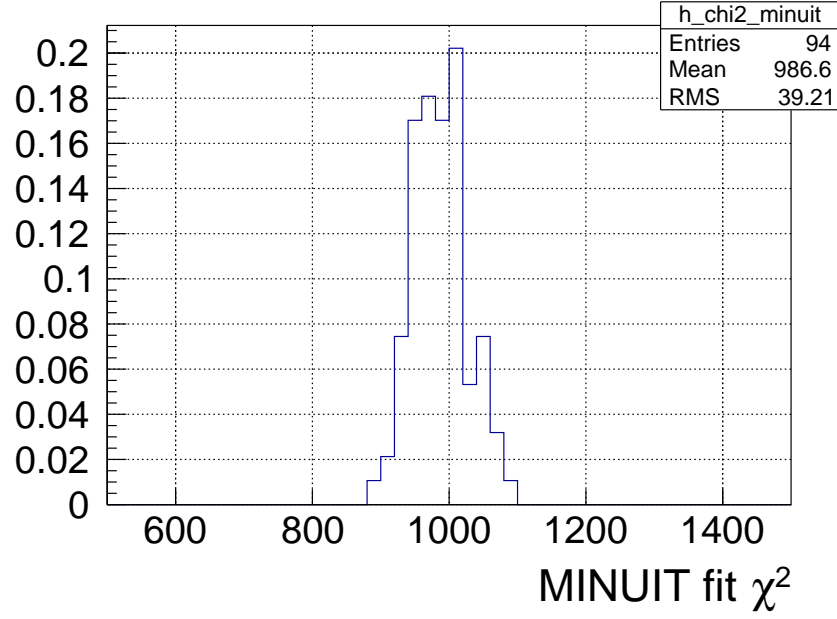


Figure B.43: Distribution of post-fit χ^2 given by MINUIT for 200 toy fits.

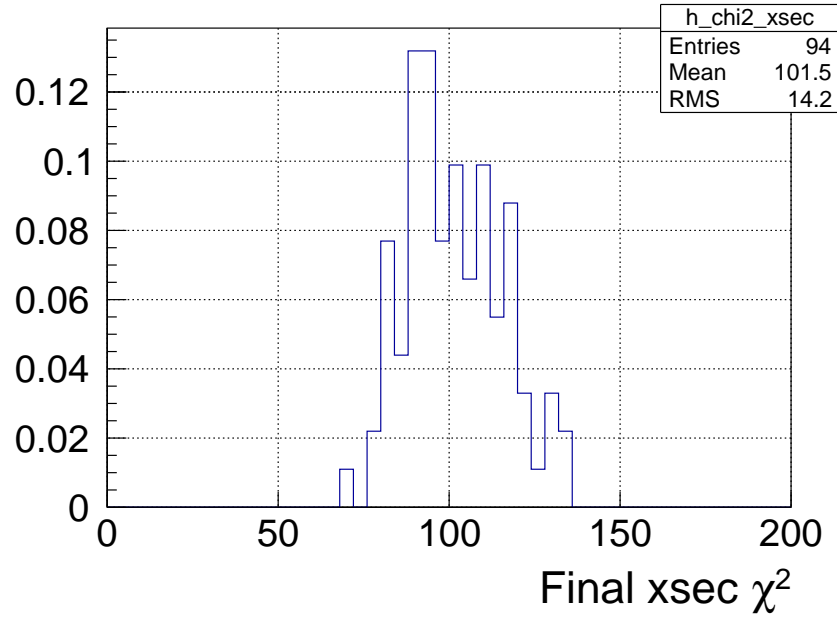


Figure B.44: Distribution of cross-section χ^2 calculated according to (5.2) for 200 toy fits (blue histogram) compared to the χ^2 p.d.f. for 116 degrees of freedom.

B.5.3 Results for statistical fluctuations and systematic parameter throw

Now 100 toy fits are run with additional systematic parameter throw. Nine of them, which did not converge, are not included in the results. The pull mean over toys in each bin and associated RMS are shown in the top plots of Fig. B.45, B.46, B.47 and B.48 for each type of fit parameters

B. Fit validation

and the distributions of the mean values in each parameter bin are shown in the associated bottom plots. Again, the pull distributions are centered at values that are compatible with zero as expected.

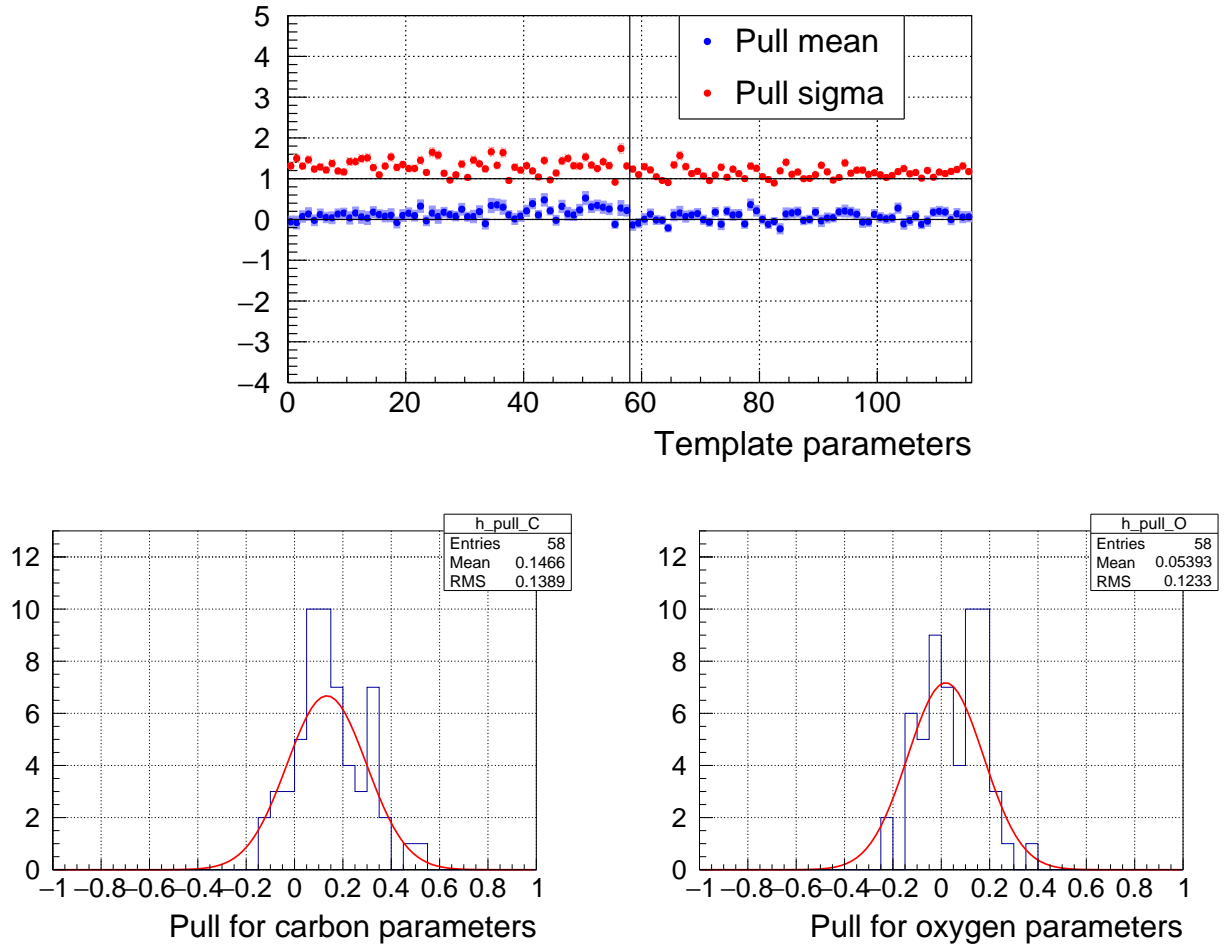


Figure B.45: Pull mean and RMS values of the template parameters (top) and their distributions (bottom). On the top the first 58 bins are the parameters for carbon (c_i 's) and the next 58 bins are for oxygen (o_i 's).

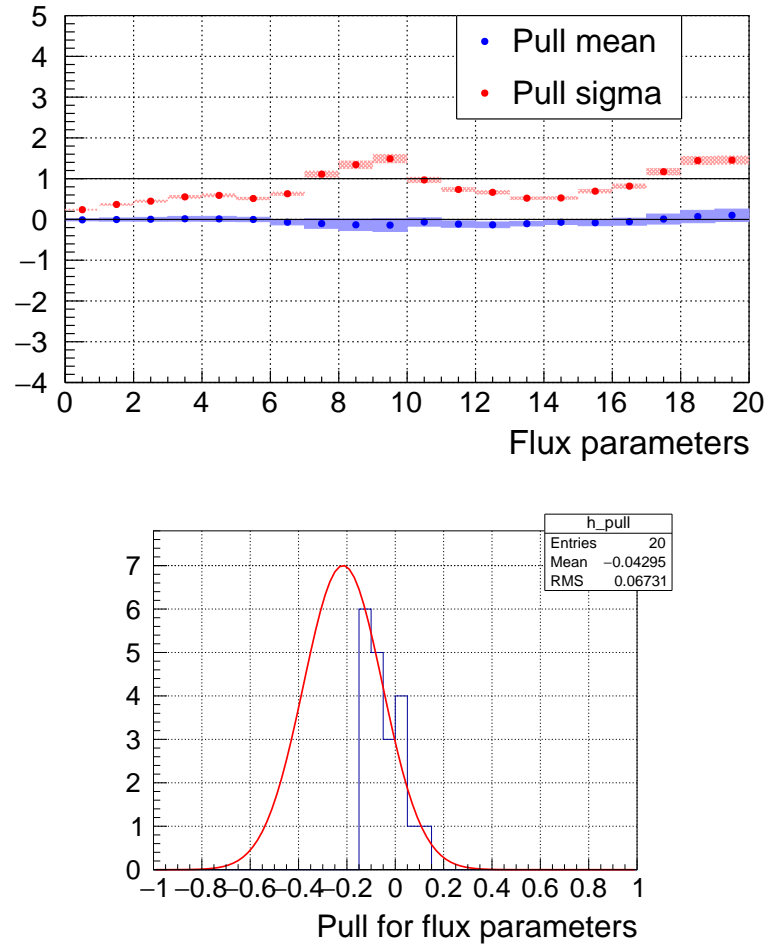


Figure B.46: Pull mean and RMS values of the flux parameters (top) and their distributions (bottom).

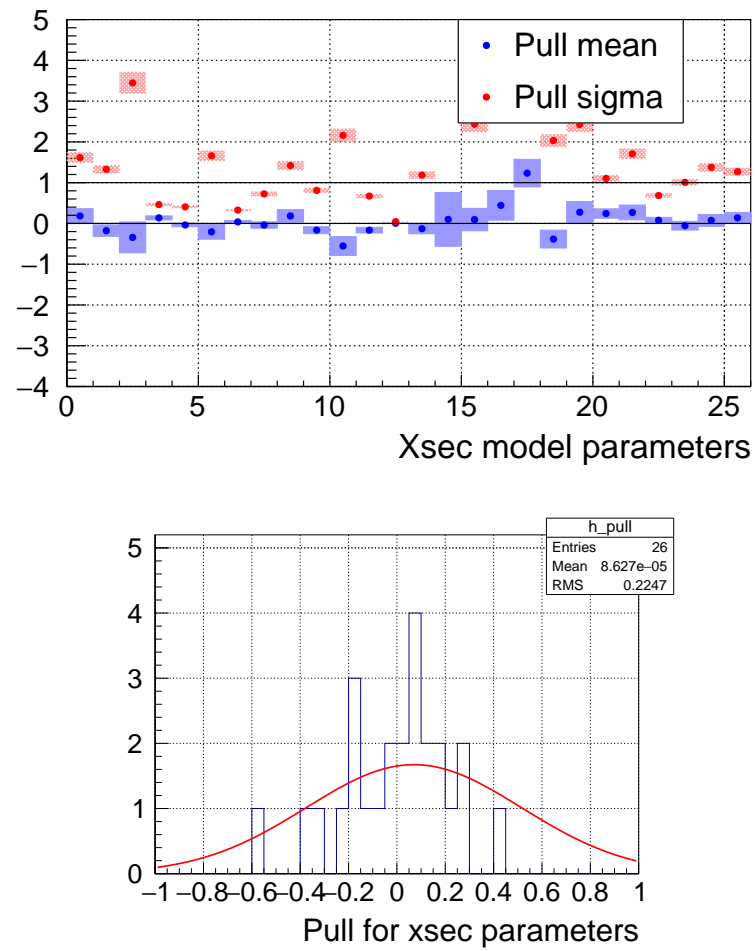


Figure B.47: Pull mean and RMS values of the cross-section model parameters (top) and their distributions (bottom).

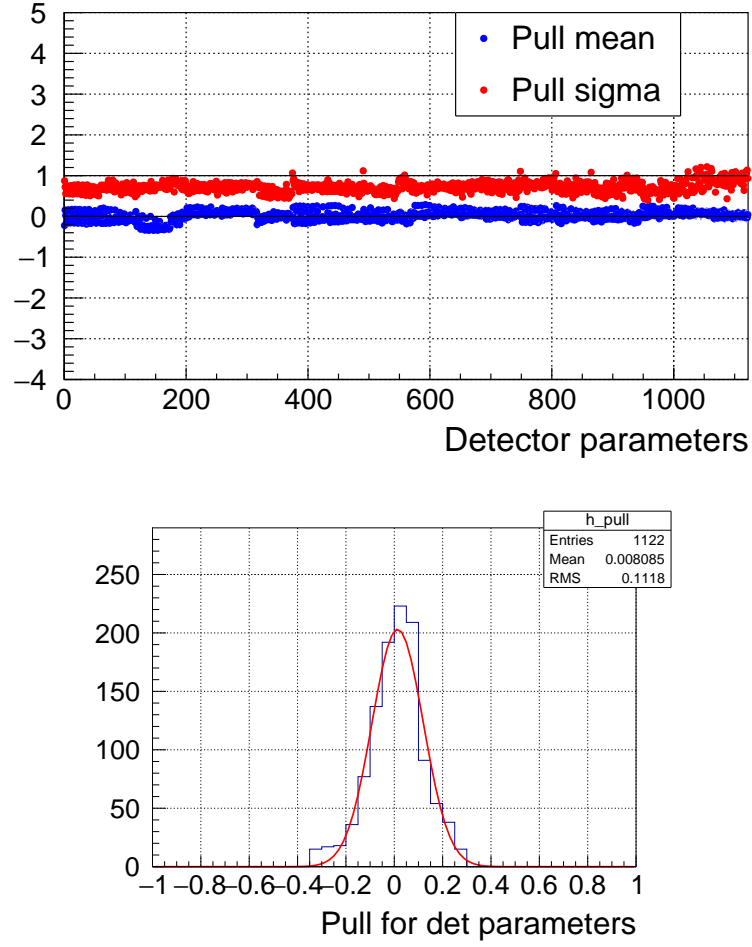


Figure B.48: Pull mean and RMS values of the detector parameters (top) and their distributions (bottom).

The $\chi^2_{\text{post-fit}}$ distribution, shown in Fig. B.49, is centered at 1000, similar to the previous value (987) and the χ^2_{xsec} distribution, plotted in Fig. B.50, is centered around 100 again. Like in the case of statistical fluctuations only these results show a good behaviour of the fit under statistical fluctuations, but also under systematic variations.

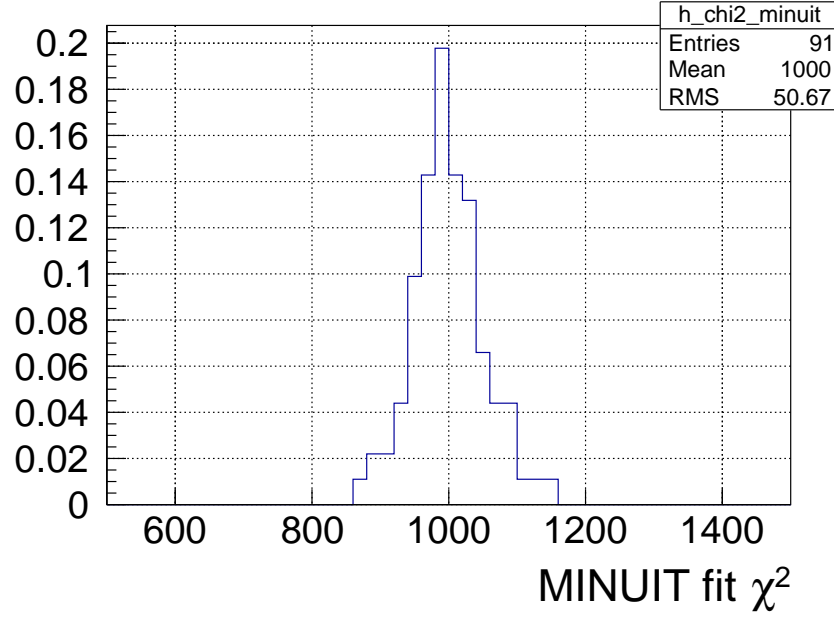


Figure B.49: Distribution of post-fit χ^2 given by MINUIT for 200 toy fits.

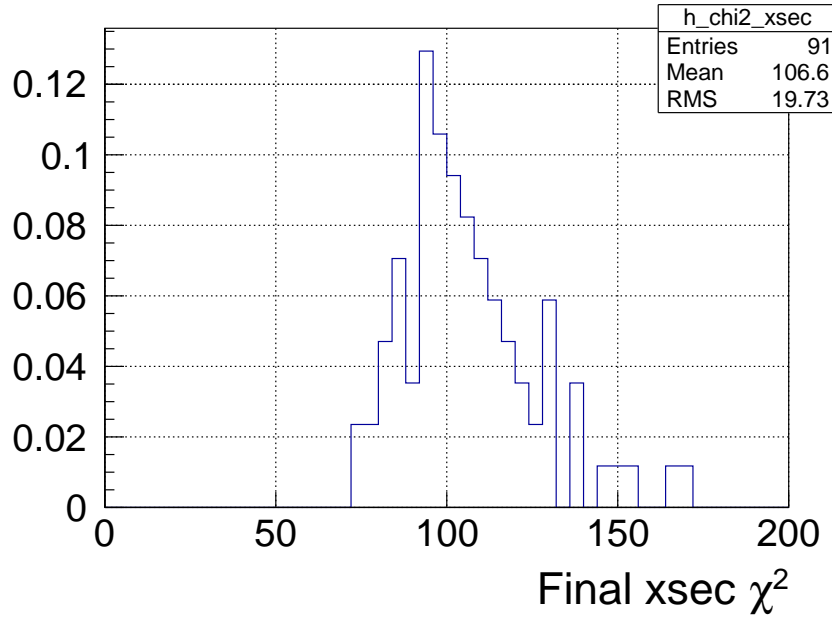


Figure B.50: Distribution of cross-section χ^2 calculated according to (5.2) for 200 toy fits (blue histogram) compared to the χ^2 p.d.f. for 116 degrees of freedom.

B.6 Signal and background biased studies

To study possible bias in the signal we vary artificially the amount of CC- 0π interactions on carbon or oxygen in the NEUT sample that is used as mock data. In this case the fake data input has the same POT than the nominal MC and no statistical fluctuations are applied, we only look at variations in the signal event numbers. Following fake data sets are built:

1. Number of signal events in carbon increased by 30 %
2. Number of signal events in carbon decreased by 30 %
3. Number of signal events in oxygen increased by 30 %
4. Number of signal events in oxygen decreased by 30 %

One can verify in Fig. B.51 that the template parameters are adapted as expected by the fitter, for instance when the number of signal events with interactions on carbon (top plots) is increased (decreased) by 30% then the template parameters on carbon are adjusted up to 1.3 (down to 0.7), whereas the systematic parameters just keep their prior values. The same happens for oxygen (bottom plots).

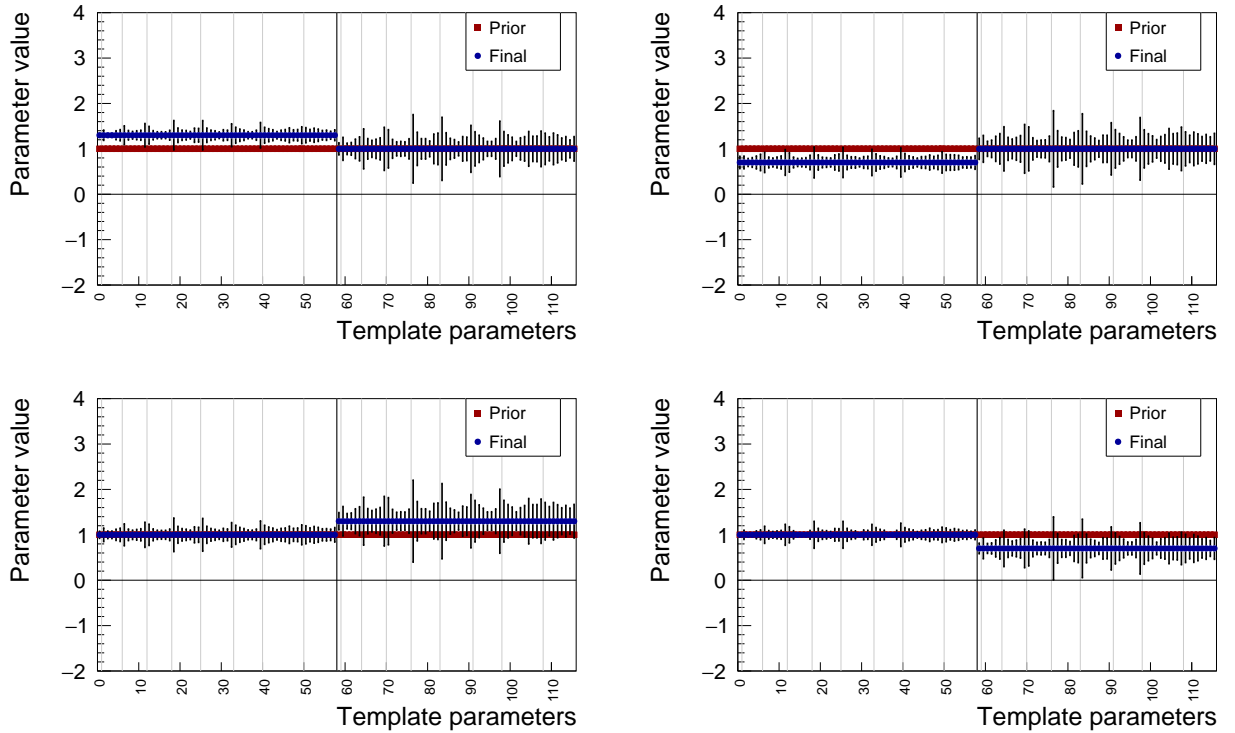


Figure B.51: Prior and post-fit template parameter values and their errors for fits to fake data with biased signal, +30% carbon (top left), -30% carbon (top right), +30% oxygen (bottom left), -30% oxygen (bottom right). The first 58 parameters correspond to the carbon parameters (c_i) and the next 58 parameters are the ones on oxygen (o_i).

One also needs to check the impact of variations in the background regions. Therefore we build following fake data sets where the number of resonant or DIS interactions are increased/decreased similarly to the signal as described above:

1. Number of resonant reactions increased by 30 %
2. Number of resonant reactions decreased by 30 %
3. Number of DIS reactions increased by 30 %
4. Number of DIS reactions decreased by 30 %

Resonant interactions are expected to happen at higher momentum range and it can be verified that the fitter behaves well by looking at the parameter results in the top plots of Fig. B.52. Indeed if the number of such interactions is increased then values of the template parameters in higher momentum bins are decreased by the fitter, as their values weight the number of signal event in each kinematic bin (top left plot) and vice versa if the number of resonant interactions is decreased (top right plot). Similar effect appears for DIS (bottom plots).

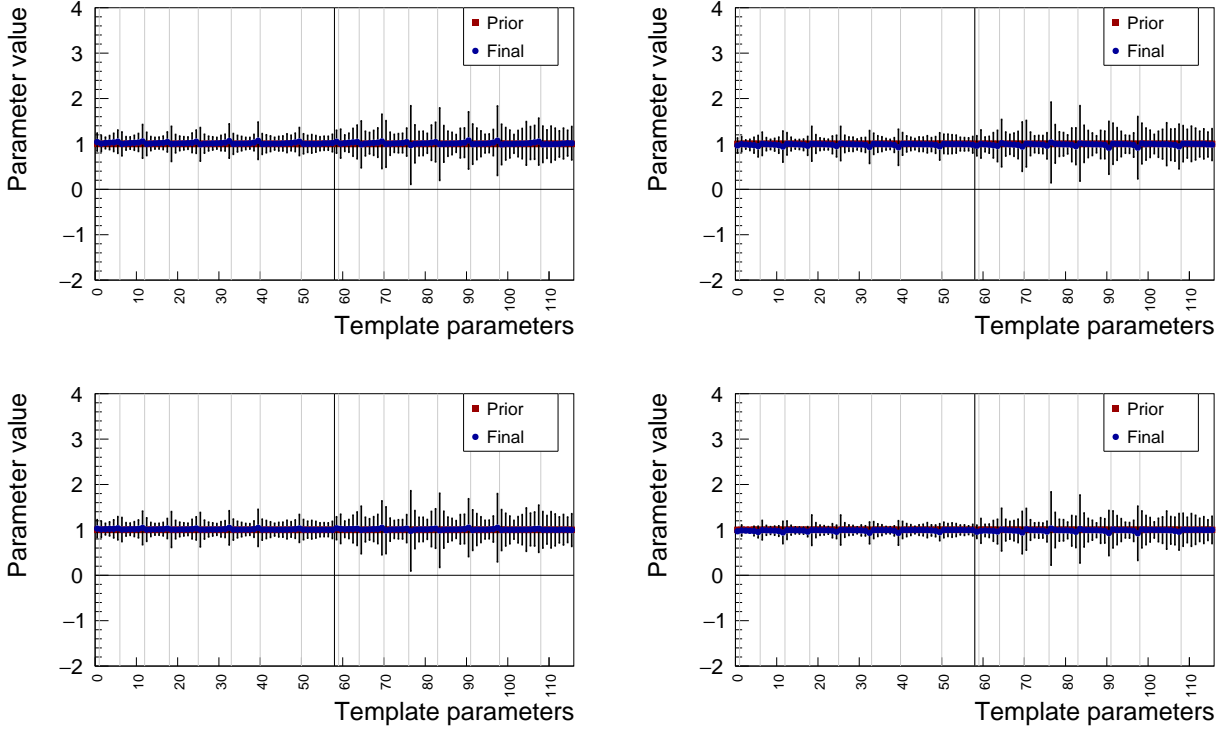


Figure B.52: Prior and post-fit template parameter values and their associated uncertainty for fits to fake data with biased backgrounds, +30% resonant (top left), -30% resonant (top right), +30% DIS (bottom left), -30% DIS (bottom right). The first 58 parameters correspond to the carbon parameters (c_i) and the next 58 parameters are the ones on oxygen (o_i).

B.7 Fake data from other event generators

Further studies are conducted by using events generated by another Monte Carlo generator as (fake) data inputs that we fit to the nominal NEUT simulated events. We use events simulated with GENIE 2.8.0 [74] as (fake) data inputs. We remind that Table 1.1 shows an overview of the models implemented in the different neutrino generator versions that are used in this analysis.

Results of the GENIE fake data fit are plotted in Fig. B.53 to B.63. The results show a good ability of the fitter to fit MC events generated by another generator than events in the nominal MC input. The post-fit and final cross-section χ^2 's have values that are smaller than the number of degrees of freedom, i.e. the number of effective fit parameters and the number of analysis bins respectively. It can be noted that the MEC normalisation parameters for carbon and oxygen are pushed close to zero (numbers 2 and 5 respectively in the left plot of Fig. B.56). It may be due to the fact that GENIE does not have 2p2h implemented and those parameters are accounting for it.

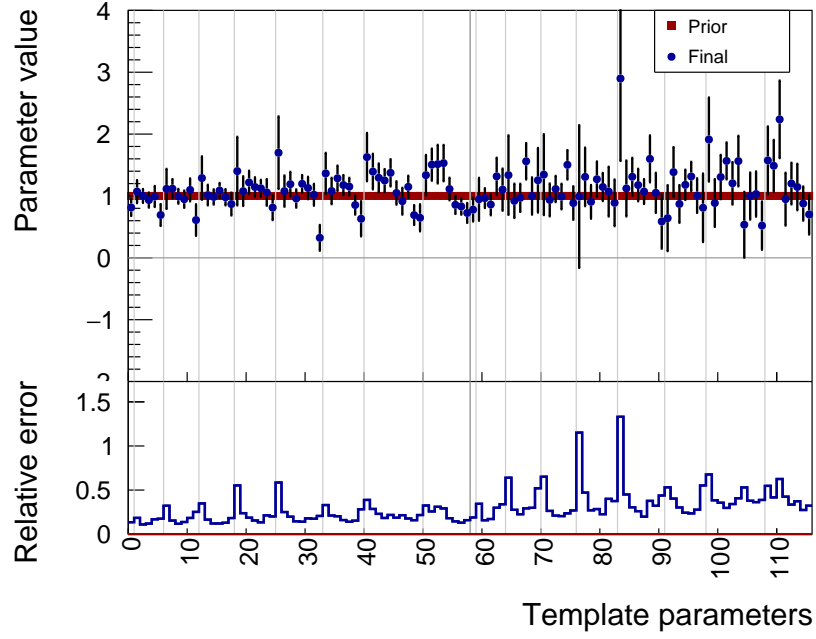


Figure B.53: Prior and post-fit template parameter values and their associated uncertainty for a fit to the (fake) data set using GENIE generated events. The first 58 parameters correspond to the carbon parameters (c_i) and the next 58 parameters are the ones on oxygen (o_i).

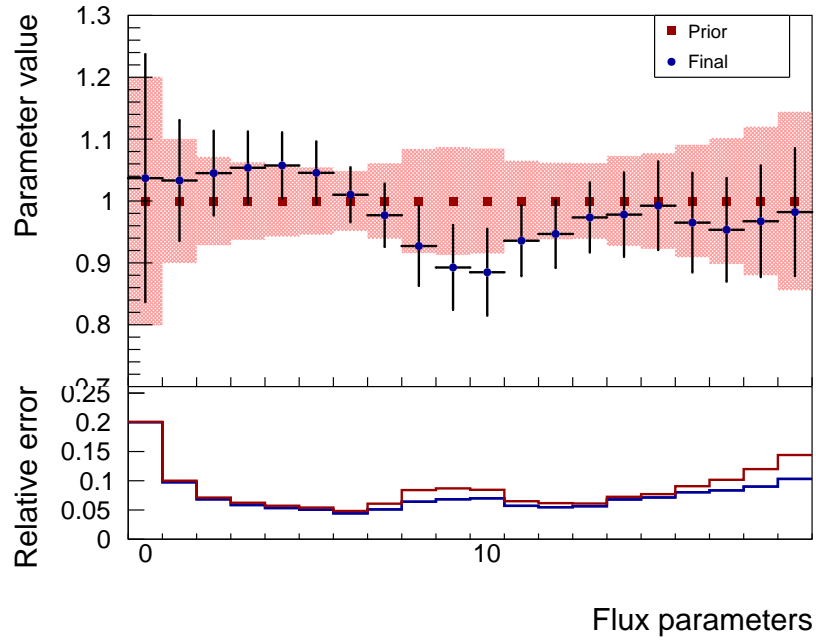


Figure B.54: Prior and post-fit flux parameter values and their associated uncertainty for a fit to the (fake) data set using GENIE generated events.

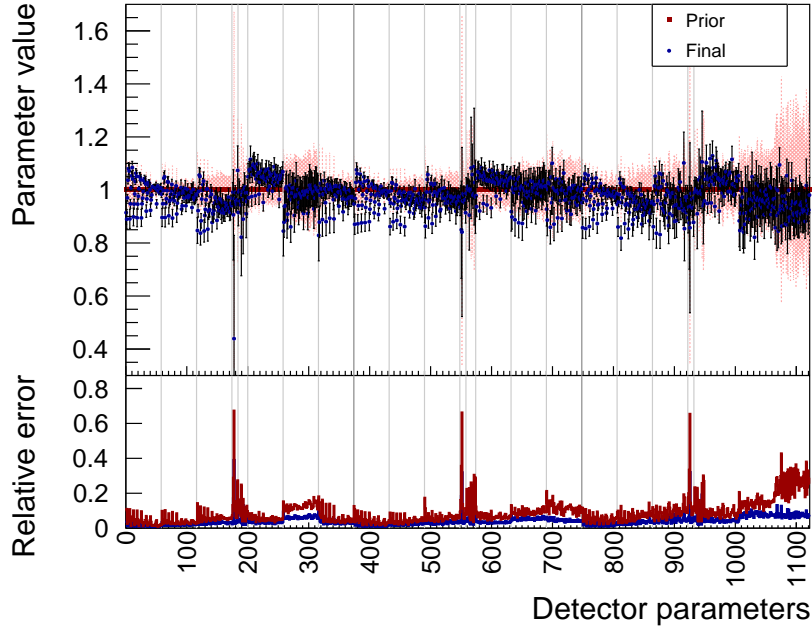


Figure B.55: Prior and post-fit detector parameter values and their associated uncertainty for a fit to the (fake) data set using GENIE generated events.

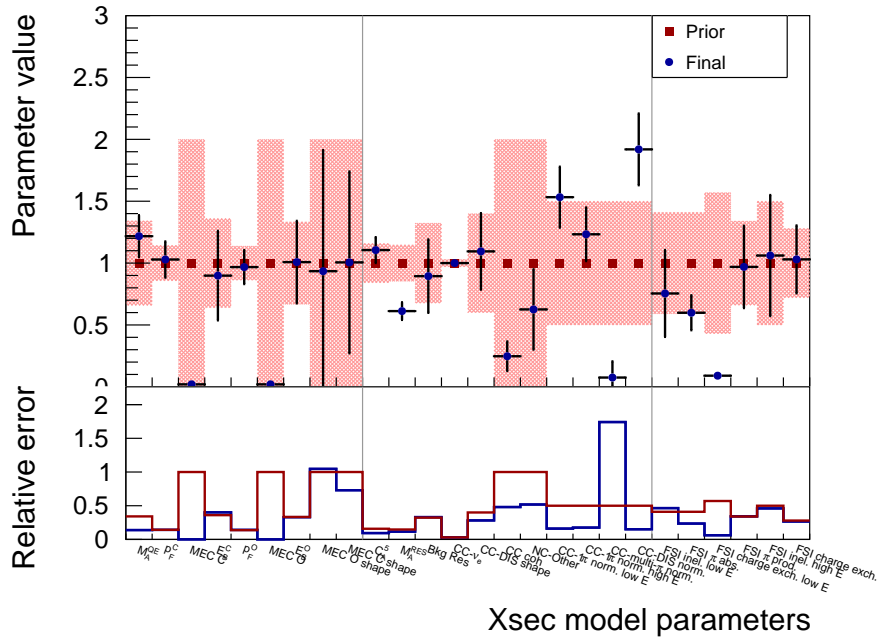


Figure B.56: Prior and post-fit cross-section model parameter values and their associated uncertainty for a fit to the (fake) data set using GENIE generated events.

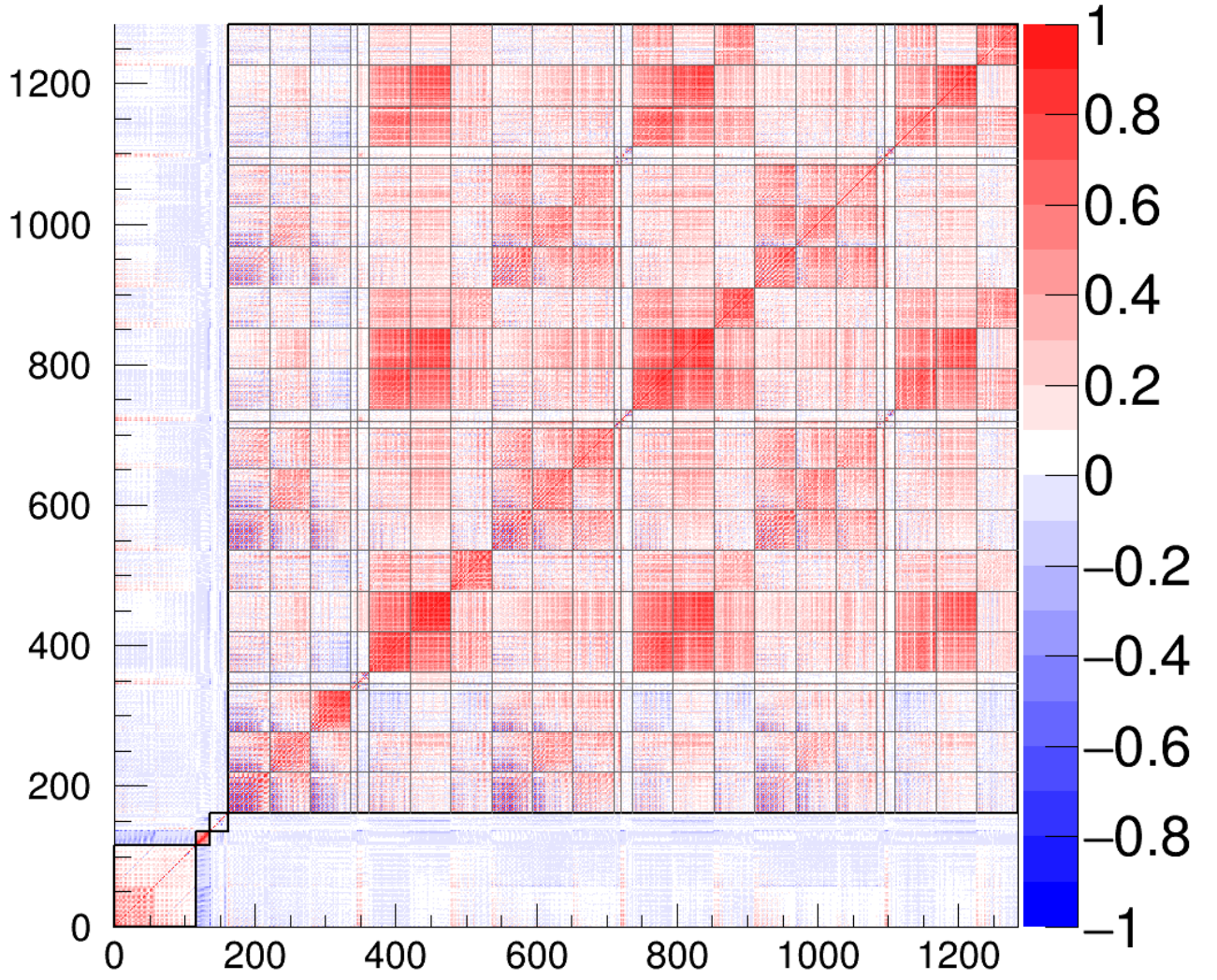


Figure B.57: Post-fit correlation matrix of all the fit parameters for a fit to the (fake) data set using GENIE generated events. The sub-matrices for the different types of parameters are separated by dashed black lines. Parameters with bins from 0 to 57 corresponds to the c_i 's, from 58 to 115 o_i 's, from 116 to 135 flux, from 136 to 161 cross-section model and from 162 to 1283 detector parameters.

B. Fit validation

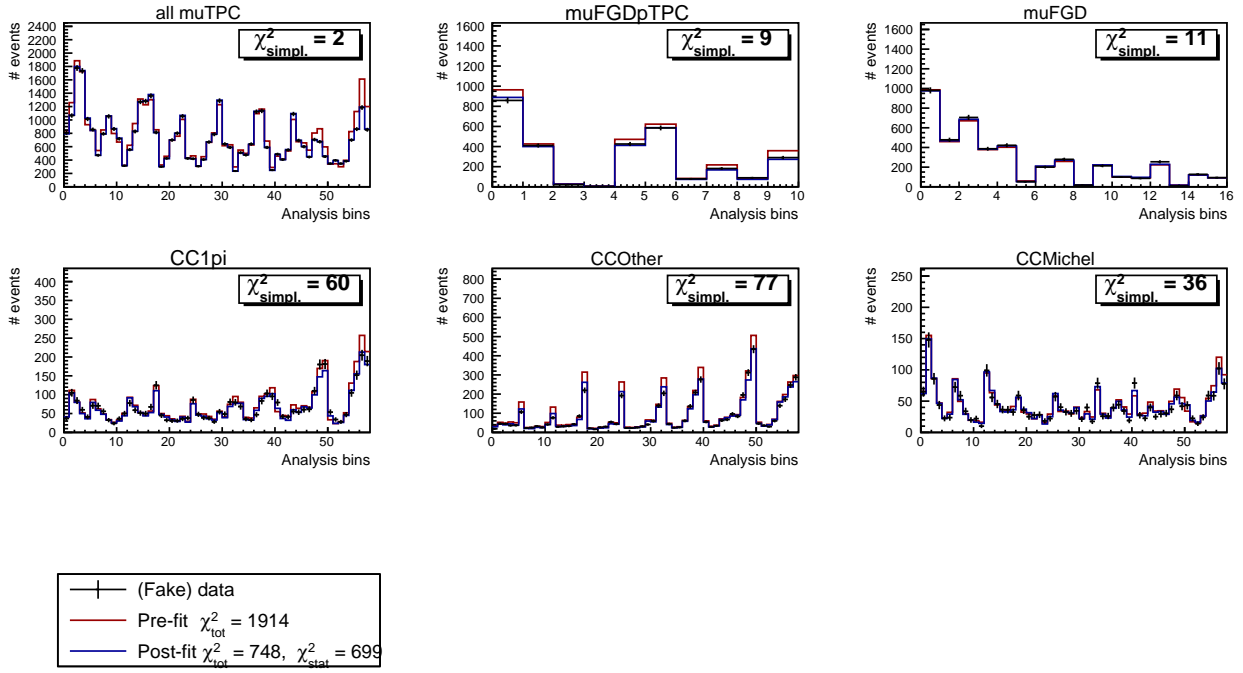


Figure B.58: Prior (blue) and post-fit (red) signal events compared to data (black) distributed in $p_\mu, \cos\theta_\mu$ analysis bins for a fit to the (fake) data set using GENIE generated events. Each plot is for a specific signal or sideband region according to its title ; all the muTPC topologies are grouped together in the top left plot.

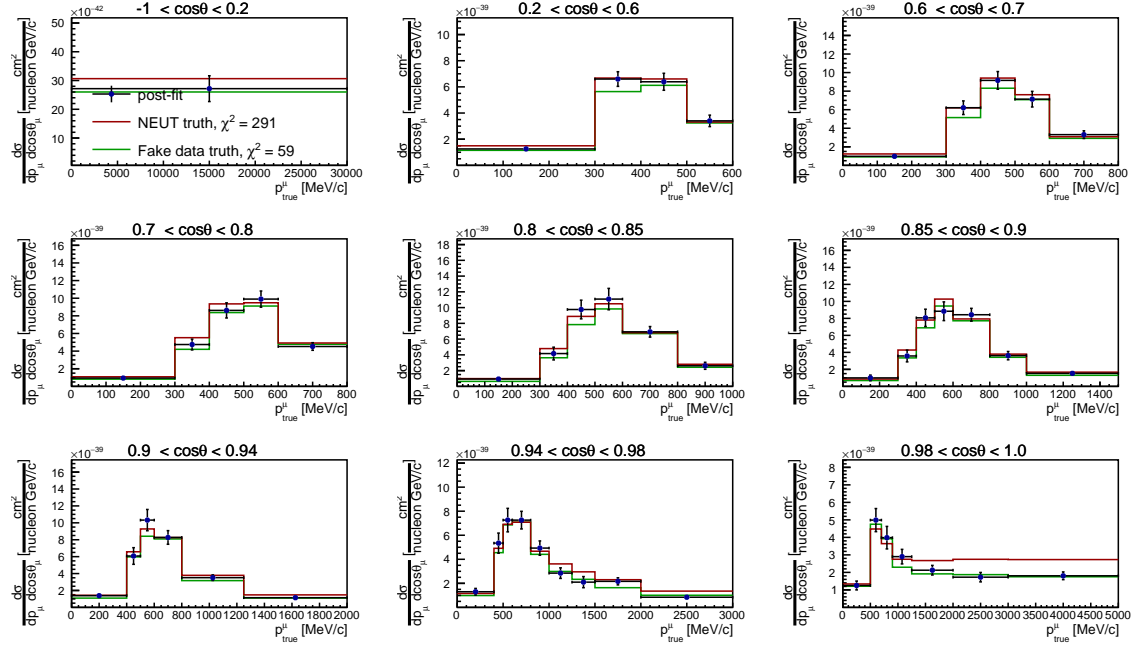


Figure B.59: Flux integrated cross section on carbon, result for a fit to the (fake) data set using GENIE generated events. Each plot is for a given angle bin according to its title and the x axis is the muon momentum.

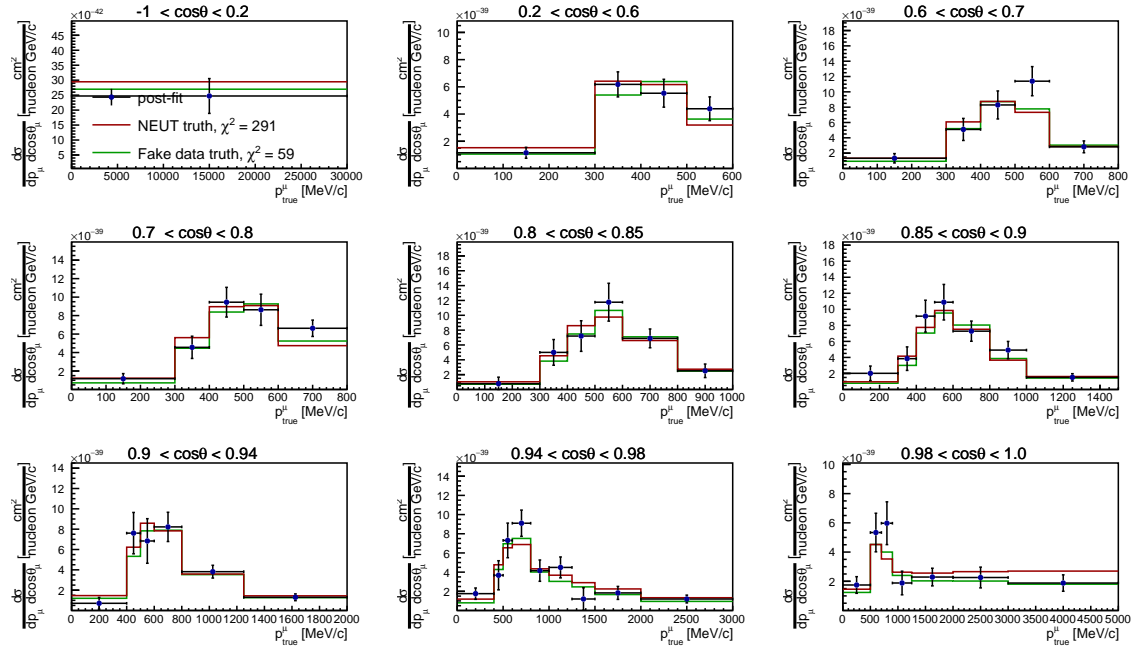


Figure B.60: Flux integrated cross section on oxygen, result for a fit to the (fake) data set using GENIE generated events. Each plot is for a given angle bin according to its title and the x axis is the muon momentum.

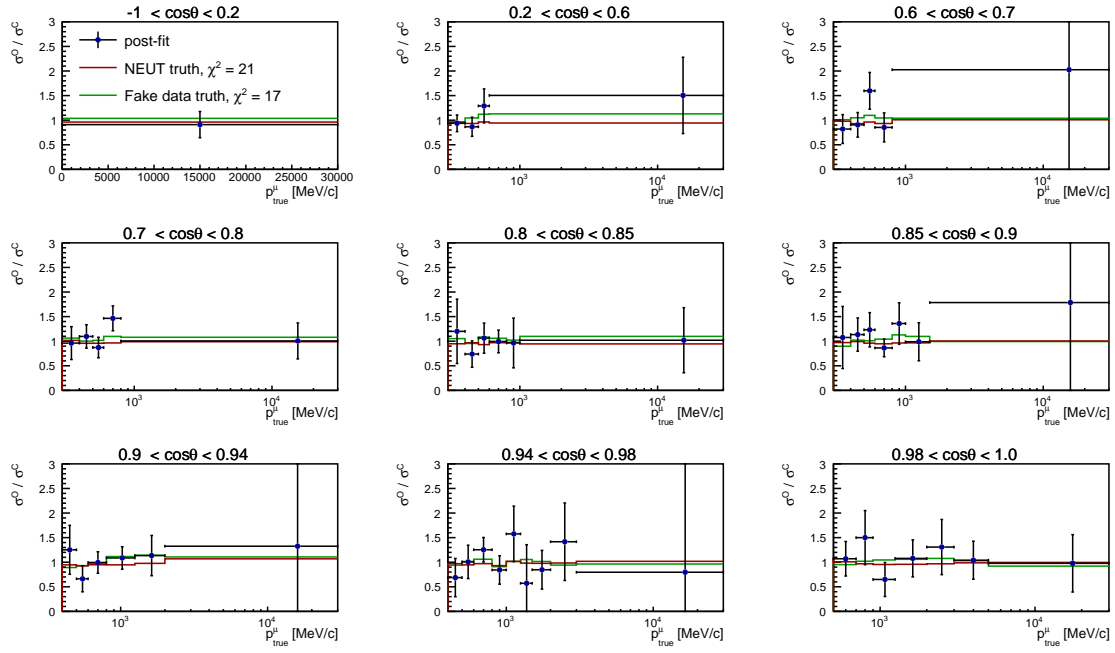


Figure B.61: Oxygen/carbon cross section ratio, result for a fit to the (fake) data set using GENIE generated events. Each plot is for a given angle bin according to its title and the x axis is the muon momentum.

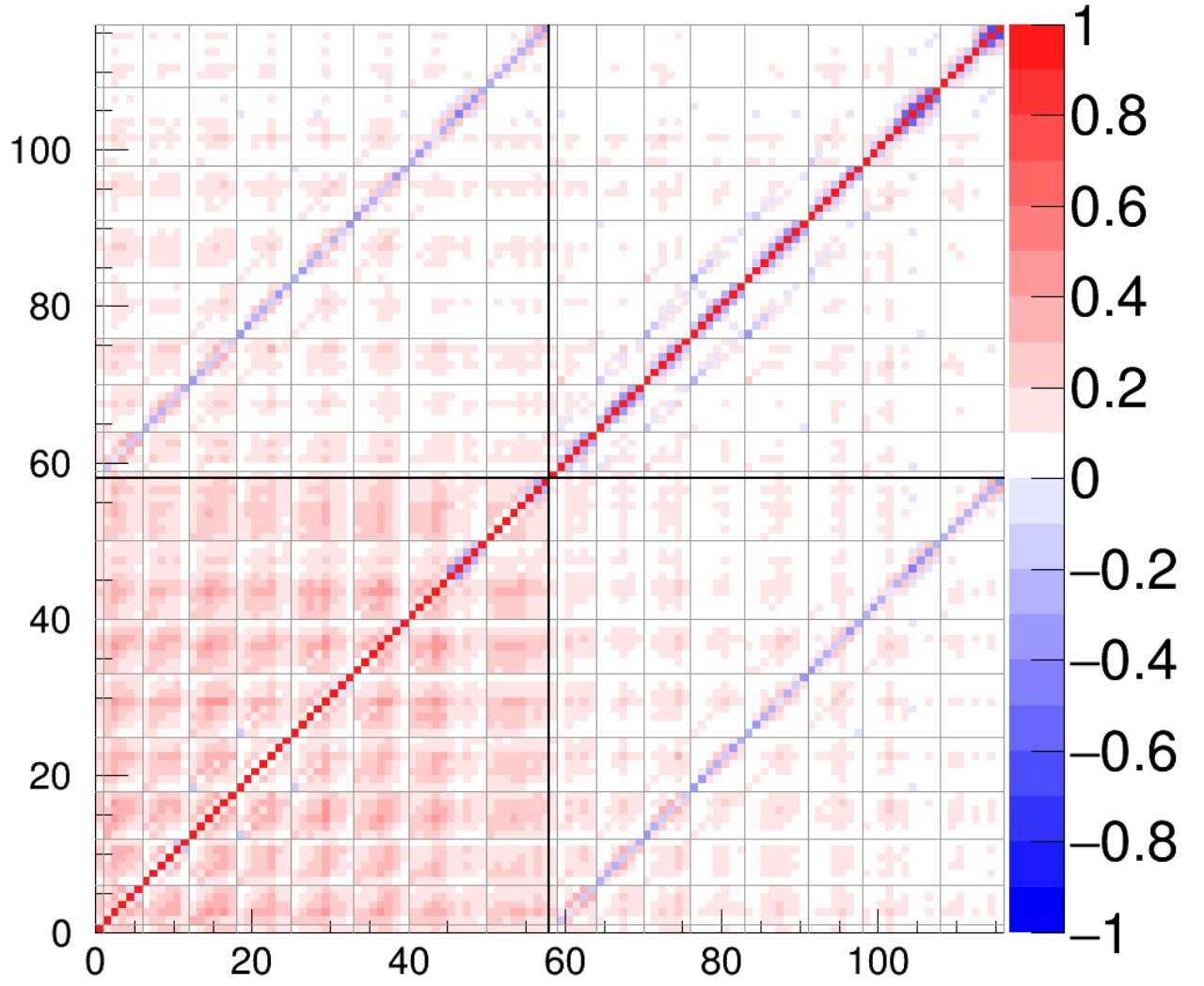


Figure B.62: Final correlation matrix for the cross-section results for a fit to the (fake) data set using GENIE generated events. The sub-matrices for the different $\cos \theta_\mu$ bins are separated by dashed black lines. Bins from 0 to 57 corresponds to carbon interactions, from 58 to 115 to oxygen interactions.

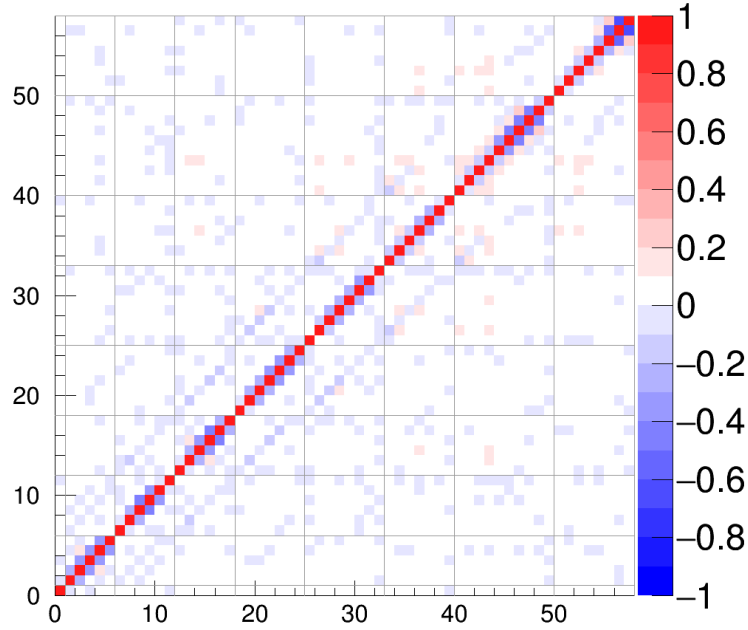


Figure B.63: Final correlation matrix for the cross-section ratio results for a fit to the (fake) data set using GENIE generated events. The sub-matrices for the different $\cos \theta_\mu$ bins are separated by dashed black lines.

B.8 Unblinded sideband studies

A first step towards unblinding real data was the use of data as control samples, whereas the signal region content is coming from NEUT MC samples. NEUT full statistics are used as nominal MC input, without any statistical fluctuations and reweighted to the data POT.

The post-fit parameters, that are plotted in Fig. B.64, B.65, B.66 and B.67, show good agreement with prior values. Then it is to be seen in the event distributions at the reconstructed level, shown by sample in Fig. B.69, that the fit has a good ability to recover from simulated to real data discrepancies in the background regions. This validates the test of the purpose of this data control sample fit. The final extracted cross-section results, Figures B.70 and B.71, and the cross-section ratio, Fig. B.72, show a good agreement with the cross section calculated from simulated events.

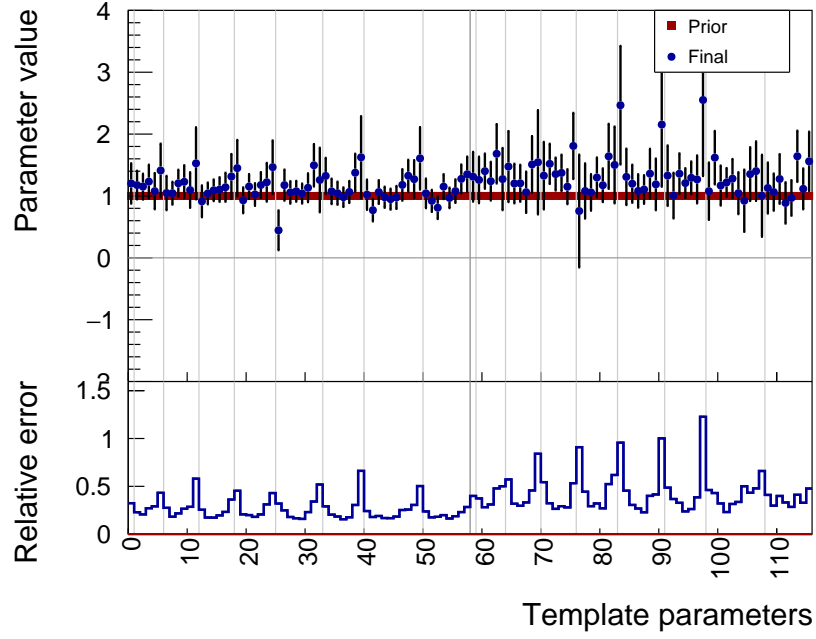


Figure B.64: Prior and post-fit template parameter values and their associated uncertainty for a fit to the (fake) data set that has signal samples from NEUT MC and control samples from real data. The first 58 parameters correspond to the carbon parameters (c_i) and the next 58 parameters are the ones on oxygen (o_i).

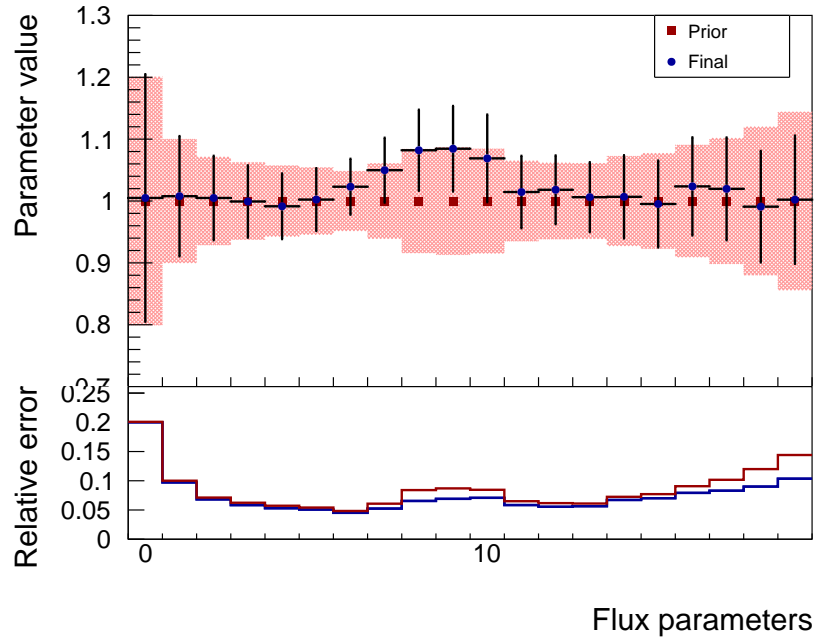


Figure B.65: Prior and post-fit flux parameter values and their associated uncertainty for a fit to the (fake) data set that has signal samples from NEUT MC and control samples from real data.

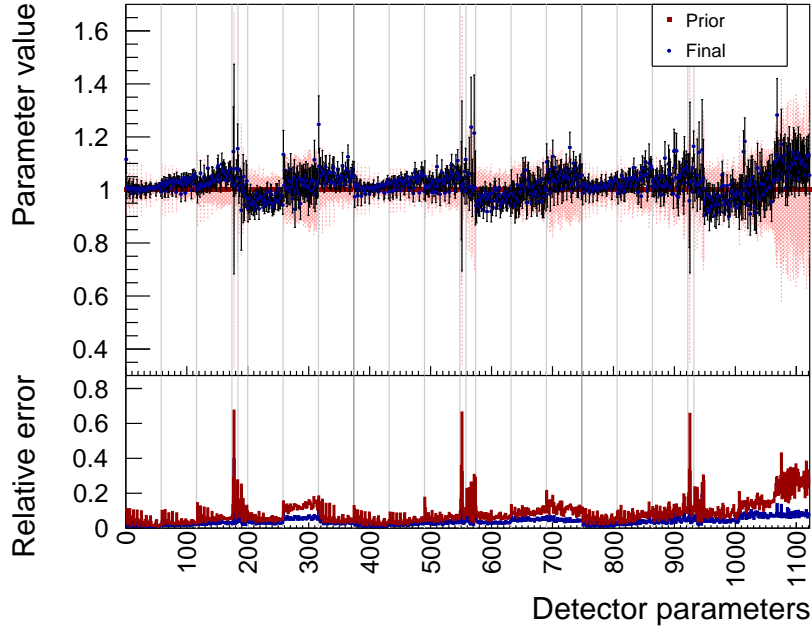


Figure B.66: Prior and post-fit detector parameter values and their associated uncertainty for a fit to the (fake) data set that has signal samples from NEUT MC and control samples from real data.

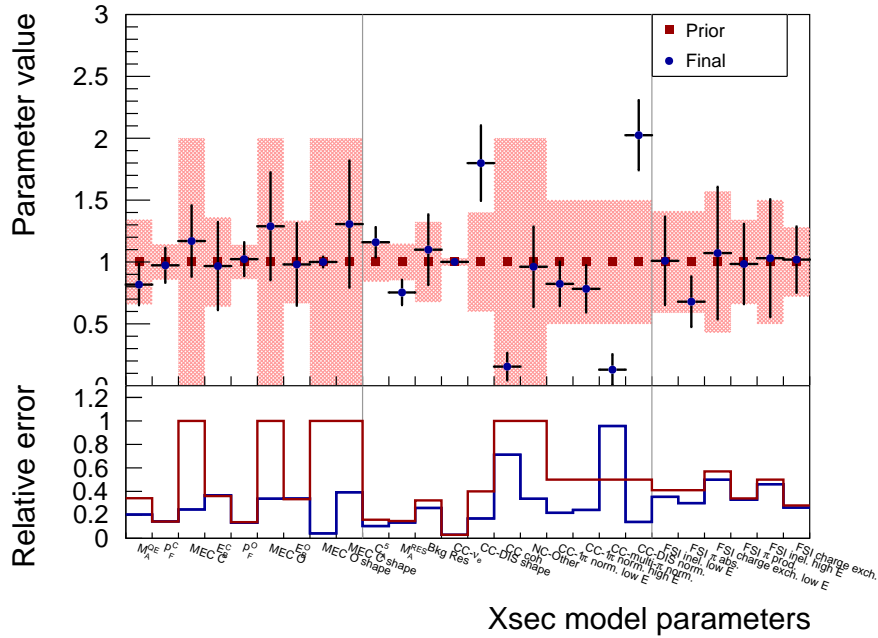


Figure B.67: Prior and post-fit cross-section model parameter values and their associated uncertainty for a fit to the (fake) data set that has signal samples from NEUT MC and control samples from real data.

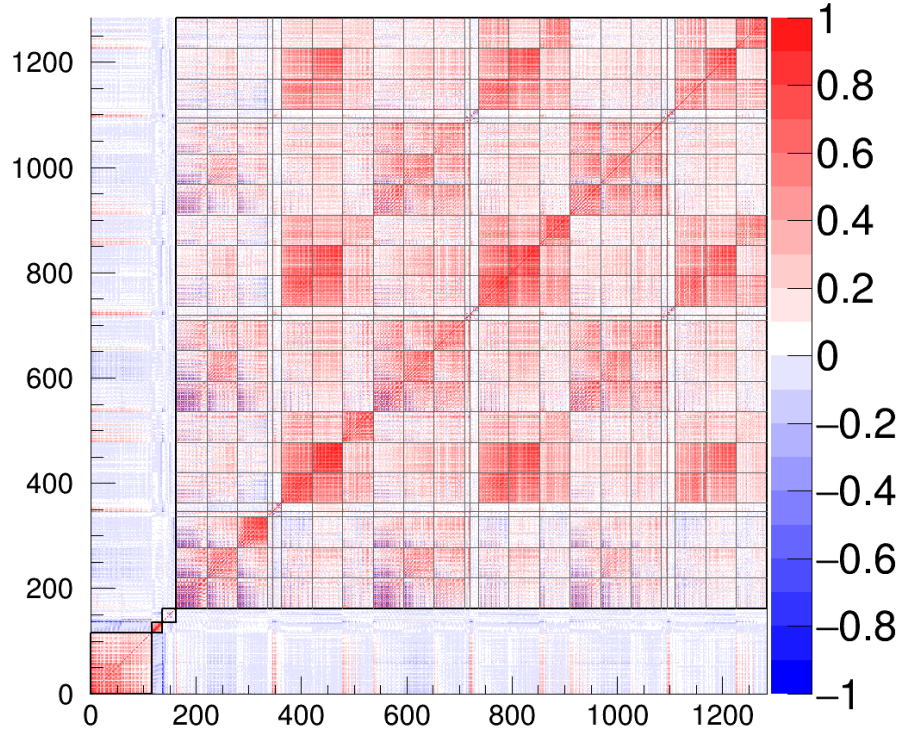


Figure B.68: Post-fit correlation matrix of all the fit parameters for a fit to the (fake) data set that has signal samples from NEUT MC and control samples from real data. The sub-matrices for the different types of parameters are separated by dashed black lines. Parameters with bins from 0 to 57 corresponds to the c_i 's, from 58 to 115 o_i 's, from 116 to 135 flux, from 136 to 161 cross-section model and from 162 to 1283 detector parameters (from 162 to 1109 for the bottom one, as the CC- $1\pi^+$ Michel electron sideband is removed).

B. Fit validation

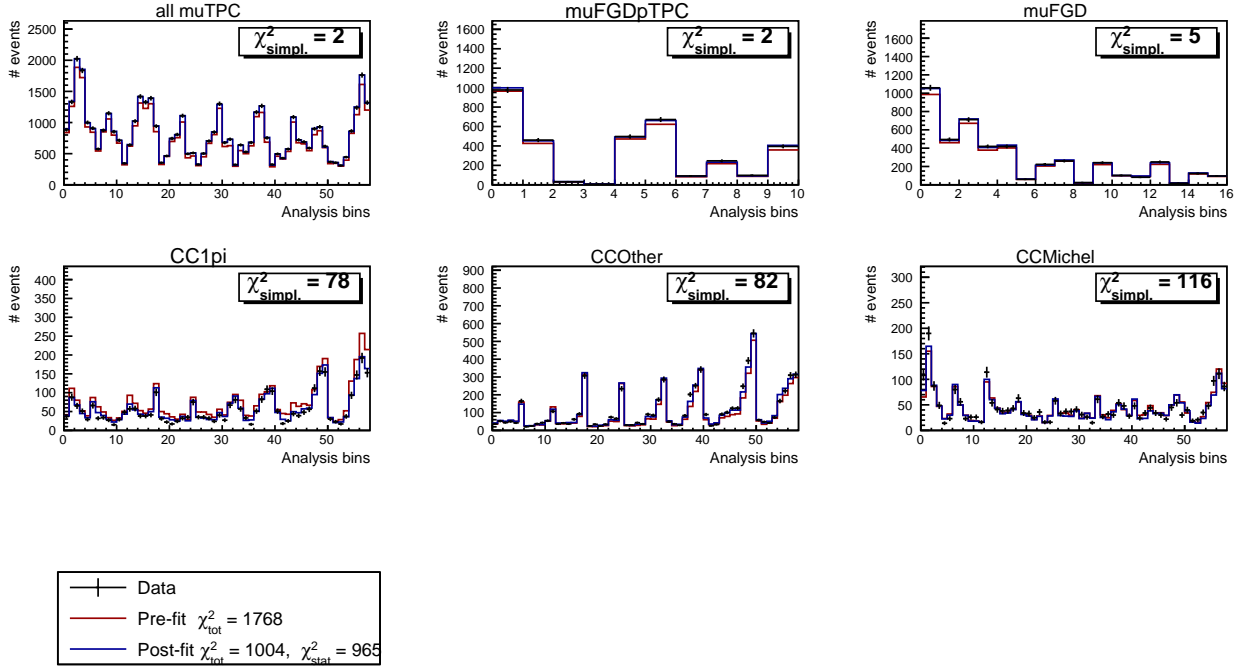


Figure B.69: Prior (blue) and post-fit (red) signal events compared to data (black) distributed in $p_\mu, \cos\theta_\mu$ analysis bins for a fit to the (fake) data set that has signal samples from NEUT MC and control samples from real data. Each plot is for a specific signal or sideband region according to its title ; all the muTPC topologies are grouped together in the top left plot.

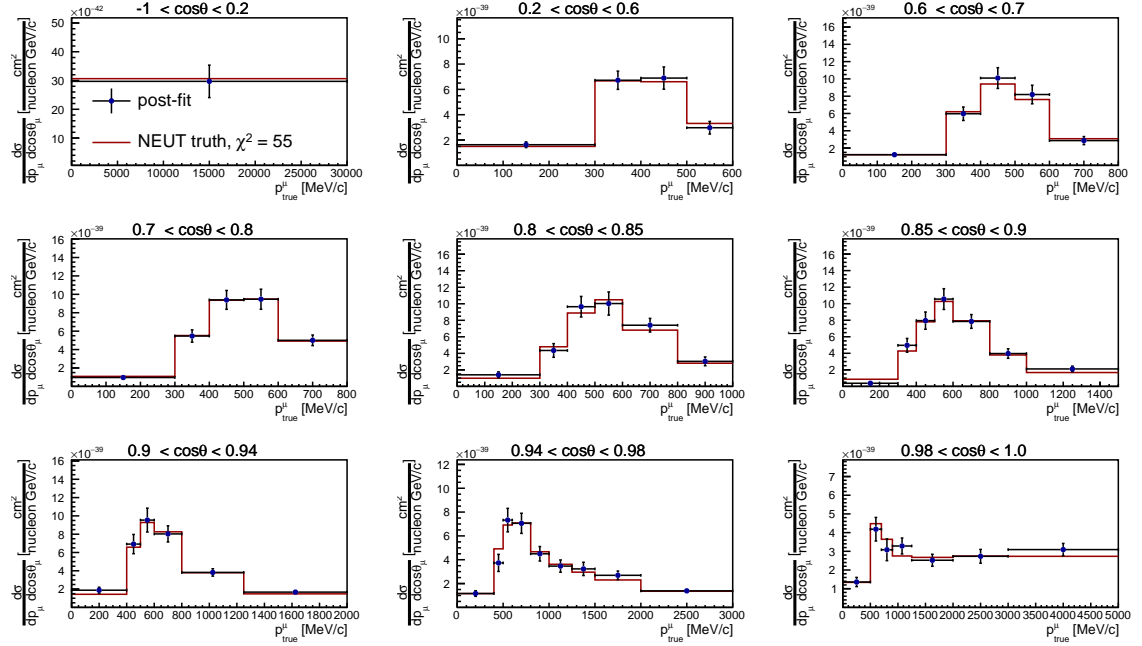


Figure B.70: Flux integrated cross section on carbon, result for a fit to the (fake) data set that has signal samples from NEUT MC and control samples from real data. Each plot is for a given angle bin according to its title and the x axis is the muon momentum.

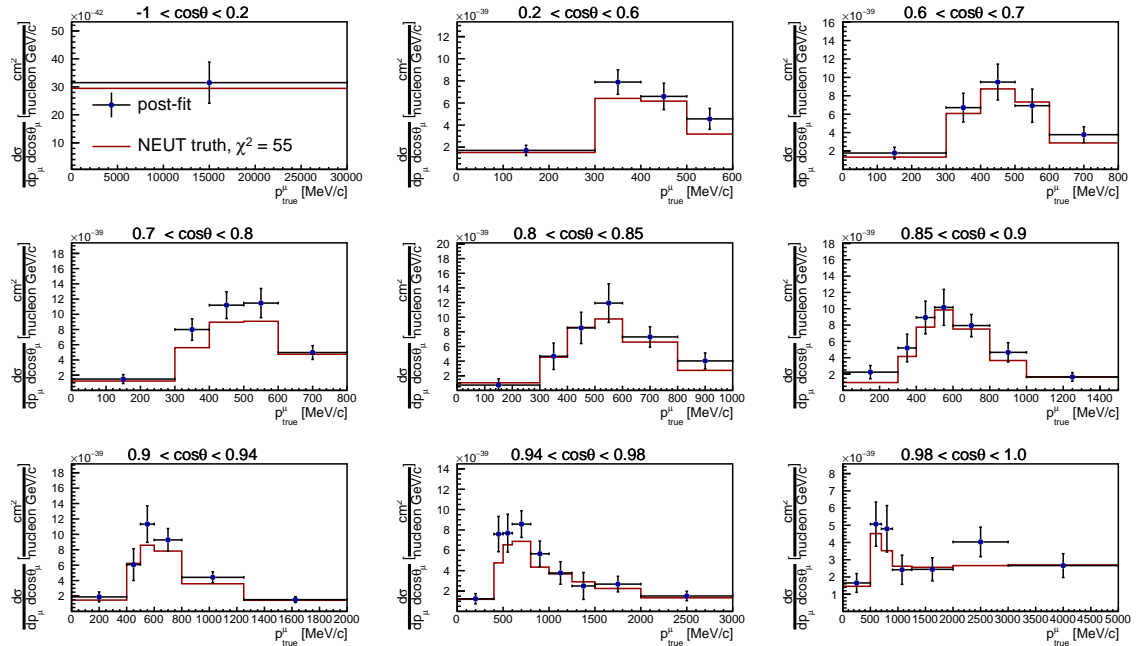


Figure B.71: Flux integrated cross section on oxygen, result for a fit to the (fake) data set that has signal samples from NEUT MC and control samples from real data. Each plot is for a given angle bin according to its title and the x axis is the muon momentum.

B. Fit validation

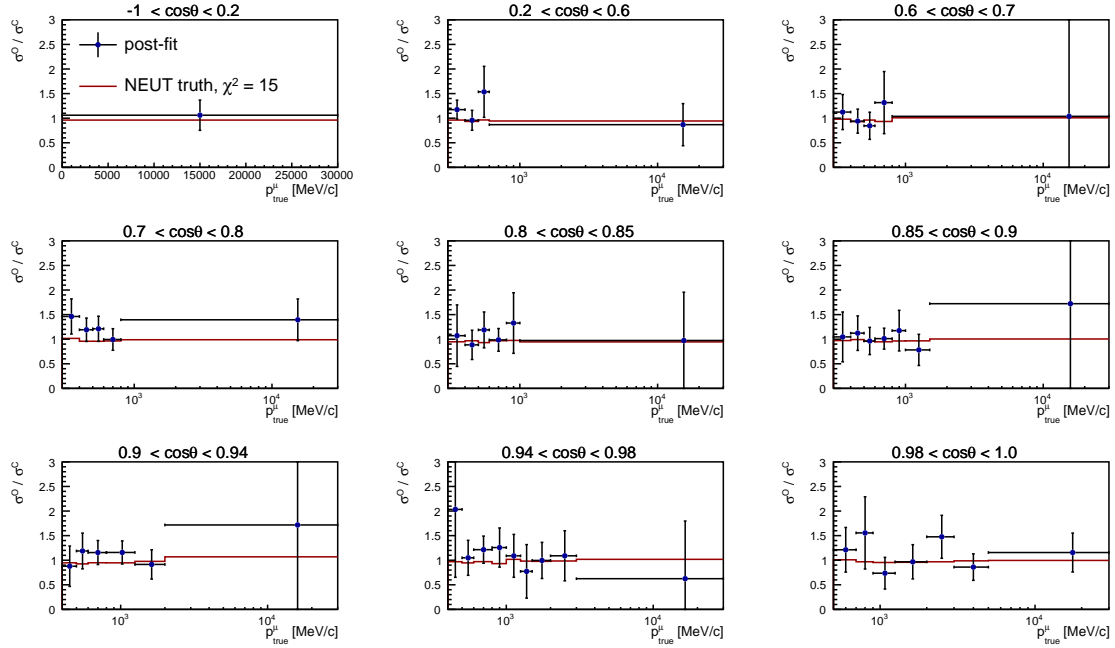


Figure B.72: Oxygen/carbon cross section ratio, result for a fit to the (fake) data set that has signal samples from NEUT MC and control samples from real data. Each plot is for a given angle bin according to its title and the x axis is the muon momentum.

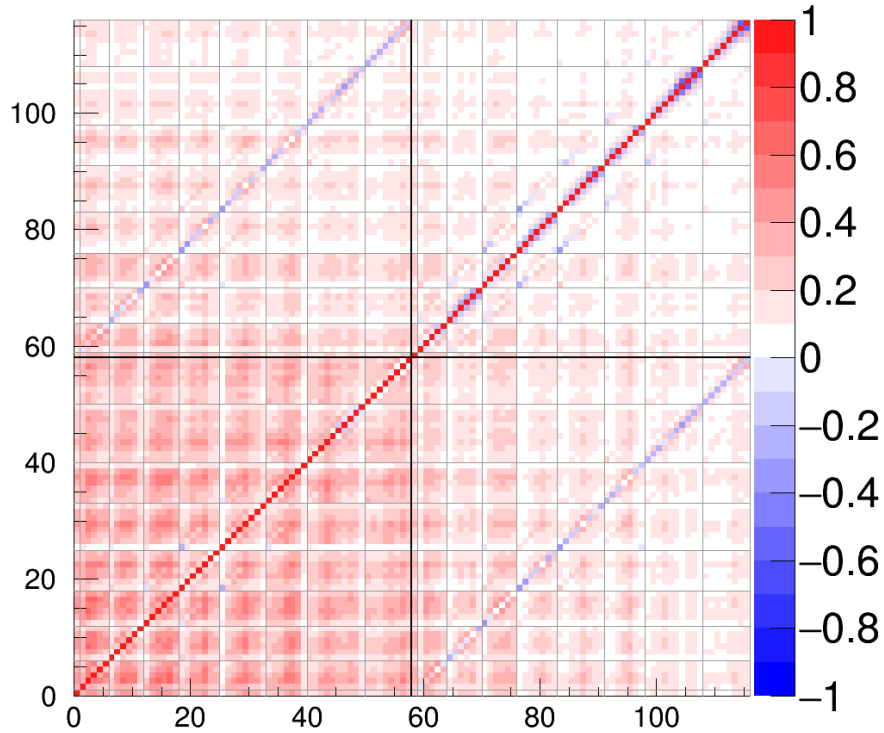


Figure B.73: Final correlation matrix for the cross-section results for a fit to the (fake) data set that has signal samples from NEUT MC and control samples from real data. The sub-matrices for the different $\cos\theta_{\mu}$ bins are separated by dashed black lines. Bins from 0 to 57 corresponds to carbon interactions, from 58 to 115 to oxygen interactions.

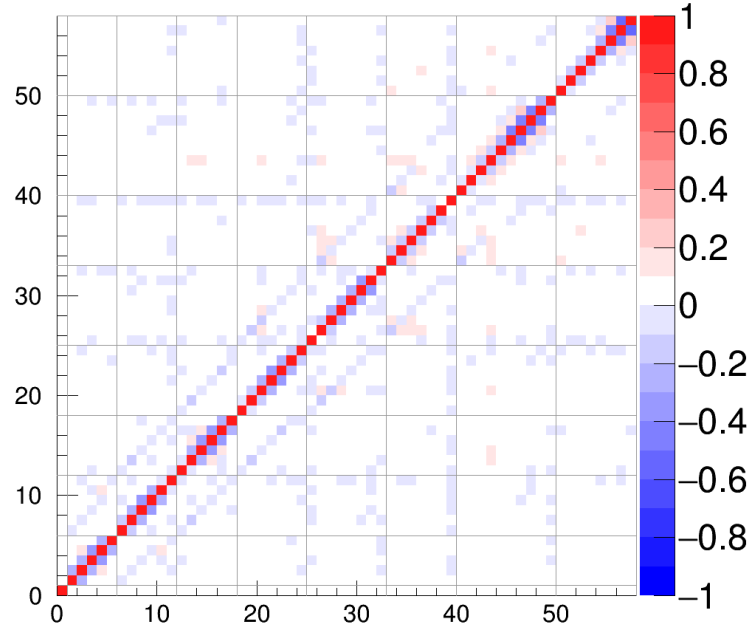


Figure B.74: Final correlation matrix for the cross-section ratio results for a fit to the (fake) data set that has signal samples from NEUT MC and control samples from real data. The sub-matrices for the different $\cos\theta_\mu$ bins are separated by dashed black lines.

B.9 Summary of the fit validation studies

Table B.1 gives an overview of χ^2 values for each fake data fit described in the previous sections (Sec.B.2-B.6-B.7). Methods to calculate the different χ^2 's are detailed in Sec.B.5.

Table B.1: Summary of the χ^2 values for the fits with different kind of fake data inputs. We remind that the number of kinematic bins is 58, thus the number of cross-section parameters is twice this number (carbon and oxygen) 116 and the number of ratio parameters is 58. The numbers indicated in brackets next to χ^2 values are their associated probability for a number of d.o.f. equal to 116 for the cross sections and equal to 58 for the ratio.

Fake data	$\chi^2_{\text{pre-fit}}$	χ^2_{postfit}	$\chi^2_{\text{xsec, N}}$	$\chi^2_{\text{xsec, FD}}$	$\chi^2_{\text{ratio, N}}$	$\chi^2_{\text{ratio, FD}}$
Nominal NEUT (Asimov)	0	0	0	0 (1.0)	0	0 (1.0)
NEUT with stat. fluct.	1135	972	115	115 (0.51)	55	55 (0.59)
NEUT with stat. fluct. and syst. param. throw	2612	1076	296	132 (0.15)	44	35 (0.99)
GENIE	1914	748	291	59 (0.999)	21	17 (0.999)
Data CS and NEUT signal	1768	1004	55	(no truth)	15	(no truth)

Bibliography

- [1] A. Sakharov. Violation of CP invariance, C asymmetry, and baryon assymetry of the universe. *Soviet Physics Uspecki*, Volume 34, 1991.
- [2] CP Violation in the Quark Sector Particle Data Group 2017. <http://pdg.lbl.gov/2017/reviews/rpp2017-rev-cp-violation.pdf>. Accessed: 10-09-2019.
- [3] Y. Fukuda et al. (Super-Kamiokande Collaboration). Evidence for Oscillation of Atmospheric Neutrinos. *Physical Review Letters*, Volume 81, 1998.
- [4] K. Abe et al. (The T2K Collaboration). Search for cp violation in neutrino and antineutrino oscillations by the t2k experiment with 2.2×10^{21} protons on target. *Physical Review Letters*, Volume 121, 2018.
- [5] E. Fermi. Versuch einer Theorie der β -Strahlen I. *Zeitschrift fuer Physik*, volume 88, 1934.
- [6] H. Bethe and R. Peierls. The Neutrino. *Nature*, Volume 133, 1934.
- [7] F. Reines and C. Cowan. The Neutrino. *Nature*, 178, 1956.
- [8] G. Danby et al. Observation of High-Energy Neutrino Reactions and the Existence of Two Kinds of Neutrinos. *Physical Review Letters*, Volume 9, 1962.
- [9] T. Lee and C. Yang. Question of parity conservation in weak interactions. *Physical Review*, Volume 104, 1956.
- [10] C. Wu et al. Experimental Test of Parity Conservation in Beta Decay. *Physical Review*, Volume 105, 1957.
- [11] R. Garwin. Observation of the Failure of Conservation of Parity and Charge Conjugation in Meson Decays: the Magnetic Moment of the Free Muon. *Physical Review*, Volume 105, 1957.
- [12] L. Landau. On the conservation laws for weak interactions. *Nuclear Physics*, Volume 3, 1957.
- [13] A. Salam. On parity conservation and neutrino mass. *Il Nuovo Cimento*, Volume 5, 1957.
- [14] T. Lee and C. Yang. Parity nonconservation and a two-component theory of the neutrino. *Physical Review*, Volume 105, 1957.

- [15] M. Goldhaber et al. Helicity of neutrino. *Physical Review*, Volume 109, 1958.
- [16] M. Perl et al. Evidence for Anomalous Lepton Production in e^+e^- Annihilation. *Physical Review Letters*, Volume 35, 1975.
- [17] S. Weinberg. A Model of Leptons. *Physical Review Letters*, Volume 19, 1967.
- [18] A. Salam. Weak and Electromagnetic Interactions. *Proceedings of the Eighth Nobel Symposium*, 1968.
- [19] A. Blondel. The third family of neutrinos. *arXiv:1812.11362v2*, 2019.
- [20] DONUT Collaboration. Observation of τ neutrino interactions. *Physics Letters B*, Volume 504, 2001.
- [21] LEP Collaborations. Tests of the Standard Model. *International Europhysics Conference on High Energy Physics*, 1999.
- [22] ALEPH, DELPHI, L3, OPAL, and SLD Collaborations, and LEP Electroweak Working Group, and SLD Electroweak Group, and SLD Heavy Flavour Group. Precision Electroweak Measurements on the Z Resonance. *Physics Reports*, Volume 427, 2006.
- [23] R. Davis, D. S. Harmer, and K. C. Hoffman. Search for Neutrinos from the Sun. *Physical Review Letters*, Volume 20, 1968.
- [24] J. N. Abdurashitov et al. Solar Neutrino Flux Measurements by the Soviet-American Gallium Experiment (SAGE) for half the 22-Year Solar Cycle. *Journal of Experimental and Theoretical Physics*, Volume 95, 2002.
- [25] M. Cribier et al. Results of the Whole GALLEX Experiment. *Nuclear Physics B - Proceedings Supplements*, Volume 70, 1999.
- [26] Y. Fukuda et al. Measurements of the Solar Neutrino Flux from Super-Kamiokande's First 300 Days. *Physical Review Letters*, Volume 81, 1998.
- [27] B. Pontecorvo. Neutrino Experiments and the Problem of Conservation of Leptonic Charge. *Journal of Experimental and Theoretical Physics*, Volume 26, 1968.
- [28] SNO Collaboration. Direct Evidence for Neutrino Flavor Transformation from Neutral-Current Interactions in the Sudbury Neutrino Observatory. *Physical Review Letters*, Volume 89, 2002.
- [29] Y. Fukuda et al. (Super-Kamiokande Collaboration). Measurement of the flux and zenith-angle distribution of upward throughgoing muons by super-kamiokande. *Physical Review Letters*, Volume 82, 1999.
- [30] Y. Ashie et al. (Super-Kamiokande Collaboration). Measurement of atmospheric neutrino oscillation parameters by super-kamiokande i. *Physical Review D*, Volume 71, 2005.
- [31] Y. Ashie et al. (Super-Kamiokande Collaboration). Three flavor neutrino oscillation analysis of atmospheric neutrinos in super-kamiokande. *Physical Review D*, Volume 74, 2006.
- [32] B. Pontecorvo. Mesonium and anti-mesonium. *Sov. Phys. JETP* 6, 1957.

-
- [33] S. Sakata Z. Maki, M. Nakagawa. Remarks on the Unified Model of Elementary Particles. *Progress of Theoretical Physics*, Volume 28, 1962.
- [34] M. Blennow, P. Coloma, E. Fernandez-Martinez, J. Hernandez-Garcia, and J. Lopez-Pavon. Non-Unitarity, sterile neutrinos, and Non-Standard neutrino Interactions. *Journal of High Energy Physics*, 2017.
- [35] W. Rodejohann. Non-unitary lepton mixing matrix, leptogenesis and low-energy CP violation. *A Letters Journal Exploring the Frontiers of Physics*, 2009.
- [36] E. Kh. Akhmedov. Neutrino Physics. *Lectures given at Trieste Summer School in Particle Physics, June 7-9, 2000*.
- [37] C. Giganti, S. Lavignac, and M. Zito. Neutrino oscillations: the rise of the PMNS paradigm. *Progress in Particle and Nuclear Physics*, Volume 98, 2017.
- [38] B. Kayser. Neutrino Oscillation Physics. *arXiv:1206.4325 [hep-ph]*, June 2012.
- [39] GALLEX Collaboration. GALLEX solar neutrino observations: results for GALLEX IV. *Physics Letters B*, Volume 447, 1999.
- [40] SAGE Collaboration. Measurement of the solar neutrino capture rate with gallium metal. III. Results for the 2002-2007 data-taking period. *Physical Review C*, Volume 80, 2009.
- [41] GNO Collaboration. Complete results for five years of GNO solar neutrino observations. *Physics Letters B*, Volume 616, 2005.
- [42] SNO Collaboration. Independent Measurement of the Total Active ^8B Solar Neutrino Flux Using an Array of ^3He Proportional Counters at the Sudbury Neutrino Observatory. *Physical Review Letters*, Volume 101, 2008.
- [43] Borexino Collaboration. Final results of Borexino Phase-I on low-energy solar neutrino spectroscopy. *Physical Review D*, Volume 89, 2014.
- [44] M. Aartsen (IceCube Collaboration). Measurement of Atmospheric Neutrino Oscillations at 6–56 GeV with IceCube DeepCore. *Physical Review Letters*, Volume 120, 2018.
- [45] The Hyper-Kamiokande Working Group. A Long Baseline Neutrino Oscillation Experiment Using J-PARC Neutrino Beam and Hyper-Kamiokande. *Document submitted to 18th J-PARC PAC meeting in May 2014*, 2014.
- [46] The DUNE Collaboration. Long-Baseline Neutrino Facility (LBNF) and Deep Underground Neutrino Experiment (DUNE) Conceptual Design Report. *The Physics Program for DUNE at LBNF*, Volume 2, 2015.
- [47] J. K. Ahn et al (RENO Collaboration). Observation of Reactor Electron Antineutrinos Disappearance in the RENO Experiment. *Physical Review Letters*, Volume 108, 2012.
- [48] Y. Abe et al. (Double Chooz Collaboration). Ortho-Positronium Observation in the Double Chooz Experiment. *Journal of High Energy Physics*, 2014.
- [49] Y. Abe et al. (Double Chooz Collaboration). First Measurement of θ_{13} from Delayed Neutron Capture on Hydrogen in the Double Chooz Experiment. *Physics Letters B*, Volume 723, 2013.

- [50] F. P. An et al. (Daya Bay Collaboration). New Measurement of Antineutrino Oscillation with the Full Detector Configuration at Daya Bay. *Physical Review Letters*, Volume 115, 2015.
- [51] F. P. An et al. (Daya Bay Collaboration). Independant Measurement of the Neutrino Mixing Angle 13 via Neutron Capture on Hydrogen at Daya Bay. *Physical Review D*, Volume 90, 2014.
- [52] K2K Collaboration. Measurement of neutrino oscillation by the K2K Experiment. *Physical Review D*, Volume 74, 2006.
- [53] K. Abe et al. (The T2K Collaboration). The T2K Experiment. *Nucl. Instrum. Meth. A*, Volume 659, 2011.
- [54] D. Ayres et al (NOvA Collaboration). NOvA proposal to Build a 30 kiloton Off-Axis Detector to Study Neutrino Oscillations in the Fermilab NuMI Beamline. *Fermilab-Proposal-0929*, 2005.
- [55] J. A. Formaggio and G. P. Zeller. From eV to EeV: Neutrino Cross Sections Across Energy Scales. *Rev. Mod. Phys.*, Volume 84, 2012.
- [56] C. H. Llewellyn Smith. Neutrino Reactions at Accelerator Energies. *Phys. Rept.*, Volume 3, 1972.
- [57] A. Bodek et al. Vector and axial nucleon form factor: A duality constrained parameterization. *Eur. Phys. J. C* 53, 2008.
- [58] Geoffrey F. Chew and G. C. Wick. The impulse approximation. *Physical Review*, Volume 85, 1952.
- [59] D. Rein and L. Sehgal. Neutrino-excitation of baryon resonances and single pion production. *Annals of Physics*, Volume 133, 1981.
- [60] D. Rein and L.M. Sehgal. Pcac and the deficit of forward muons in π^+ production by neutrinos. *Physics Letters B*, Volume 657, 2007.
- [61] et al. O. Benhar. Electron- and neutrino-nucleus scattering in the impulse approximation regime. *Physical Review D*, Volume 72, 2005.
- [62] L. Pickering. Examining nuclear effects in neutrino interactions with transverse kinematic imbalance. *JPS Conference Proceedings*, Volume 12, 2016.
- [63] R. Gran et al. (K2K Collaboration). Measurement of the quasielastic axial vector mass in neutrino interactions on oxygen. *Physical Review D*, Volume 74, 2006.
- [64] A. A. Aguilar-Arevalo et al. (MiniBooNE Collaboration). First measurement of the muon neutrino charged current quasielastic double differential cross section. *Physical Review D*, Volume 81, 2010.
- [65] J. Nieves, I. R. Simo, and M. J. V. Vacas. Inclusive charged-current neutrino-nucleus reactions. *Physical Review C*, Volume 83, 2011.
- [66] M. Martini, M. Ericson, G. Chanfray, and J. Marteau. A unified approach for nucleon knock-out, coherent and incoherent pion production in neutrino interactions with nuclei. *Physical Review C*, Volume 80, 2009.

-
- [67] K. Abe and al. (The T2K Collaboration). Characterization of nuclear effects in muon-neutrino scattering on hydrocarbon with a measurement of final-state kinematics and correlations in charged-current pionless interactions at T2K. *Physical Review D*, Volume 98, 2018.
- [68] S. Boyd et al. Comparison of Models of Neutrino-Nucleus Interactions. *AIP Conference Proceedings*, Volume 1189, 2009.
- [69] S. Dytman. Neutrino event generators. *AIP Conference Proceedings*, Volume 896, 2007.
- [70] P. de Perio. NEUT pion FSI. *AIP Conference Proceedings*, Volume 1405, 2011.
- [71] T. Golan. Modeling nuclear effects in NuWro Monte Carlo neutrino event generator. *Ph.D thesis, University of Wroclaw*, 2014.
- [72] Y. Hayato. A neutrino interaction simulation program library NEUT. *Acta Physica Polonica B*, Volume 40, 2009.
- [73] Y. Hayato. Neut. *Nuclear Physics B - Proceedings Supplements*, Volume 112, 2002.
- [74] C. Andreopoulos et al. The GENIE Neutrino Monte Carlo Generator. *Nucl. Instrum. Meth. A*, Volume 614, 2010.
- [75] T. Golan, C. Juszczak, and J. T. Sobczyk. Effects of final-state interactions in neutrino-nucleus interactions. *Physical Review C*, Volume 86, 2012.
- [76] T. Leitner, O. Buss, L. Alvarez-Ruso, and U. Mosel. Electron-nucleus and neutrino-nucleus scattering from the quasielastic to the resonance region. *Physical Review C*, Volume 79, 2009.
- [77] D. Casper et al. The Nuance neutrino physics simulation, and the future. *Nucl. Phys. Proc. Suppl.*, Volume 112, 2002.
- [78] A. Bodek and J. L. Ritchie. Further studies of Fermi-motion effects in lepton scattering from nuclear targets. *Physical Review D*, Volume D24, 1981.
- [79] R. Gran et al. (KEK Collaboration). Measurement of the quasielastic axial vector mass in neutrino interactions on oxygen. *Physical Review D*, Volume 74, 2006.
- [80] J. Nieves, I. R. Simo, and M. V. Vacas. The nucleon axial mass and the MiniBooNE quasielastic neutrino–nucleus scattering problem. *Physical Letters B*, Volume 707, 2012.
- [81] M. Gluck, E. Reya, and A. Vogt. Dynamical parton distributions revisited. *The European Physical Journal J.*, Volume C5, 1998.
- [82] A. Bodek and U. K. Yang. Modeling Neutrino and Electron Scattering Cross Sections in the Few GeV Region with Effective LO PDFs. *AIP Conference Proceedings*, Volume 670, 2003.
- [83] M. Martini et al. Energy reconstruction effects in neutrino oscillation experiments and implications for the analysis. *Physical Review D*, Volume 85, 2012.
- [84] J. Nieves et al. Neutrino energy reconstruction and the shape of the charged current quasielastic-like total cross section. *Physical Review D*, Volume 85, 2012.

- [85] A. Ankowski et al. Comparison of the calorimetric and kinematic methods of neutrino energy reconstruction in disappearance experiments. *Physical Review D*, Volume 92, 2015.
- [86] K. Abe et al. (The T2K Collaboration). Measurement of neutrino and antineutrino oscillations by the t2k experiment including a new additional sample of ν_e interactions at the far detector. *Physical Review D*, Volume 96, 2017.
- [87] K. Abe et al. (The T2K Collaboration). Search for cp violation in neutrino and antineutrino oscillations by the t2k experiment with 2.2×10^{21} protons on target. *Physical Review Letters*, Volume 121, 2018.
- [88] K. Abe et al. (The T2K Collaboration). Design and performance of the muon monitor for the T2K neutrino oscillation experiment. *Nucl. Instrum. Meth. A*, Volume 624, 2010.
- [89] K. Abe et al. (The T2K Collaboration). The T2K Neutrino Flux Prediction. *Physical Review D*, Volume 87, 2013.
- [90] A. Fiorentini et al. Flux Prediction and Uncertainty Update with NA61 2019 Thin Target Data and Negative Focussing Mode Predictions. *T2K Technical Note 217*, May 2017.
- [91] N. Abgrall et al. Report from the NA61/SHINE experiment at the CERN SPS. *Technical Report CERN-SPSC-2010-025*, 2010.
- [92] N. Abgrall et al. Measurements of Cross Sections and Charged Pion Spectra in Proton-Carbon Interactions at 31 GeV/c. *CERN-PH-EP-2011-005*, 2011.
- [93] FLUKA version 2008.3c. <http://www.fluka.org/fluka.php>. Accessed: 16-07-2019.
- [94] GEANT3, A detector description and simulation tool. *Application Software Group, Computing and Networks Division, CERN, Geneva*, 1993.
- [95] M. Shiozawa et al. (Super-Kamiokande Collaboration). Search for proton decay via $p \rightarrow e^+ \pi^0$ in a large water cherenkov detector. *Physical Review Letters*, Volume 81, 1998.
- [96] M. Shiozawa et al. (Super-Kamiokande Collaboration). Search for proton decay via $p \rightarrow e^+ \pi^0$ and $p \rightarrow \mu^+ \pi^0$ in a large water cherenkov detector. *Physical Review Letters*, Volume 102, 2009.
- [97] D. Renkera and E. Lorenz. Advances in solid state photon detectors. *Journal of Instrumentation*, Volume 4, 2009.
- [98] K. Abe et al. (The T2K Collaboration). The T2K ND280 Off-Axis Pi-Zero Detector. *Nucl. Instrum. Meth. A*, Volume 686, 2012.
- [99] K. Abe et al. (The T2K Collaboration). Measurement of the single π^0 production rate in neutral current neutrino interactions on water. *Physical Review D*, Volume 97, 2018.
- [100] K. Abe et al. (The T2K Collaboration). First measurement of the ν_μ charged-current cross section on a water target without pions in the final state. *Physical Review D*, Volume 97, 2018.
- [101] K. Abe et al. (The T2K Collaboration). Measurement of ν_μ and $\bar{\nu}_\mu$ charged current inclusive cross sections and their ratio with the T2K off-axis near detector. *Physical Review D*, Volume 96, 2017.

- [102] K. Abe et al. (The T2K Collaboration). The T2K Fine-Grained Detectors. *Nucl. Instrum. Meth. A*, Volume 696, 2012.
- [103] S. Oser. Elemental Composition of the FGD XY Modules. *T2K Technical Note 091*, February 2010.
- [104] D. Roberge. Elemental Composition of FGD Passive Water Modules. *T2K Technical Note 198*, January 2010.
- [105] K. Abe et al. (The T2K Collaboration). Measurement of inclusive double-differential ν_μ charged-current cross section with improved acceptance in the t2k off-axis near detector. *Physical Review D*, Volume 98, 2018.
- [106] K. Abe et al. (The T2K Collaboration). First measurement of the muon neutrino charged current single pion production cross section on water with the t2k near detector. *Physical Review D*, Volume 95, 2017.
- [107] G. Charpak, J. Derré, Y. Giomataris, and Ph. Rebourgeard. Micromegas, a multipurpose gaseous detector. *Nucl. Instrum. Meth. A*, Volume 478, 2002.
- [108] K. Abe et al. (The T2K Collaboration). Time projection chambers for the T2K near detectors. *Nucl. Instrum. Meth. A*, Volume 637, 2011.
- [109] C. Giganti and M. Zito. Particle Identification with the T2K TPC. *T2K Technical Note 001*, October 2009.
- [110] K. Abe et al. (The T2K Collaboration). Measurements of the T2K neutrino beam properties using the INGRID on-axis near detector. *Nucl. Instrum. Meth. A*, Volume 694, 2012.
- [111] K. Abe et al. (The T2K Collaboration). Measurement of the ν_μ charged current quasielastic cross section on carbon with the t2k on-axis neutrino beam. *Physical Review D*, Volume 91, 2015.
- [112] K. Abe et al. (The T2K Collaboration). Measurement of the muon neutrino inclusive charged-current cross section in the energy range of 1–3 gev with the t2k ingrid detector. *Physical Review D*, Volume 93, 2016.
- [113] R. Brun et al. ROOT An object oriented data analysis framework. *Nuclear Instrumentation and Methods in Physics Research*, Volume 389, 1997.
- [114] M. Buizza Avanzini, S. Emery, and L. Maret. Measurement of flux-integrated cross-section on Oxygen and Oxygen/Carbon ratio of CC-0 π events in FGD1+FGD2. *T2K Technical Note 338*, January 2019.
- [115] L. Maret et al. Backward migration uncertainty in FGD2. *T2K Technical Note 368*, November 2018.
- [116] A. Cervera et al. CC-0 π Multi-Topology Selection and Systematics in FGD1. *T2K Technical Note 216*, January 2015.
- [117] G. D’Agostini. A Multidimensional unfolding method based on Bayes’ theorem. *Nucl. Instrum. Meth. A*, Volume 362, 1995.

- [118] Statistics Particle Data Group 2019. <http://pdg.lbl.gov/2019/reviews/rpp2018-rev-statistics.pdf>. Accessed: 29-08-2019.
- [119] S. Wilks. The Large-Sample Distribution of the Likelihood Ratio for Testing Composite Hypotheses. *The Annals of Mathematical Statistics*, Volume 9, 1938.
- [120] S. Baker and R. Cousins. Clarification of the use of chi-square and likelihood functions in fits to histograms. *Nuclear Instruments and Methods in Physics Research*, Volume 221, 1984.
- [121] T2K Neutrino Flux Release 13a. <https://t2k.org/beam/NuFlux/FluxRelease/13arelease>. Accessed: 12-07-2019.
- [122] P. Bartet et al. ν_μ CC event selections in the ND280 tracker using T2K Run 2+3+4 data. *T2K Technical Note 212*, October 2015.
- [123] C. Riccio et al. Measurement of ν_μ and $\bar{\nu}_\mu$ CC- 0π cross-section on carbon. *T2K Technical Note 337*, October 2018.
- [124] F. James. MINUIT Function Minimization and Error Analysis: Reference Manual Version 94.1. *CERN-D-504*, *CERN-D-506*, 1994.
- [125] GEANT4, A Simulation Toolkit. <https://geant4.web.cern.ch/>. Accessed: 16-08-2019.
- [126] S. Bolognesi et al. NIWG model and uncertainties for 2017 oscillation analysis. *T2K Technical Note 315*, April 2017.
- [127] K. Abe et al. (The T2K Collaboration). Measurement of double-differential muon neutrino charged-current interactions on C_8H_8 without pions in the final state using the t2k off-axis beam. *Physical Review D*, Volume 93, 2016.
- [128] S. Bolognesi, F. Gizzarelli, E. Mazzucato, and M. Zito. Measurement of the ν_μ CC- 0π oxygen over carbon cross-section ratio in the FGD2. *T2K Technical Note 305*, December 2017.
- [129] R. Barlow and C. Beeston. Fitting using finite Monte Carlo samples. *Comp. Phys. Comm.* 77, pages 219–228, March 1993.
- [130] ROOT Documentation. <https://root.cern.ch/root/html524/TFractionFitter.html>. Accessed: 16-08-2019.